



HAL
open science

Quantitative and functional ultrafast ultrasound imaging of the human brain

Marion Imbault

► **To cite this version:**

Marion Imbault. Quantitative and functional ultrafast ultrasound imaging of the human brain. Medical Physics [physics.med-ph]. Université Sorbonne Paris Cité, 2017. English. NNT : 2017USPCC158 . tel-02075045

HAL Id: tel-02075045

<https://theses.hal.science/tel-02075045>

Submitted on 21 Mar 2019

HAL is a multi-disciplinary open access archive for the deposit and dissemination of scientific research documents, whether they are published or not. The documents may come from teaching and research institutions in France or abroad, or from public or private research centers.

L'archive ouverte pluridisciplinaire **HAL**, est destinée au dépôt et à la diffusion de documents scientifiques de niveau recherche, publiés ou non, émanant des établissements d'enseignement et de recherche français ou étrangers, des laboratoires publics ou privés.

Thèse de doctorat

De l'Université Sorbonne Paris Cité

Préparée à l'Université Paris Diderot

Ecole doctorale Physique en Ile de France

Institut Langevin – Ondes et images

Quantitative and functional ultrafast ultrasound imaging of the human brain

Présentée par Marion IMBAULT

Thèse de doctorat de physique des ondes - acoustique médicale

Dirigée par Mickaël TANTER

Présentée et soutenue publiquement à Paris le 3 Mai 2017

DEVAUX Bertrand, PU-PH, Université Paris V..... Président du jury
MELODELIMA David, CR, INSERM..... Rapporteur
REMENIERAS Jean-Pierre, IR, Université Tours.....Rapporteurs
BAMBER Jeffrey, Pr., Institute of Cancer Research..... Examineur
VILGRAIN Valérie, PU-PH, Université Paris VII..... Examinatrice
TANTER Mickaël, DR, INSERM Directeur de thèse



Acknowledgments

First, I would like to express my sincere gratitude to my supervisor, the research director of the “waves for medicine and biology” team in the Institut Langevin: Mickaël Tanter. I would like to thank him for his research brilliance, unfailing support, optimism, humbleness, and for his personal energy to motivate us all in our own projects. With Mickaël, a five-minute meeting can be life changing. He was a true model example of optimism, dynamism, patience, genius ideas and human side. I would like to thank him for choosing me as a PhD student, even if my background was not in ultrasound imaging, he had confidence on me and on my work aptitudes and he supported me from engineer to PhD and beyond.

I would also like to thank my committee members, Pr. M.D. Devaux, Dr. Melodelima, Dr. Remenieras, Pr Bamber and Pr. M.D. Vilgrain.

This thesis has been the subject of several collaborations. I would like to thank the neurosurgeons M.D. Laurent Capelle and M.D. Dorian Chauvet with whom I worked within the brain elastography and the neurofunctional ultrasound imaging projects. I would like to thank them for their time, patience, and for teaching me so many things on the brain and on how this amazing organ is working. I also sincerely would like to thank the team of the surgery room for integrated me so well into their hard daily work. I would like to thank as well the Prof. M.D. Valérie Vilgrain, head of the radiology department in Beaujon hospital, for the liver clinical trial work. She and her work really inspired me and our collaboration, along with Alex Faccinetto and Marco Dioguardi, was really positive.

In the Institut Langevin I would like to thank the current director, Arnaud Tourin, for all his commitment. I would like to thank Thomas Deffieux for his help on the aberration correction work. I would thank the other investigators of the medical team, Olivier Couture, Jean-François Aubry, Jean Provost and Mathieu Pernot for the all the informal scientific discussion and advices that inspired me. I would like to thank Patricia Daenens for her support and kindness, Khadija Bertino for her efficiency and her attentiveness, and Hicham Serroune for all the chocolate and experimental material provided. I would like to thank my old brother in science Bruno Osmanski with who I learned the time reversal, the speckle noise technique and the beloved VCZ theorem.

Regarding my closest colleagues, I would like to thank the first R31 office generation: Nicolas Viard, Emilie Benoit, Baptiste Jayet, Camille Jouveau, Fabien Mézière and Amir Nahas for warmly welcoming me in the lab in a cozy atmosphere with ficus and yukulele music. Then I would like to thank the second R31 generation: Clément Dupuis, Olivier Thouvenin, Jean-Baptiste Laudereau, Yann Desailly, Vincent Bacot, Aurélien Baeld and Peng Xiao. I want to thank them for the scientific support (viva WOOD formula!), KTV, formatting abilities (beautiful curves, LaTeX font,...), food profusion in the office, etc... All the moments we shared together helped me going through this PhD with a smile. I also would like to thank my offices mates in Bastille: Mafalda Correia for being my spa and conference roommate for the best and for the worst; Justine Robin for her unfailing support and dynamism and Jerome Baranger my

favorite green thumb geek. I would like to thank the master student I worked with, Antoine Tissier for his permanent enthusiasm, Claire Rabut for her determination, and Jack Sauvage for his faith in our project. I would like to thank Alexandre Dizeux for his brilliant support in scientific video making. I would like to thank Claudia Errico, Daria Andreioli and Thu-Mai Nguyen for their attentiveness and moral support. For the kindly and festive atmosphere in the lab I would like to thank all my colleagues, especially: Elodie T., Olivier V, Eliana, Charlie, Clément, Bastien, Charlotte, Marc, Marine, Stéphane, Gioia, Elodie P., Bruno, Guillaume, Martin, Line, Victor Alexandre H., and Philippe.

I would like to thank my closest friends outside the laboratory. The high school team: Sophie, Marie-Christine, Quynh-Vy, Sévrine, Céline, Cyril, Raphaëlle, Doan and Agnès. And I would like to thank them for all their love and support before the defense. The EPF team: Valentine, Julie, Caroline, Céline, Mathieu, Corinne, Christophe, Maxence, Sophie and William. And I would like to thank them for giving me the opportunity to cook a wedding cake, cooking can help a lot during a PhD. I also would like to thank Elise, Clémence and Anaïs for their moral support.

Enfin, je tiens à remercier tout particulièrement ma famille, qui a toujours cru en moi et a su m'encourager. Mes parents, qui ont éveillés ma curiosité depuis de longues années et qui m'ont soutenu pendant toute la durée de ma thèse. Mes sœurs, Tifenn qui connaissait si bien l'Institut Langevin, qui aimait venir m'y retrouver et qui me motivait au quotidien, et Cécilia qui n'a jamais douté que j'arriverai jusqu'au bout. Je voudrais également remercier de tout cœur Liliane, Mam, Marcel et Simone, Théo, Thierry et Florence, Betty et Jean Pierre ainsi que la famille Ponchon. Toute ma famille proche a joué un très grand rôle de par son soutien sans faille. Enfin je remercie Houssam et qui a su m'épauler jour après jour pour que je donne le meilleur de moi et que je mène jusqu'au bout cette aventure si riche en rencontres constructives, en découvertes, et en émotions.

Abstract

The objective of this thesis was to explore the potential of human brain ultrasound imaging. Anatomy, blood flow and soft tissue stiffness have already been studied with ultrafast ultrasound imaging in humans and validated in several organs, such as, the breast and liver but not yet on the adult brain. The main limitation of transcranial ultrasound imaging is today the very strong skull-induced aberration artefact. Indeed, the bone, due to its composition, does not allow for ultrasound propagation as elsewhere in the human body. Therefore, this thesis was focused on the development of ultrafast ultrasound imaging for the evaluation of soft tissue stiffness and neurofunctional imaging in the adult human brain, during brain surgery to bypass the problem of skull aberration, and on an aberration correction technique for transcranial ultrasound imaging.

We first provided several evidence of the benefit of using shear wave elastography during brain surgery. We also presented our new technique for 3D shear wave elastography using a matrix array in order to be able to overcome the limitations of 2D imaging and in particular to reduce the operator dependence.

In a second phase, we demonstrated the capability of ultrasound to identify, map and differentiate in depth cortical regions of activation in response to a stimulus, both in awake patients and in anaesthetized patients. We have demonstrated that ultrasound neurofunctional imaging has the potential to become a comprehensive modality of neuroimaging with major benefits for intraoperative use.

In a third part, we developed a new sound speed estimation (SSE) technique, based on a three-step technique that estimates the sound speed accurately corresponding to the illuminated medium. This technique was tested in ultrasound phantoms and *in vivo* in patient's liver. In both cases, our method was able to find the sound speed corresponding to the medium. We demonstrated that SSE was related to the fat fraction. This analysis led to the conclusion that SSE was able to distinguish a healthy liver from a diseased liver with both biopsy and MRI as gold standard. Combined with the use of the Wood's formula, we were even able to access a fat fraction measured by non-invasive ultrasound.

Finally, by combining the phase, the amplitude and the sound speed estimation, we have developed a new aberration correction algorithm to perform transcranial ultrasound imaging. By performing numerical simulations, we obtained images that faithfully represented the medium (lateral position and depth) and characterized by one resolution and one contrast similar to those obtained with a punctual source in the medium.

Keywords: ultrasound, imaging, elastography, Doppler, functional, human, brain, aberration, quantitative, steatosis

L'objectif de cette thèse était d'explorer le potentiel de l'imagerie du cerveau humain par ultrasons. L'anatomie, le flux sanguin et la rigidité des tissus mous ont déjà été étudiés avec l'imagerie ultrasonore ultrarapide chez l'homme et validés sur plusieurs organes, tels que le sein et le foie, mais pas encore sur le cerveau adulte. La principale limitation de l'imagerie échographique transcrânienne est aujourd'hui le très fort artefact d'aberration induit par le crâne. En effet, l'os, de par sa composition ne permet pas la propagation des ultrasons comme ailleurs dans le corps humain. Dans cette thèse, nous avons utilisé l'imagerie ultrasonore ultrarapide pour l'évaluation de la rigidité des tissus mous et l'imagerie neurofonctionnelle dans le cerveau humain adulte, lors de chirurgies du cerveau afin de contourner dans un premier temps le problème des aberrations induites par le crâne. La dernière partie de cette thèse était axée sur la correction d'aberration pour l'échographie quantitative et l'imagerie ultrasonore transcrânienne.

Nous avons tout d'abord fourni plusieurs preuves de l'intérêt d'utiliser l'élastographie par onde de cisaillement pendant la chirurgie du cerveau. Nous avons également présenté notre nouvelle technique d'élastographie par onde de cisaillement en 3D à l'aide d'une sonde matricielle dans le but de pouvoir dépasser les limitations du 2D et notamment être moins dépendant de l'opérateur.

Dans un second volet, nous avons démontré la capacité des ultrasons ultrarapides à identifier, cartographier et différencier en profondeur les régions d'activation corticales en réponse à un stimulus, à la fois chez les patients éveillés et chez les patients anesthésiés. Nous avons démontré que l'imagerie neurofonctionnelle par ultrasons a le potentiel de devenir une modalité complète de neuroimagerie avec des avantages majeurs pour une utilisation peropératoire.

Dans un troisième volet, nous avons utilisé une technique en trois étapes pour calculer précisément la vitesse du son (SSE) dans un milieu. Cette technique a été testée dans des fantômes ultrasonores et *in vivo* dans les foies de patients. Dans les deux cas, notre méthode a été capable de trouver la vitesse du son correspondant au milieu. Nous avons démontré que la SSE était liée à la fraction de graisse. Cette analyse a permis de conclure que la SSE était en mesure de distinguer un foie sain et d'un foie malade aussi bien avec la biopsie qu'avec l'IRM comme méthode de référence. Combiné à l'utilisation de la formule de Wood, nous avons même pu avoir accès à une fraction de graisse mesurée par ultrasons de manière non invasive. Puis nous avons combiné la correction d'aberration de phase, d'amplitude et de vitesse du son pour faire de l'imagerie transcrânienne en simulation numérique. Nous avons atteint notre objectif en obtenant des images représentant fidèlement le milieu (position latérale et profondeur) et caractérisées par une résolution et un contraste similaires à ceux obtenus avec une source ponctuelle dans le milieu.

Mots clés : ultrason, imagerie, élastographie, Doppler, fonctionnel, humain, cerveau, aberration, quantitative, stéatose

Table of Contents

1. Medical imaging of the brain	27
1.1 Chapter introduction	27
1.2 Brain imaging: the state-of-art	27
1.2.1 Computed Tomography (CT) imaging	27
1.2.1.1 Computed tomography perfusion (CTP)	28
1.2.1.2 Computed tomography angiography	28
1.2.2 Magnetic Resonance Imaging (MRI).....	29
1.2.2.1 Magnetic resonance angiography (MRA).....	29
1.2.2.2 Functional magnetic resonance imaging (fMRI)	30
1.2.2.3 Magnetic resonance elastography (MRE).....	31
1.2.3 Nuclear imaging	32
1.2.3.1 Planar scintigraphy	32
1.2.3.2 Single-photon emission computed tomography	33
1.2.3.3 Positron emission tomography (PET).....	33
1.2.4 Optical imaging: Near Infrared Spectroscopy	34
1.2.5 Electroencephalography	35
1.2.6 Magnetoencephalography.....	35
1.2.7 Ultrasound imaging.....	36
1.3 The advent of ultrafast ultrasound imaging	37
1.3.1 Conventional ultrasound imaging	37
1.3.1.1 B-mode imaging.....	38
1.3.1.2 Blood flow imaging: the Doppler Effect	39
1.3.1.2.1 Continuous-wave (CW) Doppler.....	39
1.3.1.2.2 Pulsed-wave (PW) Doppler	40
1.3.1.2.3 Color Doppler imaging.....	40
1.3.2 Ultrafast ultrasound imaging in brain imaging.....	42

1.3.2.1	Plane-wave concept.....	42
1.3.2.2	Coherent Compounding.....	42
1.3.2.3	Brain ultrafast ultrasound imaging.....	44
1.4	Thesis objectives.....	44
1.5	Chapter bibliography.....	44
2.	Intraoperative brain Shear Wave Elastography and 3D elastography using 3D matrix array.....	55
2.1	Chapter introduction.....	55
2.2	Shear Wave Elastography (SWE) principle.....	55
2.3	Shear wave elastography in brain tumor surgery.....	57
2.3.1	Ultrasound in neurosurgery.....	57
2.3.2	Conventional Ultrasound and SWE Acquisitions.....	58
2.3.3	Patients cohort.....	59
2.3.4	Intraoperative ultrasound Imaging.....	60
2.3.5	Tumors classification using SWE.....	61
2.3.6	Stiffness analysis by subgroup comparison.....	63
2.3.7	Repeatability and reproducibility.....	64
2.3.8	Clinical illustrative cases.....	65
2.3.8.1	Error in the initial MRI diagnostic.....	65
2.3.8.2	Necrosis gradient in malignant tumors.....	66
2.3.9	SWE contribution in neurosurgery.....	66
2.4	Relationship between intracranial pressure and SWE in normal brain in patients with lesion.....	68
2.4.1	Intracranial pressure.....	68
2.4.2	Intracranial pressure monitoring.....	70
2.4.3	Hypothesis.....	71
2.4.4	In vitro study.....	71
2.4.5	In vivo study.....	73
2.4.6	Conclusion and perspectives.....	75
2.5	3D elastography using matrix array.....	76

2.5.1	From 2D to 3D elastography	76
2.5.2	Ultrasound system infrastructure.....	77
2.5.3	Image formation.....	78
2.5.3.1	Ultrafast Imaging in 3D for shear wave tracking.....	78
2.5.3.2	Shear wave velocity estimation	80
2.5.4	Phantom experiments	80
2.5.5	In-vivo 3D elastography.....	81
2.5.6	Conclusion.....	82
2.5.7	Perspectives.....	82
2.6	Chapter conclusion.....	83
2.7	Chapter bibliography	84
3.	Intraoperative neurofunctional ultrasound imaging.....	93
3.1	Chapter introduction	93
3.2	Neurovascular coupling.....	94
3.3	Intraoperative functional imaging.....	95
3.3.1	Electrocortical stimulation mapping	96
3.3.2	Functional MRI-integrated neuronavigation.....	97
3.4	Functional ultrasound (fUS) principle.....	98
3.4.1	Ultrafast Doppler imaging.....	98
3.4.2	Functional ultrasound imaging	100
3.5	Development of intraoperative fUS in humans.....	101
3.5.1	Intraoperative Ultrafast Doppler.....	101
3.5.1.1	Ultrasound acquisitions	101
3.5.1.2	Spatiotemporal clutter filtering.....	103
3.5.2	Intraoperative functional ultrasound.....	105
3.5.2.1	Computing the activation maps.....	106
3.5.2.2	Thresholding the activation map	107
3.6	Intraoperative fUS pilot clinical study.....	107
3.6.1	Cohort of patients.....	107
3.6.2	Surgery and anesthesia.....	108

3.6.3	Gold standard for intraoperative functional mapping.....	108
3.6.4	Intraoperative ultrasound imaging.....	109
3.6.5	Functional areas studied.....	109
3.6.6	Deep cortex activation maps.....	111
3.6.7	Intraoperative fUS sensitivity.....	112
3.6.8	Discussion.....	114
3.7	Chapter conclusion.....	114
3.8	Chapter bibliography.....	115
4.	Adaptive focusing in speckle noise for quantitative ultrasound and aberration correction.....	123
4.1	Chapter introduction.....	123
4.2	Adaptive focusing in speckle noise for quantitative ultrasound in the liver...123	123
4.2.1	Need for fat quantification in liver.....	124
4.2.2	Adaptive focusing in speckle noise for sound speed estimation.....	125
4.2.2.1	Spatial coherence in random media: The Van Cittert–Zernike theorem 125	
4.2.2.2	Virtual point-like source generation and iterative focusing algorithm for phase Aberration Correction.....	127
4.2.2.3	Superficial layers influence correction.....	129
4.2.3	Ultrasound data acquisition and posttreatment.....	129
4.2.4	Experimental set-up on homogeneous ultrasound phantoms.....	131
4.2.5	Pilot clinical study and proof of concept.....	132
4.2.5.1	Patient cohort.....	132
4.2.5.2	First Sound Speed Estimation in Patients.....	133
4.2.5.3	Phase Aberration Correction.....	134
4.2.5.4	Fat and muscle Influence Correction.....	135
4.2.5.5	Final Pilot Clinical Study Results.....	136
4.2.5.6	Pilot study assessment.....	138
4.2.6	Clinical study with validation cohort.....	139
4.2.6.1	Patient cohort.....	140

4.2.6.2	Intra- and interoperator variability.....	141
4.2.6.3	The Wood's fit	142
4.2.7	Conclusion and perspectives.....	146
4.3	Toward transcranial adaptive focusing.....	146
4.3.1	The state-of-art	147
4.3.1.1	Anatomy and acoustic properties of the skull.....	147
4.3.1.2	Conventional transcranial ultrasound imaging.....	148
4.3.1.3	Phase aberration correction to improve transcranial imaging.....	149
4.3.2	Numerical simulation of skull aberration correction	151
4.3.2.1	Numerical simulation parameters.....	151
4.3.2.2	Phase aberration.....	153
4.3.2.3	Amplitude modulation.....	156
4.3.2.4	Sound speed correction.....	158
4.3.2.5	Conclusion and perspectives.....	159
4.4	Chapter conclusion.....	160
4.5	Chapter bibliography	161
5.	General Conclusion and Outlook.....	171
6.	Appendix.....	175
6.1	Appendix 1: Delay law in the polar coordinate system	175
6.2	Appendix 2: the Wood's formula	176
7.	Résumé de thèse.....	181
7.1	Imagerie médicale du cerveau	181
7.2	Elastographie peropératoire du cerveau par onde de cisaillement et elastography 3D avec utilisation d'une sonde matricielle	186
7.3	Imagerie neurofonctionnelle peropératoire par ultrasons	192
7.4	Focalisation dans du bruit de speckle pour l'échographie quantitative et la correction d'aberration.....	195
7.5	Conclusion générale.....	200
8.	Scientific output	205

Table of Figures

Figure 1.1 – Illustration of computed tomography perfusion	28
Figure 1.2 – Brain CTA and dynamic 3D-CTA.....	29
Figure 1.3 – Magnetic resonance angiography (MRA).....	30
Figure 1.4 – fMRI study presenting hemispheric asymmetries in the functional activations to speech and music in the infant.....	31
Figure 1.5 - Brain MRE.....	32
Figure 1.6 – Statistical parametric mapping analysis of moderate dementia of Alzheimer’s type with SPECT.....	33
Figure 1.7 - NIRS technique applied to infant for functional imaging.....	34
Figure 1.8 – Brain ultrasound imaging in preterm infants.....	36
Figure 1.9 - Transcranial color Doppler of intracranial arteries from the Willis circle.....	37
Figure 1.10 - Conventional line-per-line ultrasound acquisition with a linear array.....	38
Figure 1.11 - Types of images and coordinate system for the different types of ultrasound probe used in this manuscript.....	39
Figure 1.12 - Pulsed-wave Doppler of the proximal right internal carotid artery (ICA)	40
Figure 1.13 – Example of color Doppler image of the superficial femoral artery (SFA) and superficial femoral vein (SFV) in the thigh of a healthy subject	41
Figure 1.14 - Comparison between conventional ultrasound imaging and ultrafast ultrasound imaging.....	43
Figure 2.1 - SWE imaging principle.....	56
Figure 2.2 - SWE clinical applications.....	57
Figure 2.3 - Distribution of all the recorded patients.....	59
Figure 2.4 - Imaging of the boundary between normal brain and tumor in a patient with meningioma.....	60
Figure 2.5 - Young’s Modulus in kPa of both tumor and normal brain for the four analysed types of tumors, meningiomas, low-grade gliomas, high-grade gliomas and metastasis.....	61
Figure 2.6 - Example of MRI images (Gadolinium-enhanced T1), ultrasound images and elastography images for each of the different analysed type of tumors.....	62
Figure 2.7 - Imaging in a patient with glioma, ranked high grade with elastography technic ...	65
Figure 2.8 – Necrosis gradient observation in a lung metastasis.....	66
Figure 2.9 - Cerebrospinal fluid (CSF) circulation.....	69
Figure 2.10 – The intracranial volume-pressure curve.....	69
Figure 2.11 – Invasive ICP monitoring	70
Figure 2.12 - Experimental set up to assess the relation between pressure and elasticity	72
Figure 2.13 – SWE increase due to the stress induced by tissue compression.....	72
Figure 2.14 - Experimental linear relationship between Young’s Modulus measured with SWE and intracortical pressure measured in the normal brain surrounding the small balloon.....	73
Figure 2.15 –Normal brain stiffness: effect of tumor growth and resection.....	74
Figure 2.16 – ICP and SWE in normal brain.....	75

Figure 2.17 – Customized 3D ultrafast ultrasound device.....	77
Figure 2.18 - 3D ultrafast ultrasound imaging framework.....	79
Figure 2.19 – 3D Ultrafast Shear Wave Elastography (SHE) imaging in phantom.....	80
Figure 2.20 – <i>In vivo</i> 3D shear wave elastography in the breast of one healthy volunteer.....	81
Figure 3.1 – Different scales of brain imaging.....	95
Figure 3.2 – Intraoperative bipolar stimulation.....	96
Figure 3.3 – Neuronavigation system used for brain tumor surgery.....	98
Figure 3.4 - Conventional Doppler imaging vs Ultrafast Doppler Imaging.....	99
Figure 3.5 – fUS imaging of the rat brain.....	101
Figure 3.6 - High-resolution sequence for ultrafast Doppler acquisition.....	102
Figure 3.7 - Singular Value decomposition (SVD) of ultrasonic signal.....	104
Figure 3.8 – Stimulation pattern for functional ultrasound imaging.....	105
Figure 3.9 – Hemodynamic response profile.....	106
Figure 3.10 – Organization in the surgical room.....	109
Figure 3.11 - Intraoperative fUS imaging of “mouth sensitive” evoked brain activation in one patient.....	111
Figure 3.12 - The sensory (left) and the motor (right) cortical homunculi.....	112
Figure 3.13 - Comparison between intraoperative functional imaging of motor and somatosensory cortex.....	113
Figure 4.1 - Sound Speed Estimation based on the spatial coherence assessment.....	127
Figure 4.2 - Virtual Source Generation and Iterative Focusing Algorithm for Phase Aberration Correction.....	128
Figure 4.3 – Hadamard encoding principle.....	130
Figure 4.4 - Correlation maps and sound speed estimation (SSE) in two phantoms.....	132
Figure 4.5 - Correlation maps and sound speed estimation (SSE) in two patients.....	133
Figure 4.6 - Iterative algorithm for aberration correction.....	134
Figure 4.7 - Impact of the aberration correction on the SSE.....	135
Figure 4.8 - Layer measurement for SSE correction.....	136
Figure 4.9 - Strong correlation between SSE decrease and MRI PDFF increase.....	137
Figure 4.10 - SSE and biopsy comparison with boxplot and ROC curve analysis.....	138
Figure 4.11 – Patient cohorts.....	141
Figure 4.12 – Intra- and interoperator variability.....	142
Figure 4.13 – Wood’s fit applied on both 50 patients cohort and the validation cohort.....	144
Figure 4.14 – Comparison between ultrasound fat fraction and gold standard fat fraction.....	145
Figure 4.15 – Skull structure.....	147
Figure 4.16 – Basilar arteries insonification using TCCD.....	148
Figure 4.17 – Time reversal for phase aberration correction.....	150
Figure 4.18 - Slice of the 3-D mass density map deduced from CT scans.....	152
Figure 4.19 – Pressure field.....	153
Figure 4.20 - Beam lateral profiles.....	153
Figure 4.21 – Created media for transcranial B-mode imaging.....	154
Figure 4.22 – Numerical simulation to observe phase aberration correction impact on transcranial B-mode images in two media.....	155

Figure 4.23 – Beam lateral profiles	157
Figure 4.24 - Numerical simulation to observe phase aberration correction and amplitude amplification impact on transcranial B-mode images in two media.....	158
Figure 4.25 - Numerical simulation to observe phase aberration correction, amplitude amplification and sound speed correction impact on transcranial B-mode images in two media.	159
Figure 4.26 – Head phantom developed for transcranial Doppler imaging.....	160

Thesis Outline

The thesis focuses on ultrasound ultrafast imaging for stiffness assessment, blood flow imaging, and functional imaging in the brain. Firstly, these techniques were studied during brain surgery, to circumvent aberration artifact induced by the skull. Secondly, aberration artifact correction was studied in order to improve transcranial ultrasound imaging.

In **Chapter I**, the fundamentals of ultrasound medical imaging are introduced along with the new ultrafast ultrasound imaging modality. The main different brain imaging techniques are then presented, to position brain ultrasound imaging in this context.

Chapter II focuses on stiffness imaging in the human brain. We first present Shear Wave Elastography (SWE) principle and main applications. Then we aim to evaluate SWE contribution in neurosurgery. Finally, to enlarge SWE applications field, we translated SWE to 3D imaging by using an ultrafast ultrasound prototype scanner and a matrix array.

Chapter III focuses on neurofunctional ultrasound imaging in humans. Both techniques based on direct detection of neurons electrical activity and on neurovascular coupling will be presented. A special attention will be paid to intraoperative functional brain imaging modalities. Brain functional ultrasound (fUS) imaging will be positioned in this context and the principle will be detailed. Then, the development of ultrafast Doppler sequences and data processing for fUS imaging adapted to intraoperative functional imaging on humans will be presented. Finally, the results of our pilot clinical study will be discussed.

Chapter IV focuses on aberration correction toward transcranial imaging application. The first part of this chapter is dedicated to quantitative ultrasound in phantoms and in patients' liver using the adaptive focusing in speckle noise and aberration correction technique. The second part focuses on phase, amplitude and sound speed correction toward transcranial adaptive focusing in numerical simulation.

Chapter I

Medical Imaging of the Brain

 Medical Imaging of the Brain

Table of contents

1. Medical imaging of the brain	27
1.1 Chapter introduction	27
1.2 Brain imaging: the state-of-art	27
1.2.1 Computed Tomography (CT) imaging	27
1.2.1.1 Computed tomography perfusion (CTP)	28
1.2.1.2 Computed tomography angiography	28
1.2.2 Magnetic Resonance Imaging (MRI).....	29
1.2.2.1 Magnetic resonance angiography (MRA).....	29
1.2.2.2 Functional magnetic resonance imaging (fMRI)	30
1.2.2.3 Magnetic resonance elastography (MRE).....	31
1.2.3 Nuclear imaging	32
1.2.3.1 Planar scintigraphy	32
1.2.3.2 Single-photon emission computed tomography	33
1.2.3.3 Positron emission tomography (PET).....	33
1.2.4 Optical imaging: Near Infrared Spectroscopy	34
1.2.5 Electroencephalography	35
1.2.6 Magnetoencephalography	35
1.2.7 Ultrasound imaging.....	36
1.3 The advent of ultrafast ultrasound imaging	37
1.3.1 Conventional ultrasound imaging	37
1.3.1.1 B-mode imaging.....	38

1.3.1.2	Blood flow imaging: the Doppler Effect	39
1.3.1.2.1	Continuous-wave (CW) Doppler.....	39
1.3.1.2.2	Pulsed-wave (PW) Doppler	40
1.3.1.2.3	Color Doppler imaging.....	40
1.3.2	Ultrafast ultrasound imaging in brain imaging.....	42
1.3.2.1	Plane-wave concept.....	42
1.3.2.2	Coherent Compounding.....	42
1.3.2.3	Brain ultrafast ultrasound imaging	44
1.4	Thesis objectives	44
1.5	Chapter bibliography	44

1. Medical imaging of the brain

1.1 Chapter introduction

Brain imaging is the use of various techniques to either directly or indirectly image the structure or the function of the nervous system. Structural imaging deals with the structure of the nervous system and the diagnosis of gross (large scale) intracranial disease (such as tumor), and injury. In particular, functional imaging allows to find the relationship between activity in certain brain areas and specific mental functions, and can be used to diagnose metabolic diseases and lesions on a finer scale (such as Alzheimer's disease), or for neurological and cognitive psychology research.

Brain imaging is a relatively new discipline within medicine, neuroscience, and psychology (Filler 2009). A steady series of advances in mathematics, physics, computers and clinical imaging science have progressively transformed diagnosis and treatment of neurological and neurosurgical disorders in the 122 years between the first X-ray image and the advent of high resolution functional magnetic resonance imaging (fMRI). As imaging methodology draws more subtle and complex functional capability into the diagnostic arena, the range of problems that will be available for physicians and neurosurgeons to try to treat will certainly continue to grow larger as well. The aim of this thesis is to contribute to this medical imaging development by studying new ultrasound concepts and applying them to brain medical imaging.

In this introduction chapter, firstly, we will present the main different brain imaging techniques, and position brain ultrasound imaging in this context. Secondly, we will detail the bases of conventional ultrasound imaging in order to introduce the new concept of ultrafast ultrasound imaging and its applications in the field of neuroimaging.

1.2 Brain imaging: the state-of-art

There are many imaging techniques permitting human brain exploration, allowing structural and functional imaging. This section proposes a succinct and illustrated overview of these techniques to position brain ultrasound imaging in this context.

1.2.1 Computed Tomography (CT) imaging

A computed tomography scan (CT-scan) is an imaging method based on the tissues' X-rays absorption from different angles, which produces cross-sectional images of the human body (i.e. tomographic images). The x-rays will be more or less absorbed because the density between tissues and bones is different, and this permits to identify different structures in one image. In a CT-scan, the X-rays source performs one single rotation around the patient, allowing for the local absorption evaluation of each volume of interest. Then, digital geometry processing is used to generate three-dimensional volumes from the different series of two-dimension radiographic

images taken around each axis of rotation. CT-scans are not acquired in real time and a complete scan takes several minutes on average.

In neurological and head/neck imaging, the main role of CT imaging is the in the assessment of brain and spine lesion, mainly in trauma settings, such as hemorrhages, (Kidwell et al. 2004) or for the assessment of base of skull lesions. In head and neck imaging, mass lesions previously considered unresectable are now being treated by skull base surgeons, with a resultant improvement in patient outcomes (Matsumoto et al. 2007). Multi-detector CT is extremely useful for assessment of temporal bone, paranasal sinuses, neck masses and laryngeal apparatus (Ghonge 2013).

1.2.1.1 Computed tomography perfusion (CTP)

One application of CT is CT perfusion (CTP). CTP, with contrast injection, can characterize cerebral perfusion with quantitative hemodynamic parameters such as cerebral blood volume (CBV), cerebral blood flow (CBF), and mean transit time (MTT) (Nabavi et al. 1999). CTP allows early detection of ischemic stroke (Koenig et al. 1998; Schaefer et al. 2006) (**Figure 1.1**).

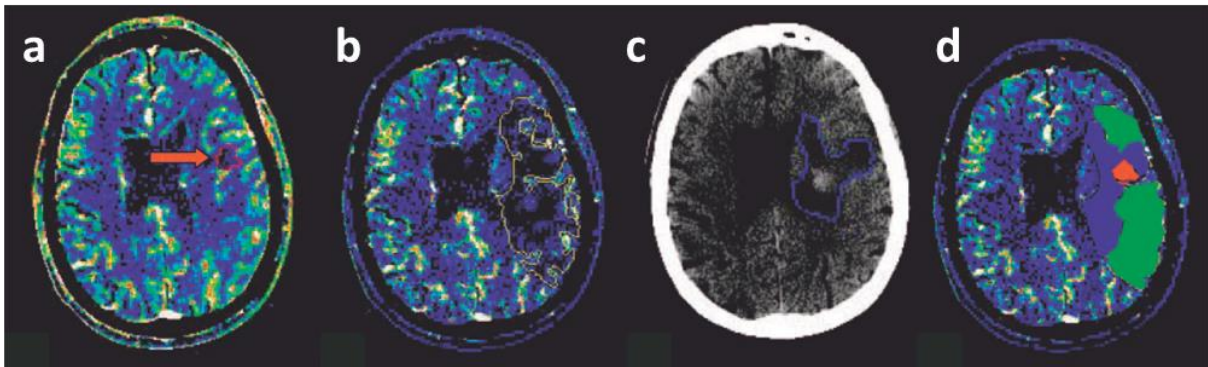


Figure 1.1 – Illustration of computed tomography perfusion. A 61-year-old male patient with right hemiparesis imaged at 2.3 hours and 3 days. Abnormal areas are outlined on (a): CBV, (b): CBF, and (c): follow-up CT images. After coregistration, three regions were defined on CBF maps (d): region 1 (red), “infarct core”; region 2 (blue), “penumbra that infarcts”; and region 3 (green) “penumbra that recovers”. (Taken from (Schaefer et al. 2006))

1.2.1.2 Computed tomography angiography

Another application of CT-scan in brain imaging is computed tomography angiography (CTA). CTA is based on the injection of iodine-rich contrast agent and CT scanning to evaluate blood vessel diseases and related conditions, such as, aneurysms or blood flow blockages. Contrast agents are injected to increase the contrast-to-noise ratio of the acquired images. Dynamic 3D-CTA provides vital information regarding the 3D vascular structure and the dynamic blood flow (Matsumoto et al. 2007) (**Figure 1.2**).

As described, computing tomography imaging is used fundamentally to assess vessel’s blood flow. It is possible to obtain images with good contrast in just a few minutes of acquisition. However, it is an imaging modality that uses high doses of ionizing radiation and requires contrast agent injections most of the times.

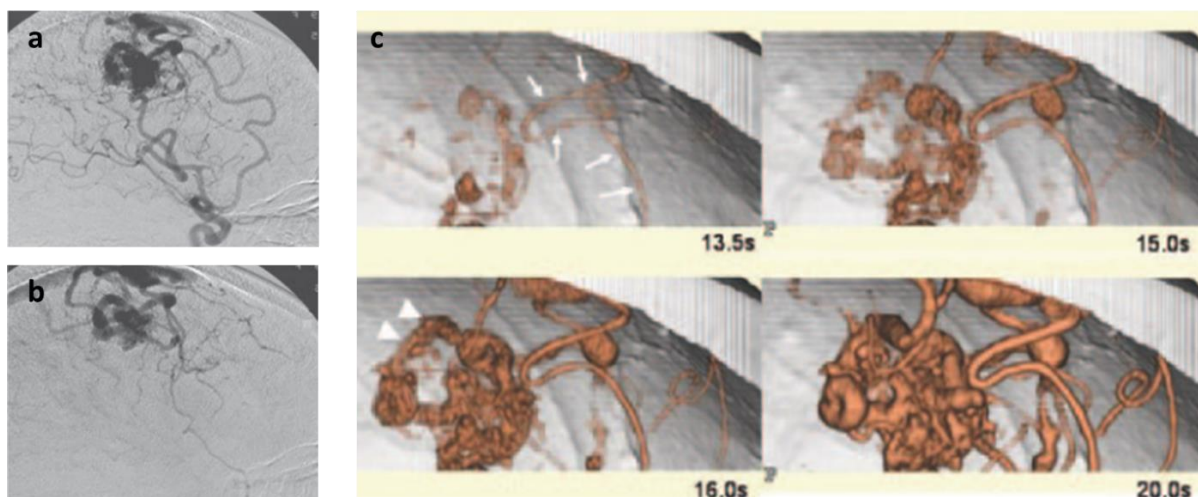


Figure 1.2 – Brain CTA and dynamic 3D-CTA. Illustration with the case of a 61-year-old woman with an arteriovenous malformation (AVM) in the left frontal lobe. Left internal carotid artery angiogram, lateral views of the arterial (a) and venous (b) phase, reveals an AVM fed by branches of the anterior and middle cerebral arteries. (c) Dynamic 3D-CTA (left lateral view) obtained at 13.5, 15, 16, and 20 seconds after contrast injection. The arterial phase (at 16 seconds) revealed a drainer (arrowheads), indicating that there is an arteriovenous shunt. Dynamic 3D-CTA provided information on the hemodynamics and the 3D vascular structures of the AVM. (Adapted from (Matsumoto et al. 2007))

Major disadvantages of CT imaging are X-ray illumination and ionizing agent contrast injection in most of cases. Although it provides valuable structural information on brain tissues and vasculature, this imaging modality does not give any information on the brain functionality itself.

1.2.2 Magnetic Resonance Imaging (MRI)

Magnetic resonance imaging (MRI) is a medical imaging technique used in radiology to form pictures of the anatomy and the physiological processes of the body. MRI scanners use strong magnetic fields, radio waves, and field gradients to generate images of the inside of the body. MRI is widely used for medical diagnosis, staging of disease and follow-up without exposing the body to ionizing radiation.

In brain imaging, MRI is the investigative tool of choice for neurological cancers, as it has better resolution than CT-scan and offers better visualization of the posterior fossa. The contrast provided between grey and white matter makes it the best choice for many conditions of the central nervous system, including demyelinating diseases, dementia, cerebrovascular disease, infectious diseases and epilepsy (American Society of Neuroradiology 2013).

1.2.2.1 Magnetic resonance angiography (MRA)

To detect cerebrovascular diseases, such as arteriovenous malformations, aneurisms, and brain occlusions, they are three main techniques of magnetic resonance angiography (MRA) (Korosec 1999): contrast agent method (contrast enhanced MRA), and methods without contrast agent (Time-of-flight (TOF) MRI and phased contrast MRI). The three techniques are illustrated in **Figure 1.3**. In the contrast enhanced MRA, a gadolinium solution is injected to the patient to

artificially increase blood magnetization. Blood signal is therefore higher than tissue signal and allow blood vessels visualization. There is a need to synchronize the contrast agent injection and the imaging system to be able to track the bolus propagation. We first observe an increase of the signal in the arteries (**Figure 1.3 a**), and then in the veins (**Figure 1.3 b**). TOF techniques (**Figure 1.3 c**) derive contrast between flowing blood and stationary tissues by manipulating the magnitude of the magnetization, such that the magnitude of the magnetization from the moving spins is large and the magnitude of the magnetization from the stationary spins is small. Phase contrast techniques (**Figure 1.3 d**) derive contrast between flowing blood and stationary tissues by manipulating the phase of the magnetization, such that the phase of the magnetization from the stationary spins is zero and the phase of the magnetization from the moving spins is non-zero. Both TOF and phase contrast techniques lead to a large signal from moving blood spins and a diminished signal from stationary tissue spins without the need of contrast agent.



Figure 1.3 – **Magnetic resonance angiography (MRA)**. 4D contrast enhanced MRA presenting contrast agent arrival first in the carotids arteries (**a**) and then in the veins (**b**) (Adapted from (Hadizadeh et al. 2014)). Circle of Willis MRA without contrast agent with the time-of-flight MRI (**c**) and with the phased contrast MRI (**d**) (Adapted from (Tanaka et al. 2006; Ross, Pelc, and Enzmann 1993)).

1.2.2.2 Functional magnetic resonance imaging (fMRI)

Since many images are taken seconds apart, brain response to different stimuli can be observed performing functional MRI (fMRI). fMRI method measures BOLD (blood oxygenation level dependent) changes in the magnetic resonance signal (Kashou 2014). Neuronal activity results in increased blood flow through local capillaries. The increased perfusion exceeds the increased demand, resulting in an increase in the oxy-deoxyhemoglobin ratio. These changes can be seen on MRI images as BOLD responses because of the different magnetic properties of deoxyhemoglobin (paramagnetic) and oxyhemoglobin (diamagnetic) (Frahm et al. 1992). Brain areas said to be “activated” by the task when BOLD signal intensity correlates with the timing of the experimental task. However, the link between the BOLD contrast mechanism and the spiking output still remains of investigation (Logothetis et al. 2001). This technique is widely used in cognitive science to study the language (Binder et al. 1995), the learning and memory (Le Bihan and Karni 1995), the emotion (Grodd et al. 1995), and the treatment of tactile (Yetkin et al. 2017), visual (Tootell et al. 1995), olfactory (Yousem et al. 1997) and hearing (**Figure 1.4**) information. fMRI is also used before brain surgery to image functionalities surrounding the lesion (Lehéricy et al. 2000).

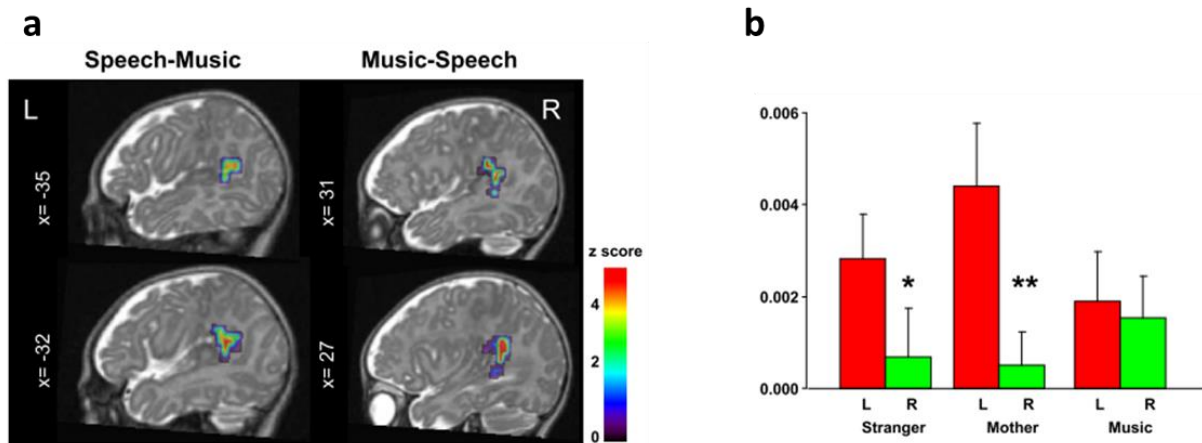


Figure 1.4 – fMRI study presenting hemispheric asymmetries in the functional activations to speech and music in the infant. (a) Asymmetric clusters of activation of the speech vs. music comparisons are projected on sagittal slices of a three-month-old T2 anatomical image. (b) Boxplot of the individual activations averaged over the left and right clusters for each of the auditory stimulus (mother's voice, stranger's voice, music). There is a significant left/right asymmetry for both speech conditions (mother's voice and stranger's voice) but music appears to be symmetrically distributed. (Adapted from (Dehaene-Lambertz et al. 2010)).

1.2.2.3 Magnetic resonance elastography (MRE)

Magnetic resonance elastography (MRE) is a noninvasive technique that quantitatively determines, analogous to manual palpation, the stiffness of tissue (Muthupillai et al. 1995). It measures the viscoelastic properties of tissue by evaluating the behavior of externally introduced mechanical shear waves as they travel through the tissue of interest. It has a proven role in the evaluation of liver fibrosis where it has replaced needle biopsies in a growing number of practices (Yin et al. 2007).

MRE study of the brain has presented unique challenges because of the difficulty in introducing shear waves through the skull and processing the complex wave fields resulting from the curved skull and fixed falx (meningeal layer of dura mater between the cerebral hemispheres of the human brain). Several groups have implemented strategies to overcome these challenges to investigate the use of MRE in the brain (Green, Bilston, and Sinkus 2008; Kruse et al. 2008; Sack et al. 2008).

Thus far, MRE of the brain has been applied to study global changes in cerebral viscoelasticity induced by physiological aging (Sack et al. 2009), multiple sclerosis (Wuerfel et al. 2010), hydrocephalus (Freimann et al. 2012; Streitberger et al. 2010) and Alzheimer's disease (Murphy et al. 2011). An example of brain MRE data from a healthy volunteer is shown in **Figure 1.5**.

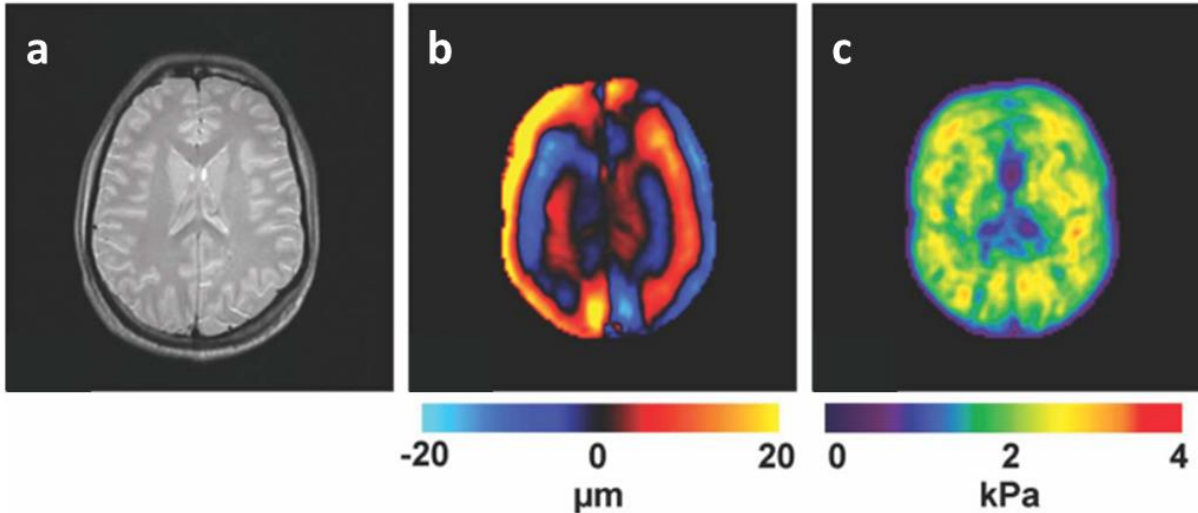


Figure 1.5 - Brain MRE. (a) Axial MR magnitude image of the brain showing white matter, gray matter, and cerebrospinal fluid. (b) A single wave image from MRE performed at 60 Hz. Vibrations at 60 Hz were introduced into the brain with the help of a pressure-activated driver placed under the head. (c) The corresponding elastogram is presented. (Adapted from (Mariappan, Glaser, and Ehman 2010)).

MRI suffers several limitations including cost, contra-indications (pace-maker, claustrophobia) and poor availability.

1.2.3 Nuclear imaging

Nuclear imaging relies on non-invasive measurements of injected radiotracers performed by external radiation sources and detectors to perform functional imaging. Nuclear imaging allows for quantitative measurement of biochemical and physiological processes in both research and clinical applications. This imaging modality includes several techniques that are differentiated according to the radiotracer or detectors used. Radiotracers are essentially carrier molecules bonded to a radioactive atom and the type of radiotracer depends on the exam purpose. For example, some tracers employ molecules that interact with a specific protein, others tracers interact with glucose in an organ.

Nuclear imaging includes several modalities: planar scintigraphy, single-photon emission computed tomography (SPECT) and positron emission tomography (PET).

1.2.3.1 Planar scintigraphy

Planar scintigraphy is used in clinical routine as it allows fast acquisitions over a large area at a relatively low cost. This modality uses gamma-rays cameras to collect the photons of the radiotracers. However, the main disadvantage is the lack of information regarding the three-dimensional spatial distribution of radioactivity in the body. Moreover, images can exhibit limited contrast since the radioactivity signal from an imaging region of interest is often combined with the signal from overlapping structures.

1.2.3.2 Single-photon emission computed tomography

Single-photon emission computed tomography (SPECT) is based on the injection of radioactive tracers into the blood vessels that produce gamma-photon signals and perform 3D-imaging. These signals are then detected by a radiation detector and a collimator determines the direction and location of incidence of these gamma-photons. Images of thin slices of the brain can be produced from all different directions and angles. These images are examined to look for tracer location. Computer graphics can be used to create a 3-D images of the target of the slices images. SPECT may be used noninvasively in the brain to measure blood flow, perfusion (**Figure 1.6**), metabolic function, receptor density, and drug delivery. Both planar scintigraphy and SPECT use photon-emitting radiopharmaceuticals, such as Technetium-99m. Sensitivity and contrast are better for SPECT compared to planar scintigraphy, however, the acquisition times are higher.

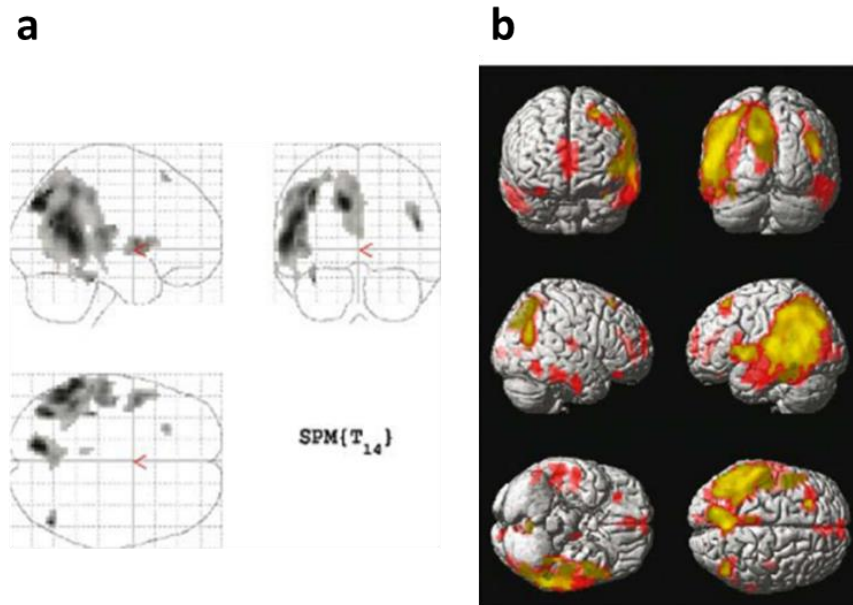


Figure 1.6 – Statistical parametric mapping analysis of moderate dementia of Alzheimer's type with SPECT. Comparison of a subject with 15 age-matched healthy volunteers. **(a)** Glass brain representation of significant decreases in perfusion (gray scale). **(b)** 3D rendering on a template MR image, the decreases in perfusion are shown for two thresholds $p=0.01$ (red) and $p=0.001$ (yellow). (Adapted from (Hutton, Braun, and Slomka 2006))

1.2.3.3 Positron emission tomography (PET)

Positron emission tomography (PET) imaging uses positron emitting radiotracers and can produce 3-D images of radiotracers distribution in the body. This modality is based on the coincidence detection of photons emitted from radiolabeled tracers decay. These injected tracers are specifically chosen to map a particular physiological process. As an example, fludeoxyglucose (FDG), an analogue of glucose, is a tracer used to observe metabolic activity. Subsequent annihilation of the positron (by a collision with a free electron) results in the production of two γ -rays emitted in opposite directions. These γ -rays are detected in coincidence at opposite sides of the PET detector ring. A PET scanner consists of several stationary 360° detector rings

allowing simultaneous detection of coincidence events in all directions (3-D) or in each plane (2-D). PET is a highly sensitive nuclear imaging technique (i.e. higher sensitivity than SPECT).

SPECT and PET are most often used in combination with a structural imaging modality, such as CT-scan or MRI, in order to have a high-resolution image to combine with the functional or molecular cartography obtained with the nuclear imaging. According to one reference book about quantitative analysis in nuclear medicine imaging (Hutton, Braun, and Slomka 2006), depending on the tracer used, brain applications of SPECT and PET are the following: dementia (**Figure 1.6**), epilepsy (focal epilepsy is accompanied with moderate to severe metabolic and perfusion related disturbances, and both SPECT and PET can demonstrate these abnormalities), cerebrovascular diseases (SPECT cerebral perfusion imaging can be used to immediately diagnose stroke and is predictive to outcome), movement disorders (metabolic or perfusion brain imaging is useful in the differential diagnosis of extrapyramidal disorders), brain tumors (PET with FDG injection allow similar brain tumors evaluation and allow a sensitive differentiation between necrosis and tumor recurrence in postoperative or post-radiotherapeutical setting), and traumatic brain injuries (a negative perfusion SPECT investigation virtually excludes functional sequels).

However, nuclear imaging presents some risks, for instance, the tracer injection and the ionizing radiation exposure.

1.2.4 Optical imaging: Near Infrared Spectroscopy

Near-infrared spectroscopy (NIRS) uses a small source-detector array running in the near infrared (these wave length being relatively transparent to biological tissue) to measure changes in the hemoglobin oxygenation state associated in neural activity in the human brain (Jöbsis 1977).

This noninvasive optical technique has been oriented toward use for clinical monitoring of tissue oxygenation (Hirtz 1993; Wyatt et al. 1986). Meanwhile, since it has been demonstrated that NIRS is a potential tool for functional mapping studies (Hoshi and Tamura 1993; Villringer et al. 1993; Hoshi 2003), NIRS has also been applied to human brain cortical mapping. An example in infant is presented **Figure 1.7**.

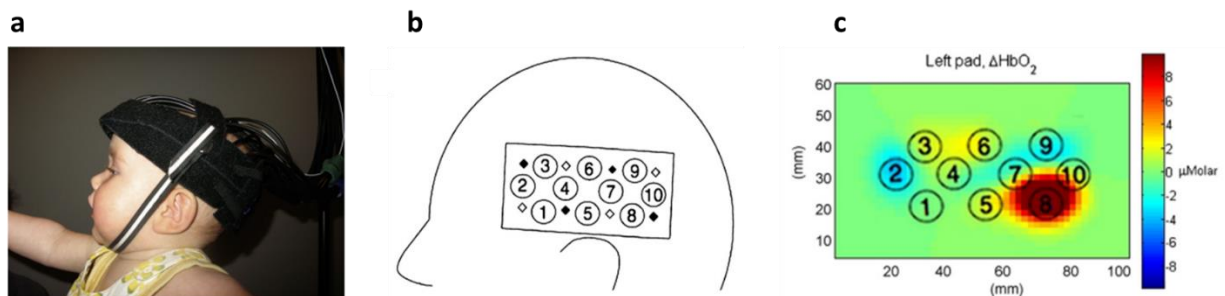


Figure 1.7 - NIRS technique applied to infant for functional imaging. (a) An infant wearing NIRS probes attached to one headgear. (b) The source-detector arrangement of the optical array used to collect the data. (c) A linear reconstruction of changes in oxy-haemoglobin showing the spatial localization of the haemodynamic response to an experimental stimulus. (Adapted from (Lloyd-Fox, Blasi, and Elwell 2010))

A good agreement was found between NIRS and fMRI measurements of cortical oxygenation changes in young and elderly subjects during brain activation (Mehagnoul-Schipper et al. 2002). There are many medical applications of functional NIRS in neurology, psychiatry, psychology/education and basic research. An interested reader can refer to the review of Marco Ferrari on human functional NIRS (Ferrari and Quaresima 2012).

The term Diffuse Optical Tomography (DOT) is used for three-dimensional NIRS. DOT is used mainly to detect changes in optical properties of tissue simultaneously from multiple measurement points and display the results in the form of a map or image over a specific area, whereas NIRS provides quantitative data in absolute terms on up to a few specific points. DOT is also used to investigate human brain tumors in animal model (van der Sanden et al. 1999) and to assess resting-state functional connectivity in the human brain (White et al. 2009).

The main drawback of NIRS and DOT, is their limited use to cortical tissue investigation.

1.2.5 Electroencephalography

Electroencephalography (EEG) is an electrophysiological monitoring method using electrodes (along the scalp or implanted) to record electrical activity of the brain. EEG measures direct voltage fluctuations resulting from ionic current within the neurons of the brain (Niedermeyer and Silva 2005). In clinical contexts, EEG refers to the recording of the brain's spontaneous electrical activity over a period of time (Niedermeyer and Silva 2005), as recorded from multiple electrodes (from ten to hundreds) placed on the scalp. This technique allows precise cartography of the electric activity of the brain.

Diagnostic applications generally focus on the spectral content of EEG, that is, the type of neural oscillations (i.e. brain waves) that can be observed in EEG signals. EEG is most often used to diagnose epilepsy, which causes abnormalities in EEG readings (Misulis 2013). It is also used to diagnose sleep disorders, coma, encephalopathies, brain death, tumors diagnosis, stroke and other focal brain disorders (Tong and Thakor 2009).

Despite limited spatial resolution, EEG continues to be a valuable tool for research and diagnosis, especially when millisecond-range temporal resolution (not possible with CT or MRI) is required.

1.2.6 Magnetoencephalography

Magnetoencephalography (MEG) is a functional neuroimaging technique. MEG uses very sensitive magnetometers, such as superconducting quantum interference devices, to record magnetic fields produced by electrical currents occurring naturally in the brain. Brain neuronal activity generates electrical currents, which in turn generate electrical field potentials detectable by the electroencephalogram (EEG). These neuronal currents also produce a magnetic field that is detectable by MEG. However, while the EEG measures extra cellular currents, the MEG is a measure of the intracellular currents. One of the major advantages of the MEG over the EEG is that the skull and the intervening soft tissues between the brain and the scalp do not distort the MEG signals (Ray and Bowyer 2010).

MEG has become a recognized part of the preoperative evaluation of patients with epilepsy and patients with brain tumors and also reveals how the brain processes information normally, such as in language and memory (Stufflebeam, Tanaka, and Ahlfors 2009).

MEG technique provides the combination of millisecond temporal resolution and high spatial resolution (<5 mm) in a safe, noninvasive imaging modality, but its cost remains very high.

1.2.7 Ultrasound imaging

In infants, where the skull is thinner than in adults, and where ultrasound can benefit from the fontanelles, conventional ultrasound imaging can reveal anatomical structures (**Figure 1.8**), and can even be a diagnostic tool, such as for late-onset circulatory dysfunction assessment (Shin and Chai 2016).

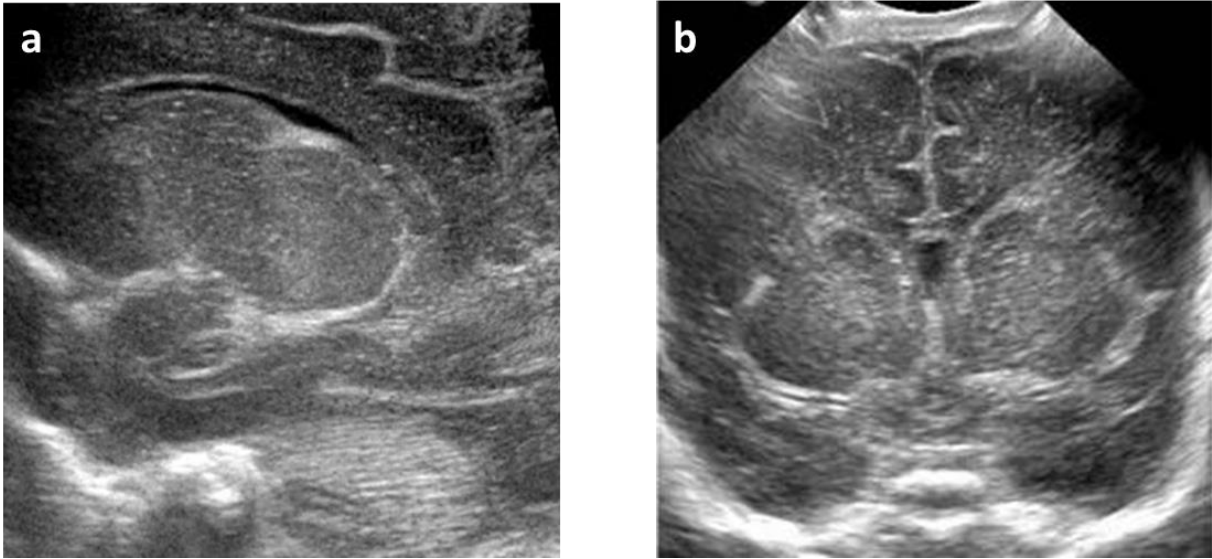


Figure 1.8 – Brain ultrasound imaging in preterm infants. (a) Sagittal brain ultrasound imaging. (b) At age 25 days, coronal brain sonograms show normal range of periventricular echogenicity. (Adapted from (Shin and Chai 2016))

In adults, anatomic images are not available with ultrasound imaging (with a few exceptions such as cerebral peduncles). Through adult skull, only blood vessel imaging is so far possible.

This non-invasive technique is called transcranial Color Doppler (TCCD). TCCD imaging is a technique implemented in ultrasound scanners nowadays (see **Figure 1.9**). It is performed placing a low-frequency (≤ 2 MHz) transducer on the scalp of the patient over specific acoustic windows, in order to visualize the intracranial arterial vessels and to evaluate the cerebral blood flow velocity and its alteration in many different conditions. However, its clinical use is still limited to single local velocities measurements in large arteries (**Figure 1.9**), such as the anterior or middle cerebral arteries (Padayachee et al. 1986).

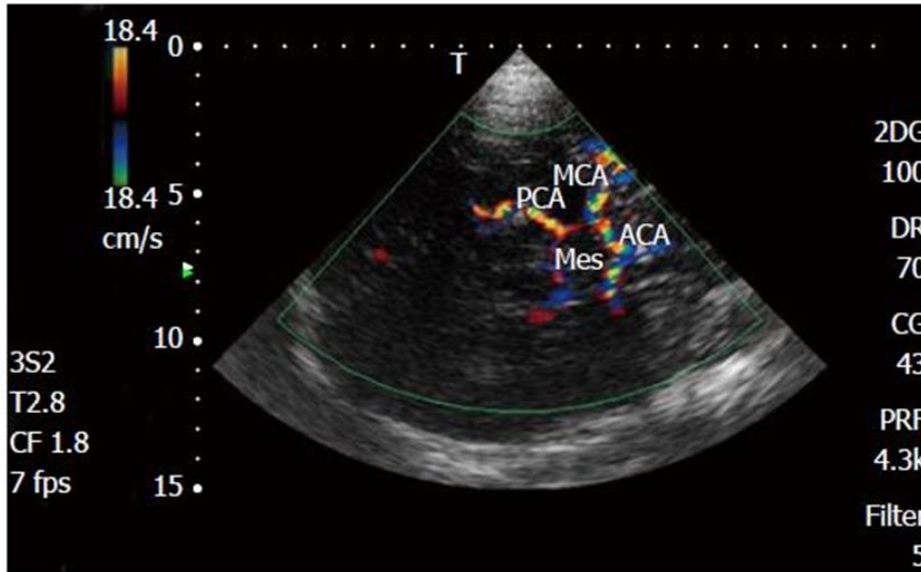


Figure 1.9 - Transcranial color Doppler of intracranial arteries from the Willis circle. MCA: Middle cerebral artery; PCA: Posterior cerebral artery; ACA: Anterior cerebral artery; Mes: Mesencephalon (Midbrain). (Adapted from (D'Andrea et al. 2016))

This limitation to large vessel imaging is due to the conventional ultrasound imaging on which it relies on. Indeed, ultrasound imaging has still not provided a highly sensitive answer on how to overcome the presence of the most important bony structure in the body: the skull. Ultrasound beams passage is restrained through bones, which are source of aberration artifacts. This is the reason why brain is really challenging to image with ultrasound.

1.3 The advent of ultrafast ultrasound imaging

In order to overcome conventional ultrasound imaging limits, ultrafast ultrasound imaging was developed in our laboratory (Laurent Sandrin et al. 2002; L. Sandrin et al. 1999; Mickaël Tanter et al. 2002). In this section, firstly, we introduce the bases of conventional ultrasound imaging, and secondly, we present the new concept of ultrafast ultrasound imaging which has the potential to overcome conventional ultrasound imaging limits and enable new brain imaging modes such as neuroimaging.

1.3.1 Conventional ultrasound imaging

Ultrasound imaging was largely used in the medical field for more than 40 years. This imaging method is non-invasive, safe, easy-to-use, relatively portable and allowing for real time millimetric spatial-resolution acquisitions. Ultrasound waves are transmitted by an ultrasound transducer, consisting of piezoelectric crystals that oscillate at certain frequencies (KHz or MHz range) when an electric field is applied across their volume. The conventional approach for ultrasound imaging relies on a line-by-line scan of the medium by using focused ultrasonic beams. The geometry of the probes, along with their frequency bandwidths, defines penetration and the resolution of ultrasound imaging systems. Diagnostic ultrasound imaging falls in the frequency range between 1 and 8 MHz, however lower frequencies (down to 320KHz) can be used for transcranial ultrasonic neuro-stimulation (Younan et al. 2013) as well as higher frequencies (up to 15-20MHz)

can be employed to image small animals (Macé et al. 2011; Osmanski et al. 2014; van Raaij et al. 2011) or superficial structures (Maresca, Tanter, and Pernot 2014). Ultrasound medical imaging relies on the variation of the acoustic properties (i.e. stiffness and density) of biological tissues to create an image from backscattered acoustic echoes. Many different types of images can be formed using conventional ultrasound imaging, such as B-mode and Doppler imaging.

1.3.1.1 B-mode imaging

B-Mode (Brightness mode) is a two-dimensional ultrasound image display composed of bright pixels representing the ultrasound echoes. The brightness of each pixel is determined by the amplitude of the returned echo signal. These images allow for anatomical structures visualization. Lesions such as tumors and atherosclerotic plaques can be identified and the extent of disease burden can be quantified. In conventional ultrasound imaging, one image is obtained by focusing an ultrasonic beam on each line of the medium and by re-focusing in reception the backscattered echoes coming from the heterogeneity of the tissues (**Figure 1.10**). Since each focused beam will lead to the reconstruction of one image line, the two focusing steps, in emission and in reception, will have to be repeated sequentially and multiple times in order to reconstruct the whole field of view (Szabo 2004). For this reason, conventional ultrasound imaging has limited frame rates ($\sim 60\text{Hz}$), as the time needed to create a single image (B-mode image) depends on the time of the transmission of the beam, the reception, and the processing of the backscattered echoes per each image line (synthetic focusing in reception).

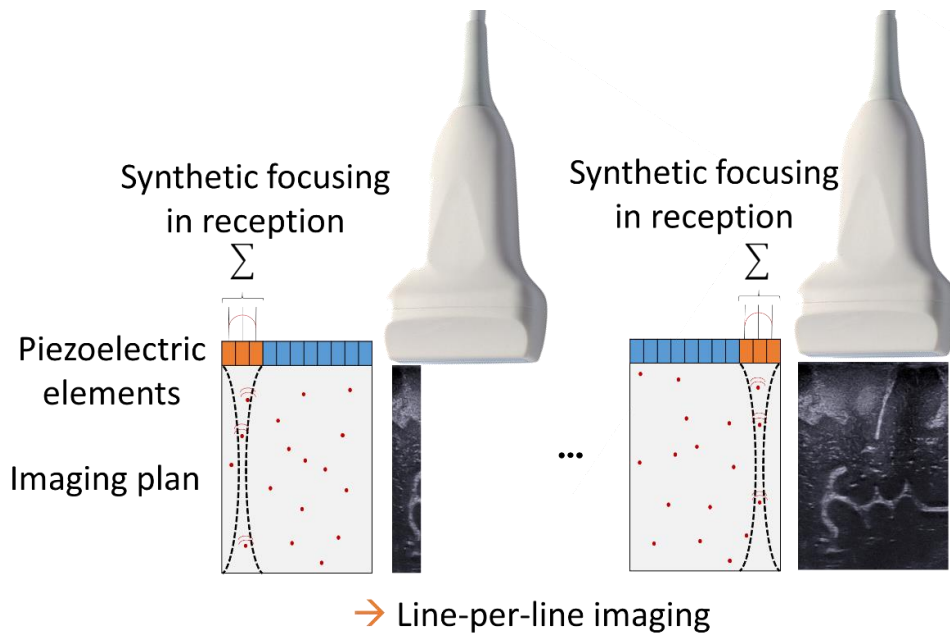


Figure 1.10 - Conventional line-per-line ultrasound acquisition with a linear array. The piezoelectric transducer regularly shifts a focused beam in the imaged medium to recover the whole field of view. The medium is insonified one line at a time. In reception, a synthetic focus algorithm reconstructs the ultrasound image. This image is a brain B-mode images after craniotomy, recorded during brain tumor surgery.

The geometry of the probes (i.e. linear-, curved- or phased-array probes) (**Figure 1.11**) and their frequency bandwidth determine the penetration, resolution and field of view (FOV). In terms of resolution, ultrasound imaging allows for millimetric spatial resolution typically.

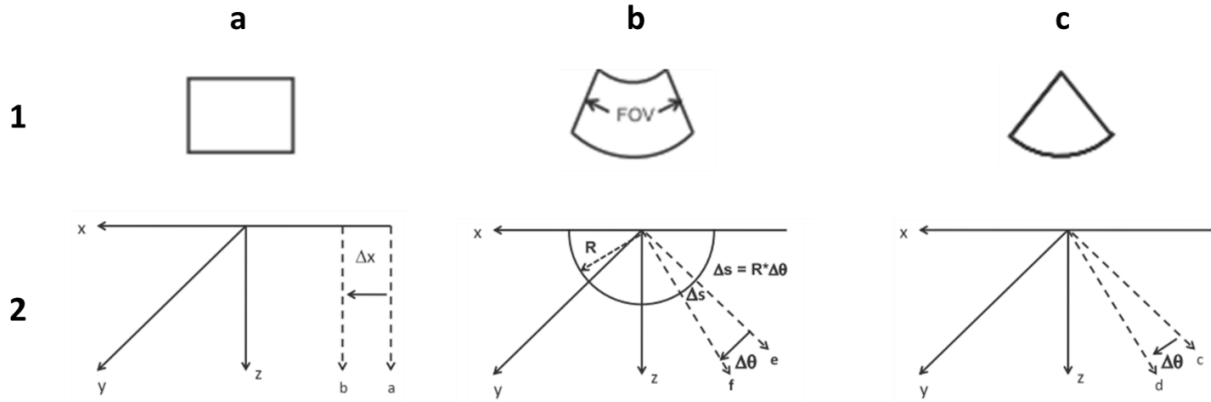


Figure 1.11 - Types of images and coordinate system for the different types of ultrasound probe used in this manuscript. (a) Linear-array: (a1) 2D rectangular images, (a2) Cartesian reference system for linear scanning in the xz plane from acoustic line a to line b by increment Δx . (b) Curved-array: (b1) 2D convex or curved where the maximum angular extent is the field of view (FOV), (b2) Coordinate system for a curved linear or convex array for sector scans in the xz plane where an acoustic line is moved to position f by an angular increment $\Delta \theta$. (c) Phased-array: (c1) 2D sector, (c2) Coordinate system for sector scans in the xz plane where an acoustic line is moved to position d by an angular increment $\Delta \theta$. (Adapted from (Szabo and Lewin 2013)).

1.3.1.2 Blood flow imaging: the Doppler Effect

In order to image, detect and quantify the blood flow velocity, specified methods were developed. Those methods are based on the Doppler Effect, and are systematically used in clinical practice.

1.3.1.2.1 Continuous-wave (CW) Doppler

Continuous-wave Doppler was the first method to be developed to measure the blood flow velocity. The one-dimensional method is based on the Doppler frequency shift between the emitted and received signals. In this method, the transmitted signal is focused deep in the vessel at a given frequency f_0 and by using only one sup-aperture of the probe. The ultrasound probe receives the signal coming from the vessel (i.e. the backscattered echoes) using another sup-aperture of the probe and at a frequency $f_0 + f_d$, where f_d is the Doppler frequency. The Doppler frequency can be calculated by the standard Doppler equation given by:

$$f_d = \frac{2v_z \cos \theta}{c} f_0$$

Equation 1.1 - Doppler frequency equation, with θ being the angle between the ultrasonic beam and the blood flow direction, c the sound speed and v_z the axial velocity of the moving scattered.

This method allow for the accurate axial velocity estimation only in one line of the image without any velocity limitation. The main limitations of the Continuous-wave Doppler are: the range

ambiguity (i.e. the method is sensitive to all vessels crossing the entire beam), 1-D velocity assumption, and the dependence of the angle between the probe and the blood flow direction.

1.3.1.2.2 Pulsed-wave (PW) Doppler

The pulse-wave Doppler approach was developed to overcome the range ambiguity and to control the region of active insonification. Like the bat, a pulsed-wave Doppler system sends ultrasound beams of a chosen length several times to a target at a certain range. This 1-D technique is the most used in clinical practice to assess and quantify blood flow. It allow the axial velocity distribution to be displayed in function of the time at one vessel point and at one depth (**Figure 1.12**), by applying the Fourier Transform (FT) on the received backscattered signals. Then by the Doppler frequency equation (**Equation 1.1**) the blood velocity can be estimated (**Equation 1.1**). The estimated axial velocity depends on beam-angle transmission (Evans 1991). The main difference between pulsed- and continuous-wave Doppler is the sampling frequency which is undersampled in the case of the pulse-wave approach.

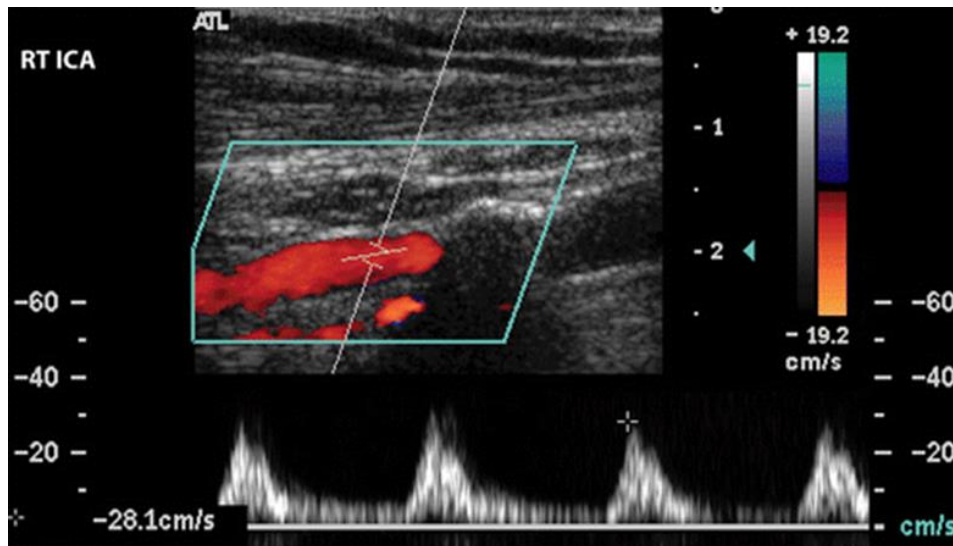


Figure 1.12 - Pulsed-wave Doppler of the proximal right internal carotid artery (ICA). The blood velocity was estimated at -28cm/s (Taken from (Tahmasebpour et al. 2005)).

The main limitations of this technique are: the range resolution, the dependence of angle between the probe and the blood flow direction, and the aliasing limit related to the incapability to accurately estimate high blood velocities.

1.3.1.2.3 Color Doppler imaging

Color Doppler imaging, also called Color Flow imaging, was one of the big technological boost of the diagnostic ultrasound imaging. Pulsed-wave Doppler allowed velocities evaluation from a single volume sample within the human body, but Color Doppler introduced images of velocities simultaneously over a large region-of-interest, providing a rapid blood flow evaluation. For this reason, this approach has been integrated in almost all ultrasound scanners. It is a 2-D imaging approach combining anatomical information (derived from the ultrasonic pulse-echo techniques) and tissue/blood flow velocities information (derived from the ultrasonic Doppler techniques). This method allows generating color-coded maps of blood flow velocity superimposed on grey-scale images of tissue anatomy.

The Color Doppler imaging principle is similar to the pulse-echo principle that allows anatomical images (i.e. B-mode images). However, in this approach, the information of each target location in the human body (i.e. each image pixel) is derived from the knowledge of the ultrasonic pulse direction and the round-trip transit time, which is analysed in term of Doppler shift. In this approach, the velocity is estimated by taking into account the phase-shifts or time-delays between echoes coming from the same sample volume during subsequent pulses. The phase shift can be interpreted as frequency shift and the target velocity can be calculated with the Doppler frequency equation (**Equation 1.1**). In principle, the velocity can be estimated by only two pulses insonification, however, in practice, several pulse transmissions are necessary for a good velocity estimation. This is essentially due to the stochastic nature of blood echoes, and also to the clutter filtering requirement (i.e. it is necessary to filter the received echoes in order to reject clutter coming from the surrounding tissues and masking the real blood signal). The need to sample a target several time imposes several limitations on different factors. In particular, on the used frame rate and on the number of used scan lines to create a full image.

In Color Doppler imaging, a moving color picture gives the global view of the dynamic blood flow, wherein the direction of blood flow is assigned by the red or blue color, respectively indicating flow toward or away from the ultrasound transducer (**Figure 1.13**).

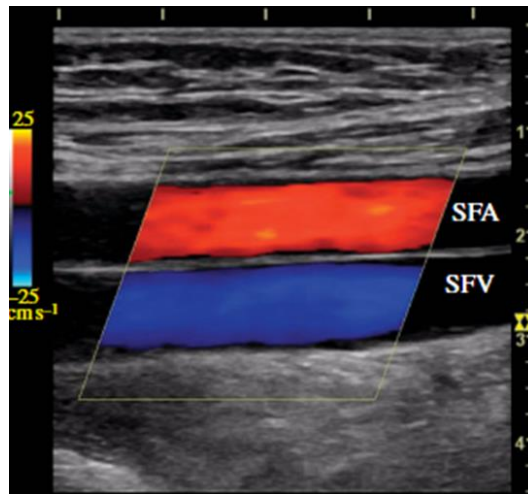


Figure 1.13 – Example of color Doppler image of the superficial femoral artery (SFA) and superficial femoral vein (SFV) in the thigh of a healthy subject (Taken from (Evans, 1991)).

Since its application in diagnostic imaging, conventional ultrasound has been an important tool to observe anatomical and pathological condition of the body. Starting from the early 70's, the state-of-art of ultrasound imaging has been based on the use of focused ultrasonic waves investigating the soft biological tissues on a line-per-line scan approach. The main disadvantage of this technique is its limited frame rate, preventing from imaging fast events, such as neuroimaging.

1.3.2 Ultrafast ultrasound imaging in brain imaging

In the past decade, a new method has been introduced in the ultrasound community. It relies on the concept of successive transmissions of ultrasonic plane- or diverging-waves rather than a line-per-line scan of the medium. With such approach, a single plane wave illumination is sufficient to produce an image of the whole field of view. The frame rate reaches up to several thousands of frames per second and allows the implementation of plane-wave imaging on new ultrasound imaging modes.

1.3.2.1 Plane-wave concept

In ultrafast ultrasound imaging, the medium is completely insonified with an unfocused beam (Laurent Sandrin et al. 2002; L. Sandrin et al. 1999; Mickaël Tanter et al. 2002) (**Figure 1.14 b**). Plane-waves are generated by applying a flat delay on the transmitted elements of the ultrasound probe. For linear-array probes, plane-wave insonification is generally used. To use ultrafast imaging with phased-array probes, that have small apertures, there is a need of using diverging-waves (Couade et al. 2009). Diverging-waves are generated by applying a circular delay on transmit elements. Circular delays are created using one single virtual source placed behind the ultrasound probe.

After the medium illumination, the backscattered echoes recollected from the tissues in the whole field of view are stocked in the random-access memory (RAM) of the ultrasound scanner. They are then processed and beamformed in parallel (digital parallel beamforming).

In ultrafast ultrasound imaging, it is possible to reconstruct an entire image with only one single wave transmission, unlike in conventional line-per-line ultrasound imaging. Consequently, the imaging frame-rate is hundred times higher, reaching frame-rates higher than thousand frames-per-second. However, since the focusing step is removed, ultrafast images quality is reduced in resolution and in contrast (**Figure 1.14 b**).

1.3.2.2 Coherent Compounding

Different approaches have been proposed to reduce the imaging speckle noise and clutter, and to increase the signal-to-noise ratio (SNR) overcome the imaging quality limitation of plane-wave illumination. These approaches are based on incoherent (Mickael Tanter et al. 2008) and coherent plane-wave summation, such as in synthetic aperture imaging (Jensen et al. 2006), plane-wave (Montaldo et al. 2009) and diverging-wave (Papadacci et al. 2014) spatial compounding.

In coherent plane-wave spatial compounding, the backscattered echoes from successive tilted plane-waves were transmitted with a high frame-rate and were then coherently summed to restore a focus in transmit (**Figure 1.14 c**). This concept was also extended to diverging-waves imaging, where diverging-wave were generated by different spatially distanced virtual sources behind the ultrasound probe.

It has been demonstrated that it was possible to reconstruct synthetic focal regions equivalent to the ones generated by conventional ultrasound imaging with only 40 coherently compounded plane- or diverging-waves (Montaldo et al., 2009; Papadacci et al., 2014).

Coherent compounded ultrafast ultrasound imaging can be applied on conventional imaging methods, such as B-mode, pulse-wave and color-Doppler imaging. Moreover, as it allows higher frame rate, better spatiotemporal resolution, and ultrafast ultrasound imaging can also be used to expand the ultrasound imaging field of application with new techniques such as Shear Wave Elastography (SWE) and functional ultrasound (fUS). Those two techniques will be detailed and illustrated in the next chapters of this thesis.

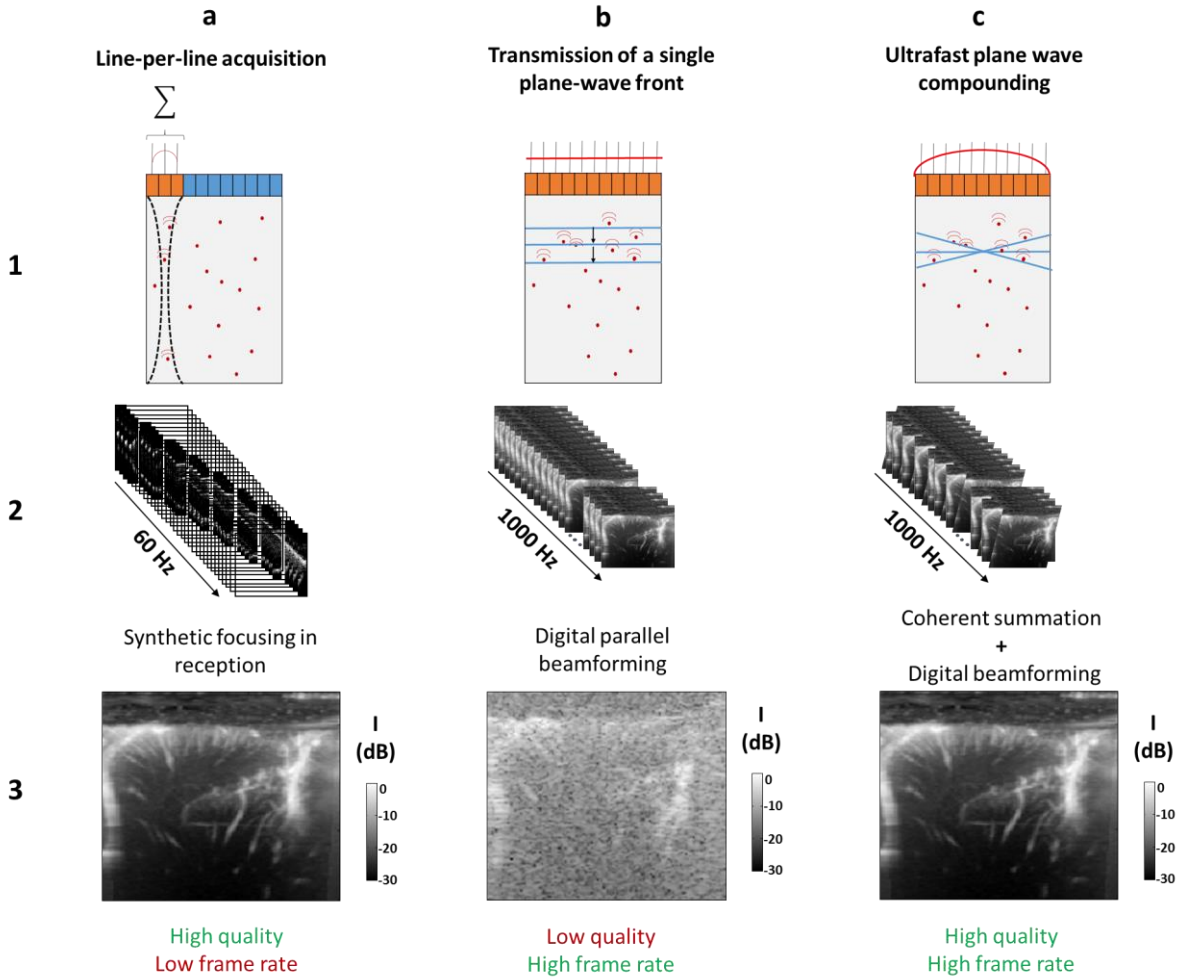


Figure 1.14 - Comparison between conventional ultrasound imaging and ultrafast ultrasound imaging. (a) Conventional ultrasound acquisition. The piezoelectric transducer regularly shifts a focused beam in the image medium to recover to whole field of view. The medium is insonified one line at a time with a slow frame rate imaging. In reception, a synthetic focus algorithm reconstructs the ultrasound image. (b) In plane wave imaging, the medium is completely insonified with a single plane-wave illumination. Compared to the conventional ultrasound imaging, such approach is faster as the digital parallel beamforming can simultaneously process all the backscattered echoes coming from the medium. However high framerate can compromise the image quality. (c) Coherent plane-wave compounding imaging increases the ultrasound image quality performing a coherent sum of the backscattered echoes coming from the medium and properly insonified with multiple tilted plane-waves. These images are brain B-mode images after craniotomy, recorded during brain tumor surgery.

1.3.2.3 Brain ultrafast ultrasound imaging

Applied to brain imaging, ultrafast ultrasound imaging enabled both sagittal and coronal cerebral vascular network non-invasive reconstruction in newborns thank to the high spatiotemporal resolution of the ultrasensitive Doppler imaging (Demené et al. 2014). In this case, the method was facilitated by the presence of a pre-existing anatomical soft window in the infant, the fontanel. The same facilitation applies to all the studies available today where the animals had to go through a craniotomy (rat) (Sieu et al. 2015), or where the animals had a thinned-skull window surgery (rat) (Osmanski et al. 2014). Even using ultrafast ultrasound imaging, the need of contrast agent (Errico et al. 2015) or the complete elimination or reduction of the thickness of the skull are taken as the only options so far to prevent the bone from hindering the penetration of the ultrasonic waves into the brain.

1.4 Thesis objectives

In the recent years, anatomy, blood flow and stiffness have been demonstrated with ultrafast ultrasound imaging in humans and validated on several organs, but not yet in the adult brain. With the advent of ultrafast ultrasound imaging, the echography has the potential to enrich brain imaging field as a non-invasive and non-ionizing modality for anatomical, blood flow, functional and stiffness imaging.

The objective of this thesis was to explore ultrafast ultrasound imaging potential in the human adult brain. One part of this thesis was focused on ultrasound ultrafast imaging for stiffness mapping (Chapter II), and neuro functional imaging (Chapter III) in the adult human brain. In both those chapters, these techniques were studied in the context of brain tumor surgery, which also allows to circumvent aberration induced by the skull as it remains the main limitation for transcranial ultrasound imaging nowadays. Chapter IV was focused on sound speed estimation and aberration correction using virtual time reversal focusing in speckle noise. The latter was first studied in the human liver as a preliminary step with a promising application in liver steatosis staging and secondly its feasibility for transcranial ultrasound imaging with aberration correction was demonstrated in numerical simulation.

1.5 Chapter bibliography

- American Society of Neuroradiology. 2013. “ACR–ASNR–SPR PRACTICE PARAMETER FOR THE PERFORMANCE AND INTERPRETATION OF MAGNETIC RESONANCE IMAGING (MRI) OF THE BRAIN.”
- Binder, Jeffrey R., Stephen M. Rao, Thomas A. Hammeke, Julie A. Frost, Peter A. Bandettini, Andrzej Jesmanowicz, and James S. Hyde. 1995. “Lateralized Human Brain Language Systems Demonstrated by Task Subtraction Functional Magnetic Resonance Imaging.” *Archives of Neurology* 52 (6): 593–601. doi:10.1001/archneur.1995.00540300067015.
- Couade, M., M. Pernot, M. Tanter, E. Messas, A. Bel, M. Ba, A. A. Hagege, and M. Fink. 2009. “Ultrafast Imaging of the Heart Using Circular Wave Synthetic Imaging with Phased Arrays.” In *2009 IEEE International Ultrasonics Symposium*, 515–18. doi:10.1109/ULTSYM.2009.5441640.

- D'Andrea, Antonello, Marianna Conte, Raffaella Scarafile, Lucia Riegler, Rosangela Cocchia, Enrica Pezzullo, Massimo Cavallaro, et al. 2016. "Transcranial Doppler Ultrasound: Physical Principles and Principal Applications in Neurocritical Care Unit." *Journal of Cardiovascular Echography* 26 (2): 28. doi:10.4103/2211-4122.183746.
- Dehaene-Lambertz, G., A. Montavont, A. Jobert, L. Alliol, J. Dubois, L. Hertz-Pannier, and S. Dehaene. 2010. "Language or Music, Mother or Mozart? Structural and Environmental Influences on Infants' Language Networks." *Brain and Language*, Special Issue on Language Development, 114 (2): 53–65. doi:10.1016/j.bandl.2009.09.003.
- Demené, Charlie, Mathieu Pernot, Valérie Biran, Marianne Alison, Mathias Fink, Olivier Baud, and Mickaël Tanter. 2014. "Ultrafast Doppler Reveals the Mapping of Cerebral Vascular Resistivity in Neonates." *Journal of Cerebral Blood Flow & Metabolism* 34 (6): 1009–17. doi:10.1038/jcbfm.2014.49.
- Errico, Claudia, Juliette Pierre, Sophie Pezet, Yann Desailly, Zsolt Lenkei, Olivier Couture, and Mickael Tanter. 2015. "Ultrafast Ultrasound Localization Microscopy for Deep Super-Resolution Vascular Imaging." *Nature* 527 (7579): 499–502. doi:10.1038/nature16066.
- Evans, D. H., ed. 1991. *Doppler Ultrasound: Physics, Instrumentation, and Clinical Applications*. Repr. Chichester: Wiley & Sons.
- Ferrari, Marco, and Valentina Quaresima. 2012. "A Brief Review on the History of Human Functional near-Infrared Spectroscopy (fNIRS) Development and Fields of Application." *NeuroImage* 63 (2): 921–35. doi:10.1016/j.neuroimage.2012.03.049.
- Filler, Aaron G. 2009. "The History, Development and Impact of Computed Imaging in Neurological Diagnosis and Neurosurgery: CT, MRI, and DTI." *Nature Precedings* 7 (1): 1–69.
- Frahm, Jens, Harald Bruhn, Klaus-Dietmar Merboldt, and Wolfgang Hänicke. 1992. "Dynamic MR Imaging of Human Brain Oxygenation during Rest and Photic Stimulation." *Journal of Magnetic Resonance Imaging* 2 (5): 501–5. doi:10.1002/jmri.1880020505.
- Freimann, Florian Baptist, Kaspar-Josche Streitberger, Dieter Klatt, Kui Lin, Joyce McLaughlin, Jürgen Braun, Christian Sprung, and Ingolf Sack. 2012. "Alteration of Brain Viscoelasticity after Shunt Treatment in Normal Pressure Hydrocephalus." *Neuroradiology* 54 (3): 189–96. doi:10.1007/s00234-011-0871-1.
- Ghonge, Nitin. 2013. "Computed Tomography in the 21st Century: Current Status & Future Prospects." *Journal International Medical Sciences Academy* 26(1):35-42 (January).
- Green, Michael A., Lynne E. Bilston, and Ralph Sinkus. 2008. "In Vivo Brain Viscoelastic Properties Measured by Magnetic Resonance Elastography." *NMR in Biomedicine* 21 (7): 755–64. doi:10.1002/nbm.1254.
- Grodd, W, F Schneider, U Klose, and T Nägele. 1995. "Functional magnetic resonance tomography of psychological functions exemplified by experimentally induced emotions." *Der Radiologe* 35 (4): 283–89.
- Hadizadeh, D. R., C. Marx, J. Gieseke, H. H. Schild, and W. A. Willinek. 2014. "High Temporal and High Spatial Resolution MR Angiography (4D-MRA)." *RöFo - Fortschritte Auf Dem Gebiet Der Röntgenstrahlen Und Der Bildgebenden Verfahren* 186 (9): 847–59. doi:10.1055/s-0034-1366661.
- Hirtz, Deborah G. 1993. "Report of the National Institute of Neurological Disorders and Stroke Workshop on Near Infrared Spectroscopy." *Pediatrics* 91 (2): 414–17.
- Hoshi, Yoko. 2003. "Functional Near-infrared Optical Imaging: Utility and Limitations in Human Brain Mapping." *Psychophysiology* 40 (4): 511–20. doi:10.1111/1469-8986.00053.

- Hoshi, Yoko, and Mamoru Tamura. 1993. "Detection of Dynamic Changes in Cerebral Oxygenation Coupled to Neuronal Function during Mental Work in Man." *Neuroscience Letters* 150 (1): 5–8. doi:10.1016/0304-3940(93)90094-2.
- Hutton, B. F., M. Braun, and P. Slomka. 2006. "Image Registration Techniques in Nuclear Medicine Imaging." In *Quantitative Analysis in Nuclear Medicine Imaging*, edited by Habib Zaidi, 272–307. Boston: Kluwer Academic Publishers. http://link.springer.com/10.1007/0-387-25444-7_9.
- Jensen, Jørgen Arendt, Svetoslav Ivanov Nikolov, Kim Løkke Gammelmark, and Morten Høgholm Pedersen. 2006. "Synthetic Aperture Ultrasound Imaging." *Ultrasonics, Proceedings of Ultrasonics International (UI'05) and World Congress on Ultrasonics (WCU)*, 44, Supplement (December): e5–15. doi:10.1016/j.ultras.2006.07.017.
- Jöbsis, Frans. 1977. "Noninvasive, Infrared Monitoring of Cerebral and Myocardial Oxygen Sufficiency and Circulatory Parameters."
- Kashou, Nasser. 2014. "A Practical Guide to an fMRI Experiment." In *Advanced Brain Neuroimaging Topics in Health and Disease - Methods and Applications*, edited by T. Dorina Papageorgiou, George I. Christopoulos, and Stelios M. Smirnakis. InTech. <http://www.intechopen.com/books/advanced-brain-neuroimaging-topics-in-health-and-disease-methods-and-applications/a-practical-guide-to-an-fmri-experiment>.
- Kidwell, Chelsea S., Julio A. Chalela, Jeffrey L. Saver, Sidney Starkman, Michael D. Hill, Andrew M. Demchuk, John A. Butman, et al. 2004. "Comparison of MRI and CT for Detection of Acute Intracerebral Hemorrhage." *JAMA* 292 (15): 1823–30. doi:10.1001/jama.292.15.1823.
- Koenig, M, E Klotz, B Luka, D J Venderink, J F Spittler, and L Heuser. 1998. "Perfusion CT of the Brain: Diagnostic Approach for Early Detection of Ischemic Stroke." *Radiology* 209 (1): 85–93. doi:10.1148/radiology.209.1.9769817.
- Korosec, Frank R. 1999. "Basic Principles of Phase-Contrast, Time-of-Flight, and Contrast-Enhanced MR Angiography." <http://mer.chemia.polsl.pl/biometrologia/materialy/angio/Angiografia-MR-2847-56865.pdf>.
- Kruse, Scott A., Gregory H. Rose, Kevin J. Glaser, Armando Manduca, Joel P. Felmlee, Clifford R. Jack Jr., and Richard L. Ehman. 2008. "Magnetic Resonance Elastography of the Brain." *NeuroImage* 39 (1): 231–37. doi:10.1016/j.neuroimage.2007.08.030.
- Le Bihan, Denis, and Avi Karni. 1995. "Applications of Magnetic Resonance Imaging to the Study of Human Brain Function." *Current Opinion in Neurobiology* 5 (2): 231–37. doi:10.1016/0959-4388(95)80031-X.
- Lehéricy, Stéphane, Hugues Duffau, Philippe Cornu, Laurent Capelle, Bernard Pidoux, Alexandre Carpentier, Stéphanie Auliac, et al. 2000. "Correspondence between Functional Magnetic Resonance Imaging Somatotopy and Individual Brain Anatomy of the Central Region: Comparison with Intraoperative Stimulation in Patients with Brain Tumors." *Journal of Neurosurgery* 92 (4): 589–598.
- Lloyd-Fox, S., A. Blasi, and C. E. Elwell. 2010. "Illuminating the Developing Brain: The Past, Present and Future of Functional near Infrared Spectroscopy." *Neuroscience & Biobehavioral Reviews* 34 (3): 269–84. doi:10.1016/j.neubiorev.2009.07.008.
- Logothetis, Nikos K., Jon Pauls, Mark Augath, Torsten Trinath, and Axel Oeltermann. 2001. "Neurophysiological Investigation of the Basis of the fMRI Signal." *Nature* 412 (6843): 150–57. doi:10.1038/35084005.

- Macé, Emilie, Gabriel Montaldo, Ivan Cohen, Michel Baulac, Mathias Fink, and Mickael Tanter. 2011. “Functional Ultrasound Imaging of the Brain.” *Nature Methods* 8 (8): 662–64. doi:10.1038/nmeth.1641.
- Maresca, D., M. Tanter, and M. Pernot. 2014. “Ultrasound Microangiography of the Metacarpophalangeal Joint Using Ultrafast Doppler.” In *2014 IEEE International Ultrasonics Symposium*, 425–27. doi:10.1109/ULTSYM.2014.0105.
- Mariappan, Yogesh K., Kevin J. Glaser, and Richard L. Ehman. 2010. “Magnetic Resonance Elastography: A Review.” *Clinical Anatomy* 23 (5): 497–511. doi:10.1002/ca.21006.
- Matsumoto, M., N. Kodama, Y. Endo, J. Sakuma, Ky Suzuki, T. Sasaki, K. Murakami, Ke Suzuki, T. Katakura, and F. Shishido. 2007. “Dynamic 3D-CT Angiography.” *American Journal of Neuroradiology* 28 (2): 299–304.
- Mehagnoul-Schipper, D. Jannet, Bas F.W. van der Kallen, Willy N.J.M. Colier, Marco C. van der Sluijs, Leon J.Th.O. van Erning, Henk O.M. Thijssen, Berend Oeseburg, Willibrord H.L. Hoefnagels, and René W.M.M. Jansen. 2002. “Simultaneous Measurements of Cerebral Oxygenation Changes during Brain Activation by near-Infrared Spectroscopy and Functional Magnetic Resonance Imaging in Healthy Young and Elderly Subjects.” *Human Brain Mapping* 16 (1): 14–23. doi:10.1002/hbm.10026.
- Misulis, Karl E. 2013. *Atlas of EEG, Seizure Semiology, and Management*. Oxford: Oxford University Press, USA. <http://public.eblib.com/choice/publicfullrecord.aspx?p=1426695>.
- Montaldo, G., M. Tanter, J. Bercoff, N. Benech, and M. Fink. 2009. “Coherent Plane-Wave Compounding for Very High Frame Rate Ultrasonography and Transient Elastography.” *IEEE Transactions on Ultrasonics, Ferroelectrics and Frequency Control* 56 (3): 489–506. doi:10.1109/TUFFC.2009.1067.
- Murphy, Matthew C, John Huston 3rd, Clifford R Jack Jr, Kevin J Glaser, Armando Manduca, Joel P Felmlee, and Richard L Ehman. 2011. “Decreased Brain Stiffness in Alzheimer’s Disease Determined by Magnetic Resonance Elastography.” *Journal of Magnetic Resonance Imaging: JMRI* 34 (3): 494–98. doi:10.1002/jmri.22707.
- Muthupillai, R., D. J. Lomas, P. J. Rossman, J. F. Greenleaf, A. Manduca, and R. L. Ehman. 1995. “Magnetic Resonance Elastography by Direct Visualization of Propagating Acoustic Strain Waves.” *Science* 269 (5232): 1854–57.
- Nabavi, Darius G., Aleksa Cenic, Rosemary A. Craen, Adrian W. Gelb, John D. Bennett, Roman Kozak, and Ting-Yim Lee. 1999. “CT Assessment of Cerebral Perfusion: Experimental Validation and Initial Clinical Experience.” *Radiology* 213 (1): 141–49. doi:10.1148/radiology.213.1.r99oc03141.
- Niedermeyer, Ernst, and F. H. Lopes da Silva. 2005. *Electroencephalography: Basic Principles, Clinical Applications, and Related Fields*. Lippincott Williams & Wilkins.
- Osmanski, Bruno-Félix, Sophie Pezet, Ana Ricobaraza, Zsolt Lenkei, and Mickael Tanter. 2014. “Functional Ultrasound Imaging of Intrinsic Connectivity in the Living Rat Brain with High Spatiotemporal Resolution.” *Nature Communications* 5 (October): 5023. doi:10.1038/ncomms6023.
- Padayachee, T. S., F. J. Kirkham, R. R. Lewis, J. Gillard, M. C. E. Hutchinson, and R. G. Gosling. 1986. “Transcranial Measurement of Blood Velocities in the Basal Cerebral Arteries Using Pulsed Doppler Ultrasound: A Method of Assessing the Circle of Willis.” *Ultrasound in Medicine & Biology* 12 (1): 5–14. doi:10.1016/0301-5629(86)90138-9.

- Papadacci, C., M. Pernot, M. Couade, M. Fink, and M. Tanter. 2014. “High-Contrast Ultrafast Imaging of the Heart.” *IEEE Transactions on Ultrasonics, Ferroelectrics, and Frequency Control* 61 (2): 288–301. doi:10.1109/TUFFC.2014.6722614.
- Raaij, Martijn E. van, Liis Lindvere, Adrienne Dorr, Jianfei He, Bhupinder Sahota, F. Stuart Foster, and Bojana Stefanovic. 2011. “Functional Micro-Ultrasound Imaging of Rodent Cerebral Hemodynamics.” *NeuroImage* 58 (1): 100–108. doi:10.1016/j.neuroimage.2011.05.088.
- Ray, Amit, and Susan M. Bowyer. 2010. “Clinical Applications of Magnetoencephalography in Epilepsy.” *Annals of Indian Academy of Neurology* 13 (1): 14–22. doi:10.4103/0972-2327.61271.
- Ross, M. R., N. J. Pelc, and D. R. Enzmann. 1993. “Qualitative Phase Contrast MRA in the Normal and Abnormal Circle of Willis.” *American Journal of Neuroradiology* 14 (1): 19–25.
- Sack, Ingolf, Bernd Beierbach, Uwe Hamhaber, Dieter Klatt, and Jürgen Braun. 2008. “Non-Invasive Measurement of Brain Viscoelasticity Using Magnetic Resonance Elastography.” *NMR in Biomedicine* 21 (3): 265–71. doi:10.1002/nbm.1189.
- Sack, Ingolf, Bernd Beierbach, Jens Wuerfel, Dieter Klatt, Uwe Hamhaber, Sebastian Papazoglou, Peter Martus, and Jürgen Braun. 2009. “The Impact of Aging and Gender on Brain Viscoelasticity.” *NeuroImage* 46 (3): 652–57. doi:10.1016/j.neuroimage.2009.02.040.
- Sanden, Boudewijn PJ van der, Arend Heerschap, Louis Hoofd, Arjan W. Simonetti, Klaas Nicolay, Annette van der Toorn, Willy NJM Colier, and Albert J. van der Kogel. 1999. “Effect of Carbogen Breathing on the Physiological Profile of Human Glioma Xenografts.” *Magnetic Resonance in Medicine* 42 (3): 490–499.
- Sandrin, L., S. Catheline, M. Tanter, X. Hennequin, and M. Fink. 1999. “Time-Resolved Pulsed Elastography with Ultrafast Ultrasonic Imaging.” *Ultrasonic Imaging* 21 (4): 259–72. doi:10.1177/016173469902100402.
- Sandrin, Laurent, Mickaël Tanter, Stefan Catheline, and Mathias Fink. 2002. “Shear Modulus Imaging with 2-D Transient Elastography.” *IEEE Transactions on Ultrasonics, Ferroelectrics, and Frequency Control* 49 (4): 426–35.
- Schaefer, P. W., L. Roccatagliata, C. Ledezma, B. Hoh, L. H. Schwamm, W. Koroshetz, R. G. Gonzalez, and M. H. Lev. 2006. “First-Pass Quantitative CT Perfusion Identifies Thresholds for Salvageable Penumbra in Acute Stroke Patients Treated with Intra-Arterial Therapy.” *American Journal of Neuroradiology* 27 (1): 20–25.
- Shin, Su-Mi, and Jee Won Chai. 2016. “Brain Ultrasonographic Findings of Late-Onset Circulatory Dysfunction due to Adrenal Insufficiency in Preterm Infants.” *Ultrasonography (Seoul, Korea)* 35 (3): 258–64. doi:10.14366/usg.16013.
- Sieu, Lim-Anna, Antoine Bergel, Elodie Tiran, Thomas Deffieux, Mathieu Pernot, Jean-Luc Gennisson, Mickaël Tanter, and Ivan Cohen. 2015. “EEG and Functional Ultrasound Imaging in Mobile Rats.” *Nature Methods* 12 (9): 831–34. doi:10.1038/nmeth.3506.
- Streitberger, Kaspar-Josche, Edzard Wiener, Jan Hoffmann, Florian Baptist Freimann, Dieter Klatt, Jürgen Braun, Kui Lin, et al. 2010. “In Vivo Viscoelastic Properties of the Brain in Normal Pressure Hydrocephalus.” *NMR in Biomedicine*, n/a-n/a. doi:10.1002/nbm.1602.

- Stufflebeam, Steven M., Naoaki Tanaka, and Seppo P. Ahlfors. 2009. "Clinical Applications of Magnetoencephalography." *Human Brain Mapping* 30 (6): 1813–23. doi:10.1002/hbm.20792.
- Szabo, Thomas L. 2004. "8 - WAVE SCATTERING AND IMAGING." In *Diagnostic Ultrasound Imaging*, 213–42. Biomedical Engineering. Burlington: Academic Press. <http://www.sciencedirect.com/science/article/pii/B9780126801453500098>.
- Szabo, Thomas L., and Peter A. Lewin. 2013. "Ultrasound Transducer Selection in Clinical Imaging Practice." *Journal of Ultrasound in Medicine* 32 (4): 573–82.
- Tahmasebpour, Hamid R., Anne R. Buckley, Peter L. Cooperberg, and Cathy H. Fix. 2005. "Sonographic Examination of the Carotid Arteries." *RadioGraphics* 25 (6): 1561–75. doi:10.1148/rg.256045013.
- Tanaka, H., N. Fujita, T. Enoki, K. Matsumoto, Y. Watanabe, K. Murase, and H. Nakamura. 2006. "Relationship between Variations in the Circle of Willis and Flow Rates in Internal Carotid and Basilar Arteries Determined by Means of Magnetic Resonance Imaging with Semiautomated Lumen Segmentation: Reference Data from 125 Healthy Volunteers." *American Journal of Neuroradiology* 27 (8): 1770–75.
- Tanter, Mickael, Jeremy Bercoff, Alexandra Athanasiou, Thomas Deffieux, Jean-Luc Gennisson, Gabriel Montaldo, Marie Muller, Anne Tardivon, and Mathias Fink. 2008. "Quantitative Assessment of Breast Lesion Viscoelasticity: Initial Clinical Results Using Supersonic Shear Imaging." *Ultrasound in Medicine & Biology* 34 (9): 1373–86. doi:10.1016/j.ultrasmedbio.2008.02.002.
- Tanter, Mickaël, Jeremy Bercoff, Laurent Sandrin, and Mathias Fink. 2002. "Ultrafast Compound Imaging for 2-D Motion Vector Estimation: Application to Transient Elastography." *IEEE Transactions on Ultrasonics, Ferroelectrics, and Frequency Control* 49 (10): 1363–74.
- Tong, Shanbao, and Nitish Vyomesh Thakor. 2009. *Quantitative EEG Analysis Methods and Clinical Applications*. Artech House.
- Tootell, Roger B., John B. Reppas, Kenneth K. Kwong, Rafael Malach, Richard T. Born, Thomas J. Brady, Bruce R. Rosen, and John W. Belliveau. 1995. "Functional Analysis of Human MT and Related Visual Cortical Areas Using Magnetic Resonance Imaging." *Journal of Neuroscience* 15 (4): 3215–3230.
- Villringer, A., J. Planck, C. Hock, L. Schleinkofer, and U. Dirnagl. 1993. "Near Infrared Spectroscopy (NIRS): A New Tool to Study Hemodynamic Changes during Activation of Brain Function in Human Adults." *Neuroscience Letters* 154 (1–2): 101–4. doi:10.1016/0304-3940(93)90181-J.
- White, Brian R., Abraham Z. Snyder, Alexander L. Cohen, Steven E. Petersen, Marcus E. Raichle, Bradley L. Schlaggar, and Joseph P. Culver. 2009. "Resting-State Functional Connectivity in the Human Brain Revealed with Diffuse Optical Tomography." *NeuroImage* 47 (1): 148–56. doi:10.1016/j.neuroimage.2009.03.058.
- Wuerfel, Jens, Friedemann Paul, Bernd Beierbach, Uwe Hamhaber, Dieter Klatt, Sebastian Papazoglou, Frauke Zipp, Peter Martus, Jürgen Braun, and Ingolf Sack. 2010. "MR-Elastography Reveals Degradation of Tissue Integrity in Multiple Sclerosis." *NeuroImage* 49 (3): 2520–25. doi:10.1016/j.neuroimage.2009.06.018.
- Wyatt, J. S., D. T. Delpy, M. Cope, Susan Wray, and E. O. R. Reynolds. 1986. "QUANTIFICATION OF CEREBRAL OXYGENATION AND HAEMODYNAMICS IN SICK NEWBORN INFANTS BY NEAR INFRARED SPECTROPHOTOMETRY."

- The Lancet*, Originally published as Volume 2, Issue 8515, 328 (8515): 1063–66. doi:10.1016/S0140-6736(86)90467-8.
- Yetkin, Z, W Mueller, T Hammeke, GL Morris, and V Haughton. 2017. “Functional Magnetic Resonance Imaging Mapping of the Sensorimotor Cortex with Tactile Stimulation.” *LWW*. Accessed February 13. http://journals.lww.com/neurosurgery/Fulltext/1995/05000/Functional_Magnetic_Resonance_Imaging_Mapping_of.5.aspx.
- Yin, Meng, Jayant A. Talwalkar, Kevin J. Glaser, Armando Manduca, Roger C. Grimm, Phillip J. Rossman, Jeff L. Fidler, and Richard L. Ehman. 2007. “A Preliminary Assessment of Hepatic Fibrosis with Magnetic Resonance Elastography.” *Clinical Gastroenterology and Hepatology: The Official Clinical Practice Journal of the American Gastroenterological Association* 5 (10): 1207–1213.e2. doi:10.1016/j.cgh.2007.06.012.
- Younan, Youliana, Thomas Deffieux, Benoit Larrat, Mathias Fink, Mickael Tanter, and Jean-Francois Aubry. 2013. “Influence of the Pressure Field Distribution in Transcranial Ultrasonic Neurostimulation.” *Medical Physics* 40 (8): 82902. doi:10.1118/1.4812423.
- Yousem, D M, S C Williams, R O Howard, C Andrew, A Simmons, M Allin, R J Geckle, et al. 1997. “Functional MR Imaging during Odor Stimulation: Preliminary Data.” *Radiology* 204 (3): 833–38. doi:10.1148/radiology.204.3.9280268.

Chapter II

Intraoperative brain Shear Wave Elastography and 3D elastography using matrix array

Intraoperative brain Shear Wave Elastography
and 3D elastography using matrix array

Table of contents

2. Intraoperative brain Shear Wave Elastography and 3D elastography using 3D matrix array	55
2.1 Chapter introduction	55
2.2 Shear Wave Elastography (SWE) principle	55
2.3 Shear wave elastography in brain tumor surgery	57
2.3.1 Ultrasound in neurosurgery.....	57
2.3.2 Conventional Ultrasound and SWE Acquisitions.....	58
2.3.3 Patients cohort.....	59
2.3.4 Intraoperative ultrasound Imaging.....	60
2.3.5 Tumors classification using SWE.....	61
2.3.6 Stiffness analysis by subgroup comparison.....	63
2.3.7 Repeatability and reproducibility.....	64
2.3.8 Clinical illustrative cases.....	65
2.3.8.1 Error in the initial MRI diagnostic.....	65
2.3.8.2 Necrosis gradient in malignant tumors.....	66
2.3.9 SWE contribution in neurosurgery.....	66
2.4 Relationship between intracranial pressure and SWE in normal brain in patients with lesion	68
2.4.1 Intracranial pressure.....	68
2.4.2 Intracranial pressure monitoring.....	70

2.4.3	Hypothesis.....	71
2.4.4	In vitro study	71
2.4.5	In vivo study	73
2.4.6	Conclusion and perspectives.....	75
2.5	3D elastography using matrix array.....	76
2.5.1	From 2D to 3D elastography	76
2.5.2	Ultrasound system infrastructure.....	77
2.5.3	Image formation	78
2.5.3.1	Ultrafast Imaging in 3D for shear wave tracking.....	78
2.5.3.2	Shear wave velocity estimation	80
2.5.4	Phantom experiments	80
2.5.5	In-vivo 3D elastography	81
2.5.6	Conclusion.....	82
2.5.7	Perspectives.....	82
2.6	Chapter conclusion.....	83
2.7	Chapter bibliography.....	84

2. Intraoperative brain Shear Wave Elastography and 3D elastography using 3D matrix array

2.1 Chapter introduction

In this Chapter we aim to evaluate Shear Wave Elastography (SWE) contribution in neurosurgery, and to enlarge SWE application field to 3D imaging using matrix array.

Before presenting this thesis contribution, SWE principle and main applications are introduced in **section 2.2**.

In this chapter, we first used intraoperative SWE to quantify normal brain and brain tumor stiffness. We wanted to study the potential ability of tissue stiffness to be a biomarker to differentiate benign from malignant lesions in intraoperative conditions, therefore we conducted an *in vivo* study on this subject. The impact of these results for brain tumor characterization and resection is discussed in **section 2.3**.

Secondly, our objective was to study the existence of any relationship between normal brain stiffness measured with SWE and Intracranial pressure (ICP). We conducted one *in vitro* study on veal brain and one preliminary clinical study on this topic. Advanced and limitations are presented in **section 2.4**.

Finally, after studying 2D SWE contribution in neurosurgery, the last section focuses on 3D SWE using matrix array. A unique 3D scanner was built for this purpose. This adapted scanner and the corresponding imaging technique are described in **section 2.5**, along with the first experiments in ultrasound phantoms and *in vivo*.

2.2 Shear Wave Elastography (SWE) principle

To date, the first and main medical application of ultrafast ultrasound imaging is soft tissues' stiffness imaging. This technique was designated as Shear Wave Elastography (SWE).

Elastography is a family of techniques that image the elastic properties of soft tissues. Its development started more than 20 years ago and since then it has been showed that its results are highly clinically relevant. Tissue stiffness can be estimated from the strain analysis of the tissue under stress (quasi-static methods), or by imaging an induced mechanical shear wave (dynamic methods). The assessed physical parameter, corresponding to the tissue stiffness, is the Young's modulus (E). To estimate the Young's modulus, all shear wave elastography techniques rely on the same basis: the application of an external force in a tissue that generates a shear wave; and the tracking of the propagation of this wave. The different shear wave Elastography methods are differentiated by the properties of the used external force. In this manuscript, only the dynamic methods (i.e. where a time varying external force is applied) using the acoustic

radiation force, will be described. For further information on other elastography methods, a review is given by Gennisson *et al.* (Gennisson et al., 2013).

In the dynamic methods, a time-varying force is applied to the tissue and, as consequence, mechanical wave will propagate as compressional waves (at ~ 1500 m/s and high frequencies) or as shear waves (ate $\sim 1-50$ m/s and at low frequencies). The shear wave velocity is directly related to the shear modulus by:

$$\mu = c_s^2 \rho$$

Equation 2.1 - The shear modulus equation, where c_s is the shear wave velocity and ρ the tissue density.

In an incompressible isotropic medium, as in the case of most of the biological tissues, the Young's modulus is directly related to shear modulus by $E \approx 3\mu$. Thus, by determining the shear wave velocity, the Young's modulus can be estimated quantitatively.

In Shear Wave Elastography (SWE) technique, as describe by Bercoff et al. (Bercoff et al., 2004), the application of an acoustic radiation force (i.e. focused push beam) in the tissue allows a quasi-plane shear wave to propagate in the imaging plane (**Figure 2.1 a**). Then, by using ultrafast imaging (with unfocused beams illumination and good temporal resolution) the shear wave propagation can be followed over time (**Figure 2.1 b**). Finally, by using tissue Doppler algorithms, the shear wave velocity can be assessed. However, in order to accurately track and estimate the shear wave velocities, the pulse-repetition frequency and the maximum number of unfocused waves emitted should be adapted (i.e. maintain as high as possible the temporal resolution or the imaging frame-rate and the image quality).

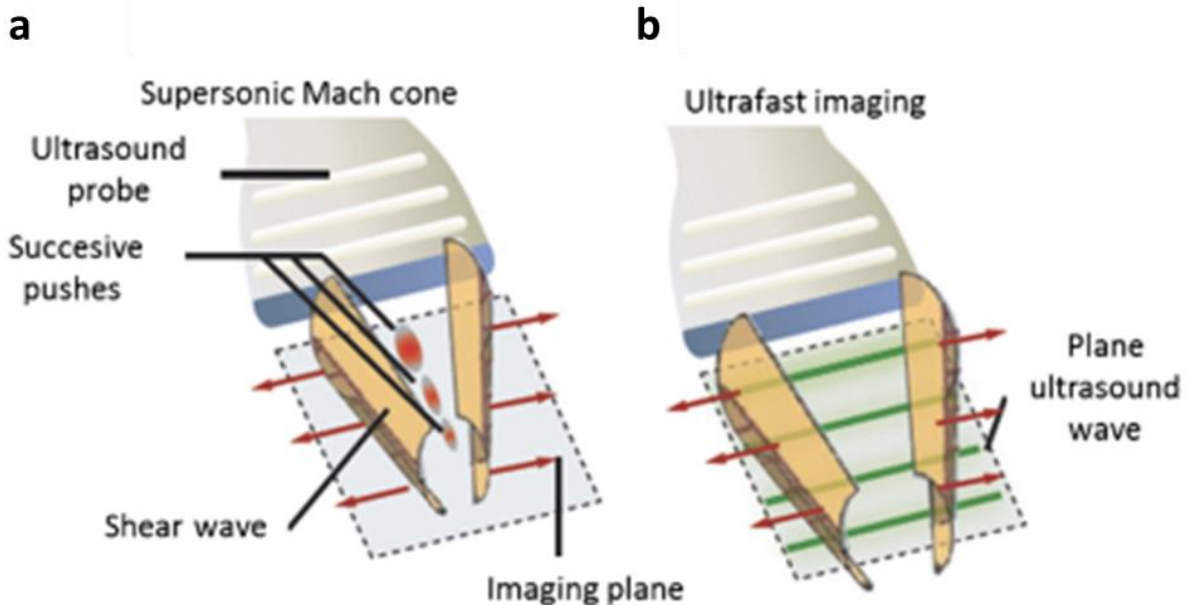


Figure 2.1 - SWE imaging principle (Taken from (Gennisson et al., 2013)).

Shear-wave imaging has become a major mode in ultrasound imaging in the last 10 years. The technique has been used *in vivo* and in clinical practice, with different medical diagnostic applications, such as breast tumor diagnosis (Tanter et al., 2008a) (**Figure 2.2 a**), thyroid nodes

diagnosis (Sebag et al., 2010) (Figure 2.2 b) or liver fibrosis evaluation (Bavu et al., 2011) (Figure 2.2 c).

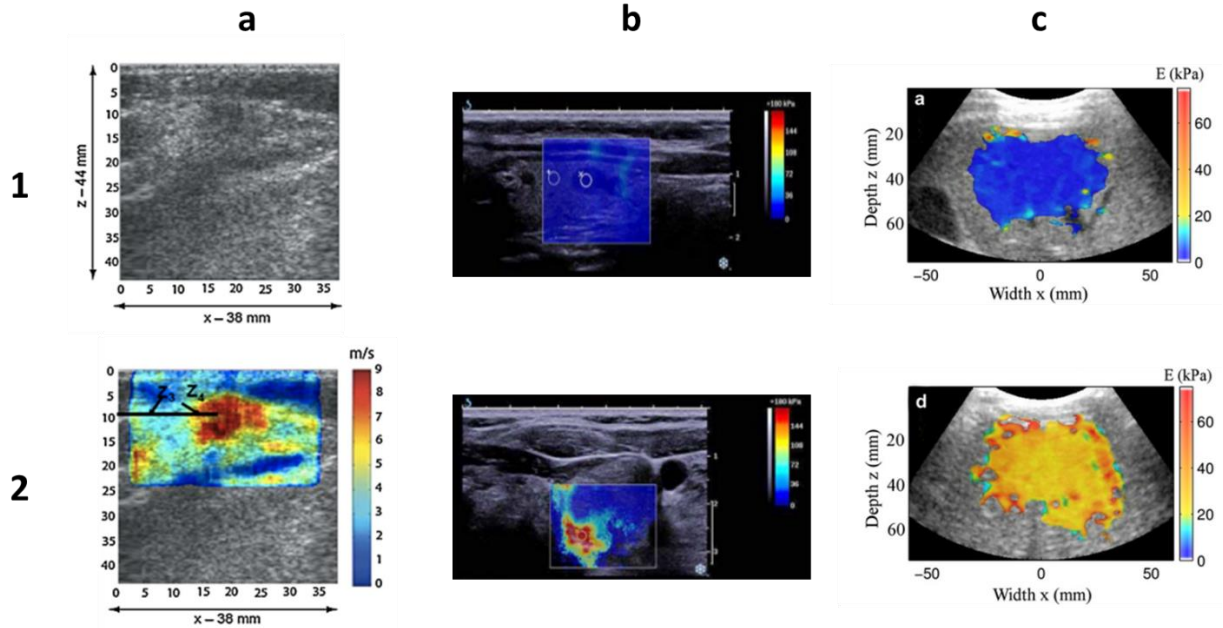


Figure 2.2 - SWE clinical applications. (a) An in vivo result of a B-mode image and a shear wave elasticity map of a ductal infiltrating carcinoma. The B-mode image (a1) doesn't reveal the malignant tumor, whereas the elasticity imaging (a2) clearly brings out a very stiff mass at more than 150 kPa (7.1 m/s) (Taken from (Gennisson et al., 2013)). (b) Thyroid nodule images obtained on US elastography of a benign thyroid nodule (b1) and a malignant papillary carcinoma (b2) (Taken from (Sebag et al., 2010)). (c) Bidimensional liver elasticity maps assessed using the supersonic shear imaging (SSI) technique superimposed to the corresponding B-scan. The Young's modulus representing the liver stiffness is represented in color levels. (c1): patient grade F1, $E = 4.78 \pm 0.83$ kPa (c2): patient grade F4, $E = 27.43 \pm 2.64$ kPa (Taken from (Bavu et al., 2011)).

The basics of SWE principle and its main applications were presented. In the next session, we aim to evaluate Shear Wave Elastography (SWE) contribution in neurosurgery, and to enlarge SWE application field to 3D imaging using matrix array.

2.3 Shear wave elastography in brain tumor surgery

We conducted a 93 patients clinical study to quantify the stiffness of normal brain tissue and brain tumors. The study and its results will be presented in this section. Moreover, the ability of tissue stiffness to stand as a biomarker to differentiate benign from malignant lesions in intraoperative conditions will be studied.

2.3.1 Ultrasound in neurosurgery

Ultrasonography remains a major technology to visualize tumors in brain surgery. This imaging modality has been employed by neurosurgeons for several years (Selbekk et al., 2013; Unsgaard et al., 2002) as it offers a real-time control of tumor resection. It has been proven that the use of intraoperative ultrasonography could have a benefit on the quality of life of patients with

intracranial gliomas (Jakola et al., 2011). Ultrasonography will be a decisive issue in the next decade to improve brain tumor resection, regarding its portability, free-hand ability, real-time imaging acquisition, absence of brain shift and finally, ensuring cost efficiency. Three-dimension ultrasonography-based navigation has also been developed to eradicate the intraoperative brain shift issue (Lindner et al., 2006; Rasmussen et al., 2007). Standard B mode has been successfully used in intraoperative conditions to help tumor resection monitoring by delineation of tumor margins (Shinoura et al., 2006).

Tissues palpation has always been used by surgeons to differentiate normal brain tissue and lesions. But this remains a very subjective assessment. Ultrasonography now offers new modalities to assess living tissues stiffness, so called elastography methods. Dynamic elastography is based on the concept of shear wave propagation which allows to quantify stiffness by measuring the local speed of shear waves generated directly within the tissue (Sarvazyan et al., 1998). As shear waves propagate at typical speed of 1 to 10 m.s⁻¹, ultrafast ultrasound imaging (Tanter and Fink, 2014) at frame rates higher than 1000 fps are mandatory for the real time tracking of these transient mechanical vibrations (Bercoff et al., 2004; Gennisson et al., 2013; Tanter et al., 2002). Preliminary approaches based on shear wave propagation have been evaluated in the framework of neurosurgery. Recently, the Supersonic Shear Imaging technique (SSI) was tested during intraoperative surgery through the shear wave elastography mode (SWE) to help physicians to detect focal symptomatic epilepsy region (Chan et al., 2014). In this study no obvious lesion was detected with B-mode ultrasound, but a focal area of increased stiffness was revealed by SWE approximately 1.5 cm under the brain surface. Nowadays, SSI is routinely used in many specialties, as for instance in liver fibrosis assessment (Ferraioli et al., 2014; Yoon et al., 2014) and in breast imaging (Berg et al., 2012). It also enables differentiation between benign and malignant lesions in multiple pathologies such as breast cancer (Lee et al., 2014; Tanter et al., 2008b), or thyroid nodules (Bhatia et al., 2012).

2.3.2 Conventional Ultrasound and SWE Acquisitions

Ultrasound images and stiffness maps were acquired with an ultrafast ultrasonic device (Aixplorer®, Supersonic Imagine, Aix-en-provence, France) driving a linear array (SL10-2, Supersonic Imagine, Aix-en-provence, France, 6 MHz central frequency, 192 elements). Conventional B-mode images were recorded during surgery in order to monitor brain tumor resection. The image size was typically 38.4 x 40.0 mm. Stiffness maps were acquired with the same probe during surgery by using SSI technique as described in Bercoff *et al.* (Bercoff et al., 2004). Briefly, shear waves were generated in the brain by focusing ultrasound during a short time (~100 μs). Then a movie of the shear wave propagation was caught in real time by using an ultrafast ultrasonic scanner (up to 20 000 images/s). Stiffness maps were then extracted by analysis of the shear wave speed from recorded movies, since shear wave speed is directly linked to the stiffness in isotropic, locally homogeneous and quasi-incompressible media through the relationship: $E = 3\rho V_s^2$ (where E the Young's modulus (stiffness), ρ the density (~1000 kg/m³) and V_s the shear wave speed in m/s). At last, stiffness was color-coded in kilopascals (kPa) and displayed over the classical B-mode image. The bluest coloration represented the softest

elasticity, the reddest represented the hardest. Stiffness quantification (and shear wave speed quantification) was then done by applying a Region Of Interest (so called Qbox®) in the desired anatomic region giving access to a mean value of stiffness and its standard deviation in kPa.

2.3.3 Patients cohort

Between December 2012 and March 2014, a total of 93 patients with a brain lesion requiring surgery were included in the study. All types of tumor were recorded; emergency surgeries were not take into account. All patients gave their informed consent. Ethical considerations had been previously validated by our institutional ethics committee, “Comité de Protection des Personnes – Ile-de-France VI – Pitié Salpêtrière” (CPPIDF6). The patients cohort was characterized by a mean age of 53 years of age (with the total sample set ranging from 24 to 85 years of age), including 39% male and 61% female.

In this cohort, 63 patients were included within four categories that correspond to the main brain tumors types: low-grade glioma (WHO grade II), high-grade glioma (WHO grade III and IV), metastasis and meningioma. 25 patients with other lesion types (such as hemangioblastomas, cavernomas, *etc.*) were recorded but excluded from the present study because of their heterogeneity and rarity. Five patients had non-workable results, due to a very small surgical aperture. The four subgroups were shared out as follow: 16 meningiomas, 14 low-grade gliomas, 18 high-grade gliomas and 15 metastasis (Figure 2.3). To summarize, 30 benign tumors (meningiomas and low-grade gliomas) and 33 malignant tumors (high-grade gliomas and metastasis) were studied.

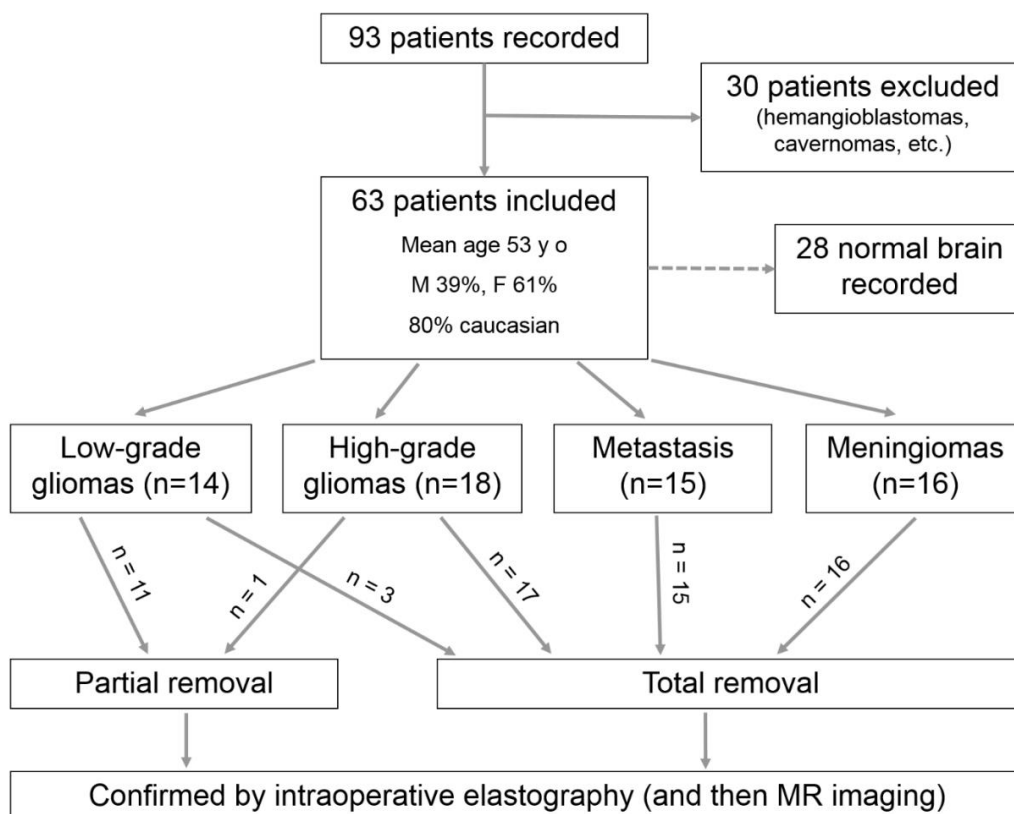


Figure 2.3 - Distribution of all the recorded patients.

For all high-grade gliomas (except one), metastasis and meningiomas, a macroscopic tumor removal was achieved during the surgery and confirmed by both imaging modalities. Regarding low-grade gliomas, which were all operated under awake condition, a complete removal was performed and confirmed by ultrasound imaging in three cases (21%). The remaining 11 cases (79%) could not benefit from a complete resection because of functional brain areas surrounding the lesion.

2.3.4 Intraoperative ultrasound Imaging

At least one surgeon and one researcher were present at each session. Both senior and junior neurosurgeons had the same ease. Contrary to the surgeon, the researcher was always a blind observer, never aware of the diagnosis. In the operative room, the probe was disinfected following our institution protocol and then inserted in a sterile plastic cap with sterile ultrasound gel on the top of the probe. During surgery, before or after dural opening, a standard B-mode acquisition was performed to detect the tumor and to assess its shape, boundaries, possible heterogeneities within the lesion and anatomical relations with normal surrounding tissues. The ultrasound standard imaging had a very high resolution ($\sim 200\mu\text{m}$), comparable to MR imaging (Figure 2.4, a-b). The ability to get the whole tumor in the ultrasound beam was dependent on the lesion size; as a reminder the probe had a 38.4 mm width. Brain normal structures were also visualized, such as surrounding cortex, ventricles, etc. SWE was then made at different locations by the surgeon: within the tumor, at the border of it and within normal brain when feasible. Special attention was paid when unusual structures were seen within the tumor, such as calcification or liquid cyst. Thus, elastographic windows were focused on these particularities to assess consistency changes within the tumor, with objective stiffness parameters. At last, lesion elasticity was quantified on the ultrasound device with full objectivity by the researcher blinded to the diagnosis. To average tumor elasticity, Qbox were designed in different locations in each image, with a minimum of six images per patient. The diameter of the Qbox was always as big as possible, 7 mm minimum. As shown in (Figure 2.4, c), for one Qbox, mean, minimum value,

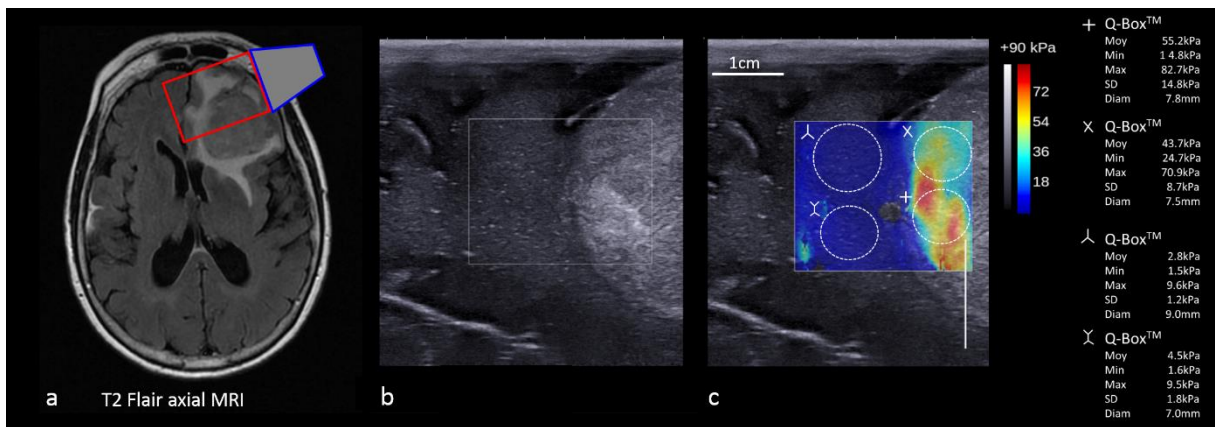


Figure 2.4 - Imaging of the boundary between normal brain and tumor in a patient with meningioma. (a) T2 flair axial MRI, (b) Standard ultrasound B-mode, (c) Stiffness map and stiffness quantitative measurements in kPa (m/s) with Qbox®. Dimensions of ultrasound images: 38.4 mm wide, 45.0 mm depth. Blue trapezium: ultrasound probe. Red rectangle: imaging plan.

maximum value, standard deviation inside the Qbox and diameter of the Qbox were obtained.

At the convenience of the neurosurgeon during surgery, a Doppler acquisition was performed to observe the surrounding vessels and at the end of the operation, a final ultrasound imaging was made to confirm the quality of resection, with B-mode and SWE. Postoperative brain MRI assessed the final quality of removal. As the reference standard, type and grade of each tumor was ascertained by anatomopathology analysis after surgery. For all patients, the imaging was easy and not time-consuming. Quantification of stiffness was feasible in all patients (95%). The average time of the procedure was five minutes (min 3, max 10). Neither infection nor side effect was recorded.

2.3.5 Tumors classification using SWE

Classification into four categories of tumors was made by using histological results: meningiomas, low-grade gliomas, high-grade gliomas and metastasis. All patients were pooled by subgroups with mean values and standard deviation from the mean of stiffness (Young's Modulus in kPa, Shear Wave Speed in m/s) within the Qbox: 33.1 ± 5.9 kPa (3.3 ± 0.6 m/s), 23.7 ± 4.9 kPa (2.8 ± 0.6 m/s), 11.4 ± 3.6 kPa (1.9 ± 0.6 m/s) and 16.7 ± 2.5 kPa (2.4 ± 0.4 m/s) respectively in meningiomas, low-grade gliomas, high-grade gliomas and metastasis (Figure 2.5).

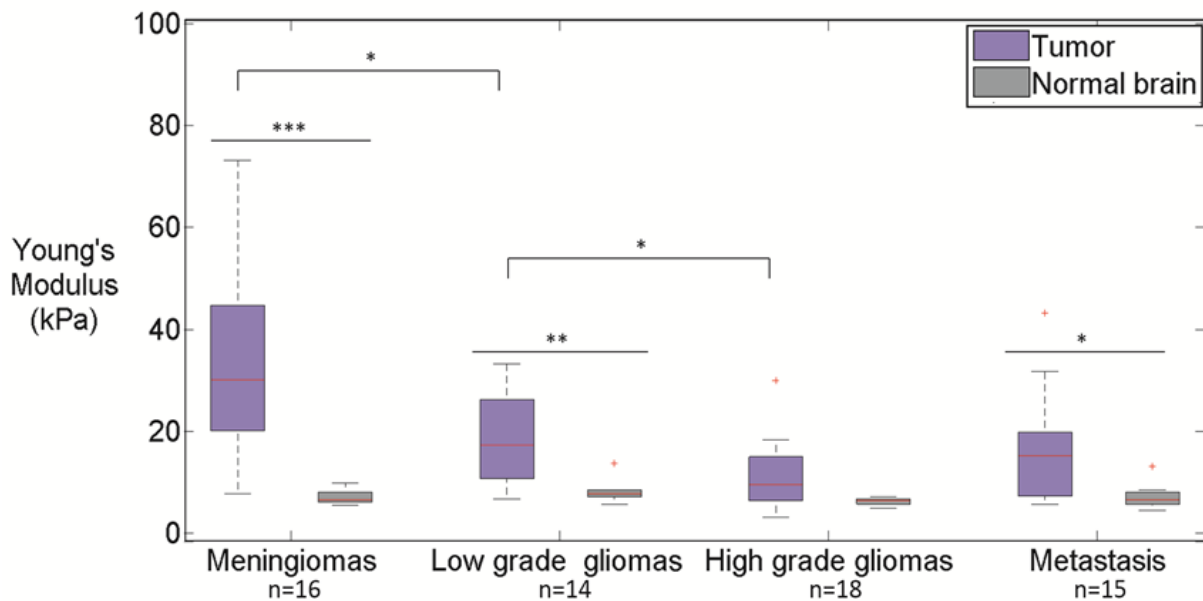


Figure 2.5 - Young's Modulus in kPa of both tumor and normal brain for the four analysed types of tumors, meningiomas, low-grade gliomas, high-grade gliomas and metastasis. The line through the middle of the box represents the median (50th percentile). The top and bottom of the boxes are 75th and 25th percentiles. Between the upper and the lower adjacent lines are about 99% of the values (Turkey Boxplot). All plus signs above these lines represent the outliers. For each category the n represent the number of patients. * $p < 0.05$, ** $p < 0.01$, *** $p < 0.001$ stand for each type of tumor for the p value between normal brain and tumor. The star (*) between low-grade and high grade gliomas stand for the p-value between these two tumorous tissues.

Normal brain measurement was consistently tried and was feasible in 44% of the cases. Non-feasibility was due to small surgical aperture, difficult access or loss of signal. Stiffness assessment of normal brain was similar within the subgroups. A global mean elasticity of 7.3 ± 2.1 kPa (1.6 ± 0.5 m/s) was observed for normal brain tissue, all types of patient combined. This results are in accordance with cortex (gray matter) stiffness found with MRE (Kruse et al., 2008).

In **Figure 2.6**, one patient of each studied tumor type is presented. MRI images were used to help during location with ultrasounds.

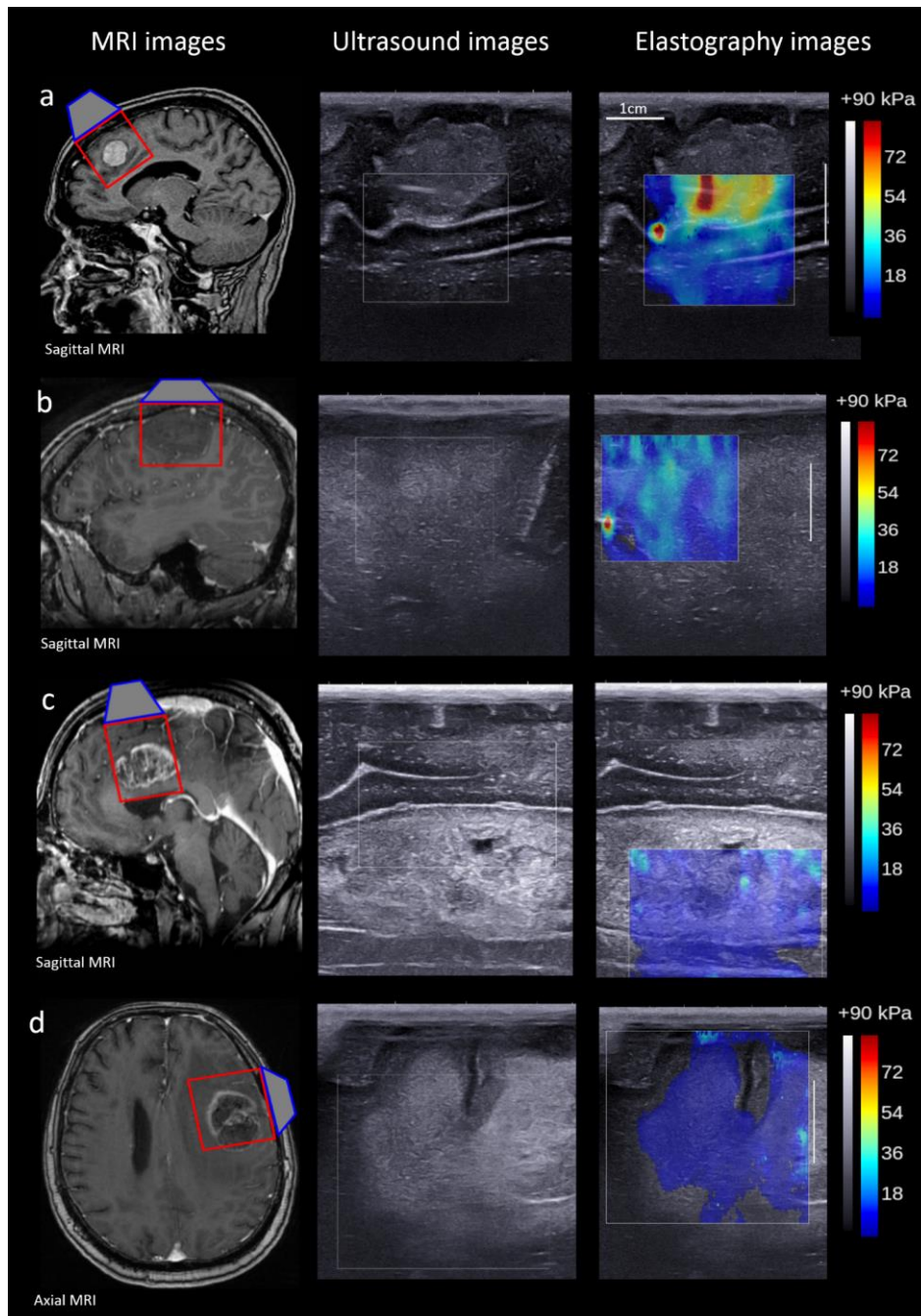


Figure 2.6 - Example of MRI images (Gadolinium-enhanced T1), ultrasound images and elastography images for each of the different analysed type of tumors. (a) Meningioma, (b) Low-grade gliomas, (c) High- grade gliomas and (d) metastasis. Dimensions of ultrasound images: 38.4 mm wide, 45.0 mm depth. Blue trapezium: ultrasound probe. Red rectangle: imaging plan.

Ultrasound images reveal echogenicity differences. Stiffness images reveal stiffness inside a region of interest (ROI). One can noticed that when the shear wave propagation is not possible (obstacle, depth), there is no stiffness value (no colored pixel) on the stiffness image ROI (for example in the top middle and bottom left of the ROI in the elastography imaging, (**Figure 2.6**, d).

2.3.6 Stiffness analysis by subgroup comparison

Regarding mean stiffness values found for each subgroup, the Mann-Whitney U test was used to observe how tissue stiffness could be a criterion to enable differentiation between the different types of tumor (**Table 2.1**).

	Mann-Whitney test: p-value	Mann-Whitney U
High-grade gliomas vs Metastasis	$p = 0.17$	96 (80)
High-grade gliomas vs Meningiomas	$p = 10^{-4}$	29 (86)
High-grade gliomas vs Low-grade gliomas	$p = 0.01$	60 (74)
Low-grade gliomas vs Metastasis	$p = 0.33$	82 (59)
Low-grade gliomas vs Meningiomas	$p = 0.04$	54 (64)
Metastasis vs Meningiomas	$p = 3.10^{-3}$	40 (70)

Table 2.1 - P-value for the stiffness comparison between the different types of tumor. By conventional criteria, two-tailed P values under 0.05 are statistically valuable. To be statistically significant, Mann-Whitney U has to be equal to or less than the critical value in bracket, according to table of critical U values for the Mann-Whitney test for different group sizes, for a two-tailed test at the 0.05 significance level.

In practice, the main issues for surgeons were to distinguish in real time: high-grade and low-grade gliomas, low-grade gliomas and normal brain, metastasis and high-grade gliomas. The comparison of these subgroups was then considered.

First, the comparison between low-grade and high-grade gliomas was examined. With a mean elasticity of 23.7 ± 4.9 kPa, low-grade gliomas are significantly stiffer ($p = 0.01$) than high grade-gliomas, characterized by a mean elasticity of 11.4 ± 3.6 kPa (**Figure 2.5**, **Table 2.1**). ROC curve analysis shows that SWE could enables differentiation between low-grade and high-grade gliomas (area under ROC curve = 0.76, $p = 0.002$, Sensitivity: 77.8 %, Specificity: 64.3%) as shown in the **illustrative case (2.3.8)**.

More generally statistical analysis using ROC curve analysis shows that SWE could enables differentiation between benign tumors (low-grade gliomas, meningiomas) from malignant tumors (high-grade gliomas, metastasis). The area under ROC curve which estimate the performance

diagnostic of elastography to differentiate benign and malignant tumors was 0.77 [0.64 – 0.87] (95 % confidence interval) ($p < 10^{-4}$, Sensitivity: 87.9 % [71.8 % – 96.6 %], Specificity: 60.7 % [40.6 % – 78.5 %]). The optimal cut-off for clinical use to be selected was 20 kPa.

This differentiation between benign and malignant tumors can even be noticed by observing the color code in the SWE images (**Figure 2.6**). All stiffness images have the same scale, from 1 kPa (dark blue) to 90 kPa (dark red). One can notice that for benign tumors we can observe color like red, yellow and cyan, whereas for malignant almost only dark blue is present.

Furthermore, intraoperative measurement of stiffness allows the differentiation between low-grade gliomas and normal brain ($p = 7.10^{-3}$). With a mean elasticity of 23.7 ± 4.9 kPa low grade gliomas are significantly stiffer than normal brain characterized by a 7.3 ± 2.1 kPa mean elasticity (**Figure 2.5**).

Concerning metastasis and high-grade tumors, unfortunately the measurement of Young’s modulus in intraoperative surgery does not allow differentiation between these two types of tumors. Both malign, these tumors have low mean elasticity values and can not be significantly differentiated by using stiffness criteria. Nevertheless, the MRI features of both types of tumors are often precise enough to get a preoperative idea of their pathological nature.

2.3.7 Repeatability and reproducibility

As the reproducibility of SWE has already been proved in organs like breast (the BE1 Study Group et al., 2012) and liver (Ferraioli et al., 2014), inter and intraoperator variability was briefly studied. For five patients of the study, two surgeons were requested to assess intraobserver and interobserver reproducibility.

Repeatability						Reproducibility					
(kPa)	Surgeon 1		Surgeon 2			(kPa)	Surgeon 1		Surgeon 2		
	Mean 1	SD1	Mean 2	SD2	%RSD		Mean 1	SD1	Mean 2	SD2	%RSD
Patient 1	15.5	1.8	15.3	4.2	19.8	Patient 1	13.3	1.6	11.6	2.0	15.5
Patient 2	34.3	0.3	44.1	5.7	16.4	Patient 2	35.3	1.9	38.0	2.4	6.8
Patient 3	24.7	2.0	24.3	2.1	7.9	Patient 3	18.3	1.8	30.4	6.5	32.1
Patient 4	5.0	0.6	3.4	0.3	22.5	Patient 4	6.1	1.4	4.5	0.9	26.3
Patient 5	12.8	0.4	13.2	0.8	5.1	Patient 5	9.5	2.6	13.5	2.0	26.2

Table 2.2 - Inter- and intra-operator analysis. To assess inter-observer repeatability and reproducibility mean elasticity and standard deviation (SD) was calculate for surgeon 1 over five acquisitions, then for surgeon 2 over five other acquisitions, finally relative standard deviation from the mean (%RSD) was assessed inter-operatively for every patient.

Regarding to the intra and inter-variability during stiffness measurement by using SWE, the best ICC was obtained for intra-operator repetition ($ICC = 0.99$) and reproduction ($ICC = 0.99$). Concerning inter-operator reliability ICC was also good for both repetition ($ICC = 0.96$) and reproduction ($ICC = 0.93$). Mean and standard deviation were studied in every case (Table 2.2). The relative standard deviation was mostly below 30%.

2.3.8 Clinical illustrative cases

In this thesis, two cases illustrating the clinical interest of intraoperative SSE are presented.

2.3.8.1 Error in the initial MRI diagnostic

A patient without past medical history was admitted in our department regarding brain tumor suspicion. Brain MRI revealed a left insular glioma without gadolinium enhancement (Figure 2.7, b). MR spectroscopy was in favor of a low-grade tumor. Awake surgery was performed. Intra-operatively, SWE showed that the lesion was very soft (10 kPa) tending to demonstrate that the tumor was a rather high-grade one. In Figure 2.7 c one can notice the dark blue color ROI, quantitative stiffness was measured with Qbox. Final pathology report confirmed that the glioma had high-grade features of an anaplastic glioma (classified WHO grade III). This observation was remarkable as the SWE had given new intraoperative data to foresee the nature of a brain tumor.

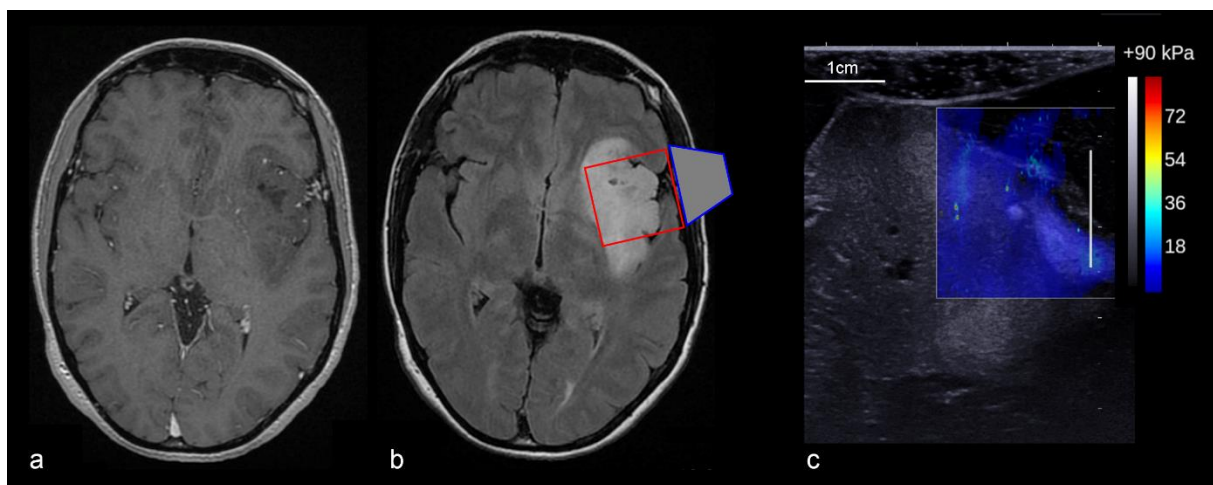


Figure 2.7 - Imaging in a patient with glioma, ranked high grade with elastography technic. (a) Gadolinium-enhanced T1 axial MRI, that shows no enhancement of the glioma, (b) T2 Flair axial MRI of the corresponding tumor, (c) SWE image, that shows low elasticity value (global mean elasticity: 10kPa). Dimensions of ultrasound images: 38.4 mm wide, 45.0 mm depth. Brain MRI revealed a left insular glioma without gadolinium enhancement and MR spectroscopy was in favour of a low-grade tumor. Intra-operative SWE showed that the lesion was very soft (10 kPa) tending to demonstrate that the tumor was a rather high-grade one. Final pathology report confirmed that the glioma had high-grade features of an anaplastic glioma (classified WHO grade III).

2.3.8.2 Necrosis gradient in malignant tumors

In addition to benign and malignant tumor differentiation, intraoperative SWE was able to reveal evidence of necrosis gradient in malignant tumors such as in a lung metastasis (**Figure 2.8**). A lower stiffness value was observed in the tumor necrotized center.

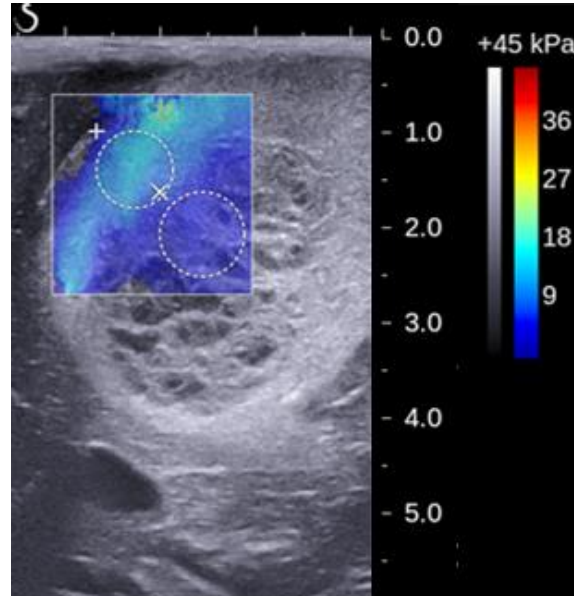


Figure 2.8 – Necrosis gradient observation in a lung metastasis. A mean of 12 kPa was found in the tumor's rim. Only 4 kPa was measured in its necrotized center.

2.3.9 SWE contribution in neurosurgery

Improving quality of brain tumor resection is an ultimate goal for neurosurgeons. Despite dissection under microscope, surgeons can not always differentiate normal tissue and brain tumor. This is the reason why tissue palpation by surgeons is routinely used, but this is far from scientific guidelines. In the present study, it has been attempted to define a stiffness atlas of brain tumors, divided in the four main types of lesions. This study is the first on ultrasonic elastography of brain tumors, demonstrating that stiffness of the most frequent tumors are significantly different.

According to our intraoperative data, SWE technique could be an important tool to differentiate *in vivo* malignant and benign lesions with a good sensitivity (87.9 %) and for a relative good specificity (60.7 %). More specifically stiffness measurement could be invaluable in helping surgeons to quantitatively distinguish high-grade and low-grade gliomas. This differentiation is very important because the tumor grade is very much tied to prognosis and treatment strategies, whereas it is not always obvious to differentiate benign and malignant gliomas regarding MR imaging and intraoperative features. The use of SWE can therefore decrease the risk of error in intraoperative grading appraisal, help to adapt the resection regarding the grade and clarify the best intraoperative strategy.

On the other hand, stiffness measurement can improve differentiation between low-grade gliomas and normal brain ($p < 0.01$). In this case, SWE can help surgeons during resection by improving resection margin definition which is not trivial to the naked eye, reducing leftover or avoiding

extra resection. . In the case of glioma, invasive cerebral disease extending along white matter, surgery is an elaborate compromise between neurology and oncology where tumor grade and boundaries are decisive information for neurosurgeons to maximize tumor resection while minimizing the risk of permanent neurological morbidity.

Our study provides evidence to justify the use of intraoperative SWE in brain tumor surgery: such imaging helps surgeons to quantitatively distinguish benign and malignant brain tumors (especially in gliomas) and thus to provide the optimum extent of resection.

From this finding, it seems obvious that ultrasound elastography can bring complementary data for diagnosis, additionally to preoperative MR imaging (see **illustrative case 2.3.8**). In 2005, Scholz et al. (Scholz et al., 2005) described the first assessment of tumor stiffness by comparison with the normal brain, using a “vibrography” technique. This pioneer study demonstrated that normal brain tissue and brains tumors have enough elastic properties to be detected and differentiated. With SWE it is now possible to measure quantitatively the elasticity of tissue, which offers an objective, precise and reproducible evaluation.

As an operative time as short as possible is a major concern in neurosurgery, it is important to notice that stiffness measurement is not time consuming. Furthermore, this technology appears to be safe, neither side effect nor postoperative infections have been observed. Comparing with other intraoperative image-guided neuronavigation, SWE is not impacted in the same way by the brain shift (Ohue et al., 2010), which can create a significant gap to locate the lesion within the brain. It seems obvious that future neuronavigation systems will come from co-registration of preoperative MR imaging and 3D intraoperative ultrasonography (Coenen et al., 2005) and/or from intraoperative MRI improvement(Sommer et al., 2013). Because of the intuitive manageability of our ultrasonic device and the good reproducibility of our stiffness data, SWE could reinforces even more the surgical intraoperative guidance, in a perspective of total resection. This has to be confirmed on larger series.

Despite our promising results, this work presents some limitations. Firstly, the probe has a defined maximal imaging field that cannot always include the whole tumors, depending on the size of it. Though, this does not constitute a major issue as one can easily move the probe in the skull aperture to get a complete screening of the tumor. Concerning the depth of the field, no problem was encountered to get the whole lesion in the image, as the device enables 40 mm deep acquisitions. However, images could not be performed below this point, so that deep normal brain surrounding tissues and/or contralateral cerebral hemisphere were not always seen. With the device used in this study, only 5% of the cases were lost due to a lack of signal in the tissues. This can be solved by using a lower frequency probe. As an example, 150 mm deep acquisitions can be obtained at 3 MHz but with a loss in resolution.

Despite the fact that SWE remains to date limited to intraoperative brain imaging and diagnosis, one could envision to extend it transcranially while replacing the remote vibration induced by the acoustic radiation force by the tracking of natural brain vibrations induced by brain pulsatility. Such elegant approach was recently proposed in MRI (Zorgani et al., 2015) and could potentially be translated to ultrasound elastography.

Finally, recent studies in MR-Elastography showed that in the case of neuropathology, such as Alzheimer’s disease (Murphy et al., 2011) and Parkinson’s disease (Lipp et al., 2013), a significant softening of the brain parenchyma or of the basal ganglia region occurs respectively. The use of SWE in such studies is currently limited by skull bones and definitively needs a craniotomy. Nevertheless classical low frequency (usually 2 MHz) transcranial Doppler (TCD) (Purkayastha and Sorond, 2013) was developed to facilitate ultrasonic waves passing through skull natural windows (temporal or occipital window). TCD technique could be improved in order to solve this issue, as an example the use of aberration corrections techniques – such as using the time-reversal concept in therapeutic high-intensity focused ultrasound (Lindsey and Smith, 2013; Osmanski et al., 2012; Tanter et al., 1998) – could be implemented to the ultrasound elastography field. In perspective after some development, transcranial SWE could be envisioned preoperatively through the skull windows.

2.4 Relationship between intracranial pressure and SWE in normal brain in patients with lesion

After demonstrating that intraoperative SWE can accurately measure normal brain and tumor stiffness, in this section, we will investigate to find a relationship between intracranial pressure and normal brain stiffness measured with SWE during tumor surgery. We conducted one *in vitro* study on veal brain and one preliminary clinical study on this topic. Advanced and limitations are presented in this section.

2.4.1 Intracranial pressure

Intracranial pressure (ICP) is determined by the volume of brain parenchyma (i.e. functional tissue in the brain including neurons and glial cells) (80%), blood (12%), and cerebrospinal fluid (CSF) (see **Figure 2.9**) (8%) within a rigid cranial vault (Ruskin et al., 2013).

ICP is measured in millimeters of mercury (mmHg) and, at rest, is normally inferior to 10–15 mmHg for a supine adult (Dunn, 2002). Because the cranial compartment is enclosed by a rigid skull, it has a limited ability to accommodate additional volume. Since Monro published his observations on the nature of the contents of the intracranial space in 1783 (Monro, 1783), there has been lot of investigations of the unique relationship between the contents of the skull and the ICP. When intracranial contents increase in volume (such as tumor growth, changes in blood volume or swelling), initially, circulating blood and CSF are displaced to offset the extra volume and ICP remains unchanged. However, beyond a certain threshold, if intracranial contents continue to increase in volume, then ICP will quickly increase.

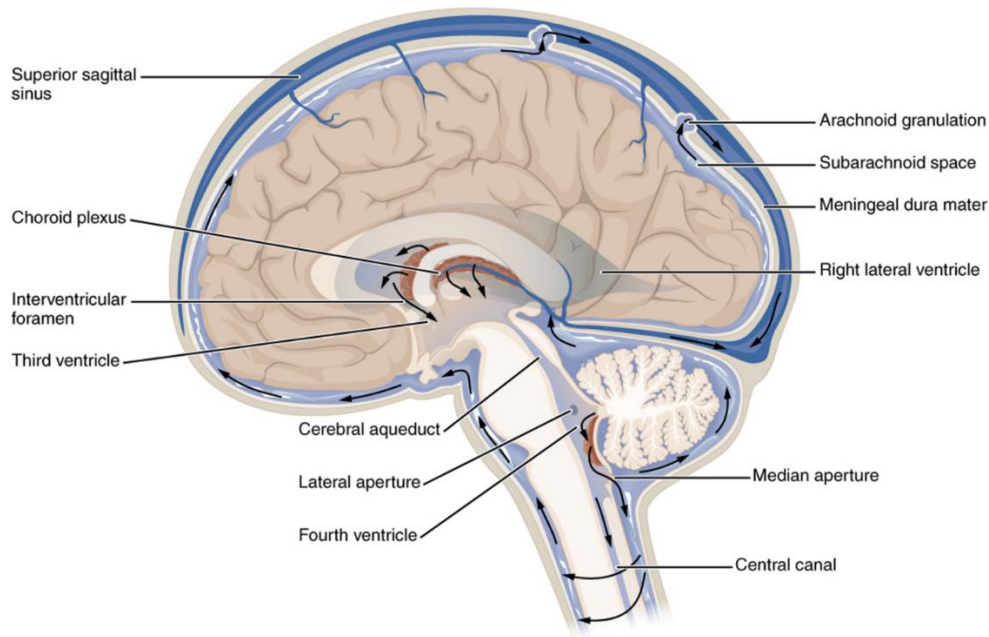


Figure 2.9 - Cerebrospinal fluid (CSF) circulation. The CSF circulate (black arrows) in the subarachnoid space around the brain and spinal cord and is then drain by the sinus (veins) trough arachnoid granulation. (Taken from (OpenStax, 2016) “Download for free at [The intracranial volume–pressure curve demonstrates how small increase in volume of one of the intracranial components can be compensated by a reduction in CSF or blood volume in the compensation phase \(**Figure 2.10**, phase A\). However, these compensatory measures are quickly exhausted and any subsequent increase in volume leads to an exponential increase in ICP \(**Figure 2.10**, phase B\). According to conventional terminology, this volume–pressure relationship should be referred to as elastance \(change in pressure per unit change in volume, \$\frac{\Delta V}{\Delta P}\$ \) \(Drummond, 1995\). Due to the exponential nature of the volume–pressure relationship as depicted in **Figure 2.10**, being able to quantify elastance is attractive clinically as, in theory, it will increase during the volume compensation phase more rapidly than ICP and should therefore be predictive of impending volume decompensation.](http://cnx.org/contents/14fb4ad7-39a1-4eee-ab6e-3ef2482e3e22@8.24.”))</p>
</div>
<div data-bbox=)

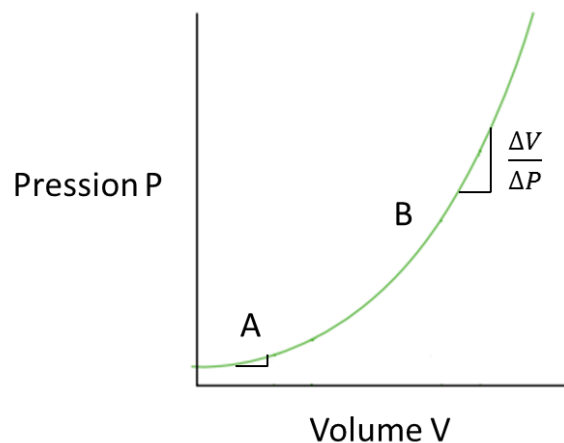


Figure 2.10 – The intracranial volume-pressure curve. A: compensation phase. B: decompensation phase. $\frac{\Delta V}{\Delta P}$ is the elastance.

Accurate monitoring of intracranial pressure (ICP) is essential in neurosurgery and neuro-intensive care.

2.4.2 Intracranial pressure monitoring

The two techniques most commonly used in clinical practice to monitor ICP are via an intraventricular or intraparenchymal catheter with a microtransducer system. Both techniques are invasive and are thus associated with complications such as hemorrhage and infection. For this reason, significant research effort has been directed towards development of a non-invasive method to measure ICP.

ICP monitoring via intraventricular catheter is performed by inserting a catheter into either lateral ventricle through a small frontal hole (**Figure 2.11 (a)**). An advantage of measuring ICP using an intraventricular catheter is the opportunity to perform drainage of CSF as an ICP lowering therapy.

In cases where intraventricular ICP monitoring is not possible, an intraparenchymal device can be placed (**Figure 2.11 (b)**). Intraparenchymal ICP monitoring devices are typically placed via a small hole into the white mater of the non-dominant frontal hemisphere. These devices measure a compartmentalized local pressure.

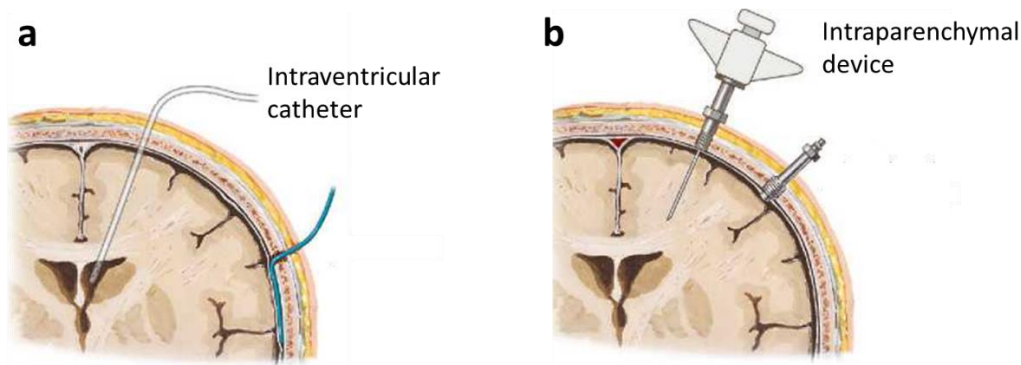


Figure 2.11 – Invasive ICP monitoring. (a) Intraventricular ICP monitoring. (b) Intraparenchymal ICP monitoring. (Taken from(Netter, 2016))

For a non-invasive measure of ICP to replace the commonly used invasive measures above, the technique must provide an accurate absolute measure of ICP that can be performed continuously at the bedside. There is no current technique that satisfies these criteria. An in depth review of all of the available technologies has already been covered in detail (Kristiansson et al., 2013; Raboel et al., 2012; Rosenberg et al., 2011). Techniques considered include imaging based studies using for instance CT scan, magnetic resonance imaging (MRI), near-infrared spectroscopy (NIRS) or transcranial Doppler (TCD). Among these, approaches using TCD and ONSD have perhaps received the most clinical interest. Using low frequency TCD, it is possible to measure flow velocity (FV) in the middle cerebral artery (MCA) (Aaslid et al., 1982). Several authors have published researches on indirect ICP estimation using TCD to measure cerebral blood volume and radial (wrist) arterial blood pressure measurement (Goldstein et al., 2012; Kashif et al., 2012).

In the following session we studied how SWE of normal brain can give information on ICP during brain surgery.

2.4.3 Hypothesis

This is well known that pressure in the brain is hydrostatic. Hydrostatic pressure is a force applied by a liquid on the surface of an immersed body. Inside the circulatory system it depends on the weight of the blood column between the heart and a given level. In neurosurgical patients, the hydrostatic pressure plays an important role in cerebral perfusion. The mean arterial pressure (Pa), the CSF pressure (CSFP) and the pressure in the jugular vein (JVP) are the hydrostatic determiners of the cerebral perfusion pressure (CPP) (Hans, 1994). CPP is the net pressure gradient causing cerebral blood flow to the brain (brain perfusion). It must be maintained within narrow limits because too little pressure could cause brain tissue to become ischemic (inadequate blood flow in the brain), and too much pressure could raise intracranial pressure (ICP).

Hydrostatic pressure doesn't imply neither volume increase nor changes in tissue stiffness. However, there is one phenomena that can lead to local changes in brain stiffness: intracranial expansive processes, such as tumor, edema and hemorrhage. In these cases, the lesion applies a stress along preferred directions on the neighboring tissues.

In the case of brain surgery, the only parameter influencing ICP which is not controlled by the anesthetist is cerebral parenchyma growth. Our hypothesis is that local SWE of normal brain close to the lesion can provide information on global ICP, when CSF and blood are well controlled.

2.4.4 In vitro study

Firstly, we designed an *in vitro* study to challenge our hypothesis on the influence of expansive process on the ICP, and to test if there is a link between local SWE measurement and intraparenchymal pressure. We started an *in vitro* study in collaboration with the Master student Mathieu Mossad on 5 veal brains. We inserted one small balloon and one pressure probe inside each veal brain cortex before fixing it in a glass box. The inside of the glass box was then immersed in a gelatin gel (10% gelatin). The pressure probe was connected to a pressure Codman® measurement device. We were able to fill the small balloon up to 10 mL of water with a syringe, in order to mimic the increase of pressure consecutive to tumor growth. The ultrasonic data for SWE measurement were acquired using one SL10-2 probe maintained by a metallic arm and driven by an Aixplorer® system. The protocol is illustrated in **Figure 2.12**.

In order to study the impact of an external stress on nearby normal brain stiffness inside veal brains, we increased the volume of the small balloon millimeter per millimeter, and at each time we imaged the brain for stiffness (ultrasound scanner) and we recorded the pressure (pressure probe).

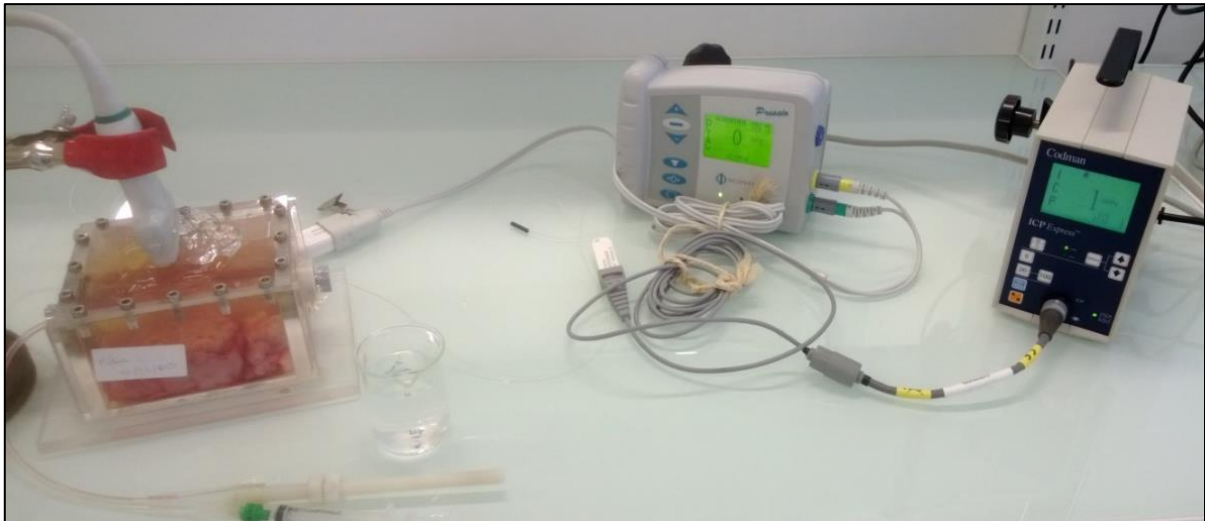


Figure 2.12 - Experimental set up to assess the relation between pressure and elasticity. On the left, the plastic box containing the veal brain. The SL10-2 probe is by a metallic arm. The syringe is linked to the small balloon inside the brain. On the right, stand the device for pressure measurement.

Figure 2.13 present one of the image we obtained using SWE, firstly without liquid in the small balloon (a), secondly with 10 ml of liquid in the small balloon (b). We noticed that small balloon growth induced stiffness increase in the neighboring brain tissues.

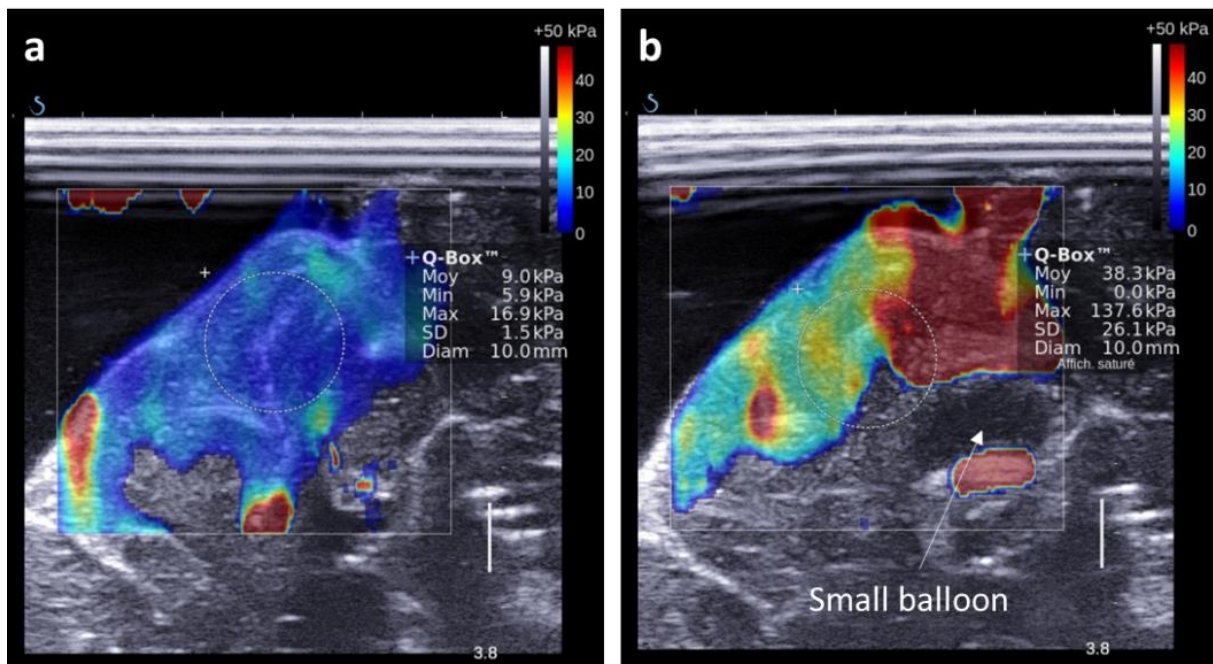


Figure 2.13 – SWE increase due to the stress induced by tissue compression. (a) Initial conditions: no liquid in the small balloon, 1 mmHg pressure measured in the cortex. (b) 10 ml of liquid were injected in the small balloon: a pressure increase of 80 mmHg in the cortex was measured in the cortex, along with a stiffness increase in the neighbouring brain tissues, from 9 (initials conditions) to 38 kPa.

We have repeated this experiment on 5 veal brains. Data are presented in **Figure 2.14**, where the evolution of normal brain stiffness is studied function of the pressure measured in the brain cortex.

A linear relationship was found between Young’s Modulus in kPa and intracortical pressure in mmHg for each veal brain **Figure 2.14**, demonstrating that SWE can detect parenchyma local compression responsible of intracortical pressure increase. For the five veal brains, a mean increase of 0.30 ± 0.23 kPa/mmHg was found.

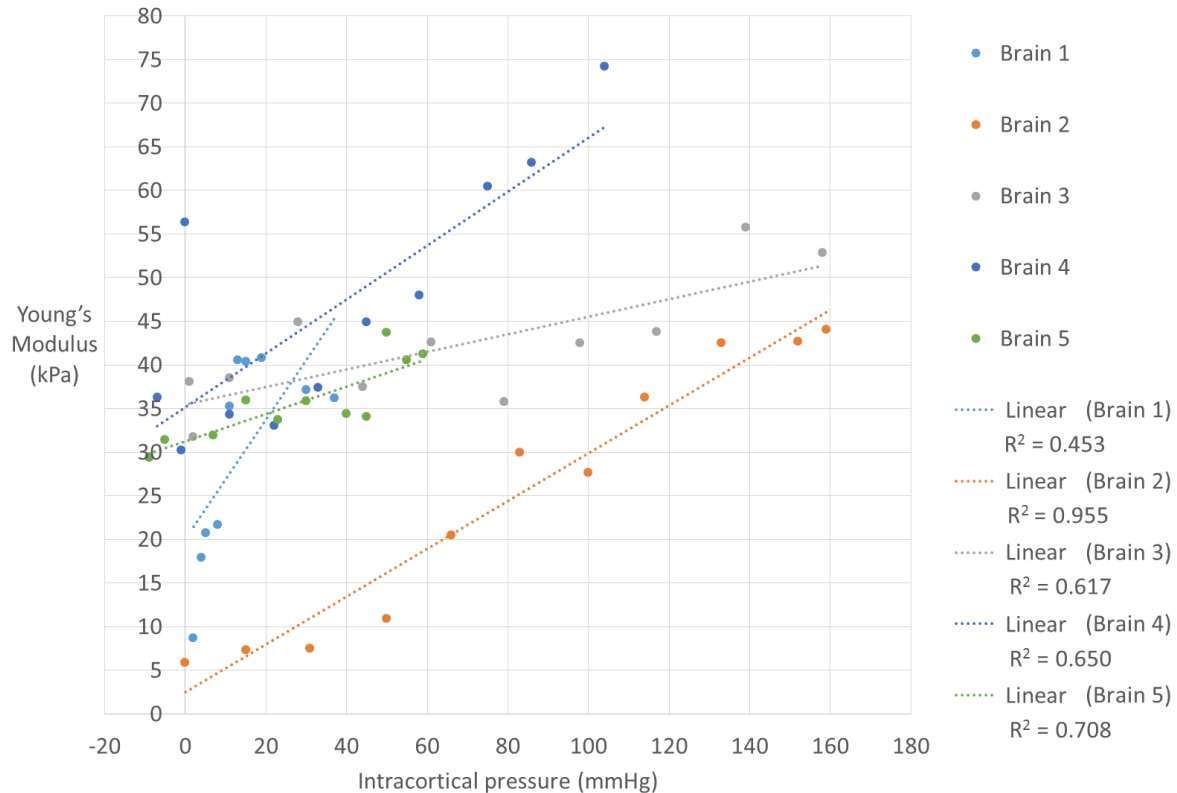


Figure 2.14 - Experimental linear relationship between Young’s Modulus measured with SWE and intracortical pressure measured in the normal brain surrounding the small balloon, realized *in vitro* on five veal brains. The increase of intracortical pressure is obtain by fluid injection in the small balloon, up to 10ml. Colored lines represent a linear fit calculated over elasticity as a function of intracortical pressure

Nevertheless, most of time neurosurgeons face ICP between 0 to 20 mmHg, and according to our results presented in **Figure 2.14**, this ICP range correspond to a very few kPa variation. The next step is to try our technique *in vivo* during brain surgery to evaluate SWE potential to detect small changes in stiffness in normal brain surrounding the lesion along with ICP variations.

2.4.5 In vivo study

In vivo study was performed during brain surgery in the Neurosurgery service of Hôpital Salpêtrière, PARIS 13^{ème}, FRANCE. Data were acquired on four patients with malignant brain lesions (1 metastasis and 3 high grade gliomas). Ethical considerations had been previously validated by our institutional ethics committee, “Comité de Protection des Personnes – Ile-de-France VI – Pitié Salpêtrière”, and all patients gave their informed consent.

For each patient, the surgeon made an aperture in the skull bone, and stiffness measurements were performed using SL10-2 driven by an Aixplorer® scanner. The stiffness values were

displayed a posteriori by the Q-box® system. Our four patients had normal compensation (ICP < 25 mmHg), and normal brain surrounding the tumor was characterized by a mean stiffness of 14.7 ± 9.9 kPa before tumor resection and 6.5 ± 1.6 kPa after resection.

We decided to study the mean stiffness inequality before tumor resection to find its origin (Figure 2.15). Our four patients had malignant brain tumors, and in agreement with our previous study on brain tumor stiffness, we found very low stiffness values in tumors (<14 kPa). Tissue compression should therefore be linked to the tumor’s volume.

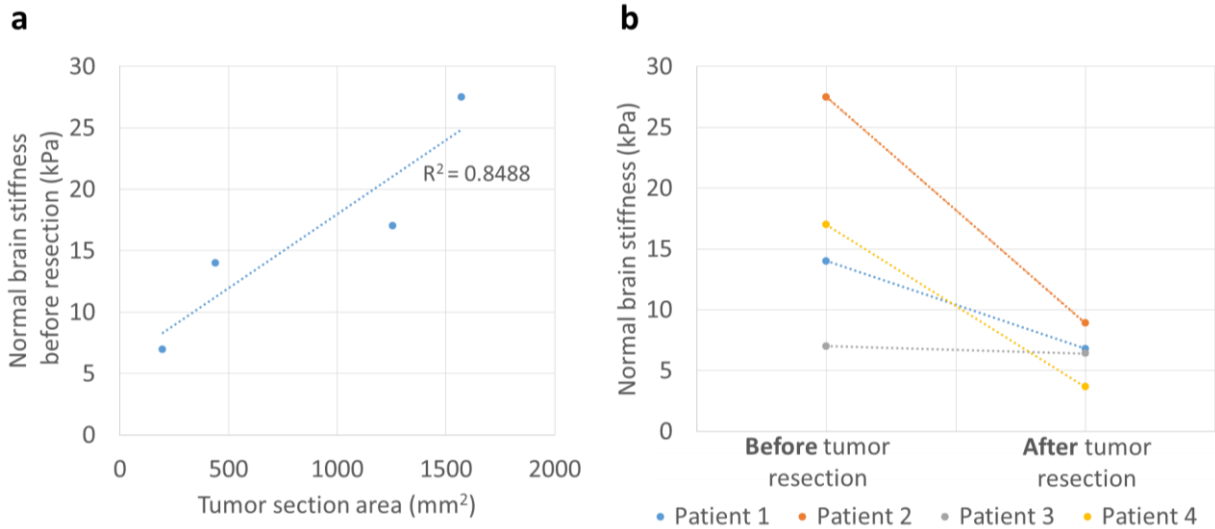


Figure 2.15 –Normal brain stiffness: effect of tumor growth and resection. (a) Linear relationship between tumor section area and SWE in normal brain before resection for the four studied patients. (b) Evidence of decrease in normal brain stiffness after tumor resection.

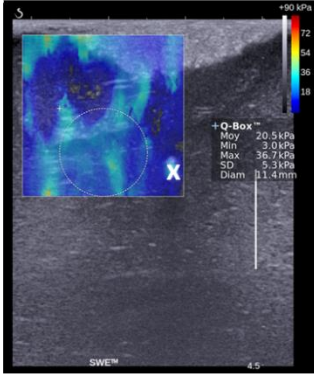
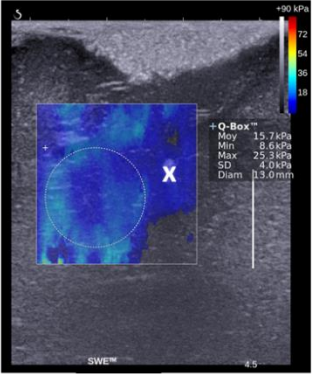
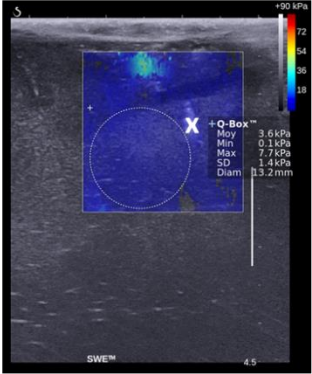
We calculated tumor section area in the SWE imaging plan, and we noticed a linear correlation between normal brain stiffness and tumor section area, characterized by an increase of 0.012 kPa/mm² (Figure 2.15, a). Then, after tumor resection, we observed for all patients that normal brain stiffness went back down to lower values (<10 kPa) (Figure 2.15, b) in accordance to the results of our first study (see section 2.3).

We demonstrated that SWE can detect changes in normal brain stiffness due to external stress increase (such as tumor growth) and decrease (such as tumor resection).

In the next paragraph, we studied the possible relationship between normal brain stiffness and ICP, however we had so far data for only one patient. For this patient, a pressure probe was introduced in the cortex after craniotomy and before dura matter opening. We measured intraparenchymal ICP and normal brain stiffness before dura matter opening, after dura matter opening, and after complete tumor resection. Results are presented in Figure 2.16. We observed that both dura matter opening and tumor resection have high impact on ICP, whereas only tumor resection highly modifies normal brain stiffness measured with SWE. This is coherent with our previous results demonstrating that normal brain stiffness is link to applied external stress.

Regarding the preliminary results of both our *in vitro* and *in vivo* study, normal brain stiffness measured with SWE is not correlated with ICP, when blood volume or CSF changes are

implicated. However, normal brain stiffness and ICP seems to be correlated when ICP changes are caused by, and only by, brain parenchyma volume changes.

	Before dura mater opening	After dura mater opening	After tumor resection
ICP (mmHg)	17	7	1
Mean stiffness (kPa)	18.3 ± 2.6	15.5 ± 3.9	3.7 ± 0.9
			

X Pressure probe

Figure 2.16 – ICP and SWE in normal brain, before and after dura matter opening, and after complete tumor resection. ICP was measured with an intraparenchymal pressure probe. Mean stiffness in normal brain is the mean stiffness of 5 Q-box designed in the same imaging plane after ultrasound probe repositioning.

In the case of brain surgery, the only parameter influencing ICP which is not controlled by the anesthetist is cerebral parenchyma increase or decrease. In this case, when CSF and blood are well controlled, normal brain stiffness measured by SWE could be an indicator of intracranial hypertension. These results need to be confirmed in a larger clinical study, to determine if a cut-off stiffness value can be found to predict intracranial hypertension. This information could beneficiate to the neurosurgeon before dura matter opening.

2.4.6 Conclusion and perspectives

Intracranial hypertension could be caused by non-compensation of an increasing volume of brain parenchyma, cerebral blood flow or cerebrospinal fluid. SWE cannot detect ICP change neither due to increasing volume of cerebral blood flow (Gefen and Margulies, 2004) nor cerebrospinal fluid. But SWE can detect changes due to increasing volume of brain parenchyma, such as in case of tumor growth or edemas. SWE could enable to draw a cut-off line between compensation and decompensation. A larger clinical study, including patients with normal ICP, mild, moderate and severe intracranial hypertension, need to be conducted to precisely determinate the cut-off value to identify patients with intracranial hypertension during brain surgery.

2.5 3D elastography using matrix array

After studying 2D SWE contribution in neurosurgery, this section focuses on 3D SWE using matrix array. A unique 3D ultrafast scanner for this purpose. This adapted scanner and the corresponding imaging technique are described in this section. The first experiments in ultrasound phantoms and *in vivo* are then presented.

2.5.1 From 2D to 3D elastography

In elastography, most of the methods proposed only give access to a 2D imaging plane because of software and hardware limitations. On major consequence of 2D imaging is regarding physical assumptions on the shear wave propagation and the associated inverse problem. Another issue concern imaging workflow because the positioning of the probe remains operator dependent. Moreover, having access to the elastic characterization of a large region or even the entire organ, such as the brain, is of a major interest from a physician's point of view to reduce time-sampling artifacts in heterogeneous media. To address these problems, several solutions were proposed in the literature to extend shear-wave imaging to 3D. One approach was to use a translating 1D linear array, which allows for the plane-by-plane reconstruction of the elastic volume using a 2D imaging system. For instance, such a technique was used to map the shear modulus of a breast cancer tumor in an entire volume and monitor it during chemotherapy (Ossa, 2012). However, because the push beam location remains confined to each individual 2D imaging plane, inverse problems cannot be extended to benefit from the three-dimensional propagation of the shear wave, which can be used to estimate complex mechanical properties such as anisotropy. To palliate this issue, Wang and colleagues combined a spherical transducer, used to generate a shear wave by acoustic radiation force, with a 2D matrix array to image shear wave propagation (Wang et al., 2013a, 2013b). By imaging in a sequential manner the propagation of the shear wave plane by plane, they were able to synthetically reconstruct the shear wave propagation in the entire volume. One advantage of this technique is that the pushing beam is maintained at the same location while the tracking beams are shifted in different directions, which effectively allows for the quantification of the elastic anisotropy. However, because acquisitions must be repeated sequentially to acquire the full volume, the technique yields a low volumetric frame rate and is therefore limited in presence of motion due, e.g., to breathing or pulsatility. Moreover, although this proof of concept of 3D ultrasound imaging for shear-wave imaging is promising, the clinical applicability of the proposed setup is complex because it relies on two separated transducers for acoustic force generation and 3D imaging.

We extended the initial research work to a clinically applicable approach for real-time 3D shear wave elastography (SWE). Firstly, in order to avoid any artifact linked to breathing or pulsatile motion, we acquired the entire volume of the imaged organ instantaneously. To address this issue, the concept of ultrafast imaging (Tanter and Fink, 2014) was extended to 3D ultrafast volumetric imaging. To do so, we developed 3D Ultrafast Ultrasound Imaging based on the emission of diverging or plane waves emanating from virtual sources located behind a 2D-array ultrasound probe. By coherently compounding multiple emissions and by sampling the data of 1024 piezoelectric elements, we demonstrated that it is possible to perform 3D ultrasound imaging

at thousands of volumes per second with large contrast and high resolution. We assembled a 3D ultrafast ultrasound scanner allowing for the simultaneous acquisition of hundreds of channels along with the appropriate electronics for the generation of a shear wave using acoustic radiation force.

In this section, firstly, the adapted ultrasound scanner and the imaging sequence based on a sparse virtual array located behind the probe are described. Then the results obtained in a homogeneous, isotropic, and elastic breast phantom are presented. Finally, we demonstrate the clinical feasibility of the approach in vivo in the breast of one healthy volunteer in order to show the potential of 3D SWE for future clinical applications.

2.5.2 Ultrasound system infrastructure

We built a fully programmable, 1024-channel research ultrasound platform (Figure 2.17 a) able to drive a 32×32 matrix array centered at 3 MHz with a 50% bandwidth at -3 dB and a 0.3 mm pitch (Vermon, Tours, France) (Figure 2.17 b).



Figure 2.17 – Customized 3D ultrafast ultrasound device. (a) Construction steps of the 3D ultrafast ultrasound scanner. 1024 emitting channels, 512 receiving channels, up to 10 000 volume/s. **(b)** 2D matrix array, 1024 elements, (32×32) with 0.3 mm² pitch.

The 1024 independent channels could be used simultaneously in transmission, whereas receive channels were multiplexed to 1 of 2 transducer elements. Therefore, each emission was repeated twice, with the first half of the elements receiving during the first emission, and the second half of the elements receiving during the second emission.

Delay-and-sum volume beamforming was performed in post-acquisition on graphic processing units (K6000, Nvidia, Santa Clara, CA) at the rate of a few volumes per second. Real-time bi-plane beamforming was also implemented for positioning, while volume beamforming was performed in postprocessing. The whole beamforming and shear wave movie calculation was performed in less than 1 min in post-acquisition. 3D rendering also was done in post-acquisition by using Amira software (Visualization sciences Group, Burlington, Ma, Usa).

2.5.3 Image formation

Two steps were necessary to perform 3D shear wave elasticity measurements. Firstly, a spherical law was programmed in emission to focus ultrasound within the medium and create shear waves (Sarvazyan et al., 1998). Secondly, all elements were used simultaneously to insonify the region of interest during 100 μ s. Ultrafast imaging of the shear wave propagation was performed by using ultrasound plane wave compounding (Montaldo et al., 2009; Tanter and Fink, 2014) in 3D.

2.5.3.1 Ultrafast Imaging in 3D for shear wave tracking

Single framework consisting of virtual sources positioned behind the probe was used for compounding emissions (**Figure 2.18**). More specifically, synthetic beamforming was performed using virtual sources forming a virtual array located behind the probe (**Figure 2.18 a**). For each source, a physical subaperture and a set of delays were computed (**Figure 2.18 b**). Transmissions from individual sources were performed sequentially, and the radio-frequency data was recorded for each element of the entire physical probe. Volumes were beamformed using delay-and-sum algorithms for each virtual source and subsequently coherently compounded to form a final, high quality volume. Virtual arrays can be tailored to adjust resolution, contrast, signal-to-noise ratio, volume rate, and the field of view in a quasi-continuous fashion, therefore allowing for the selection of the optimal imaging sequence for a specific application (Lockwood et al., 1998; Montaldo et al., 2009; Nikolov, 2002; Nikolov et al., 2010; Papadacci et al., 2014). Indeed, a number of trade-offs between contrast, resolution, volume rate, and field of view exist. For example, as the number of sources is increased, the contrast and resolution improve but the volume rate decreases, and as the distance of the virtual array decreases, the field of view increases but the contrast decreases. More specifically, positioning virtual sources onto the probe itself is equivalent to standard synthetic beamforming, with a high resolution and large field of view, but resulting in a poor volume rate and signal-to-noise ratio at larger depths. As the virtual array is moved behind the probe (**Figure 2.18 c**), additional physical elements can be recruited to contribute to one emission (i.e. the subaperture) and therefore increased energy is propagated into the tissue and larger signal-to-noise ratios are obtained (Lockwood et al., 1998).

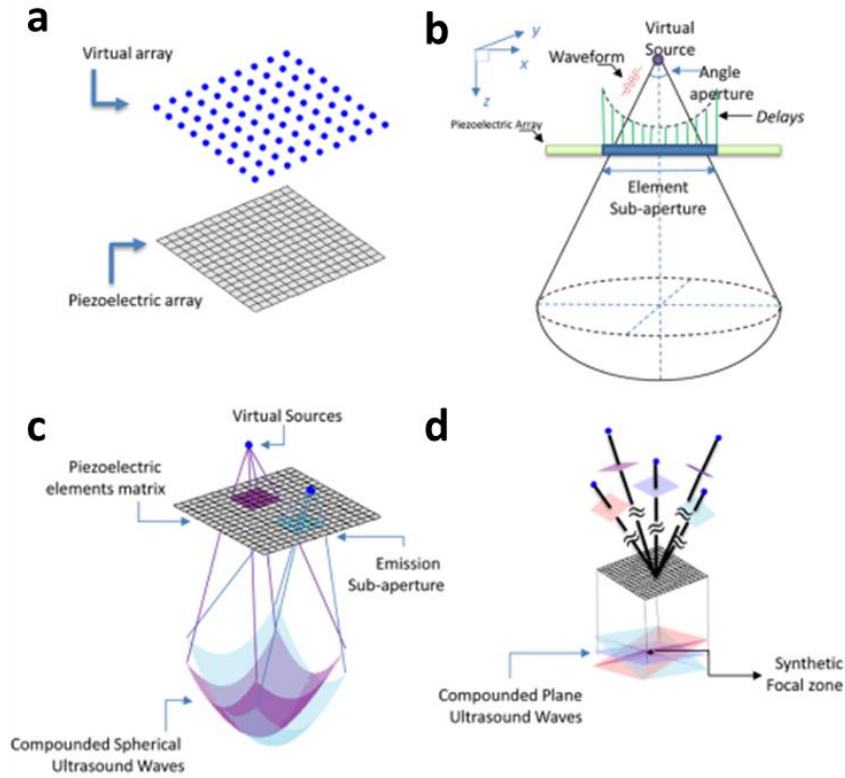


Figure 2.18 - 3D ultrafast ultrasound imaging framework. (a) Acquisitions are defined by a virtual array located behind the probe, which is then used to synthetically form an entire imaging volume. (b) For each individual source, delays are computed and a sub-aperture is defined. (c) When virtual sources are located near the physical probe, the sub-aperture used is smaller and the curvature of the emitted waveform is increased, which results in the insonification of a large field-of-view at the cost of a lower propagated energy. (d) When sources are located far behind the probe, larger sub apertures result in larger emitted energy, at the cost of a smaller field of view. In the extreme case of sources located at infinity behind the probe, tilted plane waves are obtained. (As described in our article (Provost et al., 2014))

The volume rate can also be adjusted by either increasing the pitch or decreasing the aperture of the virtual array up to the extreme case of using a single source (Provost et al., 2011), which is useful for applications requiring very high volume rates such as Ultrafast Doppler Imaging or Shear-Wave Imaging. Placing sources farther behind the probe leads to larger emission subapertures and a smaller field of view. Indeed, a virtual array at infinity (or very far, e.g. at 60 000 mm in this case) results in the emission of plane waves (**Figure 2.18 d**) with an imaging field of view corresponding to the 2D aperture of the physical probe.

In our case, $N = 4$ tilted ultrasound plane waves were emitted ($\alpha = [-1^\circ \ 1^\circ]$, $\beta = [-1^\circ \ 1^\circ]$) at a pulse repetition frequency (PRF) of 11 900 Hz. These four tilted ultrasonic plane waves were then compounded to increase the single-to-noise ratio. The angles' influence and the method used to compound images was fully described in Montaldo and colleagues (Montaldo et al., 2009). Because a synthetic receive aperture was used, each plane wave was emitted twice, resulting in a final, effective frame rate of 1488 volumes/s.

2.5.3.2 Shear wave velocity estimation

After 3-D ultrafast imaging utilization for shear wave propagation tracking through 3D plane wave coherent compounding, the Kasai and colleagues autocorrelation method (Kasai et al., 1985) was applied to obtain shear wave propagation cine loop.

A 3D directional filtering approach was proposed to filter the artifacts coming from reflected shear waves (extended from (Deffieux et al., 2011)). Finally, the shear wave velocity was estimated in a full volume through the Eikonal equation application, as described in our article (Gennisson et al., 2015).

2.5.4 Phantom experiments

We used one breast phantom dedicated to elastography (Madsen et al., 2006) to test our 3D elastography technique. Several pushes were combined to create a single elastic volume. Pushes were positioned at the five corners of a pentagon (**Figure 2.19 a**) inscribed in a 10-mm circle. Reconstructed shear wave speed volumes were compounded using both a geometrical mask to exclude the push central region and a weighted mean based on individual shear wave acquisition energy (Deffieux et al., 2012). To be able to compare these preliminary results, stiffness measurements were also performed in 2D with an Aixplorer device (V9.1, supersonic Imagine, Aix-en-Provence, France) working in shear wave elastography mode with a 1D curved array (SC 6-1, 3 MHz central frequency, super-sonic Imagine, Aix-en-Provence, France).

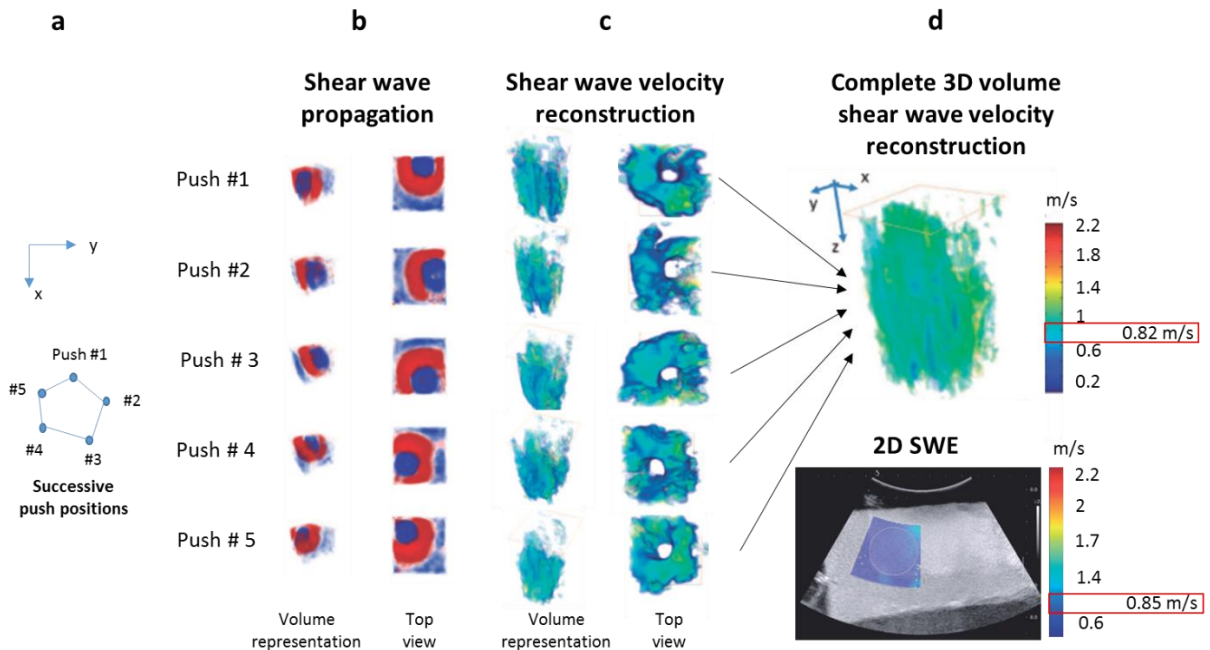


Figure 2.19 – 3D Ultrafast Shear Wave Elastography (SWE) imaging in phantom. (a) Five push-beams in different spatial locations were performed to recover the shear wave velocity in a full volume. (b) Volume and top view representations of the shear wave propagation at the five push-beams locations. (c) Volume and top view of shear wave velocity reconstruction at the five push-beams locations by using a 3D time of flight and 3D directional filter. (d) Comparison between shear wave velocities measured in the phantom at the same location with 3D and 2D SWE.

Multiple volumetric frames depicting the propagation of the shear wave are shown in the imaging volume in an isometric representation and in top view (**Figure 2.19 b**). Because shear wave speeds cannot be reconstructed at the push location, i.e., the shear wave source, 5 successive pushes were performed on the side of the volume, leading to 5 independent shear wave movies. The shear wave speed volume was retrieved in meters per second for each push location by applying 3D directional filters and the 3D time-of-flight estimation algorithm, (**Figure 2.19 b**). In the top view, the hole in the re-construction depicts the push location.

The concatenation of the 5 acquired volumes (**Figure 2.19 c**) and the distribution histogram of the volume shear-wave speed values is presented in **Figure 2.19 d**. The mean value of the shear wave speed in a region of interest of $10 \times 10 \times 10$ mm located in the middle of the volume was found to be 0.82 ± 0.13 m/s (2.0 ± 0.05 kPa). In parallel, a two-dimensional shear wave speed map was acquired in the same homogeneous phantom with a 1D conventional linear array (**Figure 2.19 d**). The mean value of the shear wave speed was found to 0.85 ± 0.15 m/s (2.2 ± 0.07 kPa) in a 30-mm-diameter region of interest with minimum and maximum values of 0.65 m/s (1.3 kPa) and 1.08 m/s (3.5 kPa), respectively.

2.5.5 In-vivo 3D elastography

In-vivo measurement was performed on one healthy volunteer in the upper right quadrant of the breast; the volunteer had read and signed an informed consent.

Shear wave propagation for one single push in vivo in healthy breast is presented in **Figure 2.20**. The ultrasound sequence used was the same as the one used for breast phantom imaging. The mean value of the shear wave speed in the whole volume ($19.2 \times 19.2 \times 23.2$ mm) was found to be 1.39 ± 1.58 m/s (5.8 ± 7.5 kPa) (**Figure 2.20 b**).

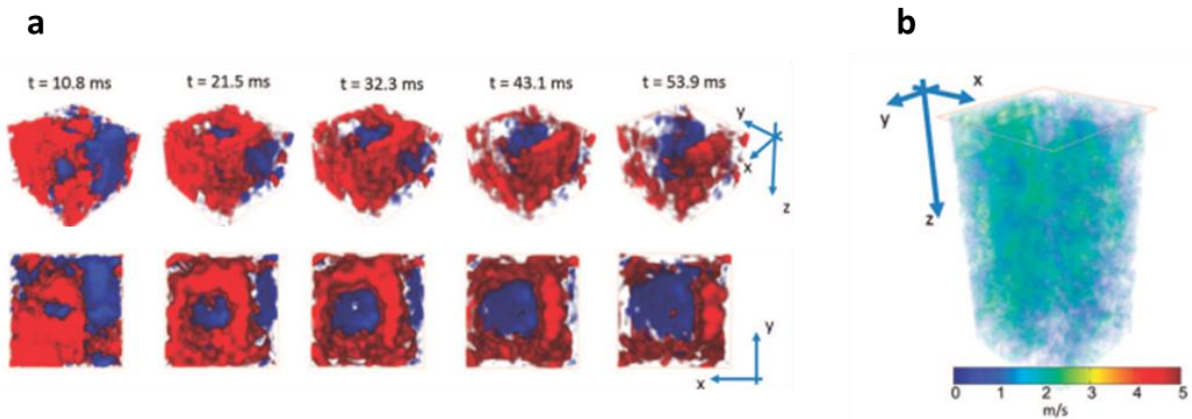


Figure 2.20 – *In vivo* 3D shear wave elastography in the breast of one healthy volunteer. (a) In vivo 3D push. Displacements are in arbitrary units. Volume ($19.2 \times 19.2 \times 11.4$ mm) and top view representation of propagating shear waves as a function time. (b) 3D shear wave speed map ($19.2 \times 19.2 \times 23.2$ mm).

In this *in-vivo* case on the breast, the total time for experiments, acquisition, and shear wave speed mapping was about 2 min (beamforming of the data takes 43 s in our configuration) on a fast personal computer (Xeon (6 cores, Intel corp., Santa Clara, ca) with 64 Gb of RAM and a graphics processing unit (K6000, nvidia corp.)). This duration will be reduced in the near future,

with improvement of computer technology in the next 4 years allowing real-time *in vivo* acquisitions. Moreover, in the presented system, for now, only the beamforming process is performed with the graphic card and the shear wave speed calculations are performed with Matlab; the time required can thus be reduced by refining the algorithms.

One other important comment is that energy deposited into tissues is relatively limited, because only one or a few pushes are necessary to generate entire 3D elasticity maps. This approach satisfies the ALARA principle (as low as reasonably acceptable), and stands in high contrast with concatenation (Ossa, 2012) or stroboscopic (Wang et al., 2013b) approaches, which typically require tens of pushes to generate one 3D volume.

2.5.6 Conclusion

We established the feasibility of performing 3D shear wave imaging, where radiation force emanating from a 2D matrix array was used to generate a shear wave, both in phantoms and in humans *in vivo*. Using a novel, customized 1024-channel ultrafast ultrasound scanner and a 3-MHz 2D array probe, we have demonstrated that the shear-wave generated by applying spherical delays to a 2D array could be tracked by using subsequent plane wave emissions. 3D shear-wave velocity estimation algorithms were based on directional filters and multiscale correlations were devised to generate volumetric maps of shear modulus in an entire 3D field of view. Results obtained in parallel with a conventional 2D imaging system in phantom were found to be in good accordance and validated 3D reconstruction. Finally, we have shown that our system was suitable for clinical translation by showing the feasibility of 3D shear wave imaging in the breast of a healthy volunteer.

Limitations to this study include the small footprint of the 2D matrix array probe. Indeed, the 10×10 mm aperture strongly limits the field of view when using plane wave imaging. This limitation could be overcome by either increasing the physical aperture—by adding more piezoelectric elements and, thus, more acquisition channels to the imaging system—or by using spherical waves (Provost et al., 2014) at the cost of a lower image quality. Additionally, although our customized system allows for imaging at thousands of volumes per second, the reliance on synthetic receive aperture, along with the larger number of compounded emissions resulting from 3D imaging, currently limits the volume rate. Probes that can emit higher pressures, along with a system in which the number of receive channels is equal to the number of transmit channels could palliate this issue.

2.5.7 Perspectives

The results shown in **Figure 2.20** illustrate the possibility of not only mapping the amplitude of the shear-wave velocity, but also its direction. This direction gives access to several novel mechanical properties of tissue, unlike 2D techniques. Perhaps most prominently, quantifying the propagation direction of a shear wave could be used to map the anisotropy of tissue using elastic tensor imaging (Lee et al., 2012; Wang et al., 2013b).

Although this technique was originally established using standard shear wave imaging, generalizing it to 3D shear wave imaging eliminates the need for a rotating motor and greatly expands the field of its potential clinical applications, from the mapping of fibers in the heart to the quantification of contraction properties of skeletal muscle. Additionally, we have also shown that the shear wave source can be controlled in 3D space, which adds a degree of freedom when compared with standard techniques. Such plane shear waves could be used to retrieve shear attenuation and dispersion maps, which would lead, in turn, to a complete 3D rheological characterization and could contribute to expand our current understanding of shear wave physics in medical applications.

Other techniques such as magnetic resonance elastography (Mariappan et al., 2010) or concatenated 2D shear-wave elastography (Ossa, 2012; Wang et al., 2013b) can provide 3D volumes of mechanical properties such as the shear modulus. However, both of these techniques require long acquisition times, and therefore suffer from motion artifacts originating from breathing or pulsatility. To the contrary, 3D shear-wave imaging provides shear wave speed amplitude and direction maps in entire 3D field of views in a single acquisition, which typically lasts less than 40 ms.

Such a technology has not been tested yet on brain during surgery (because the scanner is not yet conformed to CE marking) but is envisioned to soon overcome the current limitations of 2D shear wave elastography and to expand its field of application to novel diagnostic approaches based on volumetric shear wave data with decreased operator dependence.

2.6 Chapter conclusion

We provided evidence to justify the use of intraoperative SWE in brain tumor surgery: this imaging technique helps surgeons to quantitatively distinguish benign and malignant brain tumors (especially in gliomas) and thus to provide the optimum extent of resection.

In the neurosurgery field, we also demonstrated that SWE can detect changes due to increasing volume of brain parenchyma, such as in case of tumor growth or edemas. SWE could enable to draw a cut-off line between compensation and decompensation. A larger clinical study need to be conducted to precisely determinate the cut-off value to identify patients with intracranial hypertension during brain surgery.

Lastly, we established the feasibility of performing full 3D shear wave imaging, where radiation force emanating from a 2D matrix array was used to generate a shear wave, both in phantoms and in humans *in vivo*. Using a novel, customized 1024-channel ultrafast ultrasound scanner and a 3-MHz 2D array probe, we have demonstrated that the shear wave generated by applying spherical delays to a 2D array could be tracked by using subsequent plane wave emissions. This technique eliminates the need for a rotating motor and greatly expands the field of its potential clinical applications, from the mapping of fibers in the heart to the quantification of contraction properties of skeletal muscle.

In this chapter, we provided several evidences of the interest to use SWE during brain surgery. We also presented our new technique for 3D SWE using matrix array promising a wide application range.

2.7 Chapter bibliography

- Aaslid, R., Markwalder, T.-M., Nornes, H., 1982. Noninvasive transcranial Doppler ultrasound recording of flow velocity in basal cerebral arteries. *J. Neurosurg.* 57, 769–774. doi:10.3171/jns.1982.57.6.0769
- Bavu, É., Gennisson, J.-L., Couade, M., Bercoff, J., Mallet, V., Fink, M., Badel, A., Vallet-Pichard, A., Nalpas, B., Tanter, M., Pol, S., 2011. Noninvasive In Vivo Liver Fibrosis Evaluation Using Supersonic Shear Imaging: A Clinical Study on 113 Hepatitis C Virus Patients. *Ultrasound Med. Biol.* 37, 1361–1373. doi:10.1016/j.ultrasmedbio.2011.05.016
- Bercoff, J., Tanter, M., Fink, M., 2004. Supersonic shear imaging: a new technique for soft tissue elasticity mapping. *IEEE Trans. Ultrason. Ferroelectr. Freq. Control* 51, 396–409.
- Berg, W.A., Cosgrove, D.O., Doré, C.J., Schäfer, F.K.W., Svensson, W.E., Hooley, R.J., Ohlinger, R., Mendelson, E.B., Balu-Maestro, C., Locatelli, M., Tourasse, C., Cavanaugh, B.C., Juhan, V., Stavros, A.T., Tardivon, A., Gay, J., Henry, J.-P., Cohen-Bacrie, C., BE1 Investigators, 2012. Shear-wave elastography improves the specificity of breast US: the BE1 multinational study of 939 masses. *Radiology* 262, 435–449. doi:10.1148/radiol.11110640
- Bhatia, K.S.S., Tong, C.S.L., Cho, C.C.M., Yuen, E.H.Y., Lee, Y.Y.P., Ahuja, A.T., 2012. Shear wave elastography of thyroid nodules in routine clinical practice: preliminary observations and utility for detecting malignancy. *Eur. Radiol.* 22, 2397–2406. doi:10.1007/s00330-012-2495-1
- Chan, H.W., Pressler, R., Uff, C., Gunny, R., St Piers, K., Cross, H., Bamber, J., Dorward, N., Harkness, W., Chakraborty, A., 2014. A novel technique of detecting MRI-negative lesion in focal symptomatic epilepsy: Intraoperative ShearWave Elastography. *Epilepsia* n/a-n/a. doi:10.1111/epi.12562
- Coenen, V.A., Krings, T., Weidemann, J., Hans, F.-J., Reinacher, P., Gilsbach, J.M., Rohde, V., 2005. Sequential visualization of brain and fiber tract deformation during intracranial surgery with three-dimensional ultrasound: an approach to evaluate the effect of brain shift. *Neurosurgery* 56, 133-141-141.
- Deffieux, T., Gennisson, J.-L., Bercoff, J., Tanter, M., 2011. On the effects of reflected waves in transient shear wave elastography. *IEEE Trans. Ultrason. Ferroelectr. Freq. Control* 58, 2032–2035. doi:10.1109/TUFFC.2011.2052
- Deffieux, T., Gennisson, J.-L., Larrat, B., Fink, M., Tanter, M., 2012. The variance of quantitative estimates in shear wave imaging: Theory and experiments. *IEEE Trans. Ultrason. Ferroelectr. Freq. Control* 59. doi:10.1109/TUFFC.2012.2472
- Drummond, J.C., 1995. Elastance Versus Compliance. *J. Am. Soc. Anesthesiol.* 82, 1309–1310.
- Dunn, L.T., 2002. Raised intracranial pressure. *J. Neurol. Neurosurg. Psychiatry* 73, i23–i27.
- Ferraioli, G., Parekh, P., Levitov, A.B., Filice, C., 2014. Shear Wave Elastography for Evaluation of Liver Fibrosis. *J. Ultrasound Med.* 33, 197–203. doi:10.7863/ultra.33.2.197
- Gefen, A., Margulies, S.S., 2004. Are in vivo and in situ brain tissues mechanically similar? *J. Biomech.* 37, 1339–1352. doi:10.1016/j.jbiomech.2003.12.032

- Gennisson, J., Provost, J., Deffieux, T., Papadacci, C., Imbault, M., Pernot, M., Tanter, M., others, 2015. 4-D ultrafast shear-wave imaging. *Ultrason. Ferroelectr. Freq. Control IEEE Trans. On* 62, 1059–1065.
- Gennisson, J.-L., Deffieux, T., Fink, M., Tanter, M., 2013. Ultrasound elastography: Principles and techniques. *Diagn. Interv. Imaging* 94, 487–495. doi:10.1016/j.diii.2013.01.022
- Goldstein, B., Tasker, R.C., Wakeland, W., 2012. From Lundberg to SIM-ICP: computational physiology and modeling intracranial pressure. *Sci. Transl. Med.* 4, 129fs6. doi:10.1126/scitranslmed.3003925
- Hans, P., 1994. Pression hydrostatique et pathologie neurochirurgicale. *Ann. Fr. Anesth. Réanimation* 13, 123–126. doi:10.1016/S0750-7658(94)80195-9
- Jakola, A.S., Unsgård, G., Solheim, O., 2011. Quality of life in patients with intracranial gliomas: the impact of modern image-guided surgery. *J. Neurosurg.* 114, 1622–1630. doi:10.3171/2011.1.JNS101657
- Kasai, C., Namekawa, K., Koyano, A., Omoto, R., 1985. Real-time two-dimensional blood flow imaging using an autocorrelation technique. *IEEE Trans Sonics Ultrason* 32, 458–464.
- Kashif, F.M., Verghese, G.C., Novak, V., Czosnyka, M., Heldt, T., 2012. Model-based noninvasive estimation of intracranial pressure from cerebral blood flow velocity and arterial pressure. *Sci. Transl. Med.* 4, 129ra44. doi:10.1126/scitranslmed.3003249
- Kristiansson, H., Nissborg, E., Bartek, J., Andresen, M., Reinstrup, P., Romner, B., 2013. Measuring Elevated Intracranial Pressure through Noninvasive Methods: A Review of the Literature. *J. Neurosurg. Anesthesiol.* 25, 372–385. doi:10.1097/ANA.0b013e31829795ce
- Kruse, S.A., Rose, G.H., Glaser, K.J., Manduca, A., Felmlee, J.P., Jack Jr., C.R., Ehman, R.L., 2008. Magnetic resonance elastography of the brain. *NeuroImage* 39, 231–237. doi:10.1016/j.neuroimage.2007.08.030
- Lee, S.H., Chang, J.M., Kim, W.H., Bae, M.S., Seo, M., Koo, H.R., Chu, A.J., Gweon, H.M., Cho, N., Moon, W.K., 2014. Added Value of Shear-Wave Elastography for Evaluation of Breast Masses Detected with Screening US Imaging. *Radiology* 132443. doi:10.1148/radiol.14132443
- Lee, W.-N., Larrat, B., Pernot, M., Tanter, M., 2012. Ultrasound elastic tensor imaging: comparison with MR diffusion tensor imaging in the myocardium. *Phys. Med. Biol.* 57, 5075–5095. doi:10.1088/0031-9155/57/16/5075
- Lindner, D., Trantakis, C., Renner, C., Arnold, S., Schmitgen, A., Schneider, J., Meixensberger, J., 2006. Application of intraoperative 3D ultrasound during navigated tumor resection. *Minim. Invasive Neurosurg. MIN* 49, 197–202. doi:10.1055/s-2006-947997
- Lindsey, B.D., Smith, S.W., 2013. Pitch-catch phase aberration correction of multiple isoplanatic patches for 3-D transcranial ultrasound imaging. *IEEE Trans. Ultrason. Ferroelectr. Freq. Control* 60, 463–480. doi:10.1109/TUFFC.2013.2590
- Lipp, A., Trbojevic, R., Paul, F., Fehlner, A., Hirsch, S., Scheel, M., Noack, C., Braun, J., Sack, I., 2013. Cerebral magnetic resonance elastography in supranuclear palsy and idiopathic Parkinson’s disease. *NeuroImage Clin.* 3, 381–387. doi:10.1016/j.nicl.2013.09.006
- Lockwood, G.R., Talman, J.R., Brunke, S.S., 1998. Real-time 3-D ultrasound imaging using sparse synthetic aperture beamforming. *IEEE Trans. Ultrason. Ferroelectr. Freq. Control* 45, 980–988. doi:10.1109/58.710573

- Madsen, E.L., Hobson, M.A., Frank, G.R., Shi, H., Jiang, J., Hall, T.J., Varghese, T., Doyley, M.M., Weaver, J.B., 2006. Anthropomorphic breast phantoms for testing elastography systems. *Ultrasound Med. Biol.* 32, 857–874. doi:10.1016/j.ultrasmedbio.2006.02.1428
- Mariappan, Y.K., Glaser, K.J., Ehman, R.L., 2010. Magnetic resonance elastography: A review. *Clin. Anat.* 23, 497–511. doi:10.1002/ca.21006
- Monro, A., 1783. Observations on the structure and functions of the nervous system.
- Montaldo, G., Tanter, M., Bercoff, J., Benech, N., Fink, M., 2009. Coherent plane-wave compounding for very high frame rate ultrasonography and transient elastography. *IEEE Trans. Ultrason. Ferroelectr. Freq. Control* 56, 489–506. doi:10.1109/TUFFC.2009.1067
- Murphy, M.C., Huston, J., 3rd, Jack, C.R., Jr, Glaser, K.J., Manduca, A., Felmlee, J.P., Ehman, R.L., 2011. Decreased brain stiffness in Alzheimer’s disease determined by magnetic resonance elastography. *J. Magn. Reson. Imaging JMRI* 34, 494–498. doi:10.1002/jmri.22707
- Netter, F., 2016. The Netter Collection of Medical Illustrations Complete Package. Elsevier Science Health Science.
- Nikolov, S., 2002. Synthetic aperture tissue and flow ultrasound imaging.
- Nikolov, S.I., Kortbek, J., Jensen, J.A., 2010. Practical applications of synthetic aperture imaging, in: 2010 IEEE International Ultrasonics Symposium. Presented at the 2010 IEEE International Ultrasonics Symposium, pp. 350–358. doi:10.1109/ULTSYM.2010.5935627
- Ohue, S., Kumon, Y., Nagato, S., Kohno, S., Harada, H., Nakagawa, K., Kikuchi, K., Miki, H., Ohnishi, T., 2010. Evaluation of intraoperative brain shift using an ultrasound-linked navigation system for brain tumor surgery. *Neurol. Med. Chir. (Tokyo)* 50, 291–300.
- OpenStax, 2016. Anatomy and Physiology.
- Osmanski, B.-F., Montaldo, G., Tanter, M., Fink, M., 2012. Aberration correction by time reversal of moving speckle noise. *IEEE Trans. Ultrason. Ferroelectr. Freq. Control* 59, 1575–1583. doi:10.1109/TUFFC.2012.2357
- Ossa, H.L., 2012. In vivo monitoring of elastic changes during cancer development and therapeutic treatment (phdthesis). Université Paris-Diderot - Paris VII.
- Papadacci, C., Pernot, M., Couade, M., Fink, M., Tanter, M., 2014. High-contrast ultrafast imaging of the heart. *IEEE Trans. Ultrason. Ferroelectr. Freq. Control* 61, 288–301. doi:10.1109/TUFFC.2014.6722614
- Provost, J., Nguyen, V.T.-H., Legrand, D., Okrasinski, S., Costet, A., Gambhir, A., Hasan Garan, Konofagou, E.E., 2011. Electromechanical wave imaging for arrhythmias. *Phys. Med. Biol.* 56, L1. doi:10.1088/0031-9155/56/22/F01
- Provost, J., Papadacci, C., Arango, J.E., Imbault, M., Fink, M., Gennisson, J.-L., Tanter, M., Pernot, M., 2014. 3D ultrafast ultrasound imaging in vivo. *Phys. Med. Biol.* 59, L1. doi:10.1088/0031-9155/59/19/L1
- Purkayastha, S., Sorond, F., 2013. Transcranial Doppler Ultrasound: Technique and Application. *Semin. Neurol.* 32, 411–420. doi:10.1055/s-0032-1331812
- Raboel, P.H., Bartek, J., Andresen, M., Bellander, B.M., Romner, B., 2012. Intracranial Pressure Monitoring: Invasive versus Non-Invasive Methods—A Review. *Crit. Care Res. Pract.* 2012, 1–14. doi:10.1155/2012/950393
- Rasmussen, I.-A., Jr, Lindseth, F., Rygh, O.M., Berntsen, E.M., Selbekk, T., Xu, J., Nagelhus Hernes, T.A., Harg, E., Håberg, A., Unsgaard, G., 2007. Functional neuronavigation combined with intra-operative 3D ultrasound: initial experiences during surgical

- resections close to eloquent brain areas and future directions in automatic brain shift compensation of preoperative data. *Acta Neurochir. (Wien)* 149, 365–378. doi:10.1007/s00701-006-1110-0
- Rosenberg, J.B., Shiloh, A.L., Savel, R.H., Eisen, L.A., 2011. Non-invasive Methods of Estimating Intracranial Pressure. *Neurocrit. Care* 15, 599–608. doi:10.1007/s12028-011-9545-4
- Ruskin, K.J., Rosenbaum, S.H., Rampil, I.J., 2013. *Fundamentals of Neuroanesthesia: A Physiologic Approach to Clinical Practice*. Oxford University Press.
- Sarvazyan, A.P., Rudenko, O.V., Swanson, S.D., Fowlkes, J.B., Emelianov, S.Y., 1998. Shear wave elasticity imaging: a new ultrasonic technology of medical diagnostics. *Ultrasound Med. Biol.* 24, 1419–1435.
- Scholz, M., Noack, V., Pechlivanis, I., Engelhardt, M., Fricke, B., Linstedt, U., Brendel, B., Ing, D., Schmieder, K., Ermert, H., Harders, A., 2005. Vibrography during tumor neurosurgery. *J. Ultrasound Med. Off. J. Am. Inst. Ultrasound Med.* 24, 985–992.
- Sebag, F., Vaillant-Lombard, J., Berbis, J., Griset, V., Henry, J.F., Petit, P., Oliver, C., 2010. Shear Wave Elastography: A New Ultrasound Imaging Mode for the Differential Diagnosis of Benign and Malignant Thyroid Nodules. *J. Clin. Endocrinol. Metab.* 95, 5281–5288. doi:10.1210/jc.2010-0766
- Selbekk, T., Jakola, A.S., Solheim, O., Johansen, T.F., Lindseth, F., Reinertsen, I., Unsgård, G., 2013. Ultrasound imaging in neurosurgery: approaches to minimize surgically induced image artefacts for improved resection control. *Acta Neurochir. (Wien)* 155, 973–980. doi:10.1007/s00701-013-1647-7
- Shinoura, N., Takahashi, M., Yamada, R., 2006. Delineation of brain tumor margins using intraoperative sononavigation: Implications for tumor resection. *J. Clin. Ultrasound* 34, 177–183. doi:10.1002/jcu.20219
- Sommer, B., Grummich, P., Coras, R., Kasper, B.S., Blumcke, I., Hamer, H.M., Stefan, H., Buchfelder, M., Roessler, K., 2013. Integration of functional neuronavigation and intraoperative MRI in surgery for drug-resistant extratemporal epilepsy close to eloquent brain areas. *Neurosurg. Focus* 34, E4. doi:10.3171/2013.2.FOCUS12397
- Tanter, M., Bercoff, J., Athanasiou, A., Deffieux, T., Gennisson, J.-L., Montaldo, G., Muller, M., Tardivon, A., Fink, M., 2008a. Quantitative assessment of breast lesion viscoelasticity: initial clinical results using supersonic shear imaging. *Ultrasound Med. Biol.* 34, 1373–1386. doi:10.1016/j.ultrasmedbio.2008.02.002
- Tanter, M., Bercoff, J., Athanasiou, A., Deffieux, T., Gennisson, J.-L., Montaldo, G., Muller, M., Tardivon, A., Fink, M., 2008b. Quantitative Assessment of Breast Lesion Viscoelasticity: Initial Clinical Results Using Supersonic Shear Imaging. *Ultrasound Med. Biol.* 34, 1373–1386. doi:10.1016/j.ultrasmedbio.2008.02.002
- Tanter, M., Bercoff, J., Sandrin, L., Fink, M., 2002. Ultrafast compound imaging for 2-D motion vector estimation: application to transient elastography. *IEEE Trans. Ultrason. Ferroelectr. Freq. Control* 49, 1363–1374.
- Tanter, M., Fink, M., 2014. Ultrafast imaging in biomedical ultrasound. *IEEE Trans. Ultrason. Ferroelectr. Freq. Control* 61, 102–119. doi:10.1109/TUFFC.2014.6689779
- Tanter, M., Thomas, J.L., Fink, M., 1998. Focusing and steering through absorbing and aberrating layers: application to ultrasonic propagation through the skull. *J. Acoust. Soc. Am.* 103, 2403–2410.

- the BE1 Study Group, Cosgrove, D.O., Berg, W.A., Doré, C.J., Skyba, D.M., Henry, J.-P., Gay, J., Cohen-Bacrie, C., 2012. Shear wave elastography for breast masses is highly reproducible. *Eur. Radiol.* 22, 1023–1032. doi:10.1007/s00330-011-2340-y
- Unsgaard, G., Gronningsaeter, A., Ommedal, S., Nagelhus Hernes, T.A., 2002. Brain operations guided by real-time two-dimensional ultrasound: new possibilities as a result of improved image quality. *Neurosurgery* 51, 402-411-412.
- Wang, M., Byram, B., Palmeri, M., Rouze, N., Nightingale, K., 2013a. On the precision of time-of-flight shear wave speed estimation in homogeneous soft solids: initial results using a matrix array transducer. *IEEE Trans. Ultrason. Ferroelectr. Freq. Control* 60, 758–770. doi:10.1109/TUFFC.2013.2624
- Wang, M., Byram, B., Palmeri, M., Rouze, N., Nightingale, K., 2013b. Imaging Transverse Isotropic Properties of Muscle by Monitoring Acoustic Radiation Force Induced Shear Waves Using a 2-D Matrix Ultrasound Array. *IEEE Trans. Med. Imaging* 32, 1671–1684. doi:10.1109/TMI.2013.2262948
- Yoon, J.H., Lee, J.M., Joo, I., Lee, E.S., Sohn, J.Y., Jang, S.K., Lee, K.B., Han, J.K., Choi, B.I., 2014. Hepatic Fibrosis: Prospective Comparison of MR Elastography and US Shear Wave Elastography for Evaluation. *Radiology* 132000. doi:10.1148/radiol.14132000
- Zorgani, A., Souchon, R., Dinh, A.-H., Chapelon, J.-Y., Ménager, J.-M., Lounis, S., Rouvière, O., Catheline, S., 2015. Brain palpation from physiological vibrations using MRI. *Proc. Natl. Acad. Sci.* 112, 12917–12921. doi:10.1073/pnas.1509895112

Chapter III

Intraoperative Neurofunctional Ultrasound Imaging

 Intraoperative Neurofunctional Ultrasound Imaging

Table of contents

3. Intraoperative neurofunctional ultrasound imaging.....	93
3.1 Chapter introduction	93
3.2 Neurovascular coupling	94
3.3 Intraoperative functional imaging.....	95
3.3.1 Electrocortical stimulation mapping	96
3.3.2 Functional MRI-integrated neuronavigation.....	97
3.4 Functional ultrasound (fUS) principle.....	98
3.4.1 Ultrafast Doppler imaging.....	98
3.4.2 Functional ultrasound imaging	100
3.5 Development of intraoperative fUS in humans.....	101
3.5.1 Intraoperative Ultrafast Doppler.....	101
3.5.1.1 Ultrasound acquisitions	101
3.5.1.2 Spatiotemporal clutter filtering.....	103
3.5.2 Intraoperative functional ultrasound.....	105
3.5.2.1 Computing the activation maps.....	106
3.5.2.2 Thresholding the activation map	107
3.6 Intraoperative fUS pilot clinical study	107
3.6.1 Cohort of patients.....	107
3.6.2 Surgery and anesthesia.....	108
3.6.3 Gold standard for intraoperative functional mapping.....	108
3.6.4 Intraoperative ultrasound imaging.....	109

3.6.5	Functional areas studied	109
3.6.6	Deep cortex activation maps.....	111
3.6.7	Intraoperative fUS sensitivity	112
3.6.8	Discussion.....	114
3.7	Chapter conclusion	114
3.8	Chapter bibliography	115

3. Intraoperative neurofunctional ultrasound imaging

3.1 Chapter introduction

Functional imaging (or physiological imaging), is a medical imaging technique to detect or measure changes in metabolism, blood flow, regional chemical composition, or absorption. As opposed to structural imaging, functional imaging focuses on revealing physiological activities within a certain tissue or organ by employing medical image modalities that very often use tracers to reflect spatial distribution of them within the body. Neurofunctional imaging of the brain is the use of imaging technology to measure an aspect of brain function in order to understand the relationship between the activity in certain brain areas and specific mental functions.

A wide spectrum of methods is used to image brain activation *in vivo*. It can be directly detected by neurons electrical activity measuring such as electrocortical stimulation mapping (ESM) (Ebeling, Schmid, and Reulen 1989), calcium imaging (Grienberger and Konnerth 2012) and voltage sensitive dyes imaging (Peterka, Takahashi, and Yuste 2011). However, the brain functional activity can also be followed through its blood supply measurement, as first proposed by Lavoisier (Lavoisier 1920) and demonstrated by Mosso (Mosso 1881). Today several functional imaging modalities exploit local changes of blood flow to map the functional response to brain stimuli such as multiphoton microscopy (Sheth et al. 2003), optical coherence tomography (Chen et al. 2009), positron emission tomography (PET) (Phelps and Mazziotta 1985) and functional Magnetic Resonance Imaging (fMRI) ((Ogawa et al. 1990), (Kim and Ugurbil 2003), (Rossi 2006), (Richiardi et al. 2011)).

Localizing regions at risk regarding brain function is a real challenge during brain surgery. A precise cartography of the different functional areas surrounding the lesion can indicate to the surgeon where to stop with the resection. Tumor removal is hence performed according to functional boundaries in order to both optimize the accuracy of tumor removal and minimize the risk of postoperative functional deficits. Ultrasound has the potential to answer this need. Indeed, ultrasound imaging achieves good spatiotemporal resolution in depth and is currently intraoperatively used to localize tumor tissue and characterize both tumor and normal brain stiffness, as demonstrated in chapter 2. However the use of Doppler ultrasound has been limited until now to the imaging of major vessels due to its poor sensitivity. To overcome this limitation functional ultrasound (fUS) was developed (Macé et al. 2011). This technique enables high spatiotemporal resolution imaging (250 μ m, 1ms) of brain microvasculature dynamics in response to brain activation without needing contrast agent.

In this chapter, both techniques based on direct detection of neurons electrical activity and based on neurovascular coupling will be presented. A special attention will be paid to intraoperative functional brain imaging modalities. Brain functional ultrasound imaging will then be positioned in this context and the principle will be detailed. Then, the development of ultrafast Doppler

sequences and data processing for fUS imaging adapted to intraoperative functional imaging on humans will be presented. Finally, the results of our pilot clinical study will be discussed.

3.2 Neurovascular coupling

Study the brain in action is a major challenge of contemporary scientific research. Cerebral activity is mainly due to neuronal activity. At a microscopic scale, we can therefore study the activity of the brain by measuring the variations of neuron constants. On the one hand, a neuronal activity leads to local chemical variations. Local concentrations of molecules such as Na^+ , K^+ , Ca^{2+} or the APT (adenosine triphosphate) varies along with neuron activation. On the other hand, it is also possible to measure the electrical potential of neurons, fluctuating with their activation.

These local electrical and chemical fluctuations of neurons will lead to a demand in energy. Therefore there will be blood variation in areas of cerebral activity. This phenomenon, called neurovascular coupling, is still an intensive field of research at the moment (Attwell et al. 2010). Neuronal activation originates in neurons as electrical signals are passed between cells. During this activation the metabolic demand of neurons changes, provoking an increase in oxygen consumption, local cerebral blood flow (CBF) and oxygen delivery. A typical hemodynamic response to cortical neuronal activation in adults shows an increase in blood flow leading to an increase in oxy-hemoglobin (HbO_2) and a (relatively smaller) decrease in deoxy-hemoglobin (HHb) as it is displaced from veins, leading to an increase in total-hemoglobin (HbT) (Villringer 1997). Blood constants quantification can therefore give us an indirect picture of neuronal activity. We can thus see the brain in action through its vascular activity. The imaging of vascular constants can also be realized for the whole brain at the macroscopic scale.

The reference macroscopic imaging system of the neurovascular coupling, dating from the 90s, is functional magnetic resonance imaging (fMRI) (Ogawa et al. 1990). This type of imaging quantifies the level of oxygenation of the blood (BOLD fMRI: Blood Oxygen Level Dependent fMRI). During a functional activation of the brain, oxyhemoglobin concentration increases while deoxyhemoglobin concentration decreases. Deoxyhemoglobin changes the proton signal of the surrounding water molecules, inducing an increase in the MRI gradient echo. Functional activation therefore decreases MRI signal. **Figure 3.1** summarizes the macroscopic imaging mechanism of neurovascular coupling.

Figure 3.1 shows the complexity of the interpretation of a macroscopic blood signal. Intensive research on functional MRI (Charpak and Stefanovic 2012) is occurring to understand what is exactly measured with this technique, the link between neuronal activity and BOLD signal remaining nowadays not fully explained.

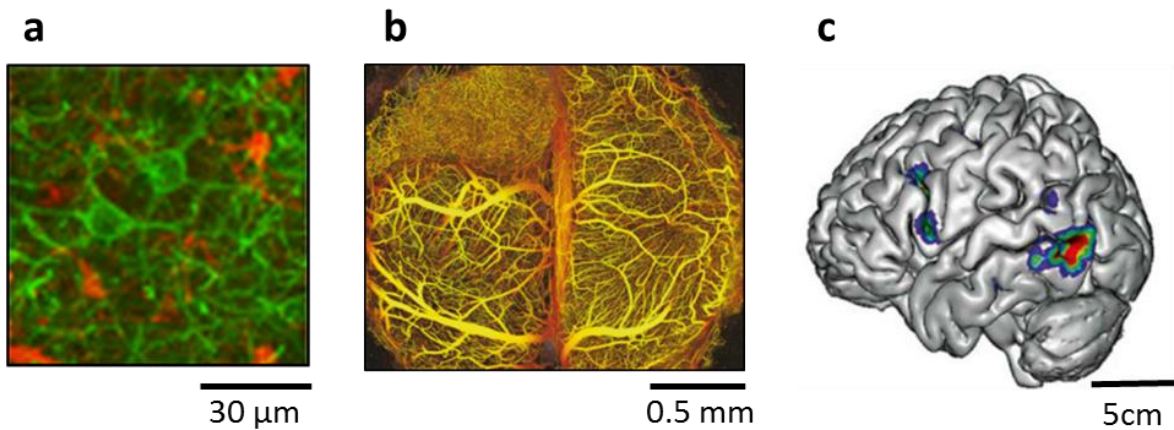


Figure 3.1 – Different scales of brain imaging. (a) Images produced with a microscope (two photons) presenting cells responsible for cerebral activity (neurons in green, astrocytes in red) on the micrometric scale. An increased activity of neurons and astrocytes induces an increase in flow blood in the surrounding capillaries (example taken from the mouse brain, adapted from (Uhlirva et al. 2016)). (b) Image produced using a scanning electron microscope. We move to the millimetric scale and we can observe a dense and complicated vascular network (example taken from the mouse brain, adapted from (Gagnon et al. 2016)). (c) MRI image function of cerebral activation. A voxel is about 1mm^3 , and this voxel therefore contains a dense network of capillaries and a large number of neurons and astrocytes (example taken from the human brain, adapted from (Lehéricy et al. 2015)).

In this section, we have seen that several techniques can image local brain activation at a macroscopic scale. However, it is still very difficult to link the signal macroscopically measured to the microscopic blood activity. It is also complicated to exactly link the microscopic blood activity to the local electrical and chemical activity of the brain.

However, these functional imaging techniques can be very important tools, especially for neurosurgeons. The aim of intraoperative brain functional mapping is to maximize tumor removal while preserving the functional brain areas and thus minimizing the postoperative deficits risk. The two techniques most commonly used for functional imaging during brain surgery are presented in the next section.

3.3 Intraoperative functional imaging

Over the last two decades, presurgical mapping using functional neuroimaging techniques – and particularly fMRI – has made considerable progress. fMRI is now commonly used in the clinical practice and not just for research applications. Presurgical functional neuroimaging with its contributions to surgical planning and to the prediction of postoperative outcome is now well established. Currently, functional intraoperative neuroimaging is considered as complementary to electrocortical stimulation mapping (ESM) providing additional information, such as information on the entire functional network and on the contralateral hemisphere, which is not accessible to ESM.

In the brain functional imaging field, it is well-known that the highest temporal and spatial resolutions are provided by optical based methods ($\sim 10\ \mu\text{m}$, $\sim 10\ \text{ms}$) (Liao et al. 2013), however they are intrinsically limited to the investigation of the cortex. Photoacoustic techniques, such

as infrared functional imaging, can go deeper and can be used on human during brain surgery (Gorbach et al. 2003) but the penetration remains poor (~ 1 mm).

Until now, there are mainly two techniques commonly used for functional imaging during brain surgery: ESM, directly detected neurons electrical activity, and fMRI, based on neurovascular coupling. These techniques are presented in the next sections.

3.3.1 Electrocortical stimulation mapping

Currently, invasive electrophysiological investigations remain the gold standard (reference procedure) for brain surgery, in particular for tumors located near or within eloquent cortical and/or subcortical structures (H Duffau 2005). Electrocortical stimulation mapping (ESM) is usually performed using a bipolar probe (Figure 3.2 a) and allows mapping of a large number of motor, somatosensory, and cognitive functions (see Figure 3.2 b). ESM also permits the study of anatomic-functional connectivity by directly stimulating white matter tracts (Keles et al. 2004). Therefore, ESM represent an accurate and reliable technique to localize cortical and subcortical regions at risk regarding brain function. Consequently, a reproducible functional disturbance induced by ESM will indicate where to stop with the resection, both for cortical and subcortical structures. Tumor removal is hence performed while taking particular care of functional boundaries in order to minimize the risk of postoperative functional deficits.

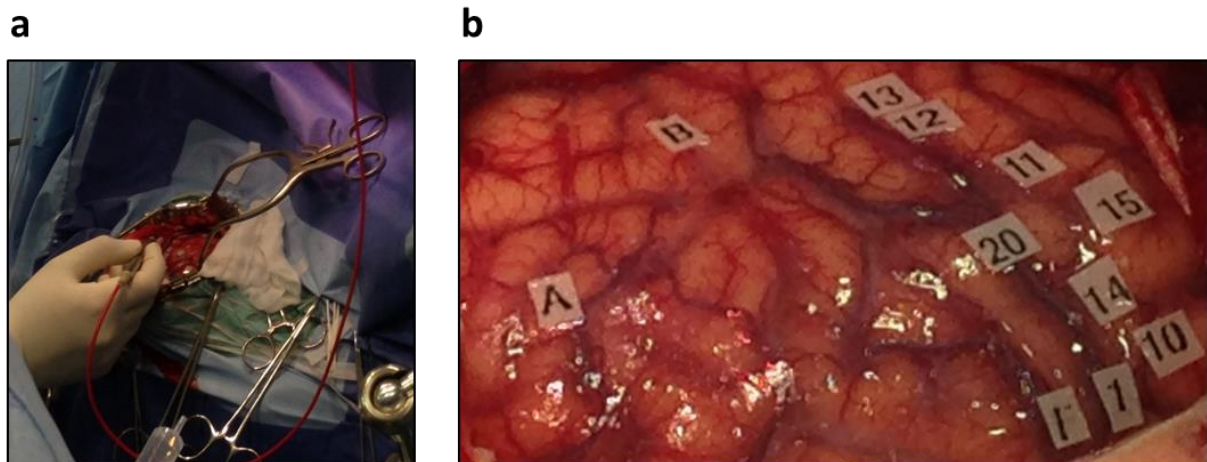


Figure 3.2 – Intraoperative bipolar stimulation. (a) During surgery, the probe is placed on the cortical surface of the patient. (b) Stimulation sites are labelled using small tags. Letters give tumor position, number from 1 to 10 stand for motor cortex and numbers from 11 to 20 stand for somatosensory cortex.

Defining the eloquent nature of cortical areas using ESM requires appropriate tasks and an accurate recording of the clinical responses to determine whether there is any interference with function during stimulation of the site. For this purpose, speech therapists or psychologists are present in the operative room in order to interpret the disorders induced by ESM (Hugues Duffau et al. 2002). Mapping of motor functions can be performed on awake patients or under general anesthesia, by inducing involuntary motor responses. Awake patients are generally passive during stimulation. Changes in movement parameters are recorded (slowdown, decrease in precision or amplitude, interruption). Sensory functions are mapped by eliciting dysesthesia

described by the patient himself intraoperatively (responses are therefore subjective). For cognitive function, the study of language (spontaneous speech, naming, comprehension, etc.), calculation, memory, reading, or writing evaluation is performed on awake patients by generating transient disturbances (Ojemann et al. 2009). The choice of the most appropriate tests is critical. Eloquent sites can be detected only if the proper function has been tested. This is why sensitive tasks are used rather than specific ones.

However, ESM have some limitations. They only allow loco-regional and not whole brain mapping. Furthermore, they are time-consuming, and the number of tasks that can be performed during surgery is limited. Moreover, there are some risks associated to ESM. Direct electrical stimulations can damage the brain. Tissue damage can result from numerous causes such as excessive heat (Doty and Bartlett 1981) or repetitive and synchronous stimulations of neurons (Fertziger and Ranck Jr. 1970). These risks are directly linked to the density of the charge applied on the probe.

The second gold standard for functional imaging describes in this manuscript, fMRI, presents less risks for the patient but is less precise and the functionalities are tested before the surgery.

3.3.2 Functional MRI-integrated neuronavigation

In presurgical functional mapping, determination of the accuracy of functional maps is essential, if images are to contribute to the presurgical localization of eloquent areas at risk in order to avoid postoperative deficits. Among the available and established functional imaging methods, functional fMRI is the most widely used (Lehéricy et al. 2015). fMRI can be easily performed on clinical magnets. Within the same session, high-resolution three-dimensional (3D) images of the brain and functional images with or without contrast injection are acquired (depending on the brain tumor entity), providing accurate anatomic detail about the respective lesion.

Validation studies of functional imaging techniques have shown the potential of fMRI to localize motor areas and also to lateralize and localize language and, more recently, memory functions (Lehéricy et al. 2015). However, particularly for cognitive brain functions, the imaging results strongly depend on the methodology requiring optimal clinical standard procedures.

In order to be used during brain surgery, fMRI data can be loaded on a neuronavigation system (**Figure 3.3**). This technique allows a 3D multiplanar anatomic and functional representation and can be used for lesion outline definition and functional area tracking.

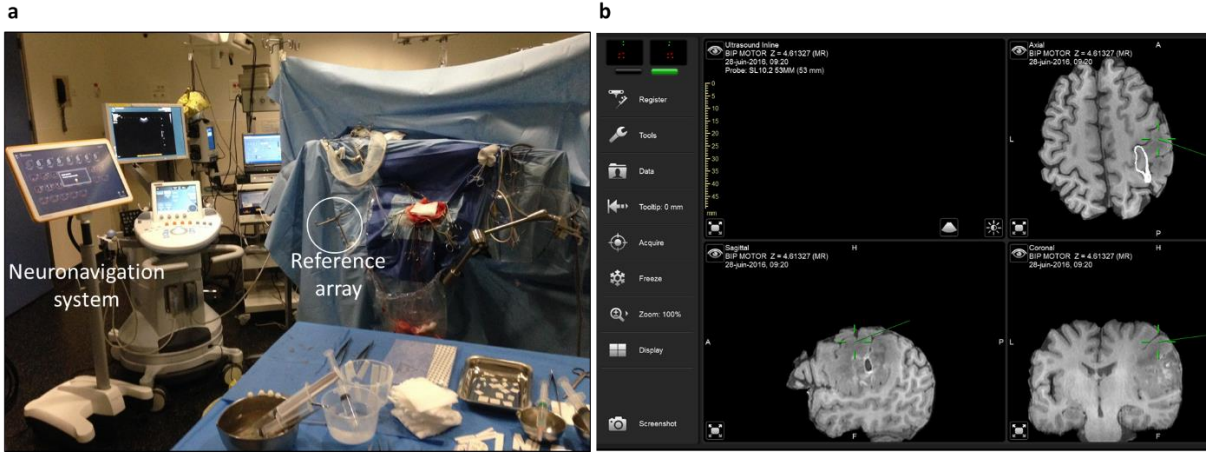


Figure 3.3 – Neuronavigation system used for brain tumor surgery. (a) The neuronavigation includes one screen and one infrared camera, and requires reference array to be fixed on the patient and on the probes. (b) Example of fMRI for a motor task. The white mark represents the functional area. The neurosurgeon can place the probe on the cortex and see the corresponding image on the screen.

Major advantages of fMRI are that it is noninvasive and routinely applicable on humans, and have an excellent penetration depth. However, fMRI also suffers from its cost, size and limited spatial ($\sim 2\text{mm}$) and temporal ($\sim 1\text{s}$) resolution. Moreover, MRI can hardly be performed in neurosurgery operating room in real time, and more importantly when opening the dura matter during surgery the brain shift has to be taken into account when using MRI neuronavigation.

3.4 Functional ultrasound (fUS) principle

Although functional neuro-imaging during intraoperative surgery would be highly beneficial, we understood in the previous sections that none of the existing techniques provides during surgery a simple, safe, high resolution and portable brain imaging modality within the depth of a sulcus. Ultrasound has the potential to answer to this need.

Ultrasound imaging achieves good spatiotemporal resolution in depth and is currently intraoperatively used to localize tumor tissue. However, the use of Doppler ultrasound has been limited until now to the imaging of major vessels due to its poor sensitivity. To overcome this limitation functional ultrasound (fUS) was developed (Macé et al. 2011). This technique enables high spatiotemporal resolution imaging ($250\mu\text{m}$, 1ms) of brain microvasculature dynamics in response to brain activation without the need for contrast agent.

In this section, the principle of the fUS technique and its existing applications are presented.

3.4.1 Ultrafast Doppler imaging

With the introduction and development of ultrafast imaging, new Doppler imaging methods were introduced to overcome the temporal resolution limitation given by the conventional ultrasound imaging approach. Ultrafast Doppler imaging, also called ultrasensitive Doppler was introduced in 2011 (Bercoff et al. 2011). This approach allows for Doppler estimation simultaneously over

the entire field of view, achieving accurately complex blood flow vascularization characterization (Figure 3.4).

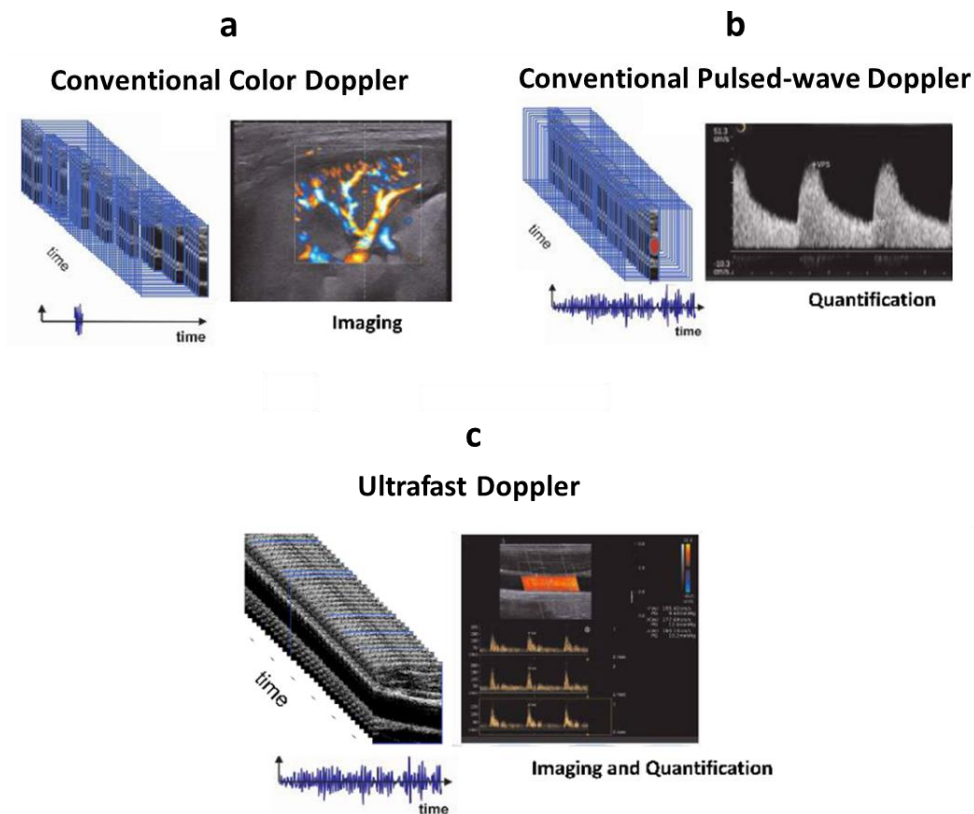


Figure 3.4 - Conventional Doppler imaging vs Ultrafast Doppler Imaging. (a) Conventional Color Doppler imaging allowing 2-D blood flow imaging. (b) Conventional Pulsed-Wave Doppler allowing for velocity quantification in one single location. (c) Ultrasensitive Doppler imaging allowing for imaging and velocity quantification in the full image. (Taken from (Errico 2016)).

Conceptually, there is no difference between the way the B-mode ultrafast imaging and the way the ultrafast sensitive Doppler imaging are conceived. Both techniques rely on plane- or diverging-wave emission and coherent sum of all the backscattered echoes is used to reconstruct the ultrasound image. Using a compounded ultrafast Doppler sequence could lead to a better contrast-to-tissue ratio (CTR), and therefore increasing the Doppler quality. The maximum number of angles that can be used to compute an image is limited by the acquisition pulse repetition frequency, related itself to the targeted Doppler velocity. With ultrafast acquisition frame rate (up to 20,000 frames per second), Doppler images can be acquired ten times faster than with the conventional Doppler approaches, improving sensitivity without scarifying neither the spatial nor the temporal resolutions.

The breakthroughs introduced by the ultrasensitive Doppler imaging made the ultrafast imaging enter the imaging field as an emerging full-fledged imaging modality for its capability to detect, with high spatiotemporal resolution and high sensitivity, subtle blood volume variation in small vessels.

3.4.2 Functional ultrasound imaging

Functional ultrasound (fUS) is a method based on ultrasensitive Doppler to measure local changes in blood volume. Neuronal activity results in increased blood volume through local capillaries and its increased perfusion can be detected by ultrasensitive power Doppler. The latter is sensitive enough to detect blood flow down to $\sim 1\text{mm}\cdot\text{s}^{-1}$ blood flow speed with a spatial resolution of $250\ \mu\text{m}$. In other words, fUS can solve in resolution down to arterioles ($10\text{-}250\ \mu\text{m}$), and can detect blood flow down to capillaries ($0.5\text{-}1.8\ \text{mm}\cdot\text{s}^{-1}$ (Hudetz 1997)). Indeed, the smallest vessel size delineated by Ultrafast Doppler imaging is limited by the spatial resolution λ (wavelength) of $250\ \mu\text{m}$ with our imaging system. Therefore, the smallest vascular path will appear as a $250\ \mu\text{m}$ wide vessel on the image. But this does not represent a threshold for detection, as scatterers (red blood cells) are much smaller, and it may be possible to detect vessels smaller than $250\ \mu\text{m}$ as long the blood flow speed is high enough and the red blood cells are numerous enough.

Repeating the acquisition of such ultrasensitive Doppler images over time enables to follow flow dynamics in such vessels modulated by local neuronal activity. To attain ultrasensitive Doppler information, this approach must be combined with an accumulation step. This step consists in exploiting hundreds of times, samples acquired at ultrafast frame rates during periods smaller than the typical brain hemodynamics observation time (typically 1 s).

In our laboratory, we have the chance to develop fUS sequences on programmable scanners (Vantage, Verasonics and Aixplorer®, SuperSonic imagine) and by modifying the emission, acquisition and beamforming parameters we can perform experiments at different acquisition frame rates, to preserve the high temporal resolution to spatially resolve the cerebral structures under investigation. Such software-based architecture enables programming of custom transmit/receive sequences where the frame rate of each acquisition can reach 20 kHz.

To date, the elevated sensitivity of fUS allows (i) to track the spatiotemporal dynamics of the activation within the rat brain following whisker stimulation or during induced epileptic seizures, presented in **Figure 3.5**, (Macé et al., 2011), as well as (ii) to detect odor-evoked stimulation (Osmanski et al., 2014a), and more remarkably (iii) to map functional connectivity in the living rat brain with a much higher spatiotemporal resolution than fMRI (Osmanski et al., 2014) (Sieu et al., 2015), presented in **Figure 3.5**.

The implementation of ultrasensitive Doppler imaging has been moving forward paving the way to human applications. A very first non-invasive study has been able to retrieve vascular resistivity maps of the brain in newborns through the fontanels, attaining the discrimination between venous and arterial flow (Charlie Demené et al. 2014). In this case, the method was facilitated by the presence of a pre-existing anatomical soft window in the infant, the fontanels. The same facilitation applies to all studies available today where animals had to go through a craniotomy (rat) (Sieu et al. 2015), or thinned-skull window surgery (rat) (Osmanski et al. 2014). Even using ultrafast ultrasound imaging, the need of contrast agent (Errico et al. 2015) or the complete elimination or reduction of the thickness of the skull are taken as the only options so far to prevent the bone from hindering the penetration of the ultrasonic waves into

the brain. For this reason, and because there is a real medical need, we decided that tumor surgery was a good condition to test the ability of fUS technique to detect functional areas.

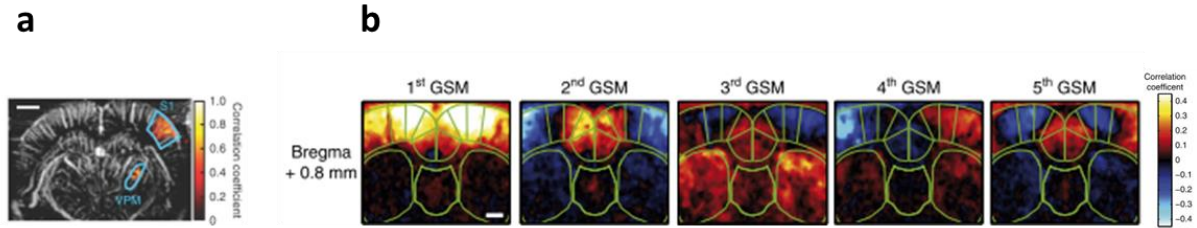


Figure 3.5 – fUS imaging of the rat brain. (a) fUS of the rat brain aiming to the detection of the sensory-motor cortex activation when stimulating the left whisker. An increase of $\sim 10\%$ in the Power Doppler signal was detectable in comparison with the baseline. (Taken from (Macé et al., 2011)) (b) Anticorrelated fUS connectivity patterns reveal distinct functional networks in the rat brain. Five global spatial modes (GSMs), representing reproducible connectivity patterns. (Taken from (Osmanski et al., 2014))

After performing ultrafast imaging intraoperative shear wave elastography for in-vivo measurements of human brain tumor elasticity in the previous chapter, we are now willing to use ultrafast ultrasound imaging to map brain functional activity on adults during brain surgery.

3.5 Development of intraoperative fUS in humans

In this section, the developments necessary to the fUS technique adaptation to intraoperative functional imaging in human will be presented.

3.5.1 Intraoperative Ultrafast Doppler

In order to use the fUS technique for intraoperative functional imaging in human, we had to work on ultrasound acquisition sequences and adapted spatiotemporal clutter filtering.

3.5.1.1 Ultrasound acquisitions

The use of ultrasound imaging arrays allows the transmission of ultrasonic waves and the reception of the backscattered echoes on the same transducer. Ultrasound images were acquired with an ultrafast ultrasonic device (Aixplorer®, Supersonic Imagine, Aix-en-Provence, France) driving a linear array (SL10-2, Supersonic Imagine, Aix-en-Provence, France, 6 MHz central frequency, 192 elements).

One dedicated Ultrafast ultrasound sequence that relied on compound plane-wave imaging (Montaldo et al. 2009) was used to image the adult brain during surgery. This sequence attempt to optimize the trade-off between frame rate and resolution. We aimed to perform functional imaging, therefore we were interested in imaging small vessel where the blood flow is less than 5 cm/s and a frame rate of 500 Hz is enough to correctly sample the data. As a consequence, with this frame rate value imposed by the blood flow itself, we chose a 6-angle ($-3^\circ, -3^\circ, 0^\circ, 0^\circ, +3^\circ, +3^\circ$) compound imaging for slow blood flows. The ultrasound sequence was calibrated with the probe on a certified calibration setup and the acoustic parameters were far below the acoustic

intensity limits recommended by the Food and Drug Administration (FDA guidance 510k-Track 3). The acoustic parameters of this ultrasound sequence were as follows: MI = 0.67 (<1.9), ISPTA = 180 mW/cm² (<720 mW/cm²) and TIS = 2.4 (<6).

The different steps of an ultrafast Doppler sequence were described in **Figure 3.6**.

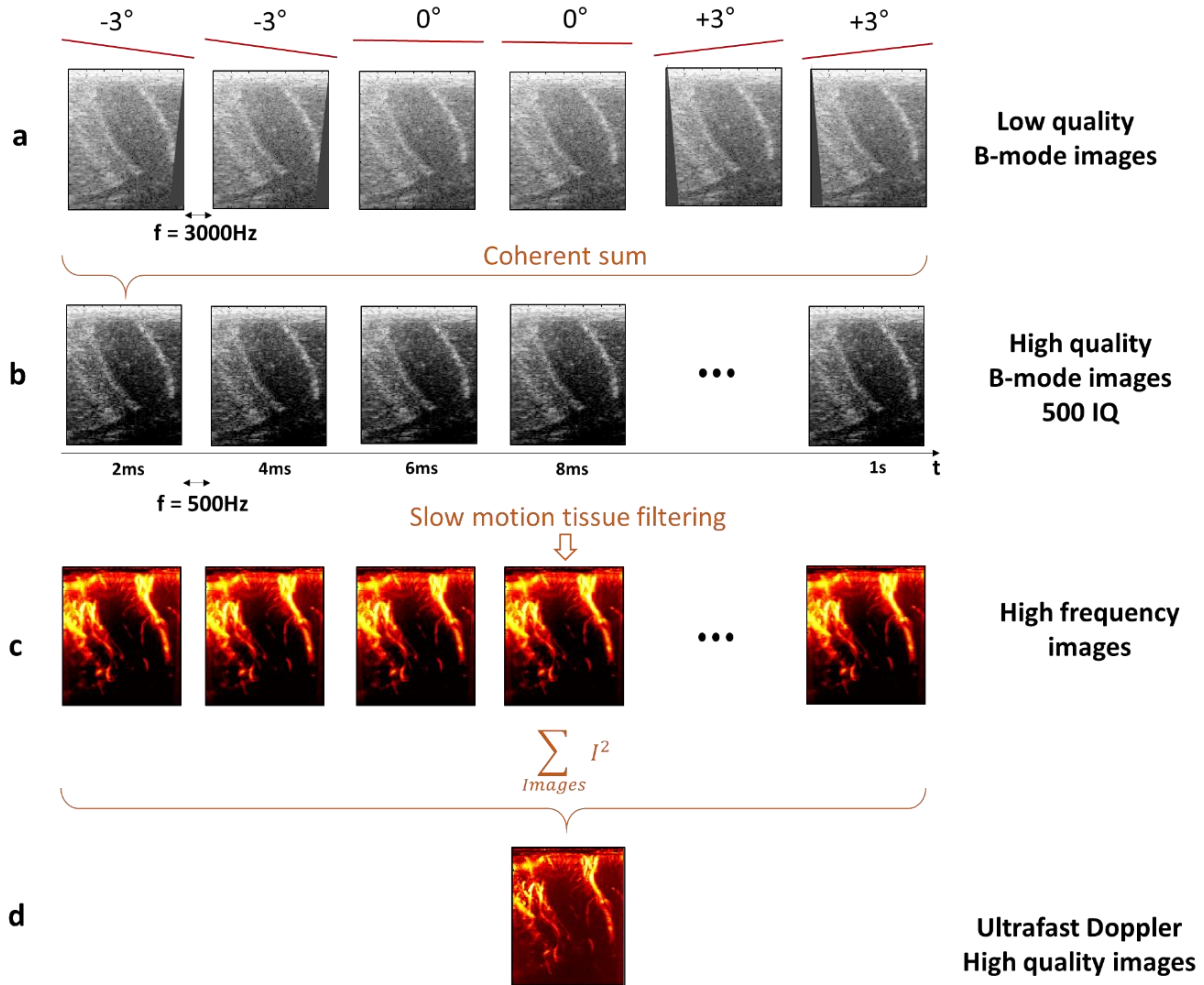


Figure 3.6 - High-resolution sequence for ultrafast Doppler acquisition. (a) An SL 10-2 probe emits an ultrasound sequence composed of six tilted plane waves (with angles $-3^\circ, -3^\circ, 0^\circ, 0^\circ, +3^\circ, +3^\circ$) at the firing frequency of 3,000 Hz. The six complex images obtained are then coherently added to form one higher contrast B mode image. (b) This sequence is repeated at 500 Hz (1/6 of 3,000 Hz) during 1 second, giving a stack of 500 compound B mode images. (c) This stack of images is then filtered to eliminate slow motion tissue from the image and obtain Doppler frames. (d) After summation of the intensity of all the Doppler frames, a final very high quality Ultrafast Doppler image is obtained.

For each compounded frame, a set of tilted plane waves (Montaldo et al. 2009) was emitted; for each tilted plane wave emitted, RF data were collected by the transducer and beam formed as an in-phase/quadrature (IQ) image (**Figure 3.6 a**). These complex images were coherently summed together to generate a compound frame. This operation was repeated at a frame rate of 500 Hz (high resolution) during 1 second, to obtain a stack of ultrafast compound frames $s(x,z,t)$ (**Figure 3.6 b**) where x is the lateral dimension along the transducer array, z is the depth inside the medium, and t is the time. As the stack of ultrasound images was the summation of the

backscatter echoes recorded from the red blood cells (RBC) and the tissue, the ultrasound images (\mathbf{x}, z, t) can be decomposed as:

$$s(\mathbf{x}, z, t) = s_{tissue}(\mathbf{x}, z, t) + s_{blood}(\mathbf{x}, z, t)$$

Equation 3.1 – Decomposition of ultrafast compound frames. $s_{tissue}(\mathbf{x}, z, t)$ and $s_{blood}(\mathbf{x}, z, t)$ are respectively the signals coming from the tissue and from the blood (red blood cells).

In order to separate the blood signals from the tissue (**Figure 3.6 c**), we implemented a spatiotemporal filter based on the singular value decomposition of the images stack (more details are discussed in the next section). After summation of the intensity of all the Doppler frames, a final very high quality Ultrafast Doppler image was obtained (**Figure 3.6 d**).

Regarding the type of filter for slow motion tissue filtering, we choose to use the singular value decomposition (SVD). This spatiotemporal clutter filter is described in the next section.

3.5.1.2 Spatiotemporal clutter filtering

In order to obtain ultrasensitive Doppler maps to do ultrasound functional imaging, backscattered echoes should be post-treated. After digital parallel beamforming, ultrasound images are made of signals coming from the tissues and from the blood flow (i.e. red blood cells). Subsequently, to recover only the signal coming from the blood flow, an intermediate clutter filtering step is necessary. Many filters including finite impulse response (FIR) (Willemetz et al. 1989) and infinite impulse response (IIR) (Tysoe and Evans 1995) high-pass filter can be applied on the beamformed images to recover the red blood cells signal. Both filters rely on the assumption that no Doppler spectrum overlap occurs between the tissue and the blood signal once they have different spectral properties. This assumption is not completely correct since, most of the times the spectra do overlap. In fact, the spectral overlapping region includes information of the low blood velocity that correspond to the small vessel hemodynamic. Due to this overlapping, the use of these Fourier-based clutter filters can cut important blood flow information. For this reason, a new clutter filtering approach (C. Demené et al. 2015) was developed for the ultrasensitive Doppler imaging taking benefit of different motion type spatial properties.

This spatiotemporal clutter filter is based on the singular value decomposition (SVD) or principal component analysis (**Figure 3.7**). In this approach, the backscattered beamformed images $s(\mathbf{z}, \mathbf{x}, t)$ are considered as a composition of $n_x \times n_z \times n_t$ spatiotemporal samples, with n_x the number of samples in lateral distance, n_z in depth, and n_t in time. Then, by considering a Casorati matrix (Candes, Sing-Long, and Trzasko 2013) (a matrix whose columns comprise vectorized frames of the image series), the singular value decomposition is a raw data matrix \mathbf{S} of dimensions $(n_z \times n_x \times n_t)$, where:

$$\mathbf{S} = \mathbf{U}\Delta\mathbf{V}^*$$

Equation 3.2 - Singular value decomposition of \mathbf{S} . Δ is a non-square diagonal matrix, \mathbf{U} and \mathbf{V} are orthonormal matrices respectively corresponding to the spatial and temporal singular vector of \mathbf{S} .

In addition, the covariance matrix of \mathbf{S} is calculated, and this orthogonal representation allows for the extraction of the respective eigenvalues (λ_i) and eigenvectors ($A_i, A_i = U_i \otimes V_i$). In each representation, each eigenvector is weighted by each eigenvalue.

In this decomposition, the tissue displacement is mainly contained in the first couples of singular values and vectors, representing a high spatiotemporal coherence (**Figure 3.7**, for $1 < i < 50$). On the contrary, the blood signal is depicted in the couples of eigenvalues and vectors exhibiting a much lower spatiotemporal coherence on ultrasonic images (**Figure 3.7**, for $51 < i < 500$).

Figure 3.7 summarizes the whole SVD process applied on one patient data.

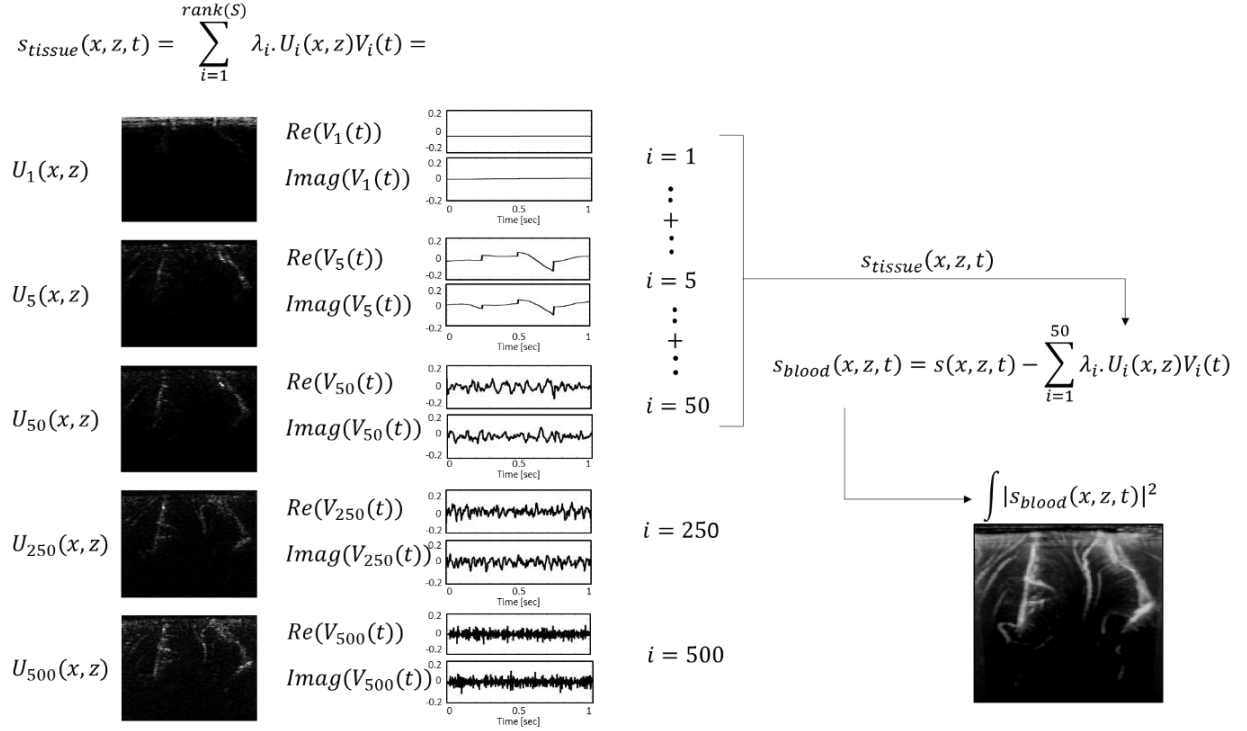


Figure 3.7 - Singular Value decomposition (SVD) of ultrasonic signal. The 3D ultrasonic acquisitions are arranged to have two spatial components representing the axial and lateral direction ($U(x, z)$) and a single time dimension consisting in the ultrasound acquisition duration ($V(t)$). By removing the 50th first Eigen vectors, in the case of intraoperative adult brain data, the signal coming from the tissue is suppressed and the energy of the remaining signal give a good quality power Doppler image of the brain vascularisation.

The blood signal can then be extracted, by filtering the tissue signal, through empirically thresholding the eigenvalue λ_i or the eigenvector A_i . In our case, as it is presented for one patient in **Figure 3.7** we chose a cut of value $i=50$ to differentiate the tissue and the blood signal, this value was empirically found after analyze of data from several patients. Blood signal can then be calculated as follow:

$$s_{blood}(x, z, t) = s(x, z, t) - s_{tissue}(x, z, t)$$

Equation 3.3 - Blood flow signal using the spatiotemporal clutter filter, where $s_{tissue}(x, z, t) = \sum_{i=1}^{\text{rank}(S)} \lambda_i U_i(x, z) V_i(t)$, and where $\text{rank}(S)$ is exactly the number of non-zero λ_i .

Then, the Power Doppler signal can be calculated as the average intensity of the Doppler signal in each pixel:

$$Power\ Doppler = \int |s_{blood}(x, z, t)|^2$$

Equation 3.4 - Power Doppler signal equation after spatiotemporal clutter filtering.

SVD applied on the IQ data allowed us to take advantage of plane wave transmission and cancel all spatially coherent motion artefacts (vessel pulsatility and vibrations) for optimized CBV mapping. We wish to underline that the robustness of the SVD algorithm is still under investigation. This new way of cluttering the signals originating from slowly moving tissue remains still a very empirical study. There is ongoing work in our laboratory to find an automatic thresholding method.

We presented the design of the ultrasensitive Doppler sequence and the way we processed the data, in the next section, we present how to perform functional ultrasound by using ultrasensitive Doppler.

3.5.2 Intraoperative functional ultrasound

Repeating the acquisition of ultrasensitive Doppler images overtime enables to follow flow dynamics in the small vessels modulated by local neuronal activity. Patients were asked to performed one adapted task in a block design paradigm, alternating six blocks of reference conditions and five blocks of task, each block lasting 20s (**Figure 3.8**) during ultrafast ultrasound acquisition. To evaluate one functional area, 220s were necessary, including 55 ultrasound acquisitions. One ultrasound acquisition lasts four seconds: one second for acquisition (one heart cycle) and three seconds for data transfer and recording.

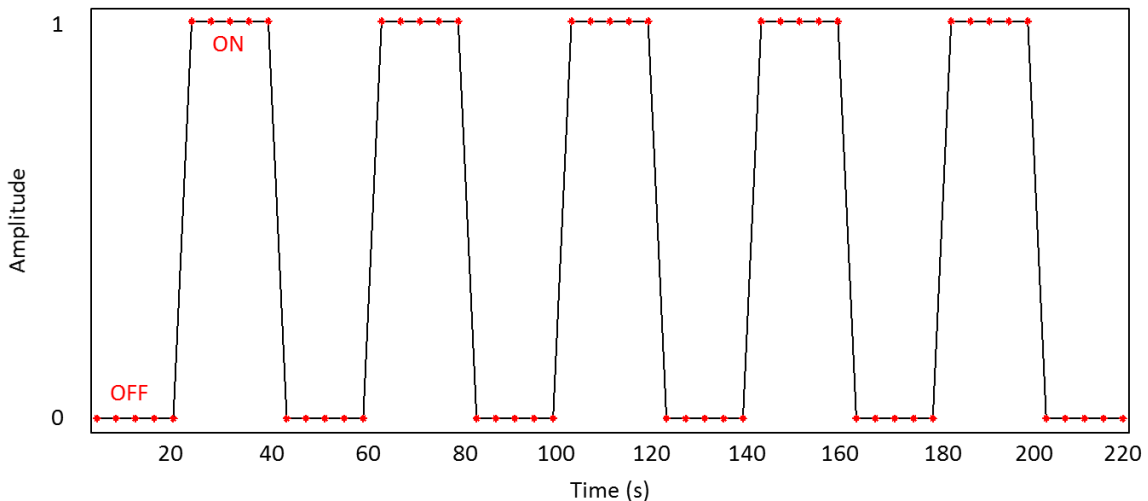


Figure 3.8 – Stimulation pattern for functional ultrasound imaging. The stimulation pattern (black line) consisted of 20s ON and 20s OFF repeated 5 times and finishing with one OFF section. Each red dot represent a 1s ultrasound acquisition.

The computation and thresholding of the activation maps is discussed in the next paragraphs.

3.5.2.1 Computing the activation maps

The chosen stimulus resulted in a steady increase in blood volume in the corresponding brain functional area, with increases in the power Doppler signal during the stimulus. Maps of activated pixels were built showing the correlation coefficient r (Equation 3.5) between the power Doppler signal and the temporal pattern of the stimulus (Figure 3.8).

Activation maps are maps of the Pearson's product-moment correlation coefficient r between the temporal pattern of the stimulus and the Power Doppler signal for each pixel:

$$r = \frac{\sum_{i=1}^{N_t} (s_{blood}(t_i) - \hat{s}_{blood})(A(t_i) - \hat{A})}{\sqrt{\sum_{i=1}^{N_t} (s_{blood}(t_i) - \hat{s}_{blood})^2} \sqrt{\sum_{i=1}^{N_t} (A(t_i) - \hat{A})^2}}$$

Equation 3.5 – Pearson's product-moment correlation coefficient r between the task pattern $A(t)$ and the power Doppler $s_{blood}(t)$ signal for each pixel. In this equation, $\hat{}$ designates the mean value of the variable.

Hemodynamic response (HR) (Figure 3.9) allows the rapid delivery of blood to active neuronal tissues. However, the time-to-peak ($\sim 5s$) and the time to return to homeostatic level ($\sim 5s$) were integrated in the calculation, to take into account the delay between the stimulus and the blood supply. The stimulation pattern (Figure 3.8) was temporally moved with a lag of 5s compare to the real stimulus start to fit with the blood volume variations.

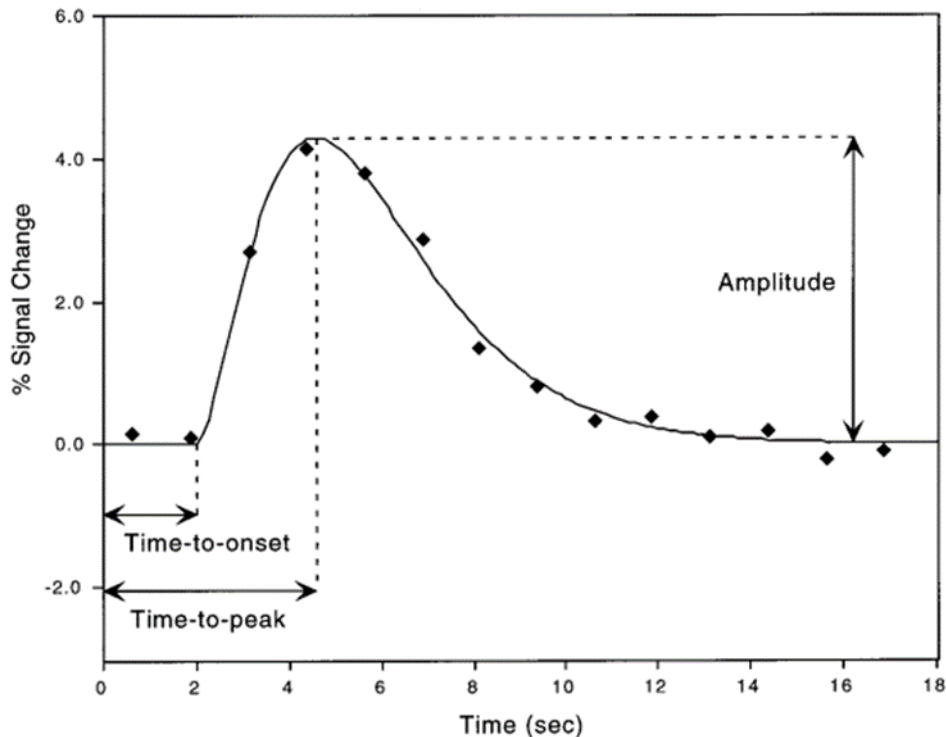


Figure 3.9 – Hemodynamic response profile. After one stimulus ($t=0s$), about 2 seconds are necessary to observe a signal increase (Time-to-onset), and about 5s to reach the maximum value (Time-to-peak). This signal increase gives evidence of local blood flow increase to meet neuronal activity. After the peak, the signal decrease indicates that as the needs of the neuronal activity are met, blood flow returns to homeostatic levels. (Figure Taken from (Miezin et al. 2000))

3.5.2.2 Thresholding the activation map

The goal of this subsection is to determine if and where a reliable activation is present in the imaging plan. Therefore, we have to find a threshold over which the activation (correlation coefficient r) can be considered significant. For five cycles (ON/OFF) and one final OFF, the time course is composed of 55 independent time points ($N_t = 55$ ultrafast ultrasound acquisition of 1s insonification). We used Fischer's transform to link z scores and the Pearson's product-moment correlation coefficient r :

$$z = \frac{\sqrt{N_t - 3}}{2} \cdot \arctan(r)$$

Equation 3.6 - Fischer's transform.

We chose a level of significance of $z > 3.1$ (corresponding to $p < 0.001$, one tailed test), which corresponds to $r > 0.41$ according to the following formula:

$$r > \tanh\left(\frac{z}{\sqrt{N_t - 3}}\right)$$

Equation 3.7 – Threshold value for the Pearson's product-moment correlation coefficient r .

This threshold value was used for all the activation map presented in this chapter. For visualization of the activation map, the correlation map was color-coded and superimposed on the ultrasensitive Doppler image.

In the next section, we will use the ultrasound sequences and the signal processing techniques presented in this section to perform intraoperative fUS in humans.

3.6 Intraoperative fUS pilot clinical study

In this section, we present the results of the pilot clinical trial we conducted on 33 adults to determine the ability of fUS to be a new neurofunctional imaging modality in human.

3.6.1 Cohort of patients

We conducted a pilot clinical study on 33 adults (19 women, 14 men, aged 24-64, mean 42) in La Pitié Salpêtrière hospital in Paris, in collaboration with the neurosurgeons Dr. Laurent Capelle and Dr. Dorian Chauvet. We wrote a biomedical research protocol and our patient are registered in Clinical Trials (Protocol C14-66: Intraoperative Functional Ultrasound (FUSIMAGINE)). The clinical investigation (N° ID-RCB 2015 A00661-48) was accepted by French regulatory agencies (ANSM, reference B150800-31) and by the Comité de Protection des Personnes CPP Ile de France VI (CPP n° 72-15). All patients gave their informed consent and all ultrasound experiments were performed in accordance with this ethics committee. All patients had low grade gliomas and were included as intraoperative functional mapping was planned to be used to remove their tumors.

3.6.2 Surgery and anesthesia

Local anesthesia with intravenous sedation (propofol, remifentanyl) was chosen for 27 patients undergoing surgery with intraoperative electrocortical simulation mapping (ESM). In these cases, local anesthesia was performed only during cranial flap opening and closing and patients did not receive any sedative during the ultrasound acquisition. 6 more patients had surgery under general anesthesia (propofol, sufentanyl, sevofluran) and ESM was performed while they were unconscious. Before imaging the patient, craniotomy and durotomy were performed on the appropriate site to further proceed to lesion resection.

For five patients, surgical complications prevented from performing fUS during the surgery: prolonged seizure at the very beginning of the ESM, dramatic difficulties for the patient to talk and think (issues to talk was the only ESM tag), very intense venous hemorrhage at the slightest electrocortical stimulation (ESM was not possible), the patient did not manage to wake up during the surgery and hematoma formation dissuaded from doing ESM, no functional area was detected by ESM. Those five patients were excluded from further analysis.

3.6.3 Gold standard for intraoperative functional mapping

Low grade gliomas are known to often extend into highly functional areas and modify the usual cortical functional anatomy, therefore intraoperative electrocortical stimulation mapping (ESM) is commonly used to assess functional cortical reorganisation. Though ESM presents some risks, especially intraoperative seizures, it is nowadays a gold standard for intraoperatively superficial functional cortical mapping (Roser and Liebsch 2016; Ille et al. 2015). We used this technique as a reference in our study.

Bipolar cortical stimulation was performed with an electrical stimulator (ball tip probe, Ball tip $\varnothing = 2.0$ mm, 1–15 mA; inomed Medizintechnik GmbH, Germany). 4.5 to 15 mA were necessary to have a response for patients under general anesthesia and 1.5 to 5.5 mA for patients under local anesthesia. Each stimulation train was limited to 2 to 4 seconds. Motor response, speech arrest, particular sensations and experiences were documented. The awake patient was able to communicate and perform tasks that depended on the location of the lesion and on the nearby functional cortex. For patients under general anesthesia, motor responses were observed by a third person. Based on the results, tags were placed over each stimulation site (central point between the electrode tips).

An average of two cortex simulations were performed for each patient. Motor cortex localization was performed by elicitation of a movement in response to electrocortical stimulation. Sensory cortex localization was ascertained by localized paresthesia reported by patients in response to primary somatosensory cortex stimulation. Localization of language/speech cortex was mostly elicited, given the cortical areas stimulated, by speech arrest and anomia in response to intraoperative cortical stimulation.

3.6.4 Intraoperative ultrasound imaging

One to three trials of fUS images were acquired for every patient; one trial consisting of blocks of rest and task periods for one chosen stimulus. A full trial session for one patient, testing in mean 2 different tasks, last about 8 minutes in total.

ESM data were used for ultrasound probe positioning on a targeted functional area. With the help of the neurosurgeon and the speech therapist, we had a very short time to choose the task to study after ESM. The ultrasound probe was placed in sterile probe cover (**Figure 3.10 a**) filled with ultrasound gel and placed directly on the cortex after skull and dura matter opening. To guarantee its immobility, the ultrasound probe was fixed to a custom autoclavable stainless steel articulated arm (**Figure 3.10 a**). Under the supervision of one speech therapist, patients were then asked to perform the specific task corresponding to the ESM tag in the case of a local anesthesia (awake patient) (**Figure 3.10 b**). In the case of general anesthesia a third person, was asked to move or stroke the limb segment of interest.

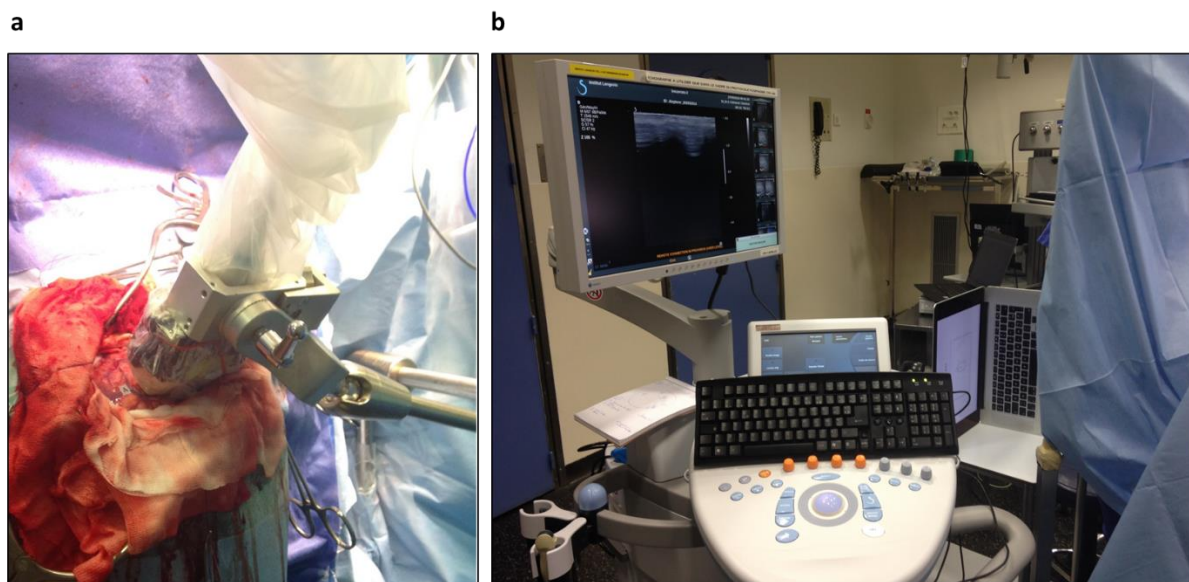


Figure 3.10 – Organization in the surgical room. (a) The ultrasound probe is placed in a sterile probe cover, put on the brain surface and fixed with a custom autoclavable stainless steel articulated arm during the ultrasound acquisition. (b) The ultrasound scanner is placed right next to the surgeon, in the surgical part of the room (delimited by the blue surgical drape). The speech therapist and the awake patient are on the other side of the surgical drape and can perform exercises (example here: naming exercise based on one computer).

3.6.5 Functional areas studied

Among the 28 patients for whom ultrasound acquisitions were feasible, 51 tasks were tested (a mean of 2 tested areas per patient). fUS succeeded to detect and map the corresponding functional areas in 48 cases when the ultrasound probe was properly positioned on the ESM tag. In 3 cases the ultrasound probe was imperfectly positioned (**Table 3.1**), therefore no functional area was detected. Depending on the lesion localization, we were able to localize functional areas

corresponding to 16 different tasks, including hand, index, thumb, wrist, elbow and mouth for both motor and sensory tasks (Table 3.1).

	(a) Good probe positioning : Successful tasks detection				(b) Imperfect probe positioning			
			Correlation				Correlation	
	Tasks	Number	Mean correlation in the functional area ($r > 0.41$)	Mean correlation outside the functional area	Tasks	Number	Mean correlation in the functional area ($r > 0.41$)	Mean correlation outside the functional area
					Wrist/elbow sensory	1	None	0.101
Tasks of interest	Hand motor	9	0.498	0.107				
	Hand sensory	4	0.515	0.131				
	Index motor	3	0.520	0.132				
	Index sensory	2	0.529	0.146				
	Thumb motor	1	0.526	0.192	Thumb motor	1	None	0.035
	Thumb sensory	2	0.483	0.119				
	Thumb/index motor	3	0.494	0.111				
	Thumb/index sensory	1	0.570	0.101				
	Ring finger/little finger sensory	1	0.507	0.114				
	Wrist motor	2	0.521	0.131				
	Wrist sensory	1	0.472	0.186	Wrist sensory	1	None	0.079
	Elbow/biceps sensory	1	0.500	0.184				
	Mouth motor	8	0.508	0.124				
	Mouth sensory	3	0.505	0.121				
	Repetition (sentences)	1	0.503	0.154				
	Count (1 to 10)	1	0.461	0.073				
Total	43	0.507	0.133	Total	3	None	0.071	

Table 3.1 - List of the different tested tasks depending on the lesion location. The number of time one task was tested is indicated in the Number column. For every tested task, the mean correlation between the task pattern and the Doppler signal is documented, along with the mean correlation calculated outside the functional area as a reference correlation value. **(a)** The ultrasound probe was properly positioned on the ESM tag, leading to a successful detection of the corresponding functional area ($r > 0.41$). **(b)** The ultrasound probe was imperfectly positioned on the ESM tag (small cranial flap regarding to the probe acoustic footprint), therefore no functional area was detected.

3.6.6 Deep cortex activation maps

In the 48 cases when the ultrasound probe was properly positioned on the ESM tag, we obtained in depth activation maps corresponding to the functional area. The context of the ultrasound acquisitions and the results are presented in **Figure 3.11** for one patient. Precise location of the task-related areas at the cortical surface was first determined by ESM. Then the ultrasound probe was placed on one chosen ESM tag during task-related stimulus (e.g. **Figure 3.11 a-b**). fUS acquisitions were performed during one heart cycle (1s) and repeated every 3s (**Figure 3.11 c**) during 220s, resulting in 55 power Doppler images. Stimulation resulted in a steady increase in blood volume in the associated cortical area, with a 20% increases in the power Doppler signal during the stimuli (**Figure 3.11 c**).

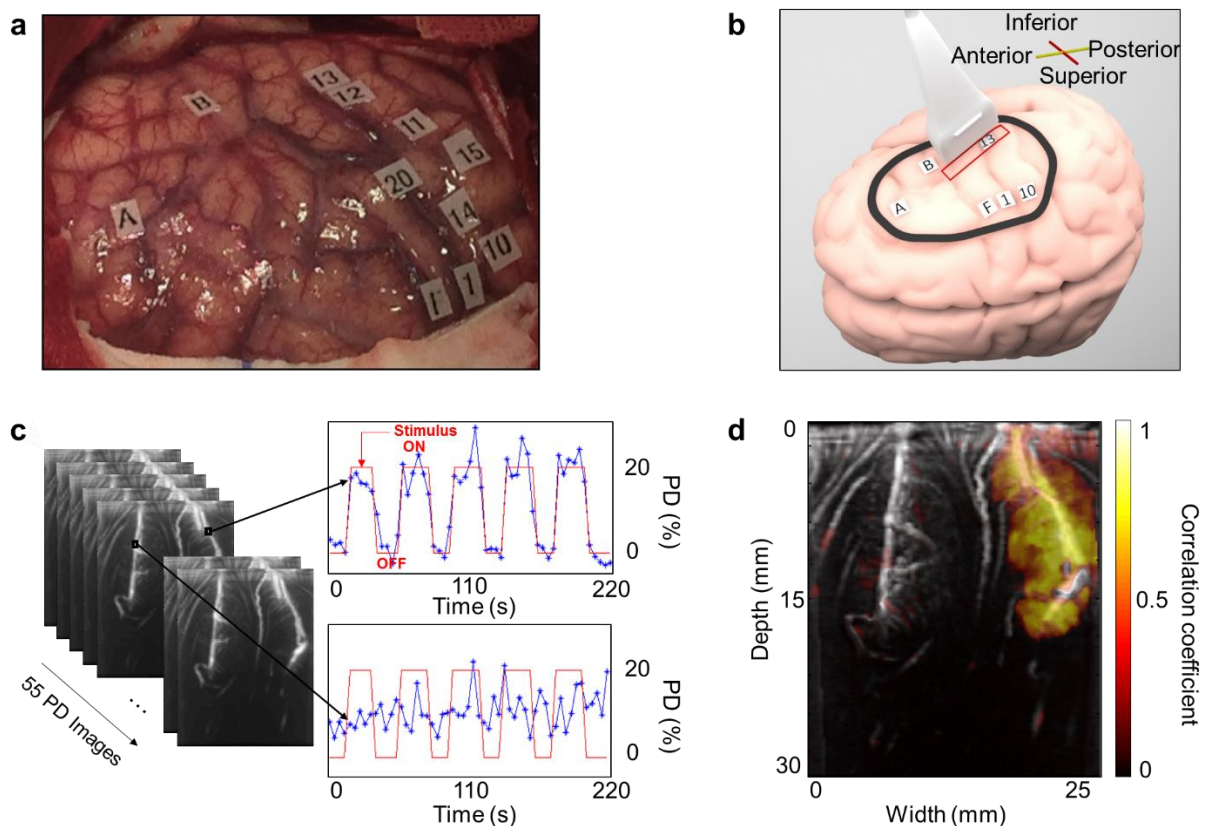


Figure 3.11 - Intraoperative fUS imaging of “mouth sensitive” evoked brain activation in one patient. (a) Superficial ESM activation map; letters give tumor position, number from 1 to 10 stand for motor cortex and numbers from 11 to 20 stand for somatosensory cortex. (b) Probe position on the cortex (red rectangle) on the “mouth sensory” ESM tag 13. Drawing of the brain was created by Alexandre Dizeux (postdoctoral researcher at Institut Langevin). (c) Power Doppler (PD) fUS images are acquired every 3s when the awake patient is doing the corresponding task (“mouth opening and closing”). This motor task was chosen to stimulate a sensitive area because the patient’s lips touching each other is a strong sensitive stimulation. The task pattern (red line) consisted of six blocks of reference conditions (OFF) and five blocks of task (ON). The power Doppler (PD) is plotted in percentage relative to baseline. Variations in blood volume during ultrasound acquisitions are presented in Supplementary video 1 for this task and this patient. (d) In depth activation map obtained for the task “mouth opening and closing” when the probe is on the “mouth sensory” ESM tag 13.

Maps of activated pixels were built showing the correlation coefficient r between the power Doppler signal and the stimulus temporal pattern. Activation maps (**Figure 3.11 d**) showed a significant and localized correlation ($r > 0.41$) between power Doppler (PD) signal and task pattern during the task.

We demonstrated that intraoperative fUS on adults can map in depth the activation in response to a stimulus with ESM as the reference technique.

As a control test, for two different tasks we used fUS imaging to verify that no correlation ($r_{\text{correlation}} \gg 0.41$) between the Doppler signal and the contralateral task pattern was found in the brain region under the ESM tag corresponding to the initial task (spatial average $r_{\text{mean}} = 0.078 \pm 0.030$) (**Table 3.1**).

3.6.7 Intraoperative fUS sensitivity

Since 1937, an homunculus representation (Penfield and Boldrey 1937) has been adopted as a physical representation of the human body, located within the brain. A cortical homunculus is like a neurological map of the anatomical divisions of the body, where sensory and motor functional areas for one body part are facing each other (**Figure 3.12**). During the surgery, we were looking for such a situation to put the ultrasound probe astride sensory and motor functional areas corresponding to the same body part. However, this configuration is not easy to obtain during tumor surgery due to normal brain remodeling consecutive to growth tumor. We faced such a situation for one patient and the results are presented below.

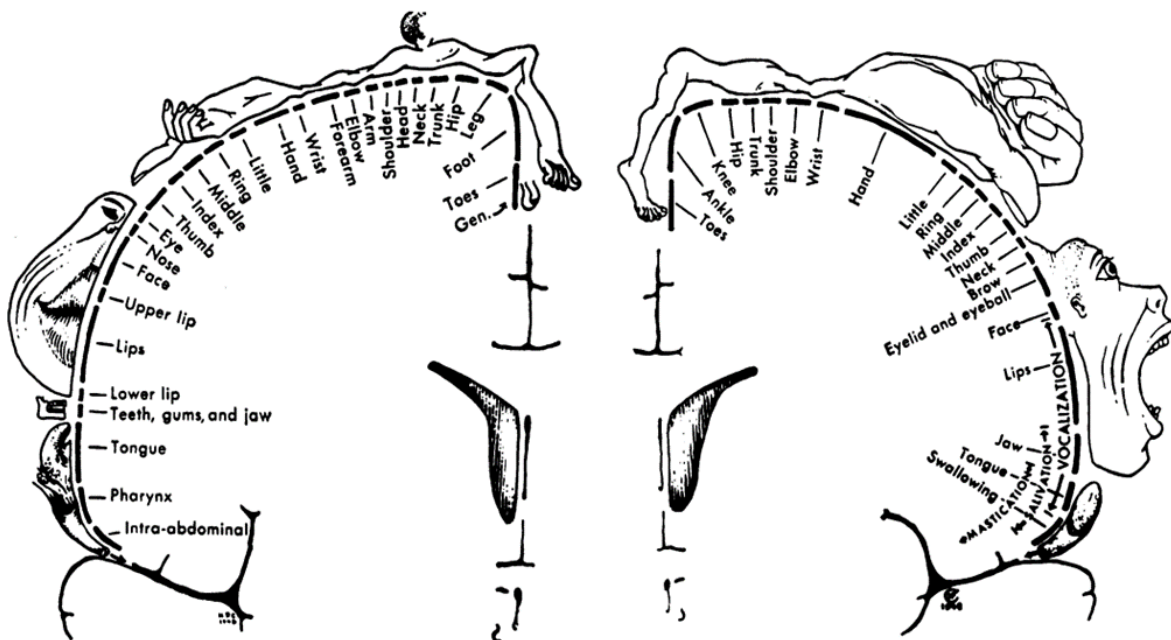


Figure 3.12 - The sensory (left) and the motor (right) cortical homunculi. This diagram represents two slices of cortex near the fissure of Rolando, running from the top of the head down toward the ear. The diagram indicates the location and amount of cortex devoted to each part of the body. (Taken from (Penfield and Rasmussen 1950))

To verify that fUS imaging enables an accurate localization of functional areas, we positioned the probe astride two functional areas (**Figure 3.13 a-b**) concerning the same body part (finger in the example presented **Figure 3.13**), one in the somatosensory cortex, and the other in the motor cortex (**Figure 3.13 b**).

For the motor task, in depth activation maps reveal that, both motor and somatosensory cortex are implicated in the task (**Figure 3.13 c**). Whereas for the sensory task, activation maps reveal that only the somatosensory cortex is implicated in the task (**Figure 3.13 d**).

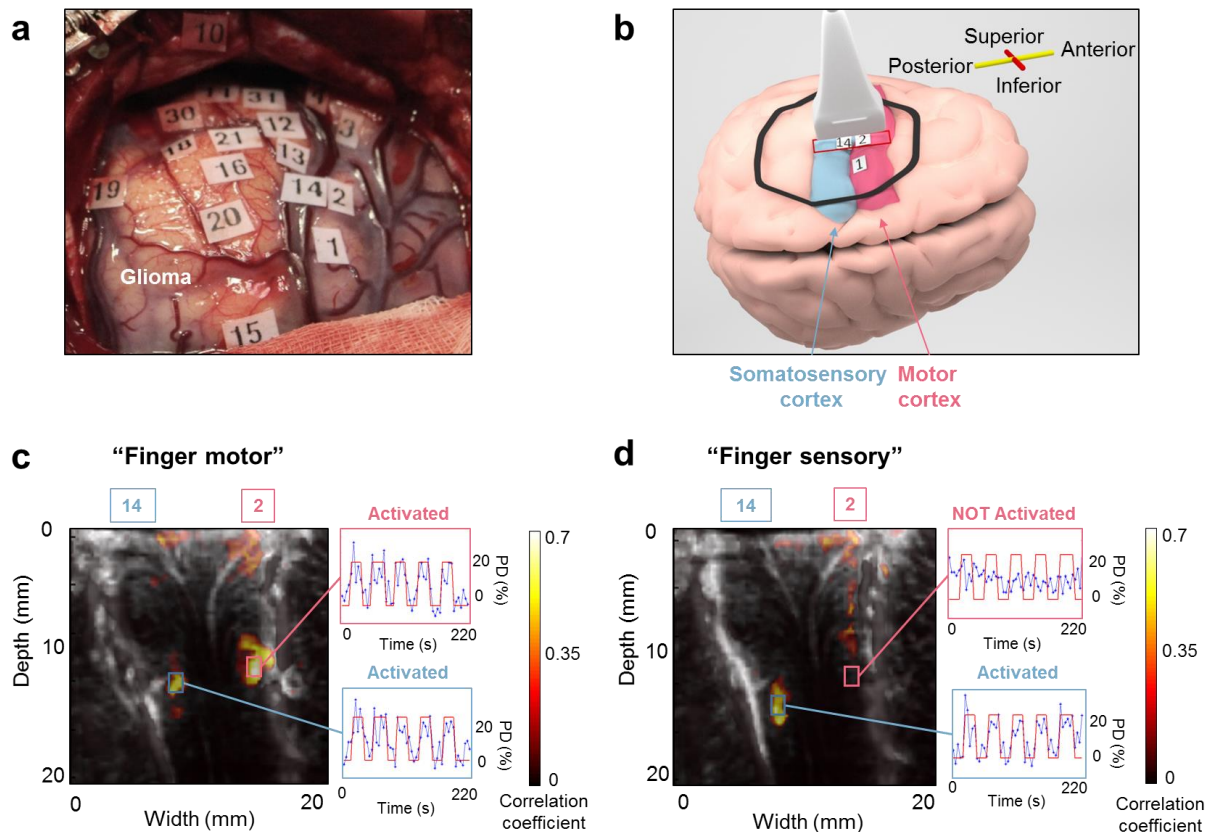


Figure 3.13 - Comparison between intraoperative functional imaging of motor and somatosensory cortex. (a) Superficial ESM activation map. Number from 1 to 10 stand for motor cortex and numbers from 11 to 20 stand for somatosensory cortex. (b) Probe position on the brain cortex (red rectangle). The probe is astride on the “2-5 fingers motor” (ESM tag 2) and “4-5 finger sensory” (ESM tag 14) for both activation map presented in (c) and (d). Drawing of the brain was created by Alexandre Dizeux (postdoctoral researcher in Institut Langevin). (c) In depth activation map obtained for the task “2-5 fingers motor”. The correlation map illustrates that both motor (ESM tag 2) and somatosensory (ESM tag 14) cortex are implicated in the task. (d) In depth activation map obtained for the task “4-5 fingers sensory”. The correlation map illustrates that only the somatosensory cortex (ESM tag 14) is implicated in this task.

We demonstrated that intraoperative fUS on adults can map in depth the activation in response to a stimulus with a sensitivity allowing differentiation of two neighboring functional areas.

3.6.8 Discussion

Determination of individual functional cortical mapping is essential to perform optimal surgery in highly functional areas, minimizing the risk of postoperative deficits. While accuracy of intraoperative ESM is high, key disadvantages can be challenged, such as protracted operative time and seizure risk. As an example, in our study ESM induced in 5 instances epileptic seizures, which were quickly medically stopped through cold physiologic serum injection. ESM can be stressful for the patient and in some cases cannot be performed, due to clinical considerations. Additionally, neurosurgeons do not normally stimulate within the depth of a non-opened sulcus (Krings et al. 2001) and therefore do not stimulate the whole cortex in depth. As for fMRI activation maps, the technique provides a non-invasive functional mapping used by the surgeon to plan lesion resection. However brain shift after dural opening remains a major issue when using MRI neuronavigation and the correlation between fMRI activation site and positive ESM sites is not always high. In this context, the ability of ultrafast ultrasound to intraoperatively map with a high SNR stimulus-based neuronal activations in deep cortex during brain surgery appears of great interest.

3.7 Chapter conclusion

In the past few years, functional ultrasound (fUS) has been validated as a novel neuroimaging modality in rodents. The objective of our work was to use the high spatiotemporal resolution and sensitivity of fUS to perform neurofunctional imaging on humans.

During brain tumor surgery, we had the perfect opportunity to test the ability of fUS to detect functional areas in humans since it is well known that the skull remains up to now a strong obstacle for ultrasound beam (Lichtenstein 2008). We carefully study existing functional imaging modality, both techniques based on direct detection of neurons electrical activity and techniques based on neurovascular coupling. A special attention was paid to intraoperative functional brain imaging modalities, to choose a robust gold standard. Then we developed ultrafast Doppler sequences and data processing for fUS imaging adapted to intraoperative functional imaging on humans.

We designed a biomedical research protocol in collaboration with the Pitié Salpêtrière neurosurgery department. We tested the fUS technique both on awake and anesthetized patients, and in both cases, fUS was able to detect functional areas activation in response to stimulus with a 20% increase in blood volume, compared to the baseline. Sixteen different stimulus were tested (**Table 3.1**), and when the ultrasound probe was correctly positioned on the corresponding ESM tag, fUS always succeed in functional area localization. We also performed control tests to verify that there was no correlation between the Doppler signal and the task pattern in case of contralateral stimulus. Finally, we demonstrated that intraoperative fUS was able to differentiate two neighboring functional areas (**Figure 3.13**) when the ultrasound probe was placed astride two different ESM tags.

We demonstrated that fUS imaging is able to identify, map and differentiate regions of brain activation during task-evoked cortical responses within the depth of a sulcus both on awake and

anesthetized patients. fUS imaging has the potential to become a full-fledged neuroimaging modality with major advantages for intraoperative use.

3.8 Chapter bibliography

- Attwell, David, Alastair M. Buchan, Serge Charpak, Martin Lauritzen, Brian A. MacVicar, and Eric A. Newman. 2010. “Glial and Neuronal Control of Brain Blood Flow.” *Nature* 468 (7321): 232–43. doi:10.1038/nature09613.
- Bercoff, J, G Montaldo, T Loupas, D Savery, Fabien Mézière, M Fink, and M Tanter. 2011. “Ultrafast Compound Doppler Imaging: Providing Full Blood Flow Characterization.” *IEEE Transactions on Ultrasonics, Ferroelectrics and Frequency Control* 58 (1): 134–47. doi:10.1109/TUFFC.2011.1780.
- Candes, Emmanuel J., Carlos A. Sing-Long, and Joshua D. Trzasko. 2013. “Unbiased Risk Estimates for Singular Value Thresholding and Spectral Estimators.” *IEEE Transactions on Signal Processing* 61 (19): 4643–57. doi:10.1109/TSP.2013.2270464.
- Charpak, Serge, and Bojana Stefanovic. 2012. “Shedding Light on the BOLD fMRI Response.” *Nature Methods* 9 (6): 547–49. doi:10.1038/nmeth.2039.
- Chen, Yu, Aaron D. Aguirre, Lana Ruvinskaya, Anna Devor, David A. Boas, and James G. Fujimoto. 2009. “Optical Coherence Tomography (OCT) Reveals Depth-Resolved Dynamics during Functional Brain Activation.” *Journal of Neuroscience Methods* 178 (1): 162–73. doi:10.1016/j.jneumeth.2008.11.026.
- Demené, C., T. Deffieux, M. Pernot, B. F. Osmanski, V. Biran, J. L. Gennisson, L. A. Sieu, et al. 2015. “Spatiotemporal Clutter Filtering of Ultrafast Ultrasound Data Highly Increases Doppler and fUltrasound Sensitivity.” *IEEE Transactions on Medical Imaging* 34 (11): 2271–85. doi:10.1109/TMI.2015.2428634.
- Demené, Charlie, Mathieu Pernot, Valérie Biran, Marianne Alison, Mathias Fink, Olivier Baud, and Mickaël Tanter. 2014. “Ultrafast Doppler Reveals the Mapping of Cerebral Vascular Resistivity in Neonates.” *Journal of Cerebral Blood Flow & Metabolism* 34 (6): 1009–17. doi:10.1038/jcbfm.2014.49.
- Doty, Robert W., and John R. Bartlett. 1981. “Chapter 4 - Stimulation of the Brain Via Metallic Electrodes.” In *Electrical Stimulation Research Techniques*, edited by MICHAEL M. PATTERSON and RAYMOND P. KESNER, 71–103. Academic Press. <https://www.sciencedirect.com/science/article/pii/B9780125474405500103>.
- Duffau, H. 2005. “Contribution of Intraoperative Electrical Stimulations in Surgery of Low Grade Gliomas: A Comparative Study between Two Series without (1985-96) and with (1996-2003) Functional Mapping in the Same Institution.” *Journal of Neurology, Neurosurgery & Psychiatry* 76 (6): 845–51. doi:10.1136/jnnp.2004.048520.
- Duffau, Hugues, Laurent Capelle, Nicole Sichez, Dominique Denvil, Manuel Lopes, Jean-Pierre Sichez, Ahmad Bitar, and Denis Fohanno. 2002. “Intraoperative Mapping of the Subcortical Language Pathways Using Direct stimulationsAn Anatomico-functional Study.” *Brain* 125 (1): 199–214. doi:10.1093/brain/awf016.
- Ebeling, U., U. D. Schmid, and H. J. Reulen. 1989. “Tumour-Surgery within the Central Motor Strip: Surgical Results with the Aid of Electrical Motor Cortex Stimulation.” *Acta Neurochirurgica* 101 (3–4): 100–107. doi:10.1007/BF01410522.

- Errico, Claudia. 2016. “Ultrasound Sensitive Agents for Transcranial Functional Imaging, Super-Resolution Microscopy and Drug Delivery.” Université Sorbonne Paris Cité. <http://www.theses.fr/2016USPCC013>.
- Errico, Claudia, Juliette Pierre, Sophie Pezet, Yann Desailly, Zsolt Lenkei, Olivier Couture, and Mickael Tanter. 2015. “Ultrafast Ultrasound Localization Microscopy for Deep Super-Resolution Vascular Imaging.” *Nature* 527 (7579): 499–502. doi:10.1038/nature16066.
- Fertziger, Allen P., and James B. Ranck Jr. 1970. “Potassium Accumulation in Interstitial Space during Epileptiform Seizures.” *Experimental Neurology* 26 (3): 571–85. doi:10.1016/0014-4886(70)90150-0.
- Gagnon, Louis, Amy F. Smith, David A. Boas, Anna Devor, Timothy W. Secomb, and Sava Sakadžić. 2016. “Modeling of Cerebral Oxygen Transport Based on In Vivo Microscopic Imaging of Microvascular Network Structure, Blood Flow, and Oxygenation.” *Frontiers in Computational Neuroscience* 10 (August). doi:10.3389/fncom.2016.00082.
- Gorbach, Alexander M., John Heiss, Conrad Kufta, Susumo Sato, Paul Fedio, William A. Kammerer, Jeffrey Solomon, and Edward H. Oldfield. 2003. “Intraoperative Infrared Functional Imaging of Human Brain.” *Annals of Neurology* 54 (3): 297–309.
- Grienberger, Christine, and Arthur Konnerth. 2012. “Imaging Calcium in Neurons.” *Neuron* 73 (5): 862–85. doi:10.1016/j.neuron.2012.02.011.
- Hudetz, A. G. 1997. “Blood Flow in the Cerebral Capillary Network: A Review Emphasizing Observations with Intravital Microscopy.” *Microcirculation (New York, N.Y.: 1994)* 4 (2): 233–52.
- Ille, Sebastian, Nico Sollmann, Theresa Hauck, Stefanie Maurer, Noriko Tanigawa, Thomas Obermueller, Chiara Negwer, et al. 2015. “Combined Noninvasive Language Mapping by Navigated Transcranial Magnetic Stimulation and Functional MRI and Its Comparison with Direct Cortical Stimulation.” *Journal of Neurosurgery* 123 (1): 212–25. doi:10.3171/2014.9.JNS14929.
- Keles, G. Evren, David A. Lundin, Kathleen R. Lamborn, Edward F. Chang, George Ojemann, and Mitchel S. Berger. 2004. “Intraoperative Subcortical Stimulation Mapping for Hemispheric Periolandic Gliomas Located within or Adjacent to the Descending Motor Pathways: Evaluation of Morbidity and Assessment of Functional Outcome in 294 Patients.” *Journal of Neurosurgery* 100 (3): 369–75. doi:10.3171/jns.2004.100.3.0369.
- Kim, Seong-Gi, and Kamil Ugurbil. 2003. “High-Resolution Functional Magnetic Resonance Imaging of the Animal Brain.” *Methods, Visualizing neural networks*, 30 (1): 28–41. doi:10.1016/S1046-2023(03)00005-7.
- Krings, T., M. Schreckenberger, V. Rohde, H. Foltys, U. Spetzger, O. Sabri, M. H. Reinges, et al. 2001. “Metabolic and Electrophysiological Validation of Functional MRI.” *Journal of Neurology, Neurosurgery, and Psychiatry* 71 (6): 762–71.
- Lavoisier, Antoine Laurent. 1920. *Mémoires sur le respiration et la transpiration des animaux*. Paris, Gauthiers-Villars. <http://archive.org/details/mmoioressurlere00lavo>.
- Lehéricy, Stéphane, Delphine Leclercq, Hugues Duffau, Pierre-François Van de Moortele, and Christine Delmaire. 2015. “Presurgical Functional Localization Possibilities, Limitations, and Validity.” In *Clinical Functional MRI*, 247–267. Springer. http://link.springer.com/chapter/10.1007/978-3-662-45123-6_9.
- Liao, Lun-De, Vassiliy Tsytsarev, Ignacio Delgado-Martínez, Meng-Lin Li, Reha Erzurumlu, Ashwati Vipin, Josue Orellana, et al. 2013. “Neurovascular Coupling: In Vivo Optical

- Techniques for Functional Brain Imaging.” *BioMedical Engineering OnLine* 12: 38. doi:10.1186/1475-925X-12-38.
- Lichtenstein, Daniel A. 2008. *General Ultrasound in the Critically Ill*. Springer Science & Business Media.
- Macé, Emilie, Gabriel Montaldo, Ivan Cohen, Michel Baulac, Mathias Fink, and Mickael Tanter. 2011. “Functional Ultrasound Imaging of the Brain.” *Nature Methods* 8 (8): 662–64. doi:10.1038/nmeth.1641.
- Miezin, F.M., L. Maccotta, J.M. Ollinger, S.E. Petersen, and R.L. Buckner. 2000. “Characterizing the Hemodynamic Response: Effects of Presentation Rate, Sampling Procedure, and the Possibility of Ordering Brain Activity Based on Relative Timing.” *NeuroImage* 11 (6): 735–59. doi:10.1006/nimg.2000.0568.
- Montaldo, G., M. Tanter, J. Bercoff, N. Benech, and M. Fink. 2009. “Coherent Plane-Wave Compounding for Very High Frame Rate Ultrasonography and Transient Elastography.” *IEEE Transactions on Ultrasonics, Ferroelectrics, and Frequency Control* 56 (3): 489–506. doi:10.1109/TUFFC.2009.1067.
- Mosso. 1881. *Ueber den Kreislauf des Blutes im menschlichen Gehirn...* Veit. <http://archive.org/details/ueberdenkreisla01mossgoog>.
- Ogawa, S, T M Lee, A R Kay, and D W Tank. 1990. “Brain Magnetic Resonance Imaging with Contrast Dependent on Blood Oxygenation.” *Proceedings of the National Academy of Sciences of the United States of America* 87 (24): 9868–72.
- Ojemann, George, Jeff Ojemann, E. Lettich, and M. Berger. 2009. “Cortical Language Localization in Left, Dominant Hemisphere.” *Collections* 112 (2): 316–26. doi:10.3171/jns.1989.71.3.0316@col.2.
- Osmanski, Bruno-Félix, Sophie Pezet, Ana Ricobaraza, Zsolt Lenkei, and Mickael Tanter. 2014. “Functional Ultrasound Imaging of Intrinsic Connectivity in the Living Rat Brain with High Spatiotemporal Resolution.” *Nature Communications* 5 (October): 5023. doi:10.1038/ncomms6023.
- Penfield, Wilder, and Edwin Boldrey. 1937. “SOMATIC MOTOR AND SENSORY REPRESENTATION IN THE CEREBRAL CORTEX OF MAN AS STUDIED BY ELECTRICAL STIMULATION.” *Brain* 60 (4): 389–443. doi:10.1093/brain/60.4.389.
- Penfield, Wilder, and Theodore Rasmussen. 1950. *The Cerebral Cortex of Man; a Clinical Study of Localization of Function*. Vol. xv. Oxford, England: Macmillan.
- Peterka, Darcy S., Hiroto Takahashi, and Rafael Yuste. 2011. “Imaging Voltage in Neurons.” *Neuron* 69 (1): 9–21. doi:10.1016/j.neuron.2010.12.010.
- Phelps, M. E., and J. C. Mazziotta. 1985. “Positron Emission Tomography: Human Brain Function and Biochemistry.” *Science* 228 (4701): 799–809. doi:10.1126/science.2860723.
- Richiardi, Jonas, Hamdi Eryilmaz, Sophie Schwartz, Patrik Vuilleumier, and Dimitri Van De Ville. 2011. “Decoding Brain States from fMRI Connectivity Graphs.” *NeuroImage, Multivariate Decoding and Brain Reading*, 56 (2): 616–26. doi:10.1016/j.neuroimage.2010.05.081.
- Roser, Florian, and Marina Liebsch. 2016. “Closer to the Edge—The Value of Intraoperative Brain Mapping.” *World Neurosurgery* 89 (May): 689–91. doi:10.1016/j.wneu.2015.11.104.
- Rossi, David J. 2006. “Another BOLD Role for Astrocytes: Coupling Blood Flow to Neural Activity.” *Nature Neuroscience* 9 (2): 159–61. doi:http://dx.doi.org.rproxy.univ-psl.fr/10.1038/nm0206-159.

- Sheth, Sameer, Masahito Nemoto, Michael Guiou, Melissa Walker, Nader Pouratian, and Arthur W Toga. 2003. “Evaluation of Coupling between Optical Intrinsic Signals and Neuronal Activity in Rat Somatosensory Cortex.” *NeuroImage* 19 (3): 884–94. doi:10.1016/S1053-8119(03)00086-7.
- Sieu, Lim-Anna, Antoine Bergel, Elodie Tiran, Thomas Deffieux, Mathieu Pernot, Jean-Luc Gennisson, Mickaël Tanter, and Ivan Cohen. 2015. “EEG and Functional Ultrasound Imaging in Mobile Rats.” *Nature Methods* 12 (9): 831–34. doi:10.1038/nmeth.3506.
- Tysoe, Colin, and David H. Evans. 1995. “Bias in Mean Frequency Estimation of Doppler Signals due to Wall Clutter Filters.” *Ultrasound in Medicine & Biology* 21 (5): 671–77. doi:10.1016/0301-5629(95)00009-G.
- Uhlirova, Hana, Kivılcım Kılıç, Peifang Tian, Martin Thunemann, Michèle Desjardins, Payam A. Saisan, Sava Sakadžić, et al. 2016. “Cell Type Specificity of Neurovascular Coupling in Cerebral Cortex.” *eLife* 5 (May): e14315. doi:10.7554/eLife.14315.
- Villringer, A. 1997. “Non-Invasive Optical Spectroscopy and Imaging of Human Brain Function.” *Trends in Neurosciences* 20 (10): 435–42. doi:10.1016/S0166-2236(97)01132-6.
- Willemetz, J. C., A. Nowicki, J. J. Meister, F. De Palma, and G. Pante. 1989. “Bias and Variance in the Estimate of the Doppler Frequency Induced by a Wall Motion Filter.” *Ultrasonic Imaging* 11 (3): 215–25. doi:10.1177/016173468901100304.

Chapter IV

Adaptive focusing in speckle noise for
quantitative ultrasound and
aberration correction

4.2.6.1	Patient cohort	140
4.2.6.2	Intra- and interoperator variability.....	141
4.2.6.3	The Wood equation.....	142
4.2.7	Conclusion and perspectives.....	146
4.3	Toward transcranial adaptive focusing.....	146
4.3.1	The state-of-art	147
4.3.1.1	Anatomy and acoustic properties of the skull.....	147
4.3.1.2	Conventional transcranial ultrasound imaging.....	148
4.3.1.3	Phase aberration correction to improve transcranial imaging.....	149
4.3.2	Numerical simulation of skull aberration correction	151
4.3.2.1	Numerical simulation parameters.....	151
4.3.2.2	Phase aberration.....	153
4.3.2.3	Amplitude modulation.....	156
4.3.2.4	Sound speed correction.....	158
4.3.2.5	Conclusion and perspectives.....	159
4.4	Chapter conclusion.....	160
4.5	Chapter bibliography	161

4. Adaptive focusing in speckle noise for quantitative ultrasound and aberration correction

4.1 Chapter introduction

In the previous chapter, we studied the advent of ultrafast imaging in the neuroimaging in humans. This was possible in *in vitro* study (veal brains) and *in vivo* on patients during brain surgery when we had a direct access to the brain. In this part of the thesis, we were interested in the correction of the aberration induced by the skull in order to progress toward transcranial ultrafast ultrasound imaging. However, the skull caused very strong phase and amplitude aberration to the ultrasound beam. The ultrasound beam deformation leads to bad focus quality and therefore degraded image quality. We decided to, firstly try our aberration correction technique in an easier experimental condition than the skull. We choose the case of the liver. Indeed, for liver imaging, we also faced an inhomogeneous medium: the ultrasound beam has to pass through subcutaneous and muscle before reaching the liver. Nevertheless, these superficial layers induced phase aberration lighter than those induced by the skull, and no amplitude distortion. In liver imaging, there is a need of quantitative imaging for disease such as fatty liver disease (hepatic steatosis). As such, we decided to apply our aberration correction technique to perform quantitative ultrasound in the liver for the hepatic steatosis diagnosis.

The first part of this chapter is dedicated to quantitative ultrasound in the liver in ultrasound phantoms and in patients using the adaptive focusing in speckle noise and aberration correction technique. The second part focuses on phase, amplitude and sound speed correction toward transcranial adaptive focusing in numerical simulation.

4.2 Adaptive focusing in speckle noise for quantitative ultrasound in the liver

In this section, we used a technique of adaptive focusing in speckle noise for quantitative ultrasound in the liver. It is known that speed of sound within soft tissues varies slightly with fat content, a relationship between sound speed and percentage of fat in the liver can be found. By calculating the precise sound speed of the liver we aim to access its fat percentage, and therefore the corresponding grade of hepatic steatosis.

After an introduction on hepatic steatosis and the need of its precise diagnostic, the detail and theory of our speckle noise technique will be presented, along with the ultrasound data acquisition process and post treatment. Then our results on phantoms and patients will be presented.

4.2.1 Need for fat quantification in liver

Hepatic steatosis due to fat accumulation in the liver is the most common cause of chronic liver disease and may lead to severe liver conditions (Wieckowska and Feldstein 2008). Biopsy and MRI are gold standard techniques to diagnose hepatic steatosis with a percentage of fat in the liver. These techniques are not without limitations. First, liver biopsy suffers from sampling problems: liver biopsies sample as little as 1/50,000 of the total mass of the liver, often resulting in insufficient information for a definitive diagnosis (Janiec et al. 2005; Ratziu et al. 2005). Second, it is an invasive method involving certain risks and added stress and expense. Finally, the histologic evaluation is subjective and dependent on the experience of the pathologist. Regarding MRI it is currently the most accurate noninvasive imaging method for diagnosing and quantifying hepatic steatosis, which estimates the Proton-Density Fat Fraction (PDFF) as a measure of fractional fat content (Leporq et al. 2014). However, MRI also has several limitations including cost, contra-indications and poor availability that could be overcome by using ultrasound. Although conventional ultrasound is widely used by radiologists for hepatic steatosis assessment, it remains qualitative. Therefore, there is a medical need to develop noninvasive techniques that can robustly quantify the degree of hepatic steatosis.

Ultrasonic imaging has been explored for many years for its ability to detect and characterize liver disease and is highly accurate to diagnose liver cirrhosis (Deffieux et al. 2015; Mishra and Younossi 2007; Tchelepi et al. 2002). Yet, current conventional ultrasonic techniques do not allow for quantification of the degree of fatty liver. Presence of liver steatosis is depicted on conventional ultrasound when the liver appears bright but this finding has poor sensitivity and requires 30% of hepatic steatosis (Dasarathy et al. 2009; Mehta et al. 2008). Moreover, this qualitative assessment is highly subjective and depends on the expertise and experience of the operator (Zwiebel 1995). Researchers have investigated the liver-kidney contrast to quantify liver fat content using the ultrasound hepatic/renal ratio and the hepatic attenuation rate from ultrasound hepatic and right kidney images (Xia et al. 2012). However, this technique still needs standardization, further testing in a clinical setting and will always suffer from the impact of variable acoustic window. Lastly, the effectiveness of ultrasound for diagnosing hepatic steatosis is reduced on patients who are morbidly obese (de Moura Almeida et al. 2008), mainly due to reverberation in abdominal tissue (Lediju et al. 2009) and wave front distortion induced by the subcutaneous fat (Browne et al. 2005).

Suzuki and coworkers observed that the ultrasonic attenuation depends on fatty infiltration of the liver and to a lesser extent on fibrosis (Suzuki et al. 1992). This theory was also used to develop an attenuation parameter based on the ultrasonic properties of the radiofrequency backpropagated signal called Controlled Attenuation Parameter (CAP) (Sasso et al. 2010). The CAP has the ability to detect minimal hepatic steatosis such as 10% steatosis assessed on pathology. This CAP technique is performed in conjunction with liver fibrosis assessment based on 1D Transient Elastography (J. Foucher et al. 2006; Sandrin et al. 2002). Other recent studies have used ultrasound to detect steatosis (Lin et al. 2015; Son et al. 2015) but they are based on a single cut-off value. Beyond such binary below/above diagnosis, there is a real clinical unmet

need for a non-expensive, widely available, and highly reliable technique to precisely grade hepatic steatosis as MRI does.

Our objective was to assess the accuracy for steatosis detection and staging of a specific ultrasonic sequence for Sound Speed Estimation (SSE). We present a method able to precisely calculate the sound speed in the liver. As it is well known that speed of sound within soft tissues varies slightly with fat content, a relationship between sound speed and percentage of fat in the liver can be found. Indeed, an increase in fat content leads to a decrease in wave speed (Duck 1990). Bamber and Hill reported higher mean sound speed in excised normal liver than in fatty human livers (Bamber and Hill 1981). In another in vivo study, researchers reported higher sound speed in normal liver than in fatty liver without fibrosis from humans (Chen et al. 1987). However, these studies were performed in excised organs. For non-invasive sound speed measurements, Jaeger and Frenz (Jaeger and Frenz 2015) proposed to measure the changing local phase of beamformed echoes when changing the transmit beam steering angle. This method is working on the liver, however it may not have the required precision to grade steatosis. The method developed in this thesis is based on the study of the spatial coherence function of the backscattered echoes resulting of an ultrasound beam focusing in the medium (Lacefield, Pilkington, and Waag 2002; Mallart and Fink 1994). The optimal sound speed is deduced by increasing the spatial coherence of echoes coming from a targeted focal spot. Before reaching the liver, the ultrasound beam crosses fatty and muscle layers of different thickness. These layers introduce distortions of the ultrasonic wavefront (Lediju et al. 2009) that hinder the robustness of SSE. The theory and the different steps of our technique, leading to the final local SSE, are described in the next section.

4.2.2 Adaptive focusing in speckle noise for sound speed estimation

The aim of this section is to present the theory for precise sound speed calculation, first in a homogeneous medium, and second in a heterogeneous medium. The first Sound Speed Estimation (SSE) is obtained by using the robust van Cittert–Zernike (VCZ) Theorem applied on the ultrasound backscattered echoes. Then, this first SSE is used as a starting point of the speckle noise technique for virtual source generation and aberration correction to correct phase aberration and improve SSE. This technique consists in trying to recreate, inside the medium, a virtual point-like reflector able to act as a virtual source generating the Green’s function between this source location in the medium and the transducer elements of the ultrasonic probe. Lastly, we studied one way to integrate superficial layers influence in the calculation in the case of heterogeneous medium.

4.2.2.1 Spatial coherence in random media: The Van Cittert–Zernike theorem

The technique used in this study starts with the transmission of an ultrasound pulse focused in the region of interest. Then the ultrasound field backscattered by the random distribution of scatterers is received on all the array elements. The similarity between the signals received by two distant elements of the array characterizes by the spatial coherence of the received wavefield.

Van Cittert and Zernike determined the degree of coherence by defining a coherence function as the averaged cross-correlation between two signals received at two points of space (Mallart 1991). The degree of coherence was determined by Van Cittert and Zernike by defining a coherence function as the averaged cross-correlation between two signals received at two different points in space. The Van Cittert–Zernike theorem states that the coherence function is the spatial Fourier transform of the intensity distribution at the focus. By calculating autocorrelations between all pairs of receiver elements, the coherence function $R(m)$ is assessed as a function of distance in number of elements m (or Element lag) (Derode and Fink 1993):

$$R(m) = \frac{N}{N - m} \frac{\sum_{i=1}^{N-m} c(i, i + m)}{\sum_{i=1}^N c(i, i)}$$

Equation 4.1 - Coherent function $R(m)$, with N the number of elements of the array and $c(i, j)$ is defined in **Equation 4.2**.

$$c(i, j) = \sum_{T_1}^{T_2} (S_i(t) - \bar{S}_i)(S_j(t) - \bar{S}_j)$$

Equation 4.2 - Cross-correlation between two signals received at two different points in space $c(i, j)$, where $[T_1 T_2]$ is the temporal window centered on the focal time and S_i is the time-delayed signal received on transducer i .

When the ultrasonic wave is focused on a point-like target in the medium, the coherence function is equal to 1 all along the array. In the case of a homogeneous medium made of randomly distributed Rayleigh scatters, the degree of coherence decreases as the distance between elements increases.

Therefore, a focused beam generated by a rectangular aperture will lead to a triangle coherence function of backscattered echoes coming from a random distribution of Rayleigh scatters in the focal spot (Mallart and Fink 1994). For a fixed depth, if the speed of sound used for focusing in the homogeneous random medium is under- or overestimated, then the focal spot size at the desired depth will increase, leading to a dramatic decrease of coherence. In this study we choose a fixed depth of 60 mm as it corresponds to the focal elevation depth of probe we used.

The method consists in proposing an algorithm that will try to better focus in the medium in post-processing with different speeds of sound. In order to perform any kind of transmit focusing, we acquire the backscattered echoes coming from a set of coded excitations and recreate the desired transmit focusing using a coherent recombination of these signals during the post-processing step. Such coherent recombination of ultrasonic backscattered echoes was in particular studied in the context of dynamic virtual transmit focusing (Cooley and Robinson 1994; Karaman, Li, and O'Donnell 1995; Lockwood, Talman, and Brunke 1998). For every try, the coherence function corresponding to the tested speed of sound is recorded. The area under the coherence function curve is then calculated (Lediju et al. 2011). To improve signal to noise ratio (SNR), the Van Cittert–Zernike theorem is applied on a 25 points grid (points separated by one wavelength, grid at 60 mm depth) and the area under the coherence function curve is average for every tested speed of sound. The estimated speed of sound providing the highest area under

the curve value is the real speed of sound in the medium (Figure 4.1) and enables the best focusing quality with the smallest focal spot.

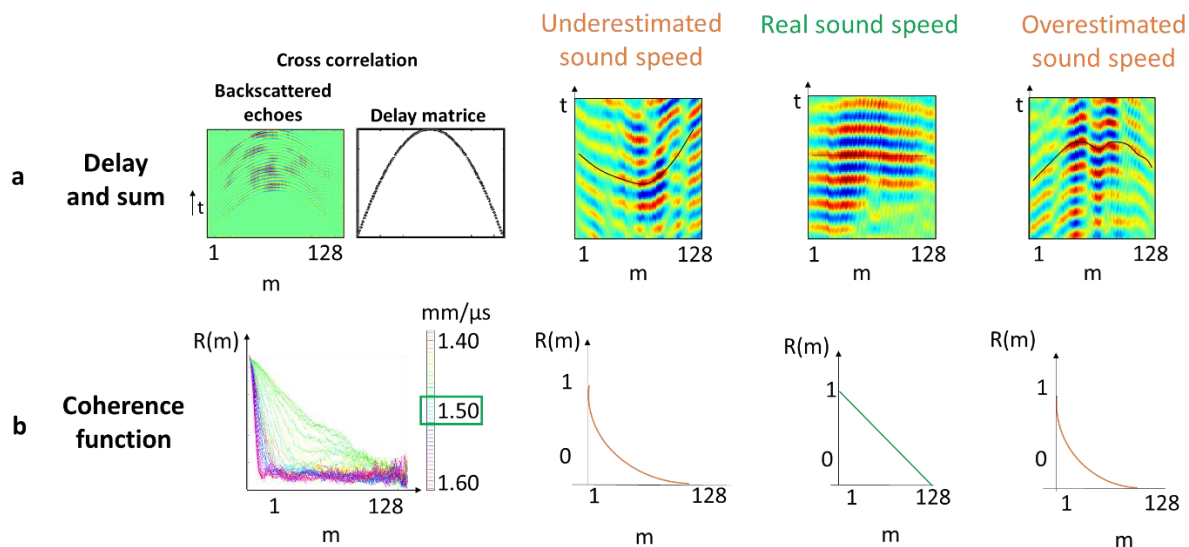


Figure 4.1 - Sound Speed Estimation based on the spatial coherence assessment. An ultrasound pulse is focused at a fixed depth in the medium with an ultrasonic probe. The backscattered echoes are received on the array and their cross-correlations are performed between pairs of transducer elements distant of m elements to compute the coherence function $R(m)$. **(a)** Flat backscattered echoes, obtained by cross correlation between backscattered echoes and delay matrix, corresponding to different tested speed of sound. **(b)** Coherence function corresponding to each tested speed of sound. The best speed of sound is the one that provide the highest area under the curve value. When an ultrasound pulse is focused at a fixed depth on the medium, the focal spot is optimized when the precise sound speed is used for the focusing. In this case the coherent function is triangle shape (green curve). When the speed of sound used for focusing is under- or overestimated (orange curve), then the focal spot will increase, leading to a dramatic decrease of coherence.

This technique is given access to the global SSE in the medium. It is a robust SSE that can be used as the first SSE value in the more precise iterative algorithm developed in the next section.

4.2.2.2 Virtual point-like source generation and iterative focusing algorithm for phase Aberration Correction

The convergence toward an optimal coherence function is possible in a perfectly homogeneous medium with a constant speed of sound. Heterogeneities in the medium result in phase aberrations along the travel path of the ultrasonic beam and hinder the precision and robustness of the method. The aim of the second step of our method is to create a virtual point-like reflector in the homogeneous random medium (under the superficial layers), in order to assess the aberrations induced by the medium and improve the precision of our SSE. These aberrations can be estimated by creating a virtual bright reflector from a random distribution of scattered below the aberrating layer using the concept of iterative time reversal focusing in speckle noise (Montaldo, Tanter, and Fink 2011) (Figure 4.2) applied on the same RF data used for the previous step. Twenty-five focus beams are virtually emitted in post-treatment at different locations nearby the desired focus (60 mm depth) by recombination of the RF issued from the

Hadamard encoded acquisitions (**Figure 4.2 (a)**). Virtual backscattered signals are recorded (**Figure 4.2 (b)**) and ‘steered’ using the time delays as if all signals were coming from the same reference location (**Figure 4.2(c)**). The summed corrected backscattered echoes lead to pulsed signals well compressed in time resulting from the created virtual point-like reflector (**Figure 4.2 (d)**).

The interested reader should also note that this aberration correction, based on time reversal focusing, could be performed directly in blood vessels when available following (Bruno-Felix Osmanski et al. 2012).

Through an aberrating layer, an iterative algorithm is necessary to converge to a well-defined wave front. In this case, we are going to take benefit on both the isoplanatic patch (Chassat 1989) and the randomness of the scattering medium. When applying the process described earlier to create a point-like reflector in a homogeneous medium, the emitted signals from this virtual bright reflector are no more matching to the heterogeneous medium. So, the initial focusing beams are not perfectly focused at their desired locations, however it provides an acceptable start as a first iteration. The new iteration step starts replacing the virtually emitted signal from the transducer by the time-reversed version of the signal emitted by the virtual point-like reflector, obtained from the first iteration (**Figure 4.2 (f)**).

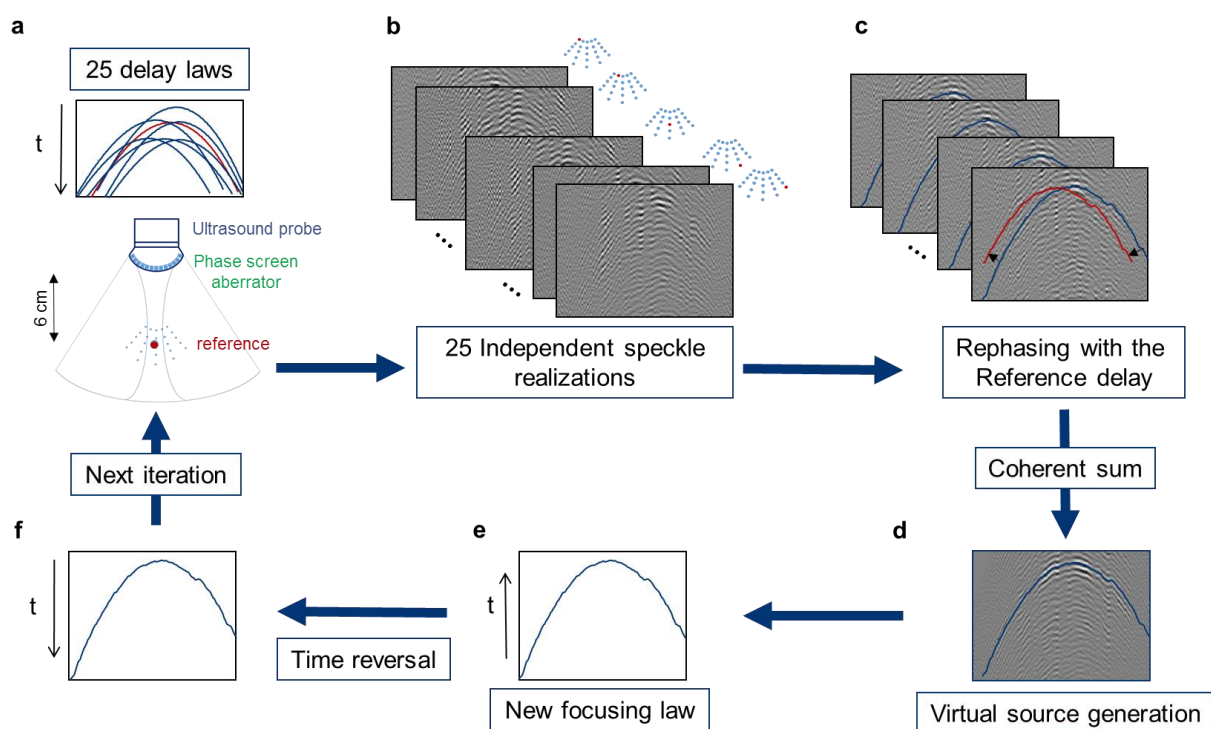


Figure 4.2 - Virtual Source Generation and Iterative Focusing Algorithm for Phase Aberration Correction. (a) Focused waves are virtually emitted in post-treatment with different delay laws to focus on 25 spots separate by one wavelength. The central point of this grid is considered as the reference point. (b) The echoes (independent speckle realizations) are recorded. (c) Correction of the additional delay compared to the reference central delay. (d) Coherent sum of the speckle realizations after correction of the additional delay, a virtual point reflector emerges. (e) A distorted waveform is obtained. (f) This waveform is time-reversed and injected as the new emission signal in the first step (a) to begin a new iteration.

At each iteration, the emitted beam profile is improved. After 10 iterations, the signal converge to a well-defined wave front. The spatial coherence in random media for the 10th iteration was studied *in vivo* in the liver for improving the precision of our SSE and is presented in **section 4.2.5**.

4.2.2.3 Superficial layers influence correction

In addition to the phase aberration correction (heterogeneous local aberrations), superficial layers thickness and speed of sound in these different layers (global averaged aberrations) have to be integrated in the calculation. One way of including superficial layers influence correction is studied and discussed: superficial layers thickness measurement.

In a multi-layer medium, sound speeds of the different layers are linked by the formula:

$$\frac{d_{tot}}{c_{cum}} = \frac{d_{medium\ 1}}{c_{medium\ 1}} + \frac{d_{medium\ 2}}{c_{medium\ 2}} + \frac{d_{medium\ of\ interest}}{c_{medium\ of\ interest}}$$

Equation 4.3 - Sound speed of the different layers in a multi-layers medium, where d_{tot} is the depth of the virtual point-like reflector creation, c_{cum} is the global SSE calculate by the algorithm, $d_{medium\ 1}$ is the thickness of the first medium crossed by the ultrasound, $c_{medium\ 1}$ is the sound speed in this first medium, $d_{medium\ 2}$ is the thickness of the second medium crossed by the ultrasound, $d_{medium\ of\ interest} = d_{tot} - (d_{medium\ 1} + d_{medium\ 2})$, $c_{medium\ of\ interest}$ is the speed of sound that we aim to determine.

$c_{medium\ of\ interest}$ is calculated with the formula:

$$c_{medium\ of\ interest} = \frac{d_{medium\ of\ interest}}{\frac{d_{tot}}{c_{cum}} - \frac{d_{medium\ 1}}{c_{medium\ 1}} - \frac{d_{medium\ 2}}{c_{medium\ 2}}}$$

Equation 4.4 - Sound speed estimation c in the medium of interest, considering the existence of multiple superficial layers.

By applying this formula to the SSE found with the VCZ theorem and after phase aberration correction, we obtained a precise and robust SSE value in the medium of interest.

4.2.3 Ultrasound data acquisition and posttreatment

For our experiment, both in ultrasound phantoms and *in vivo*, we used an ultrasonic array made of 192 piezoelectric elements (abdominal curved probe SC 6-1, Supersonic Imagine, Aix-en-Provence, France) driven by a fully programmable electronic system (Aixplorer, SuperSonic Imagine, Aix-en-Provence, France). Compared to the linear probe used in the previous chapters, we decided to use as curved probe, first to enlarge our field of view and second to enable deep examination. Indeed, the liver stands behind fat and muscle layers, and we need to access a weighty part of it.

Hadamard encoding (Chiao, Thomas, and Silverstein 1997) was used to spatially encode the waveforms, where the Hadamard matrix was multiplied to the waveforms for the multiple transmissions (128*128 transmissions using 128 elements) (see **Figure 4.3**) and where all elements were used in receiving. This type of spatiotemporal encoding virtually increase the amplitude of

the emitted signal, and allow for virtual focusing in posttreatment by combining the RF data coming from the different transmissions. The ultrasound acquisition lasted two seconds.

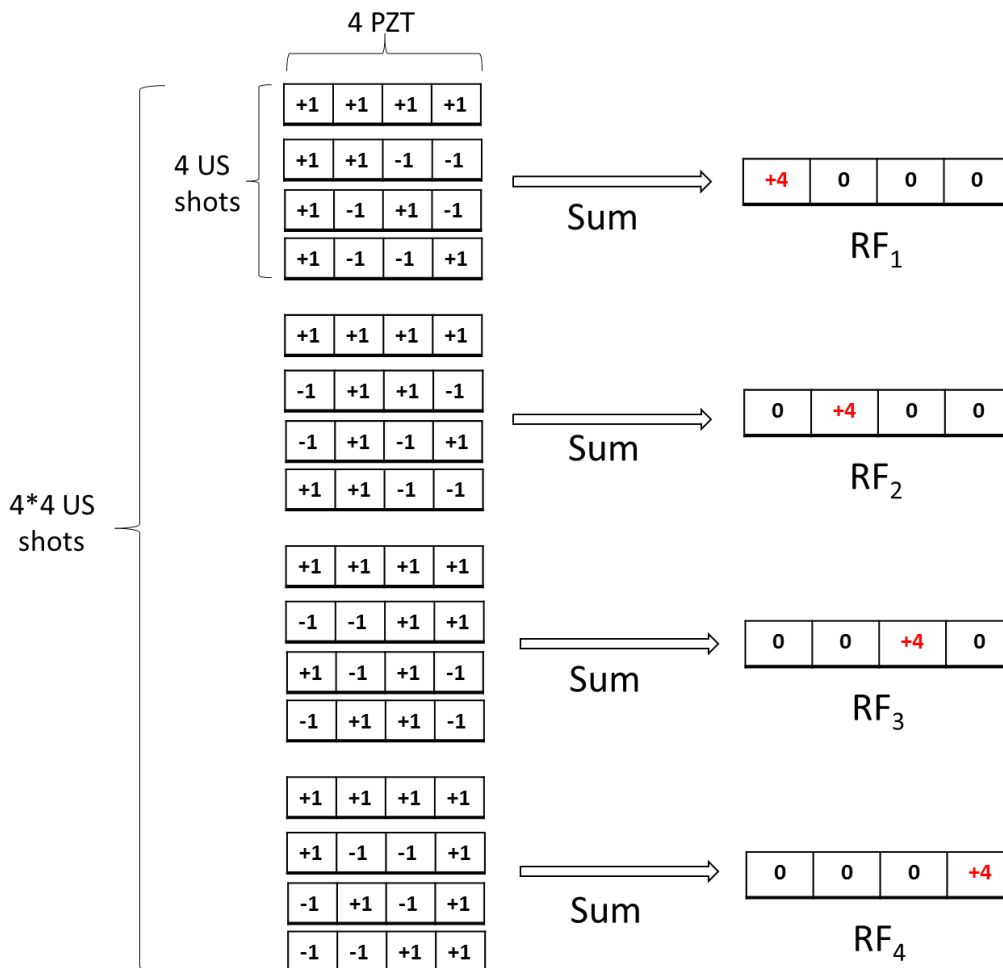


Figure 4.3 – Hadamard encoding principle. This example illustrates Hadamard encoding in the case of an ultrasound (US) probe composed of four piezoelectric elements (PZT). The Hadamard matrix (square matrix whose entries are either +1 or -1) is multiplied to the waveforms for the multiple transmissions and all elements are used in receiving. Four by four ultrasound shots are necessary to obtain four radiofrequency (RF) signals.

To enable to virtually focus in posttreatment by combining the RF data issue from the different transmissions, as we used a curved probe, we used the polar coordinate system to calculate the delay laws. The calculation details and the associated diagram are presented in **Appendix 1**, and the formula used to calculate the delay law was:

$$-\frac{1}{c} \sqrt{R^2 + R_M^2 - 2RR_M(\cos(\theta_i - \alpha))}$$

Equation 4.5 – Delay law in the polar coordinate system. The origin is in the center of curvature circle. c is the speed of sound in the medium, R is the probe radius of curvature, R_M is the distance from one point (M) to the curvature circle center, i characterize the corresponding piezoelectric elements, θ_i is the angular spacing between two piezoelectric elements, and α is the angle between the axe orthogonal to the probe centred in zero and the point (M).

All the different steps for SSE calculation and optimization, as described in section 4.2.2 (first SSE, aberration correction, and superficial layers influence correction), were performed in post treatment and lasted 4 minutes in total. This relatively short post-processing time was attained after code optimization realized in collaboration with the master student Antoine Tissier.

4.2.4 Experimental set-up on homogeneous ultrasound phantoms

Before testing our technique *in vivo* in human liver, we made experiments on ultrasound phantoms. Acquisitions were performed on two calibrated phantoms: one ATS phantom (model 551) characterized by a sound speed of $1.45 \text{ mm}\cdot\mu\text{s}^{-1}$ and one CIRS phantom (model 054) characterized by a sound speed of $1.54 \text{ mm}\cdot\mu\text{s}^{-1}$. During the ultrasound acquisition, the probe was held by an articulated arm. Raw Data were then processed using Matlab software (Mathworks) in order to calculate SSE.

First, we placed the ultrasonic probe directly on the phantom, in order to calculate a global SSE in a homogeneous medium. Second, the phantom was covered by a water layer. We repeated the experiment with three different water temperatures (corresponding to sound speeds of 1.46, 1.48 and $1.52 \text{ mm}/\mu\text{s}$) and different water layer thicknesses (ranging from 0 to 26 mm). The aim of the phantom study was to find a SSE equal to the sound speed given by the phantom manufacturer despite of the superficial aberrating water layer.

A range of sound speed from $1.400 \text{ mm}\cdot\mu\text{s}^{-1}$ to $1.600 \text{ mm}\cdot\mu\text{s}^{-1}$ with a 0.001 step was tested for the ATS phantom (model 551) (**Figure 4.4(a)**) and for the CIRS phantom (model 054) (**Figure 4.4(b)**). For each phantom and each sound speed tested, the coherent sum of the maximum correlation was calculated using **Equation 4.2** for each tested sound speed. The SSE value corresponding to the phantom was the maximum of the polynomial fit of the coherent sum of the maximum correlation. Iso-value curves are another way to visualize the influence of sound speed on the signal coherence. We plotted curves of constant minimum value of the maximum correlation for each sound speed and noticed that the sound speed characterizing the medium is assuring the highest lag for each minimum of the maximum correlation (**Figure 4.4** and **Figure 4.5**).

In order to find the mean SSE and deviation from the mean for both phantoms and to compare these results with the speed of sound indicated by the constructor, 20 acquisitions with probe repositioning were performed on each phantom. The mean SSE for the ATS phantom was found to be $1.449 \pm 0.006 \text{ mm}\cdot\mu\text{s}^{-1}$ for a sound speed given by the constructor of $1.450 \text{ mm}\cdot\mu\text{s}^{-1}$. The mean SSE for the CIRS phantom was found to be $1.544 \pm 0.003 \text{ mm}\cdot\mu\text{s}^{-1}$ for a sound speed given by the constructor of $1.540 \text{ mm}\cdot\mu\text{s}^{-1}$. These results demonstrated that in the homogeneous phantom case, the obtained SSE was in good agreement with the speed of sound indicated by the constructor.

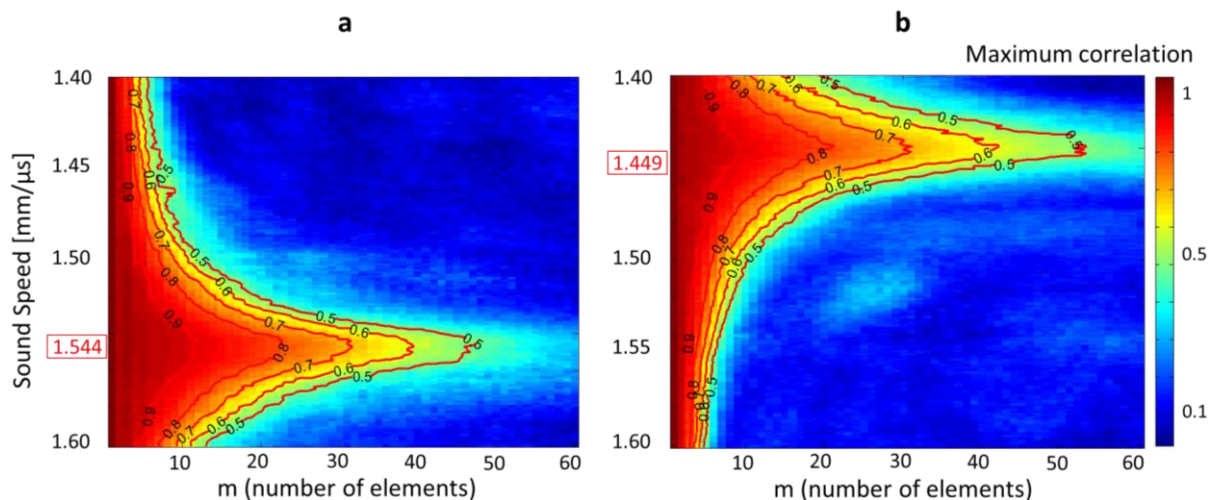


Figure 4.4 - Correlation maps and sound speed estimation (SSE) in two phantoms. Correlation maps and sound speed estimation (SSE) in two phantoms. Different sound speeds were tested for a 60 mm depth. The correlation maps were calculated in function of the lag in number of elements (m) and the red iso-value curves are curves of constant minimum value of the maximum correlation for each sound speed (each maximum correlation under one curve is at least equal to the name of the curve). The sound speed characterizing the medium is assuring the highest lag for each minimum of the maximum correlation. **(a)** SSE was found to be 1.544 $\text{mm} \cdot \mu\text{s}^{-1}$ for the CIRS phantom (model 054). **(b)** SSE was found to be 1.449 $\text{mm} \cdot \mu\text{s}^{-1}$ for the ATS phantom (model 551).

Regarding these encouraging *in vitro* results, we decided to try our technique *in vivo*. It was possible thanks to the small acquisition time (about 2 seconds), during which one patient can hold his breath.

4.2.5 Pilot clinical study and proof of concept

As a preliminary study, we started investigation on a small patient cohort. This study was conducted in collaboration with the radiologists Pr. Valérie Vilgrain and Dr. Alex Faccinnetto from Beaujon hospital in Paris.

4.2.5.1 Patient cohort

Patients referred to Beaujon hospital ultrasound unit and who underwent liver MRI and liver biopsy were consecutively included in our study from February 2015 to November 2015. All patients gave their informed consent. Ethical considerations had been previously validated by our institutional ethics committee, “Comité de Protection des Personnes – Ile-de-France VI – Pitié Salpêtrière”).

For each patient, the following clinical data were recorded: age, sex, steatosis on liver biopsy (%), MRI PDFF (%), and Body Mass Index (BMI). All examination had to be accomplished in a 6 month maximum period. BMI was calculated as body weight in kilograms divided by height in meters (kg/m^2). Definitions of obesity were based on criteria from the World Health Organization, and BMI from 25 to 29.9 kg/m^2 was considered overweight and BMI of 30 kg/m^2 or greater was considered to be obese.

Patients underwent liver MRI (3T Philips Ingenia, Eindhoven, Netherlands), conventional ultrasound examination and specific ultrasound sequence acquisition for SSE; the last two using an abdominal curved probe (SC6-1) driven by an ultrafast scanner (Aixplorer®, Supersonic Imagine, France). Right subcostal view was considered for every patient, with care taken to avoid large hepatic vessels or artifacts. Patients also had biopsy in addition to the MRI and Ultrasound examination. Histology from biopsy was used as an invasive gold standard and MRI PDFF as a non-invasive gold standard to assess the percentage of liver steatosis (Idilman et al. 2013).

A total of 17 patients with a mean age of 61 years (with the total sample set ranging from 30 to 80 years of age), including 30 % female and 70 % male were recorded.

The mean BMI was 26.4 kg/m² (range, 21.7–30.5 kg/m²). One of the 17 patients was obese and 47% (8 of 17) were overweight. No correlation between BMI and MRI PDFF was found ($R^2 = 0.09$) and the technique calculated SSE for all the BMI range. Patients had a mean of 13 mm of subcutaneous fat (range, 4-25 mm). No correlation was observed between thickness of subcutaneous fat layer and MRI PDFF ($R^2 = 0.16$) and the technique calculated SSE for all the thickness range.

4.2.5.2 First Sound Speed Estimation in Patients

For each patient, a sound speed range from 1.45 mm.μs⁻¹ (sound speed in pure fat) to 1.65 mm.μs⁻¹ was tested. SSE were calculated the same way as in the phantoms experiments. Correlation maps of two patients with different calculated SSE are presented in (Figure 4.5).

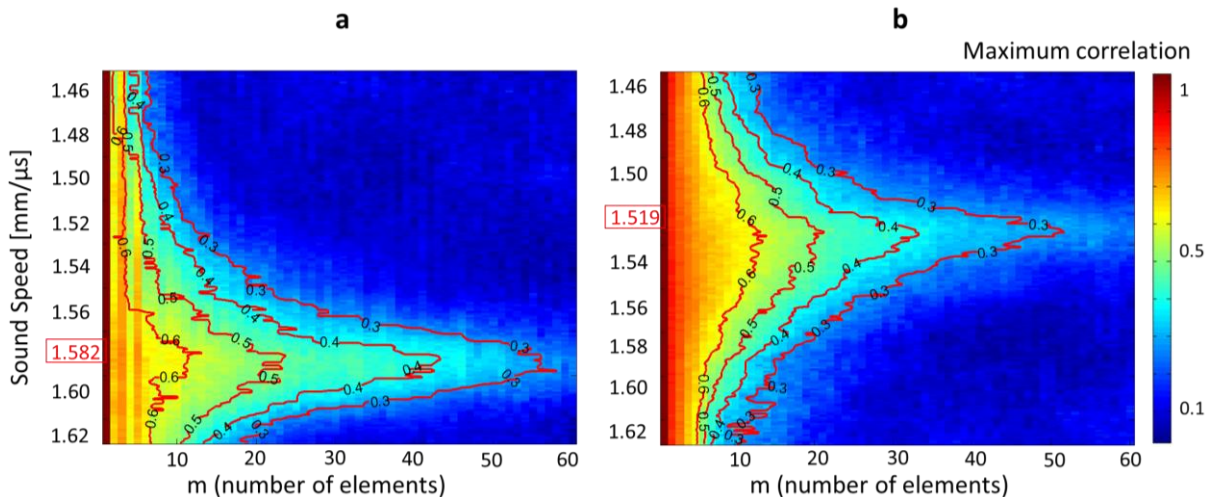


Figure 4.5 - Correlation maps and sound speed estimation (SSE) in two patients. Correlation maps and sound speed estimation (SSE) in two patients. Different sound speeds were tested for a 60 mm depth. The correlation maps were calculated in function of the lag in number of elements (m) and the red iso-value curves are curves of constant minimum value of the maximum correlation for each sound speed. The sound speed characterizing the medium is assuring the highest lag for each minimum of the maximum correlation. (a) SSE was found to be 1.582 mm.μs⁻¹ for one healthy patient (Biopsy 0%, PDFF 2%). (b) SSE was found to be 1.519 mm.μs⁻¹ for one patient with severe steatosis (Biopsy 30%, PDFF 8.5%).

We obtained SSE ranging from 1.492 mm.μs⁻¹ to 1.604 mm.μs⁻¹ for patients with MRI PDFF from 2% to 17%, and biopsy from 0% to 80% respectively.

Studying the coherence function for different sound speed gives a global SSE. The aim of the following sections is now to calculate a local speed of sound in the liver based on the previous SSE. There are two ways of SSE improvement: by correcting the phase aberration induced by the fat and muscle superficial layers, and by taking into account the thickness of these layers (cf. section 4.2.2.3). Both techniques are studied and then combined in the following sections.

4.2.5.3 Phase Aberration Correction

Fat and muscle superficial layers act as near field phase screen aberrator. The technique used in this section is based on the aberration correction algorithm. The aim is to straighten the wave front coming from the virtual point like reflector to improve the quality of the focusing. In the case of a patient with a thick superficial fat layer, the phase aberration algorithm succeeded to straighten the wave front and to improve the focusing (Figure 4.6).

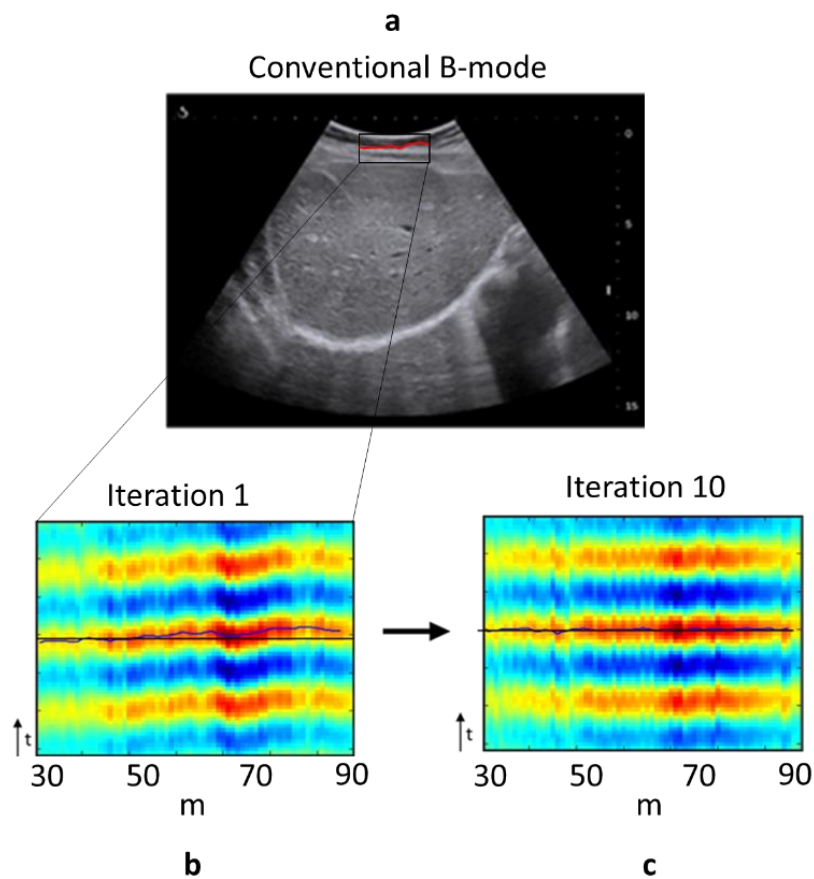


Figure 4.6 - Iterative algorithm for aberration correction. (a) Conventional B-mode of the right sub-costal liver of the patient. A 1 cm thickness fat layer is visible on the top of the liver capsule (hypoechoic superficial layer). The red line is the superficial aberrating layer shape. (b) Flat backscattered echoes coming from the virtual point like reflector at the first iteration (standard deviation to straight line $STD = 0.76$). (c) Flat backscattered echoes coming from the same virtual point after 10 iterations of the phase aberration corrective algorithm (standard deviation to straight line $STD = 0.26$).

The aberration correction algorithm succeeds in improving the focusing quality in every case and in some cases it improves the SSE (Figure 4.7). From iteration 1 to iteration 10, for all patients in this study, a range from 0 to 12% percent increase in the area under the coherent function

curve was measured. For patients with thin superficial layers and mostly composed by muscle, the aberration correction algorithm improves the coherence of the backscattered echoes and confirms the SSE (**Figure 4.7**, Patient 1). For patients with thick superficial layers and mostly composed by fat, the aberration correction algorithm also improves the coherence of the backscattered echoes but modifies the SSE (**Figure 4.7**, Patient 2). In both cases, this demonstrates that the first SSE calculated with the VCZ theorem is a robust value leading to the algorithm convergence. This convergence is illustrated by the increase of the area under the VCZ curve (**Figure 4.7 c**).

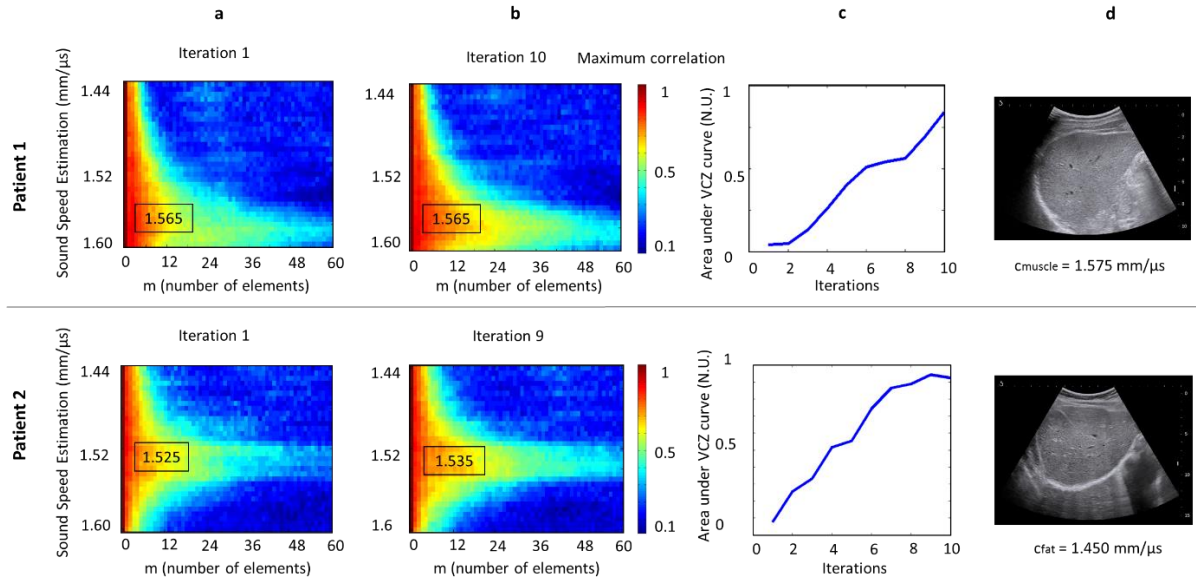


Figure 4.7 - Impact of the aberration correction on the SSE. Results are presented for two patients. (a) Correlation maps at the first iteration. (b) Correlation maps after 10 iterations of the correction aberration algorithm. (c) Evolution of the area under the coherence function curve throughout iterations. (d) Conventional B-mode of the right sub-costal liver. Hypoechoic superficial layer highlights fat and hyperechoic superficial layer highlights muscle.

However, even if this aberration correction improved our SSE and the focusing quality, we also have to take into account superficial layers (fat, muscle) thickness and their corresponding sound speed.

4.2.5.4 Fat and muscle Influence Correction

In this section, one way of including superficial layer thickness into the sound speed calculation is detailed: by superficial layers thicknesses measurement and with a good knowledge of the sound speed in these layers.

In order to include fat and muscle influence in the calculation, firstly, we went back to the phantom experiments. We used layers of water with controlled temperature to mimic superficial layers. The CIRS phantom was chosen (model 054, speed of sound: $1.54 \text{ mm} \cdot \mu\text{s}^{-1}$), and three different water temperatures (c_{water}) were tested: 37 degrees ($c_{\text{water}} = 1.52 \text{ mm} \cdot \mu\text{s}^{-1}$), 20 degrees ($c_{\text{water}} = 1.48 \text{ mm} \cdot \mu\text{s}^{-1}$), 14 degrees ($c_{\text{water}} = 1.46 \text{ mm} \cdot \mu\text{s}^{-1}$) (Boed 1998) with different thickness from 0 to 26 mm.

We observed that without layer correction, SSE varies depending on the sound speed in the superficial layer and the thickness of this layer (**Figure 4.8 a**). After layer correction, the sound speed estimation corresponds to the sound speed given by the constructor ($1.54 \text{ mm} \cdot \mu\text{s}^{-1}$) without any dependence with the superficial layer characteristic (**Figure 4.8 b**).

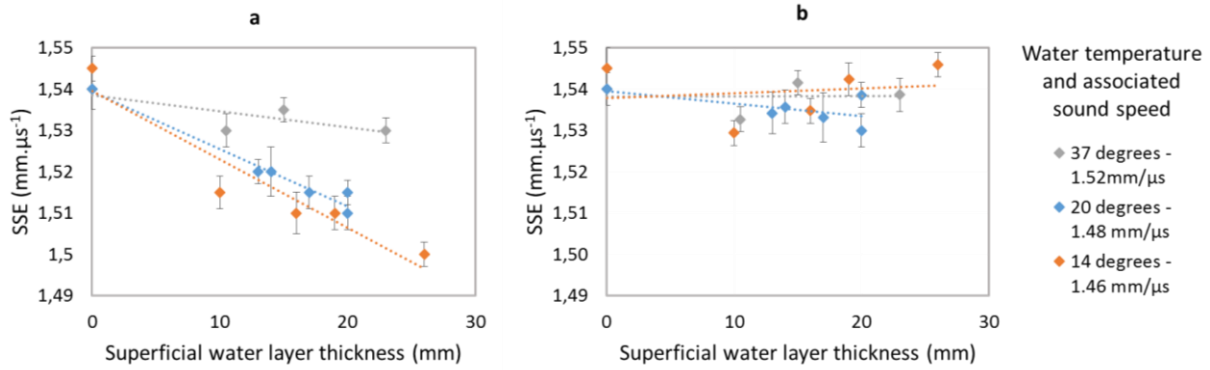


Figure 4.8 - Layer measurement for SSE correction. Error bars for SSE range from ± 0.003 to $\pm 0.006 \text{ mm} \cdot \mu\text{s}^{-1}$ and came from a mean over five successive measurements with probe repositioning. **(a)** Without layer correction, SSE varies depending on the sound speed of the superficial layer and the thickness of this layer. **(b)** With layer correction, SSE is corresponding to the sound speed given by the constructor ($1.54 \text{ mm} \cdot \mu\text{s}^{-1}$).

For the patients, fat and muscle layers thickness were measured with conventional ultrasound by the physician and were integrated in the calculation of the final SSE in the liver, using **Equation 4.3** and **Equation 4.4**. The mean sound speed used in the calculation are $1.450 \text{ mm} \cdot \mu\text{s}^{-1}$ in fat and $1.575 \text{ mm} \cdot \mu\text{s}^{-1}$ in muscle (Azhari 2010).

4.2.5.5 Final Pilot Clinical Study Results

The aim of this section was to challenge the different steps of SSE calculation and to assess its robustness with two different gold standards, biopsy and MRI PDFF.

Patients underwent ultrasound and MRI the same day and they underwent MRI and biopsy with a median of 6 months in between. A linear regression was used to study the correlation between SSE and MRI PDFF and R^2 is the coefficient of determination and indicates the proportion of the variance in the dependent variable that is predictable from the independent variable. The first SSE given by the VCZ theorem already gives a proportional relation between MRI PDFF and SSE ($R^2 = 0.595$) (**Figure 4.9 a**). As our hypothesis was to find a correlation between the sound speed in the liver (SSE) and the percentage of fat in the latter, we used the coefficient of determination R^2 as a relative comparison tool between the different improvement steps. We noticed that aberration correction and superficial layer thickness inclusion in the calculation improve both the proportional relation between MRI PDFF and SSE (respectively **Figure 4.9 (b)** and **(c)**). With the aberration correction step, aberrations are better taken into account, leading to a higher spatiotemporal coherence of backscattered signals (see **Figure 4.7**). Consequently, when adding the superficial layers correction, we reached the highest agreement we can obtain so far between MRI PDFF and SEE for this patient cohort ($R^2 = 0.691$) (**Figure 4.9 (d)**).

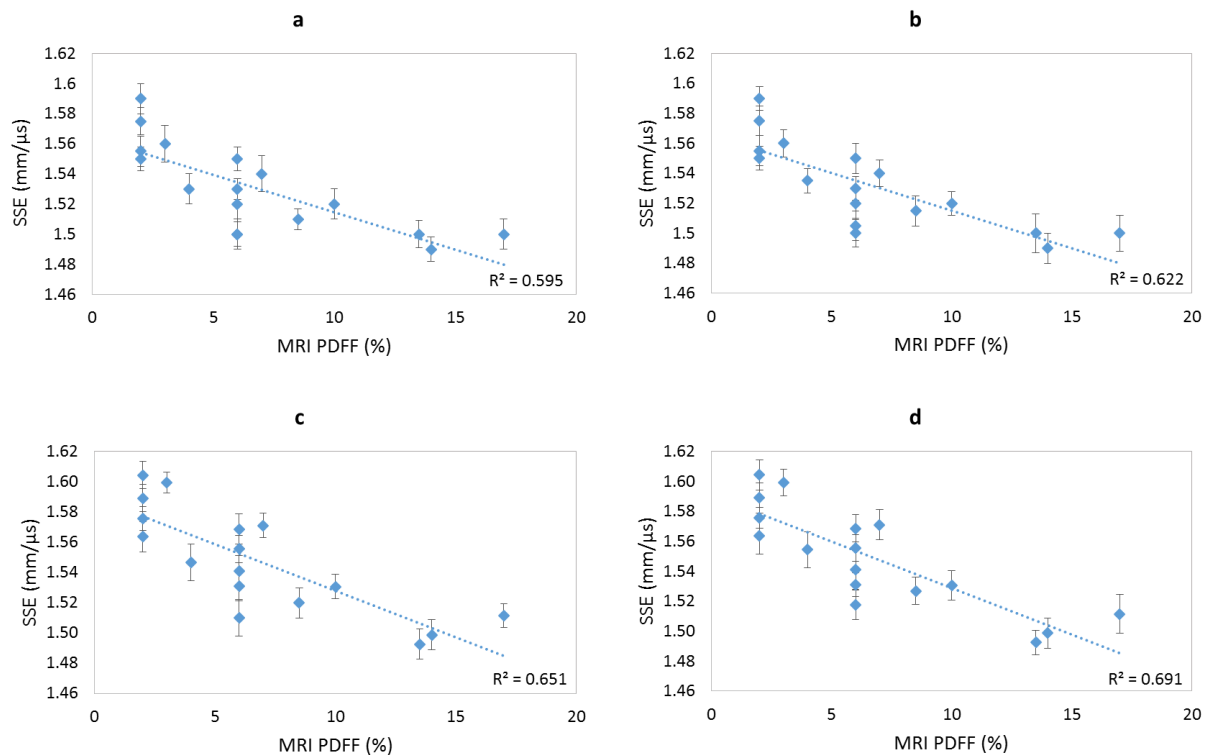


Figure 4.9 - Strong correlation between SSE decrease and MRI PDFF increase. Error bars for SSE range from ± 0.007 to ± 0.013 $\text{mm} \cdot \mu\text{s}^{-1}$ and came from a mean over four successive measurements with probe repositioning. **(a)** Step 1: SSE from VCZ theorem. **(b)** Step 2: SSE including phase aberration correction. **(c)** Step 3: SSE including superficial layers influence correction. **(d)** Step 4: optimized SSE including phase aberration correction and superficial layers influence correction.

With the MRI PDFF technique, the cut-off value between healthy and diseased patients was 5% PDFF (Idilman et al. 2013) (corresponding to the 10% used in biopsy). SSE was able to significantly differentiate healthy and diseased patients ($p < 0.0001$, AUROC = 0.942) with an associated criterion of $1.541 \text{ mm} \cdot \mu\text{s}^{-1}$.

These results are confirmed by the comparison between biopsy and SSE. A boxplot test was used to study the linear correlation between SSE and biopsy (**Figure 4.10 a**). The mean and standard deviation from the mean of the speed of sound were calculated for each Brunt steatosis stage (Grade 0: $\leq 10\%$, Grade 1: 10%-33%, Grade 2: 33%-66%, Grade 3: $\geq 66\%$) (Brunt 2010).

Receiver operating characteristic (ROC) analysis was performed in order to evaluate the ability of SSE to be a biomarker to estimate the degree of steatosis. The area under the Roc curve was estimated using the trapezoidal rule. Confidence intervals were stated at a 95% confidence level. SSE strength is its ability to grade steatosis like MRI PDFF nevertheless, the area under ROC curve which estimates the diagnostic performance of SSE to differentiate healthy liver and steatosis was 0.952 (**Figure 4.10 b**) with an associate criterion of $1.555 \text{ mm} \cdot \mu\text{s}^{-1}$.

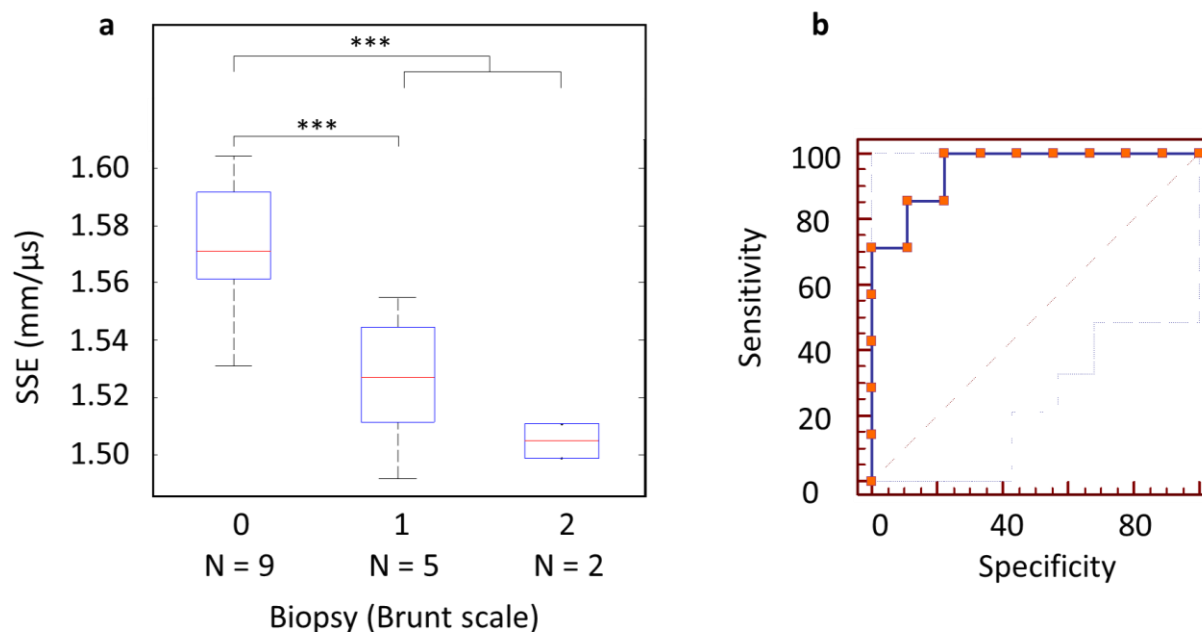


Figure 4.10 - SSE and biopsy comparison with boxplot and ROC curve analysis. (a) Patients are classified in 3 groups according to the Brunt scale. Grade 0 patients are healthy and grade 1 and 2 patients have steatosis. N is the number of patient in each category. The line through the middle of the box represents the median (50th percentile). The top and bottom of the boxes are 75th and 25th percentiles. Significant p value ($p < 0.0001$) are designated by a star (*). **(b)** ROC curve analysis to differentiate healthy liver and steatosis with SSE (AUROC = 0.952 [0.719 – 1.00] 95% CI, $p < 10^4$, Sensitivity 100 % [59.0 – 100.0] 95% CI, Specificity 77.8% [40.0 – 97.2] 95% CI).

4.2.5.6 Pilot study assessment

We developed a method for a precise and robust *in vivo* sound speed assessment. The technique was first validated on two phantoms. In the case of homogeneous phantom the SSE found was in good agreement with the speed of sound indicated by the constructor (Phantom 1, $c_{\text{constructor}} = 1.450 \text{ mm} \cdot \mu\text{s}^{-1}$ and $\text{SSE} = 1.449 \pm 0.006 \text{ mm} \cdot \mu\text{s}^{-1}$; Phantom 2, $c_{\text{constructor}} = 1.540 \text{ mm} \cdot \mu\text{s}^{-1}$ and $\text{SSE} = 1.544 \pm 0.003 \text{ mm} \cdot \mu\text{s}^{-1}$).

In this pilot clinical study, the potential of this method for noninvasive liver steatosis detection and staging was proved. Our approach enables an accurate estimate of the ultrasonic sound speed in the liver with a standard deviation below 5 %. We obtained SSE ranging from $1.492 \text{ mm} \cdot \mu\text{s}^{-1}$ to $1.604 \text{ mm} \cdot \mu\text{s}^{-1}$ for patients with MRI PDFF from 2% to 17%, and biopsy from 0% to 80% respectively. MRI PDFF and biopsy were used as gold standards with a particular attention to MRI PDFF, as it is to date considered as the most efficient approach for steatosis estimation (Idilman et al. 2013; Leporq et al. 2014). It is even considered better than liver biopsy as this latter is hindered by the non-negligible possibility to miss a steatotic region leading to false negative values (Sumida, Nakajima, and Itoh 2014). Moreover, as demonstrated by Leporq and colleagues (Leporq et al., 2014), by giving access to the percentage of fat protons regarding to the percentage of water protons, MRI PDFF allows a linear steatosis staging, instead a group classification like biopsy.

Our method is based on a three steps processing to guarantee accuracy. The first step provides an estimate of the sound speed optimizing the spatial coherence of backscattered speckle noise. As this estimation can be degraded by aberrations occurring in the first propagation layers, a virtual point like reflector can then be created in order to find and correct these aberrations. This aberration correction technique was found to be efficient as it allows in many cases ($N=14$) to increase the AUC of the spatial coherence function of the region of interest (a ratio increase of $AUC_{\text{iteration1}}/AUC_{\text{iteration10}} = 6\% \pm 1\%$). Finally a third correction step is introduced in order to correct the bias introduced by the subcutaneous layer thickness for an optimal estimation of liver sound speed. This third step, tested on multilayer phantom experiments improves SSE robustness by including superficial layers thickness in the calculation.

These successive steps lead to a very high linear correlation ($R^2= 0.69$) between MRI PDFF and SSE and therefore enable to grade hepatic steatosis. Moreover, SSE was excellent to significantly differentiate healthy and diseased patients ($p<0.0001$, AUROC = 0.942).

This analysis leads to the conclusion that SSE is able to diagnose healthy liver and steatosis as well as biopsy. Our technique can establish cut-off value between healthy patients and patients with steatosis ($SSE_{\text{criterion}} = 1.555 \text{ mm} \cdot \mu\text{s}^{-1}$).

SSE strength is its ability to grade steatosis like MRI PDFF. Moreover, with both MRI PDFF and biopsy as gold standard, SSE was demonstrated to be valuable for hepatic steatosis 10% or greater detection, which is critical on patient who undergo living donor liver transplantation because of the risks of poor graft survival, initial graft dysfunction, and other complications (Sharma et al. 2013; Trotter et al. 2007).

Our ultrasound based method has the advantage to provide a more easy-to-use and accessible imaging modality for the screening of liver steatosis. Moreover, it could be combined with stiffness (Young's Modulus) measurements using Shear Wave Elastography (Deffieux et al. 2015) or radiation force Shear Wave Speed estimation (Palmeri et al. 2005).

Some authors see the interference caused by thoracic subcutaneous fat as the limiting factor for success in obese patients (Juliette Foucher et al. 2006). However, as we included the thickness of the superficial layers and the phase aberration correction, our technique was found to be robust for all patients of this preliminary proof of concept study.

A limitation of this study is the population heterogeneity. Some patients had chronic liver diseases with various degree of fibrosis or even cirrhosis. Another study with larger patient cohort, BMI analysis, and cirrhosis studied as a confounding factor, needs to be conducted to evaluate SSE robustness in depth.

4.2.6 Clinical study with validation cohort

Considering the promising results of our pilot study, we conducted a larger clinical study, in order to challenge the robustness of our technique. In order to collect data for a large patient cohort, we designed a Graphical User Interface (GUI) in collaboration with the Master student Jérôme Baranger, to guarantee physicians autonomy in the data acquisition process. This study

was conducted in collaboration with the radiologists Pr. Valérie Vilgrain and Dr. Alex Faccinnetto from Beaujon hospital in Paris.

4.2.6.1 Patient cohort

Patients referred to Beaujon hospital ultrasound unit and who underwent liver MRI and liver biopsy, were consecutively included in our study from February 2015 to November 2015. All patients gave their informed consent. Ethical considerations had been previously validated by our institutional ethics committee, “Comité de Protection des Personnes – Ile-de-France VI – Pitié Salpêtrière”.

For each patient, the following clinical data were recorded: age, sex, steatosis on liver biopsy (%) (when available), MRI PDFF (%), and Body Mass Index (BMI). All examination was accomplished within a 6 month maximum period. BMI was calculated as body weight in kilograms divided by height in meters (kg/m^2). Definitions of obesity were based on criteria from the World Health Organization, and BMI from 25 to 29.9 kg/m^2 was considered overweight and BMI of 30 kg/m^2 or greater was considered to be obese.

Patients underwent liver MRI (3T Philips Ingenia, Eindhoven, Netherlands), conventional ultrasound examination and specific ultrasound sequence acquisition for SSE; the last two using an abdominal curved probe (SC6-1) driven by an ultrafast scanner (Aixplorer®, Supersonic Imagine, France). Right subcostal view was considered for every patient, with care taken to avoid large hepatic vessels or artifacts. Patients also had biopsy in addition to the MRI and Ultrasound examination. Histology from biopsy was used as an invasive gold standard when available and MRI PDFF was used systematically as a non-invasive gold standard, to assess the percentage of liver steatosis (Idilman et al. 2013).

For the first patient cohort, among 91 patients, we had technical issues in 18 cases and poor ultrasound signal in 23. In total 50 patients were included in the study (**Figure 4.11**, a). For the validation cohort, among 82 patients, we had technical issues in 18 cases and poor ultrasound signal in 23. In total 50 patients were included in the study (**Figure 4.11**, b).

Technical issues were patient or scanner dependent (details in **Figure 4.11**), and poor ultrasound signal was considered as a limitation of our study. In order to identify predictive factors of technical measurement failure, we compared patients with and without valid measurement by uni- and multivariate analysis. Multivariate analysis (bivariate regression model) identified only high BMI as a predictive of poor ultrasound signal (Odds ratio = 0.876 [95% 0.81-0.95, $p = 0.01$]). A ROC curve analysis was performed to identify the optimal BMI cutoff and identified a cutoff value of 26.79 kg/m^2 (AUROC = 0.73). In patients with a BMI lower than the cutoff value SSE was measurable in 85% of the cases, whereas it was measurable in 50% of patients with a BMI above this value ($p < 0.001$). A BMI above 25 kg/m^2 corresponds to overweight. However obesity is the most significant single risk factor for the development of fatty liver, both in children and in adults (James and Day 1999). The challenge of hepatic steatosis is therefore the diagnostic of patients with a BMI below 25 kg/m^2 .

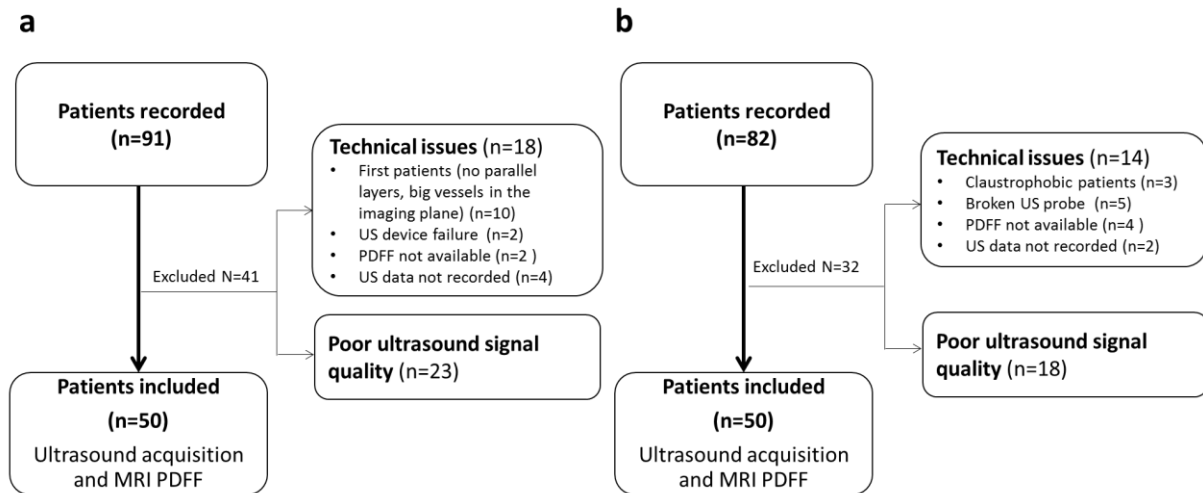


Figure 4.11 – Patient cohorts. (a) First cohort of 50 included patients. (b) Validation cohort of 50 included patients.

For the first patient cohort, 50 patients with a mean age of 58 years (with the total sample set ranging from 27 to 84 years of age), including 40 % female and 60 % male were recorded. The mean BMI was $26.3 \text{ kg}\cdot\text{m}^{-2}$ (range, $17.7\text{--}56.8 \text{ kg}\cdot\text{m}^{-2}$). 17 of the 50 patients were overweight, five were moderately obese, and two was severely obese. Patients had MRI PDFF from one to 33%, and we found corresponding SSE from 1.467 to $1.625 \text{ mm}\cdot\mu\text{s}^{-1}$.

For the validation cohort, 50 patients with a mean age of 56 years (with the total sample set ranging from 24 to 84 years of age), including 50 % female and 50 % male were recorded. The mean BMI was $24.1 \text{ kg}\cdot\text{m}^{-2}$ (range, $15.6\text{--}36.14 \text{ kg}\cdot\text{m}^{-2}$). Nine of the 50 patients were overweight, four were moderately obese, and one was severely obese. Patients had MRI PDFF from one to 33%, and we found corresponding SSE from 1.454 to $1.606 \text{ mm}\cdot\mu\text{s}^{-1}$.

4.2.6.2 Intra- and interoperator variability

In this larger clinical study, the intra- and interoperator reproducibility of the SSE evaluation was evaluated on 50 patients. For the intra-operator measurements, one operator did two acquisitions per patient for 50 patients. For the inter-operator measurements, two acquisitions were performed by two different physicians for 50 patients.

We used the Bland-Altman plot method to define the intervals of agreement to study intra- and interoperator variability. For patients with MRI PDFF varying from 1% to 33%, were are studying SSE from 1.454 to $1.625 \text{ mm}\cdot\mu\text{s}^{-1}$. The interval should not exceed $\pm 0.05 \text{ mm}\cdot\mu\text{s}^{-1}$ if we want to be able to precisely grade hepatic steatosis.

The intra-operator standardized coefficient of variation (CV) was $0.37 \pm 0.006\%$. Bland-Altman analysis also demonstrated good agreement between intra-operator measurements: $\text{MSD} \pm 0.016 \text{ mm}\cdot\mu\text{s}^{-1}$ (upper limit of agreement [ULA]: $+0.015 \text{ mm}\cdot\mu\text{s}^{-1}$; lower limit of agreement [LLA]: $-0.017 \text{ mm}\cdot\mu\text{s}^{-1}$, Mean: -0.001), see **Figure 4.12**, a.

The inter-operator standardized CV was 0.57 ± 0.008 %. Bland-Altman analysis also demonstrated good agreement between inter-operator measurements: $\text{MSD} \pm 0.024 \text{ mm} \cdot \mu\text{s}^{-1}$ ([ULA]: $+0.020 \text{ mm} \cdot \mu\text{s}^{-1}$; [LLA]: $-0.27 \text{ mm} \cdot \mu\text{s}^{-1}$, Mean: -0.003), see **Figure 4.12**, b.

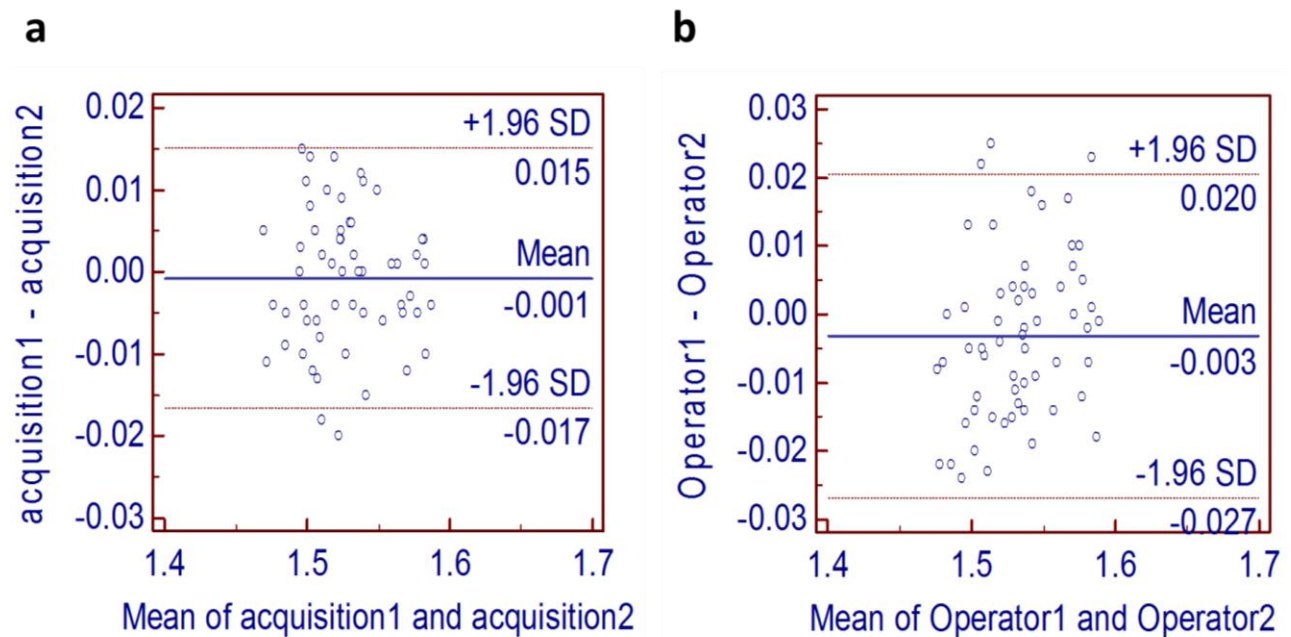


Figure 4.12 – Intra- and interoperator variability. Bland-Altman analysis was performed for (a) intraoperator variability and (b) interoperator variability. For both tests, no relationship between the difference and the magnitude of measurements was found, no systematic bias was observed, and very few outliers were detected.

SSE were found to be consistent both in case of intra- and interoperator measurements. The interval of variability can allow hepatic steatosis assessment regarding the range of sound speed we are studying the liver.

Regarding the correlation between SSE and MRI PDFFF, in the pilot study we found a linear relationship between the two variables. However, at larger scale, we observed that this relationship was not perfectly linear. We then thought of using the Wood's formula to explain sound speed variation along with fat fraction. Our approach is detailed in the next section.

4.2.6.3 The Wood equation

In his PhD thesis, Fabien Mézière (Mézière 2014) uses the Wood's formula (Wood 1930) to calculate the sound speed in the trabecular bone. This bone is a porous type of bone that was considered as a biphasic medium. In our case, we made the hypothesis that in the hepatic steatosis, the liver progressively transforms itself in a biphasic medium made of a mix of liver and fat cells. The idea is to characterize the liver by its fat fraction and find the corresponding sound speed.

In his PhD thesis, Fabien Mézière demonstrated, with numerical simulation, that the sound speed in a porous (fluid/solid) medium was between the one in the fluid and the one in the solid. However, the value was much closer to the velocity in the fluid. The sound speed in the medium is therefore not simply the mean of the sound speed in each phase.

In a homogeneous medium (HM), the relation between sound speed (c), bulk modulus (κ), density (ρ) is given by the Newton-Laplace equation:

$$c_{HM} = \sqrt{\frac{\kappa_{HM}}{\rho_{HM}}}$$

Equation 4.6 - Newton-Laplace equation.

The idea is now to write a similar relation for the sound speed c_{eff}^{th} in a porous medium, here characterized by its fat fraction φ_f , with homogenized (effective) density ρ_{eff} and bulk modulus κ_{eff} . The effective density is by definition the density of the porous medium (ratio between its mass and its volume), and can be written as:

$$\rho_{eff} = \varphi_f \rho_f + (1 - \varphi_f) \rho_l$$

Equation 4.7 – Effective density in porous medium, where φ_f is the fat fraction in the liver, ρ_f and ρ_l are respectively the density of the fat and of the liver.

A similar formula makes it possible to obtain the effective bulk modulus κ_{eff} , with however a small subtlety since in this case we must have recourse to the inverses of the bulk modulus:

$$\frac{1}{\kappa_{eff}} = \varphi_f \frac{1}{\kappa_f} + (1 - \varphi_f) \frac{1}{\kappa_l}$$

Equation 4.8 - Effective bulk modulus in porous medium, where φ_f is the fat fraction in the liver, κ_f and κ_l are respectively the bulk modulus of the fat and of the liver.

An analogy with springs makes easy to understand why we used the inverse bulk modulus. From the point of view of the propagating wave, the porous medium is similar to a succession of springs in series, with a bulk modulus κ_f or κ_l , depending on the traversed medium. Now, when two springs are in series, inverse bulk modulus are summed to obtain the equivalent inverse bulk modulus.

By using the resulting effective density and bulk modulus, the theoretical sound speed in the homogenized medium was:

$$c_{eff}^{th} = \sqrt{\frac{\kappa_{eff}}{\rho_{eff}}} = \sqrt{\frac{1}{\left(\varphi_f \frac{1}{\kappa_f} + (1 - \varphi_f) \frac{1}{\kappa_l}\right) (\varphi_f \rho_f + (1 - \varphi_f) \rho_l)}}$$

Equation 4.9 – Wood’s formula (Wood 1930), where φ_f is the fat fraction in the liver, κ_f and κ_l are respectively the bulk modulus of the fat and of the liver, ρ_f and ρ_l are respectively the density of the fat and of the liver.

After development of the Wood’s formula, presented in appendix 2, we obtain the sound speed in the patient liver ($c_{patient}$) as a function of the fat fraction:

$$c_{patient} = \sqrt{\frac{1}{b \times \varphi_f^2 + c \times \varphi_f + d}}$$

Equation 4.10 – Estimation of the sound speed in the patient’s liver using the fat fraction.

Coefficient b , c , and d , detailed in appendix 2, are expressed with ρ_f , ρ_l , κ_f and κ_l . In our case, for calculating φ_f for one patient, we took the biopsy result in percent of steatotic hepatocytes. However, it was previously demonstrated by Idilman and colleagues (Idilman et al. 2013), that the percentage of steatotic hepatocytes (biopsy) was equivalent to twice the PDFF (%). We therefore used $\varphi_f = 2PDFF$, and as the PDFF is expressed as a percentage, **Equation 4.10** became:

$$c_{patient} = \sqrt{\frac{1}{b \times \left(\frac{2PDFF}{100}\right)^2 + c \times \left(\frac{2PDFF}{100}\right) + d}}$$

Equation 4.11 - Estimation of the sound speed in the patient's liver using PDFF.

Using **Equation 4.11**, we aim to calculate what we called a theoretical model, expressing the relationship between SSE and PDFF using fixed ρ_f , ρ_l , κ_f and κ_l . As the liver has its limits, even in case of severe steatosis, the liver will not have the pure fat characteristics. For the densities, we chose $\rho_f = 0.79 \times 10^{-3}$ kg.m⁻³ and $\rho_l = 1.3 \times 10^{-3}$. ρ_f corresponds to the smallest density value recorded for a fatty liver (Goumard et al. 2014), and ρ_l correspond to upper limit density value recorded for healthy liver (Yu et al. 2004; Goumard et al. 2014). To calculate κ_f and κ_l , we use the Newton-Laplace equation (**Equation 4.6**), with $c_f = 1.48$ mm.μs⁻¹ as the mean SSE found for severe steatosis, and $c_l = 1.60$ mm.μs⁻¹ as the mean SSE found for healthy livers.

We tested the ability of this theoretical Wood equation to explain the relationship between the SSE and the fat fraction calculated with MRI (**Figure 4.13**).

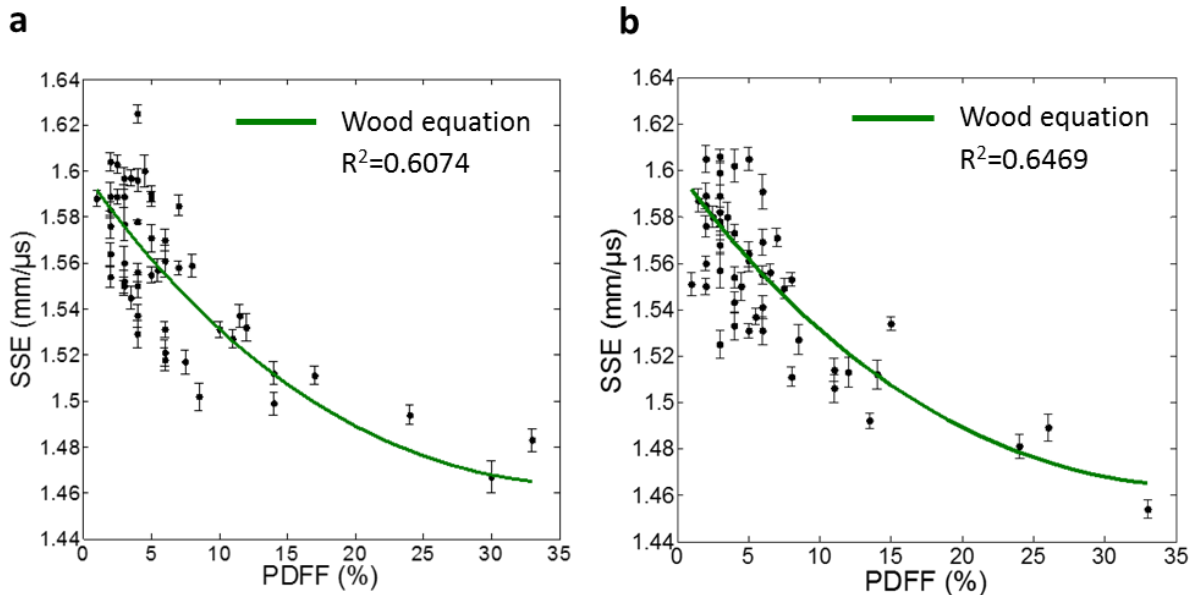


Figure 4.13 – Wood equation applied on both a 50-patient cohort and a validation cohort. (a) 50-patient cohort. (b) 50-patient validation cohort. For each patient, SSE data are the mean SSE based on two ultrasound acquisition realized by the same operator. The error bar is the corresponding to the standard deviation between these two values.

We observed, both for the first cohort and the validation cohort, that the Wood equation guaranty a significant coefficient of determination between the SSE and the fat fraction calculated with MRI ($R^2 > 0.6$) (see **Figure 4.13**).

Regarding these analysis, the Wood equation seemed to be relevant to study our data set. As a last step, for each patient cohort, we used **Equation 4.10** to calculate the ultrasound fat fraction $US\varphi_f$ for each patient:

$$US\varphi_f = \frac{-c + \sqrt{c^2 - 4b\left(d - \frac{1}{c_{patient}}\right)}}{2b}$$

Equation 4.12 - Ultrasound fat fraction $US\varphi_f$ calculation based on the sound speed measured in the patient's liver $c_{patient}$.

The comparison between the ultrasound fat fraction $US\varphi_f$ and the fat fraction of reference (2*PDFF) is presented in **Figure 4.14** for the two patient cohorts.

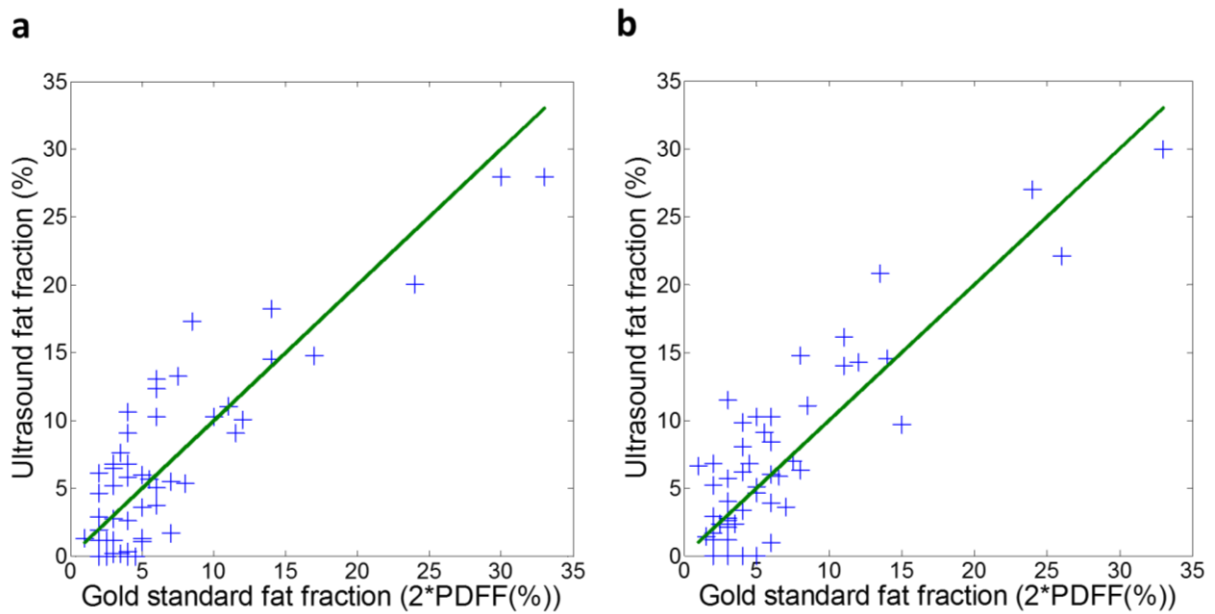


Figure 4.14 – Comparison between ultrasound fat fraction and gold standard fat fraction. Ultrasound fat fraction was calculated using the coefficient from the optimal wood's fit of the cohort and the Wood's formula. The gold standard fat fraction is the percentage of steatotic hepatocytes (biopsy), equivalent to twice PDFF (%). Comparison between ultrasound fat fraction and gold standard fat fraction **(a)** for the first 50-patient cohort, $R^2 = 0.73$, and **(b)** for the 50-patients- validation cohort, $R^2 = 0.76$.

As shown in **Figure 4.14**, the Wood equation enabled a robust correspondence between the gold standard fat fraction (%) and the ultrasound fat fraction (%). Significant coefficients of determination were found both for the first patient cohort ($R^2 = 0.73$) and the validation patient cohort ($R^2 = 0.76$).

By combining adaptive focusing and aberration correction we were able to calculate precise sound speed *in vivo* in the liver. Then, by using the Wood's equation, we found a theoretical model explaining sound speed variation along with the steatosis grade. This theoretical model provides an excellent agreement with clinical results on both cohorts of 50-patients and could be used in conjunction with the SSE technique to grade liver steatosis with Ultrasound.

4.2.7 Conclusion and perspectives

We used a three steps technique to precisely calculate sound speed (SSE) in a medium. The first step provided an estimate of the sound speed optimizing the spatial coherence of backscattered speckle noise. As this estimation can be degraded by aberrations occurring in the first propagation layers, a virtual point like reflector was created in order to identify and correct these aberrations. Finally, a third correction step was introduced for an optimal estimation of liver sound speed in order to correct the bias introduced by the subcutaneous layer thickness.

This technique based on adaptive focusing in speckle noise and aberration correction was tested in ultrasound phantoms and *in vivo* in patients. In both case our method was able to find the sound of sound corresponding to the medium.

In the case of steatosis diagnosis it was demonstrated that the SSE was related to the fat fraction. This analysis lead to the conclusion that SSE was able to diagnose healthy liver and steatosis (>10% biopsy) as well as biopsy and MRI. There are many advantages to be able to diagnose hepatic steatosis. Hepatic steatosis is an important risk factor for postoperative complications after major liver resection and living donor liver transportation (McCormack et al. 2007; Zamboni et al. 2001). Hepatic steatosis 10% or greater is known to be critical on patients who undergo living donor liver transplantation because of the risks of complications such as initial graft dysfunction and poor graft survival (Trotter et al. 2007).

In addition to differentiate healthy liver and hepatic steatosis, we demonstrated that SSE, combined with the use of the Wood equation, was able to give access to an ultrasound fat fraction (%). The latter was found to be highly correlated with gold standard fat fraction ($R^2 = 0.73$) and enabled to grade hepatic steatosis with non-invasive ultrasound.

As an important perspective, we should continue the investigation and improve the method to free the technique from physician superficial layer measurement (see Section 4.2.2.3). One other group (Jaeger et al. 2014; Jaeger and Frenz 2015) studied *in vivo* sound speed estimation and succeeded in calculating sound speed in each layers. They were able to calculate the sound speed in each layer (fat, muscle, liver) but not yet with the necessary precision to grade steatosis ($\sim 0.005 \text{ mm} \cdot \mu\text{s}^{-1}$).

With this work on quantitative ultrasound in the liver we learned how to correct phase aberration using the iterative speckle noise technique. The next section focuses on skull aberration correction towards transcranial adaptive focusing.

4.3 Toward transcranial adaptive focusing

In adults, anatomic images are not available with ultrasound imaging. Through adult skull, only blood vessel imaging is so far possible. This non-invasive technique is called transcranial Color Doppler (TCCD). In this section, we first present a state-of-art on the existing TCCD in clinical practice and on other research toward transcranial imaging improvement. Finally, we present the results we had after phase, amplitude, and sound speed correction for transcranial imaging in numerical simulation.

4.3.1 The state-of-art

In this state-of-art section, first, we present the anatomy and acoustic properties of the skull to introduce the challenge of transcranial ultrasound imaging. Then we expose conventional TCD use nowadays in clinical practice. Finally, we study different existing techniques to correct aberration induced by the skull to improve ultrasound imaging.

4.3.1.1 Anatomy and acoustic properties of the skull

The brain is one of the best protected organs of the human body. It bathes in the cerebrospinal fluid which can soften the accelerations of the head. The cranial vault, which surrounds it, is composed of different bones linked by sutures. The bone of the skull has particularly porous character at its center and a thickness that can vary from 10 mm to 1 mm in the thinnest temporal zone. Nevertheless, the temporal bone remains an extremely strong aberrator for the ultrasound beam.

The human skull is a complex medium for the ultrasound transmission because of its solid, multi-scale and different porosities layers composition. Basically, the skull presents a three-layered structure, with a porous zone, called the diploe, stacked between two dense layers, respectively, the outer and inner tables (**Figure 4.15**).

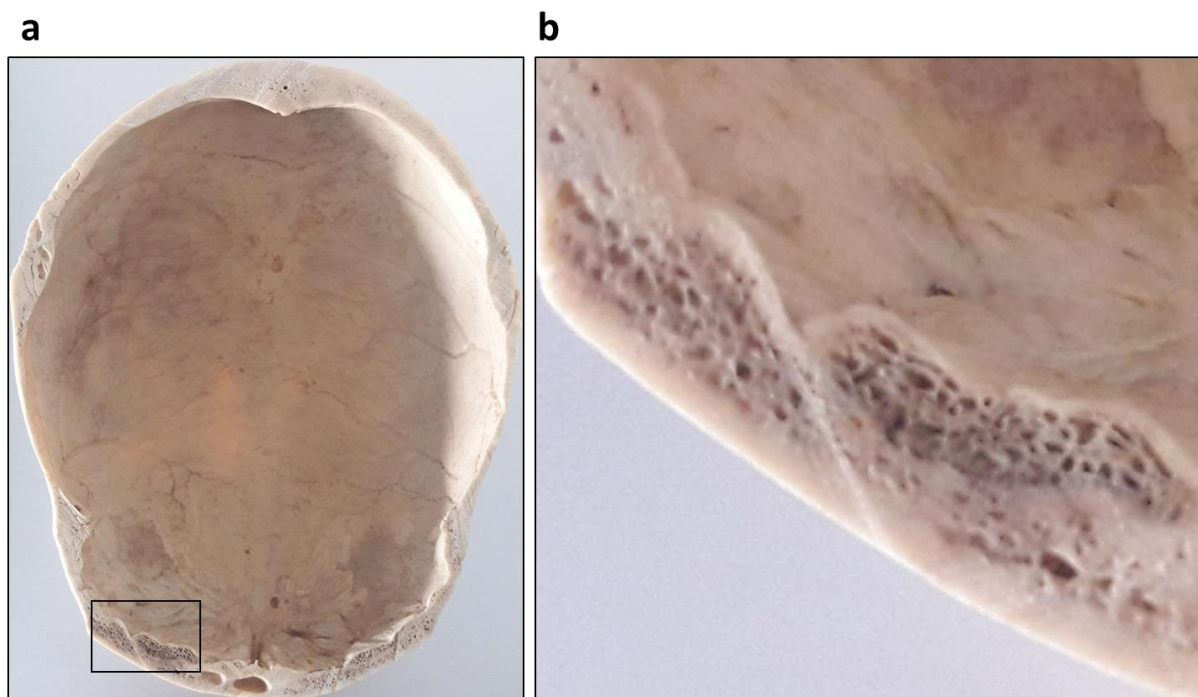


Figure 4.15 – Skull structure. (a) Half skull, coronal slice. (b) Zoom from the black rectangle in (a) on the spongy bone (Diploe, ($c \approx 2700 \text{ m.s}^{-1}$)), porous layer between two compact bones ($c \approx 3000 \text{ m.s}^{-1}$).

The skull density may vary from 1000 to 2200 kg.m^{-3} . The strong acoustic impedance rupture at the skin/bone and bone/dura mater interface is a very limited factor of acoustic transmission. The spatial variations of the speed of sound induce a phase and amplitude distortion of the wave front propagating in the medium. These aberrations degrade the spatial resolution. A large discrepancy in acoustic velocities between brain tissue ($c \approx 1500 \text{ m.s}^{-1}$) and skull (c varies from

2700 to 3000 m.s⁻¹, see **Figure 4.15 b**), and a severe attenuation of ultrasound in the skull bone severely degrade the beam shape. This problem was first discovered by White and colleagues (White et al. 1968) during investigation into brain imaging. It was later observed (Marsac 2013) that the ultrasound transmission through the skull was limited to 40% of the incident pressure field and that an incidence inferior to 30 degrees was preferable in order to limit the phase aberration.

The skull prevents, so far, from imaging brain structure with an ultrasound scanner however, blood vessel imaging is possible using transcranial Doppler through skull acoustic windows (thin skull regions).

4.3.1.2 Conventional transcranial ultrasound imaging

Transcranial Doppler (TCD) and transcranial color Doppler (TCCD) are types of Doppler that measure the velocity of blood flow through the brain's blood vessels by measuring the echoes of ultrasound waves moving transcranially (through the skull).

TCD, first described in 1982 (Aaslid, Markwalder, and Nornes 1982), is a noninvasive ultrasound technique involving the use of a low-frequency (≤ 2 MHz) transducer probe to insonify arteries from the circle of Willis through relatively thin bone windows. TCD allows dynamic monitoring of cerebral blood flow velocity (CBF-V) and vessel pulsatility over extended time periods, with a high temporal resolution. It is relatively inexpensive, repeatable and its portability offers increased convenience over other imaging methods, allowing continuous bedside monitoring of CBF-V, which is particularly useful in the intensive care setting (Moppett and Mahajan 2004).

TCCD enables the display of a two-dimensional color-coded image of big brain's blood vessels (see **Figure 4.16, b**).

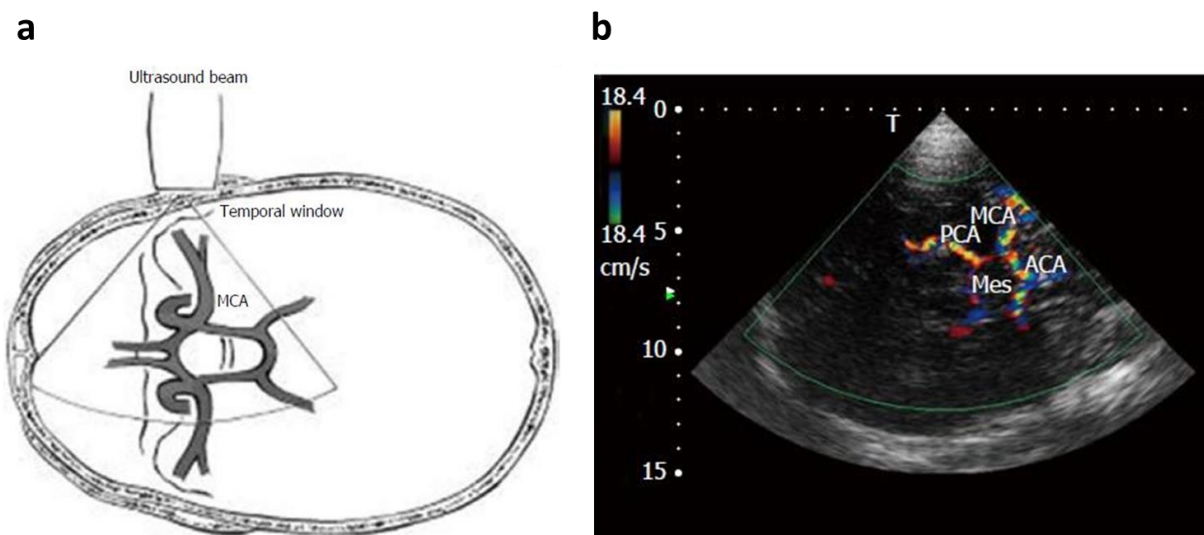


Figure 4.16 – Basilar arteries insonification using TCCD. (a) Transmission of ultrasound beam through skull using sectorial probe with a 2.0-3.5 MHz emission frequency. Probe is positioned on temporal window. (b) Circle of Willis (anterior, middle and posterior cerebral arteries) (Adapted from (D'Andrea et al. 2016)).

There are many current applications of TCD and TCCD in adults and children (D'Andrea et al. 2016) such as intra- and extracranial arterial stenosis and occlusion (Christou et al. 2001), head injury and raised intracranial pressure (ICP) (Moreno et al. 2000). However, approximately 10–20% of patients have inadequate transtemporal acoustic windows (Marinoni et al. 1997).

Ultrasound images quality depends significantly on the focus quality of the ultrasonic beam (in emission and in reception). For this reason, it is of great interest to work on improving ultrasonic beam focus quality after passing through the skull.

4.3.1.3 Phase aberration correction to improve transcranial imaging

By taking into account the aberrations induced by the skull bone, it has been proven that a complex set of transmit signals assessed using time reversal processing should exist to refocus optimally through the skull bone (Tanter, Thomas, and Fink 1998). To achieve this goal transcranially, most aberration correction methods model aberration as a phase screen or a phase and amplitude screen. The problem is thus reduced to calculating the delays (or delays and amplitudes) to be applied to each element of the ultrasound array, to obtain an optimal focus (Måsøy, Johansen, and Angelsen 2003). With a cross-correlation of speckle noise received on neighboring transducers, the signal coherence is augmented and it corrects the aberration (Flax and O'Donnell 1988; Krishnan, Rigby, and O'Donnell 1997; Li and O'Donnell 1995; Mallart and Fink 1994). This correlation method can be extended to several frequency bands for wide aberrations, where the phase screen hypothesis is no longer accurate (Ng et al. 1997). Quality factors such as speckle brightness (Nock, Trahey, and Smith 1989) or focus criterion (Mallart and Fink 1994; Li and Li 2003) can be maximized in order to correct the aberration on the acoustic image. The signal from moving particles (such as red blood cells within the blood) was also studied (Zhao, Bohs, and Trahey 1992; Bohs 1992) to correct the image. Several methods using static or moving targets in three dimensions were compared for imaging improvement Doppler (Ivancevich, Dahl, and Smith 2009).

Noninvasive brain imaging devices made of two identical “twin” linear arrays were also studied to take into account the defocusing effect of the skull (Vignon et al. 2004). The two linear arrays were located on each side of the head and the technique was tested using simulated structural transcranial images of a brain model. It was shown how to differentiate the respective influence of the two bone windows on the path of an ultrasonic wave going from one array to the other, and how to estimate at each frequency the attenuation and phase shift locally induced by each of the bone windows. This information was then used to perform adaptive focusing through the skull. Compared to uncorrected wavefronts, the spatial shift of the focal point was cancelled, the width of the focal spot was reduced, and side lobes level was decreased up to 10dB. To enhance the two matrix array probes technique, one other group (Lindsey et al. 2014) used microbubble contrast enhancement to perform 3D transcranial ultrasound imaging.

In order to use only one ultrasound probe, other methods are based on the presence of a bright reflector, inside the medium, to correct the aberration (Flax and O'Donnell 1988; C. Prada, Wu, and Fink 1991). If point-like reflectors are present in the medium, the time reversal (Fink 1992) is an effective way to focus. This method of time reversal can be summarized in three parts. (i)

The ultrasound probe emits an ultrasonic impulse which will insonify the whole medium (**Figure 4.17**). This wavefront will be deformed during its propagation due to the aberration layer and will then be reflected on the point-like reflector. (ii) The backscattered echoes will then propagate towards the probe (and will be also deformed by the aberrating layer) and will be recorded by each of the piezoelectric elements (**Figure 4.17**). (iii) Since the wave equation is invariant by time inversion (i.e. replace t by $-t$), if the recorded signal is time reversed (**Figure 4.17**), the emission of the wavefront originating from this signal will propagate in the medium, will be deformed, and will focus on the point-like reflector.

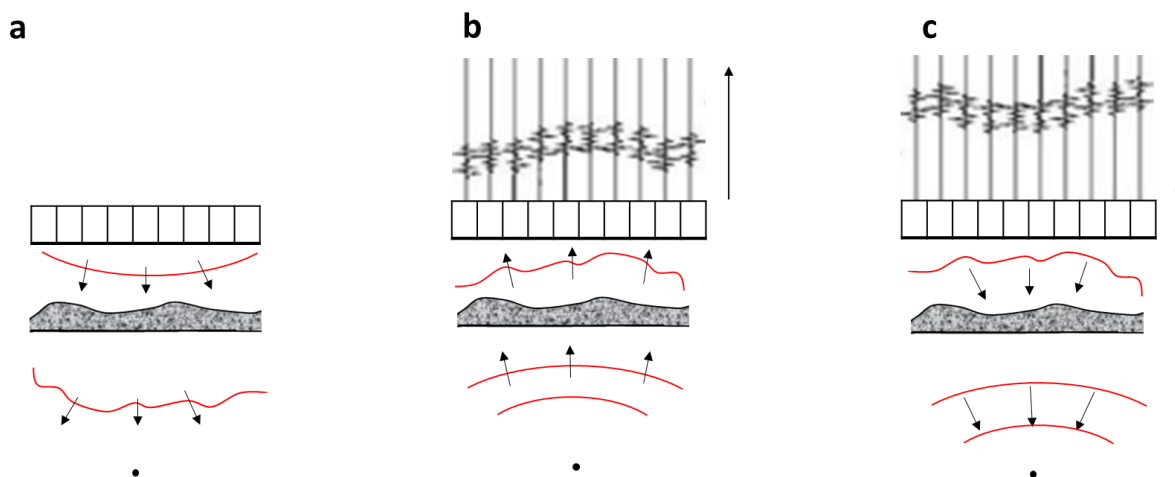


Figure 4.17 – Time reversal for phase aberration correction. (a) Ultrasound illumination, from the probe through the aberrating layer and the medium. (b) Backscattered echoes coming from a point-like reflector in the medium. (c) The received signal is time-reversed and emitted. The ultrasound beam is corrected after passing through the aberrating layer.

This method is very effective because no hypothesis is made on the aberration. If more than one reflectors are present in the medium, by iterating the method described above, this method will converge towards focus on the brightest diffuser (C. Prada, Wu, and Fink 1991). This last method only works in the case where the different point-like diffusers are at least separated by the width of the ultrasonic beam used to focus in the case optimal (C. Prada, Wu, and Fink 1991; Claire Prada and Fink 1994). In the absence of point-like reflectors, it is possible to physically create one as, for example, by generating cavitation bubble (Pernot et al. 2006).

These previous methods using time reversal are limited for imaging because only few bright reflectors are present in human tissues. For ultrasound, human tissue is seen as a random distribution of small diffusers (Rayleigh scattering), where simple diffusion dominates. An iterative time reversal technique would not work because the signal backscattered by the human tissues can be assimilated to speckle noise.

One method to solve this problem is to virtually create a point-like reflector in the medium. One method of time reversal operator decomposition has been proposed by Robert and colleagues (Robert and Fink 2008). More recently, another method for creating a virtual point-like diffuser from a random distribution of diffuser has been proposed (Montaldo, Tanter, and Fink 2011). The idea is to get independent realizations of speckle noise by micro-angling the ultrasonic beam around the target point. A coherent summation of these different acquisitions can create a virtual

point-like reflector (see section 4.2.2.2). By returning temporally its signal in an iterative algorithm, highly degraded ultrasound images can be restored. In this method, previously in this chapter in the case of the liver (see section 4.2), realizations of speckle were obtained by micro-steering of the initial beam, so the number of independent realizations of speckle is limited by the ratio between the size of the isoplanatic patch and the wavelength (Robert and Fink 2008). However, in case of strong aberration, such as those induced by the skull, this ratio decreases, leading to poor signal-to-noise ratio of the virtual point-like reflector. Instead of micro-angling the ultrasonic beam around the target point, we can also acquire independent realizations of speckle by using only the natural motion of scatterers (Bruno-Felix Osmanski et al. 2012). We can use the temporal decorrelation of particles moving in a flow, which can be assimilated to red blood cells. With time reversal of moving speckle noise we can acquire as many realizations of speckle as needed.

In the next section we used the time reversal of moving speckle noise technique to improve the focus quality of the ultrasonic beam passing through the skull in numerical simulation.

4.3.2 Numerical simulation of skull aberration correction

In this section, we used the time reversal of moving speckle noise technique to improve the focus quality of the ultrasonic beam passing through the skull. We combined phase, amplitude and sound speed correction to perform transcranial imaging in numerical simulation.

4.3.2.1 Numerical simulation parameters

In collaboration with the master student Jack Sauvage, we constructed a numerical model allowing for the simulation of the time reversal of moving speckle noise method mentioned section 4.3.1.3. The set of calculations and media construction were carried out using Matlab. The numerical simulation of the wave propagation was performed with the k-Wave toolbox[©], using a method of pseudo-spectral discretization (spatial discretization in the Fourier domain).

Since transcranial imaging is over the temporal window (limited area), it is preferable to use a probe with a large angular aperture in order to access to a large field of view. One probe fitting this exigence could be a phased array probe (e.g. XP5-1 probe, Supersonic Imaging, Aix-en-Provence, France). This probe is characterized by a 1-5MHz bandwidth, with piezo electric elements standing $\lambda/2$ apart from each other, where λ is the wavelength at the probe central frequency. We constructed our numerical simulation based on this probe. The ultrasonic probe was modeled by a linear array of 128 monopolar sources, spaced by $\lambda/2$ and emitting pulses with Gaussian impulses of central frequency 2.25 MHz. The number of cycles of these pulses was fixed at 3. We chose to create an isotropic spatial mesh ($dx = dz$) representing the propagation plan of dimensions 512×812 points. In order to properly spatially discretize the ultrasound wave, we chose a spatial step $dx = \lambda/10$ (i.e. $dx = 0.67mm$ in a medium characterized by $c = 1540m.s^{-1}$). With these parameters, we obtained a propagation plane of $512 \times dx \approx 3.4 cm$ wide and $812 \times dz \approx 4.9 cm$ in depth. The sampling frequency was set to $f_s = 75MHz$ ($dt \approx 13 ns$). Non linearity was not taken into account (Beyer's parameter $B/A = 0$).

To characterize the medium of interest, two maps were systematically constructed, a density map and a sound speed map. The density of the medium was set to an average of $\rho = 1000\text{kg.m}^{-3}$ and the sound speed was set to an average of $c_0 = 1540\text{m.s}^{-1}$. In order to get closer to the physical properties of biological tissues, a variance of these mean was added to create speckle noise.

To perform the time reversal of moving speckle noise method, we placed the targeted vessel section at 3.4 cm depth, aligned with the array center. We paid attention to have a ratio between the depth of focus and the aperture (F-number) greater than or equal to 1 (F-number).

Regarding the numerical simulation of the skull, in order to reproduce its porosity, a screen was generated from X-ray computed tomography (CT) data according to the method described by Aubry and colleagues (Aubry et al. 2003). Raw CT values were given in Hounsfield Units (H), defined by:

$$H = 1000 \frac{\mu_x - \mu_{\text{water}}}{\mu_{\text{bone}} - \mu_{\text{water}}}$$

Equation 4.13 – Formula for raw CT values in Hounsfield Unites, with μ_x , μ_{bone} , and μ_{water} , respectively, denoting the photoelectric linear attenuation coefficient of the explored tissue, bone, and water.

As the skull imaged in CT was placed in water and degassed, it was exclusively made of water and bone with a varying density. With φ the bone porosity, we used the relationship between the photoelectric linear attenuation coefficient of the explored tissue, and the attenuation coefficients of bone and water:

$$\mu_x = \varphi \mu_{\text{water}} + (1 - \varphi) \mu_{\text{bone}}$$

Equation 4.14 - Relationship between the photoelectric linear attenuation coefficient of the explored tissue, and the attenuation coefficients of bone and water.

In this case, the porosity map is directly linked to the Hounsfield map:

$$\varphi = 1 - \frac{H}{1000}$$

Equation 4.15 – Equation for the porosity map.

Density (ρ) and sound speed (c) of the skull were deduced from the porosity maps, with $\rho_{\text{bone}}=1800 \text{ kg.m}^{-3}$ and $c_{\text{bone}}=2700 \text{ m.s}^{-1}$. A slice of the 3-D density map is given in **Figure 4.18**.

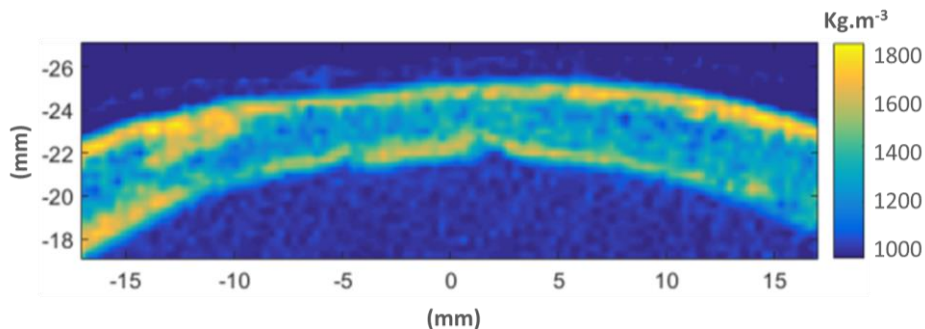


Figure 4.18 - Slice of the 3-D mass density map deduced from CT scans.

4.3.2.2 Phase aberration

We used the time reversal of moving speckle noise method, mentioned section 4.3.1.3 and based on the temporal decorrelation of particles moving in a flow, to correct phase aberration induced by the skull. We used 100 different speckle realizations to create our virtual point-like reflector, and we obtained the corrected delay laws with three iterations.

Figure 4.19 shows the improving of the focus quality, in presence of a skull (from CT scan data), after phase aberration correction.

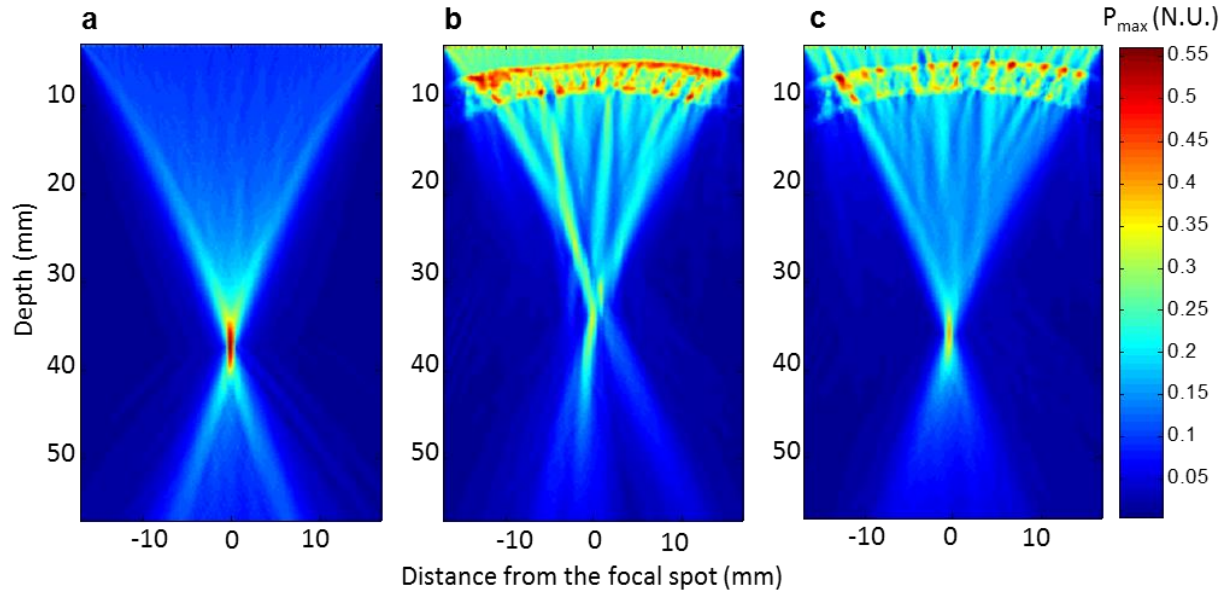


Figure 4.19 – Pressure field (a) Without aberrator, (b) With the skull (from CT scan data) but without phase aberration correction, (c) with the skull and with phase correction.

To observe in more details the impact of our phase aberration correction on the focus quality, we studied the pressure amplitude at the focal spot (Figure 4.20).

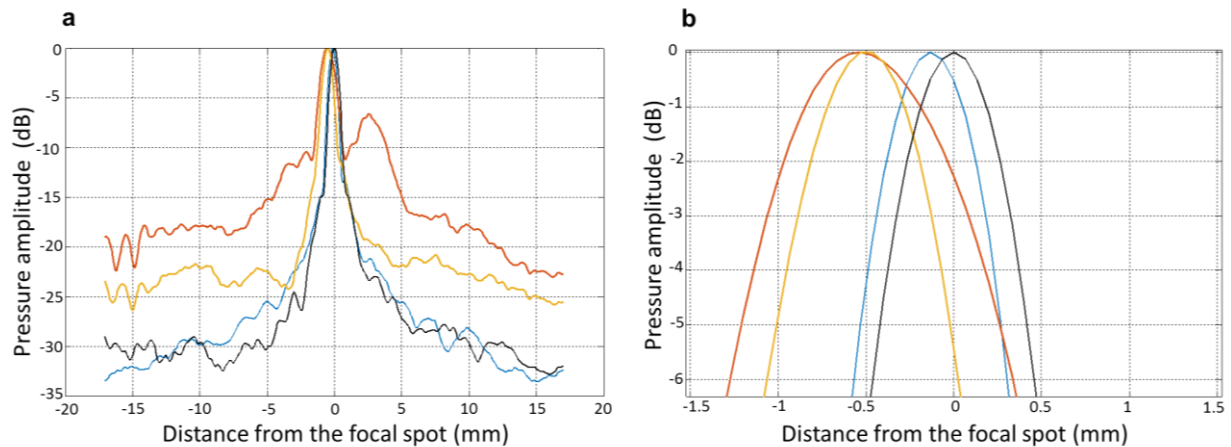


Figure 4.20 - Beam lateral profiles (a) Pressure is plotted after focusing in homogenous medium (blue line), after focusing through the skull (from CT scan data) with a punctual source at the focal depth (black line), after focusing through the skull without aberration correction (orange line), after focusing through the skull with phase aberration correction (yellow line). (b) Zoom until -6dB and centred on the focal spot for resolution comparison.

Our gold standard was the pressure field after focusing through the skull (from CT scan data) with a punctual source at the focal depth. In this case, there is no need for the speckle noise technique because there is a bright reflector in the medium, and we obtain the best focus quality (black curve). We observed a significant improve of the focus quality with the phase aberration correction (**Figure 4.20**, from the orange to the yellow line). However we also noticed a shift from the targeted focal spot (0.5 mm left). Indeed, in this case we reach the physical limits of the speckle noise technique. In presence of a thin defocusing phase aberrator, the isoplanetic patch is infinite and the focus is optimal. As soon as we used the speckle noise technique with a strong aberrator, thick and with focusing properties (lens), we can introduce a small shift (here 0.4 mm to the left, yellow and orange curves), and the iterative algorithm will converge toward the position of the first maximal pressure field.

After analyzing the impact of our phase aberration correction on the focal spot, we decided to see if this can improve a B-mode imaging. For our numerical simulation, we constructed two different media to image through the skull (see **Figure 4.21**). In the first medium, three bright reflectors were placed in the imaging plan. In the second medium, one anechoic compartment (like a cyst), characterized by no variation of impedance, was placed in the medium.

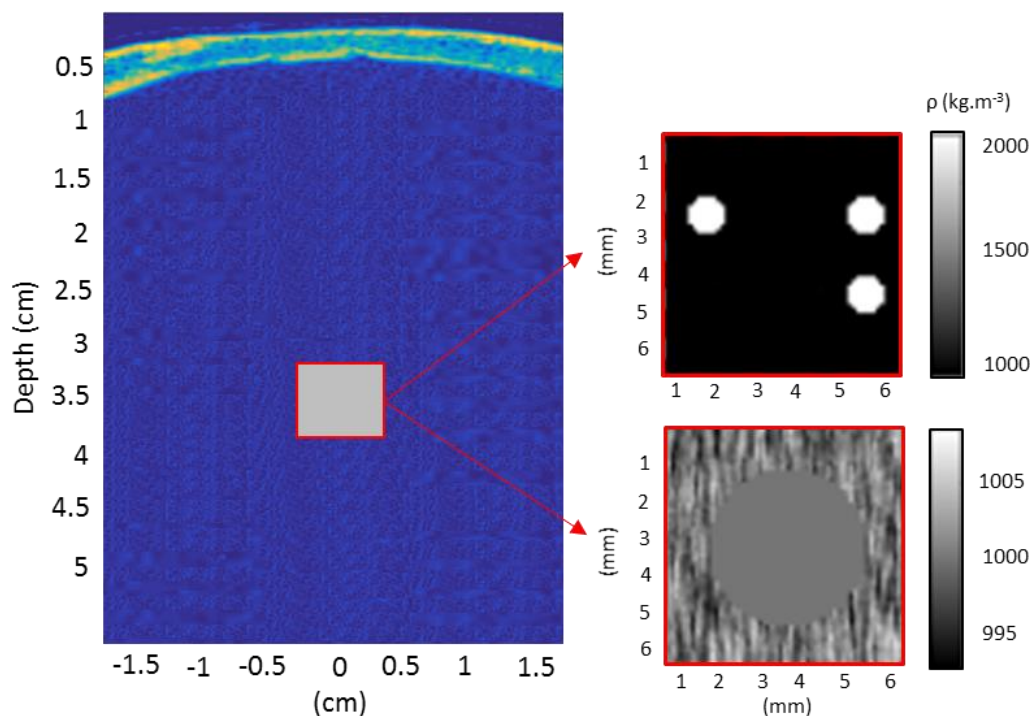


Figure 4.21 – Created media for transcranial B-mode imaging. For both numerical simulations we used the skull with speed and density maps deduced from CT scan. In the first medium (**medium 1**), three bright reflectors were place in the imaging plan. In the second medium (**medium 2**), one anechoic compartment was placed in the medium. The area of interest was located 3.5 cm depth.

There were several steps to reconstruct a B-mode image of the medium with phase aberration correction. The first step was a learning step. We considered they were a blood vessel in the area we aim to image (3.5 cm depth, centered), we used 100 different speckle realizations from this blood vessel to create our virtual point-like reflector, and we obtained the corrected delay law

with three iterations. We then used this corrected delay law in a simple beamforming based on focused ultrasound beams to reconstruct the B-mode image.

It is important to note that this obtained delay law is valid only in a small imaging zone called the isoplanetic zone (Chassat 1989; Tanter, Thomas, and Fink 1998; Montaldo, Tanter, and Fink 2011). The image will therefore be made only on a small number of pixels around the focal point (100×100 pixels, 6×6 mm) (see **Figure 4.21**). If we want to reconstruct the whole image, using focused ultrasound, we would need to apply our speckle noise technique in many spots along rows and columns, and apply each delay law to its corresponding isoplanetic zone.

In this thesis we are only presenting the image in one isoplanetic zone of interest (corresponding to the red square in **Figure 4.21**). In **Figure 4.22**, we present the image of this zone in different cases in order to observe the impact of our phase aberration correction based on time reversal of moving speckle noise. Our final aim is to get as close as possible to the image quality in the case of phase aberration correction when there is a punctual source in the medium. The latter was considered the gold standard of this study.

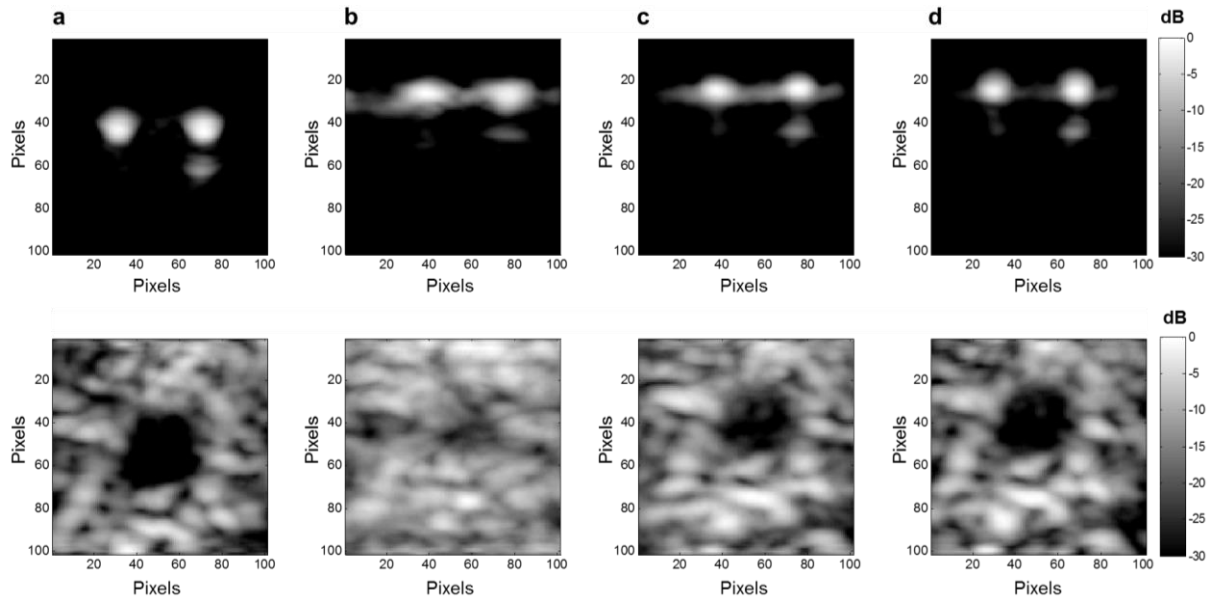


Figure 4.22 – Numerical simulation to observe phase aberration correction impact on transcranial B-mode images in two media. In each configuration, medium 1 (top) and medium 2 (bottom) are imaged. The 6×6 mm surface of interest are presented. Four configurations are detailed: **(a)** without aberrator, **(b)** with skull, without aberration correction, **(c)** with skull, phase aberration correction using the speckle noise technique, **(d)** with skull, phase aberration correction in the case of a punctual source in the medium during the learning step.

In **Figure 4.22**, we can observe that our phase aberration correction based on time reversal of moving speckle noise (**Figure 4.22 c**) significantly improves both resolution (top) and contrast (bottom) compared to the case with the skull but without phase aberration correction. However, neither the resolution, nor the contrast are as good as our gold standard phase aberration correction with a punctual source in the medium. One other phenomena we can notice is that in any case where the skull is present (**Figure 4.22 b, c, d**), there is an error in depth in the image (≈ 18 pixels, ≈ 1.1 mm). This is due to the ultrasound beam acceleration when passing through

the skull. Therefore, we had two areas of improvement to investigate, amplitude modulation and sound speed correction.

In order to get closer to our gold standard (**Figure 4.22 d**), the next parameter we studied was amplitude. Indeed the skull not only induce phase aberrations, but also amplitude distortions.

4.3.2.3 Amplitude modulation

We can observe amplitude distortions when acoustic energy propagates through an attenuating layer varying in thickness (O'Donnell and Flax 1988), and this section investigates how it is possible to modulate this distorted amplitude to improve the focusing quality.

The time reversal process described in section 4.3.2.2 accomplishes compensation for phase aberration, but does not help for an amplitude modulation originating from acoustic losses. Indeed, for phase aberration, the time reversal process changes the time delays induced by an inhomogeneous layer in their opposite. Therefore, when the time-reversed wavefront backpropagates through the aberrating layer all the delays are cancelled. On the contrary, the transducer element located in front of a region of the layer of strong absorption will receive and transmit a signal of small amplitude after the time reversal operation. Thus, when the wavefront travels back through the aberrating layer the amplitude modulation is increased by a power of two (Thomas and Fink 1996). In our technique, we didn't time-reverse and reemit the wavefront, but used the delay law issued from the time-reversed wavefront to focus in the medium. In this delay law the amplitude is equally set to one for every element. In this section our reference to compare the effect of amplitude modulation was our phase aberration correction (**Figure 4.23**, yellow line) because it corresponds to homogenized amplitudes.

It has been demonstrated that when focusing through a strongly absorbing medium like a human skull, the focusing can be improved by correcting the amplitude of the recorded signals (Thomas and Fink 1996; Tanter, Thomas, and Fink 1998). This is particularly important when working at central frequencies above 1MHz. The skull absorption is indeed increasing with the frequency, suggesting to work at low frequency. But decreasing the frequency also means decreasing the resolution.

The signal $s_i(t)$ received by each transducer i after propagation through the skull, corresponds to the signal $s_i^h(t)$ that would be received in a homogeneous medium, but with a time lag τ_i and multiplied by a factor a_i characterizing attenuation from the skull:

$$s_i(t) = a_i s_i^h(t - \tau_i)$$

Equation 4.16 – Received signal after backpropagation through the skull.

For this purpose, the amplitude modulation a_i due to skull attenuation was estimated by comparison with the reference waveform obtained in the same conditions in homogeneous medium: Accordingly to **Equation 4.16**, we deduced that the absorption factor a_i corresponds to the ratio between the amplitudes of the wave packets:

$$a_i = \frac{\max_t\{s_i(t)\}}{\max_t\{s_i^h(t)\}}$$

Equation 4.17 – Absorption factor.

Assuming that the skull is an infinitely thin layer close to the emitting array of transducers, in order to compensate amplitude, one can apply a gain on parts of the wave front that suffered a loss while passing through the skull (**Figure 4.23**, purple line). To do so, we can multiply the emission waveforms by a factor $\left(\frac{1}{a_i}\right)$. One other approach is to amplify amplitude, in order to take benefit of powerful signals (**Figure 4.23**, green line). To do so, we can multiply the emission waveforms by a factor (a_i) .

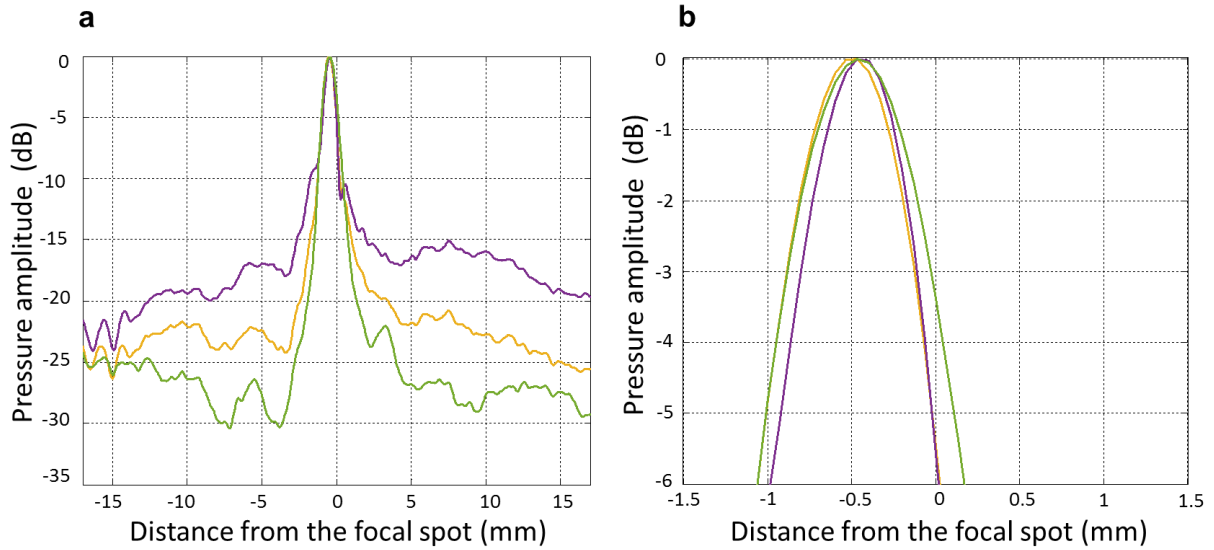


Figure 4.23 – Beam lateral profiles (a) Pressure is plotted after focusing through the skull with phase aberration correction (yellow line), phase aberration correction and amplitude compensation ($/a_i$) (purple line), phase aberration correction and amplitude amplification ($*a_i$) (green line).

In figure **Figure 4.23**, we can observe that amplitude compensation ($/a_i$) (purple line) increases the resolution but degrades the contrast, compared to phase aberration correction only (yellow line). On the opposite, amplitude amplification ($*a_i$) (green line) increases the contrast but degrades the resolution, compared to phase aberration correction only (yellow line). The effects of amplitude amplification on resolution and contrast can be observed in **Figure 4.24**.

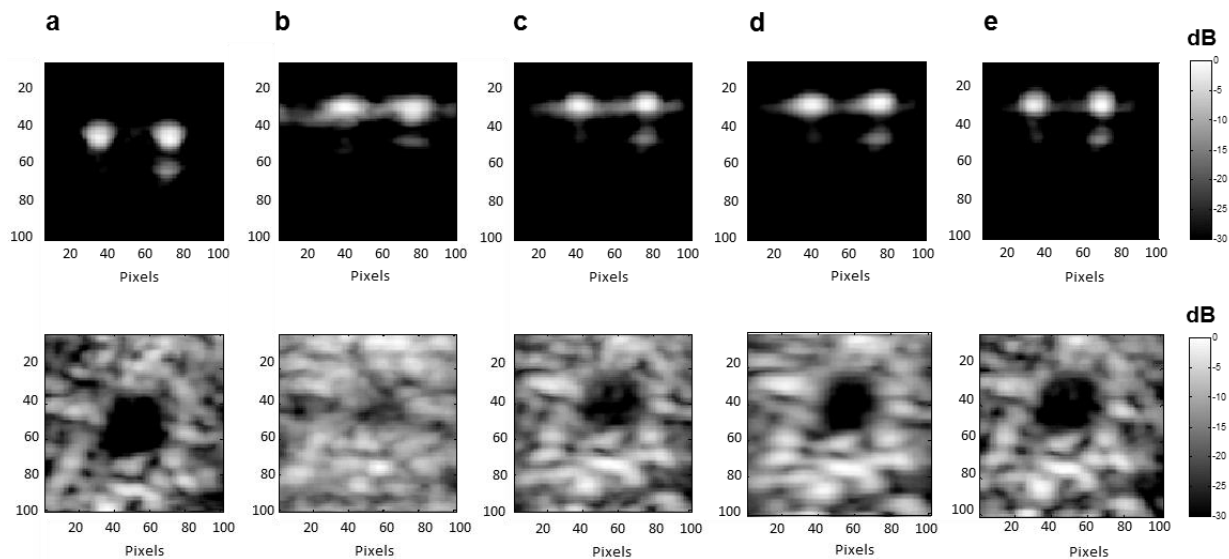


Figure 4.24 - Numerical simulation to observe phase aberration correction and amplitude amplification impact on transcranial B-mode images in two media. In each configuration, medium 1 (top) and medium 2 (bottom) are image. The 6×6 mm surface of interest are presented. Five configurations are detailed: **(a)** without aberrator, **(b)** without any correction, **(c)** with phase aberration correction using the speckle noise technique, **(d)** with phase aberration correction and amplitude amplification using the speckle noise technique, **(e)** with phase aberration correction and amplitude amplification, in the case of a punctual source in the medium during the learning step.

We demonstrated that in order to improve phase aberration correction, we can chose to compensate or to amplify the amplitude, depending on the application (compromise between contrast and resolution). However, in section 4.3.2.2, we also noticed that the phase aberration correction doesn't correct the influence of sound speed changes due to skull passage. Indeed, this technique considers the aberrating layers as a thin phase screen. In the next section we used our previous work to estimate global sound speed from the array to the focal spot and integrate it to the correction process.

4.3.2.4 Sound speed correction

In this section, we used the spatial coherence in random media, based on the Van Cittert-Zernike theorem adapted to ultrasound propagation, to calculate the global sound speed in the medium.

This technique was described in section 4.2.2.1, and for this application, we used 100 independent speckle realizations and three iterations to obtain one global sound speed estimation (SSE) of the ultrasound beam from the array to the focal spot. Then we used this global sound speed in the beamformer to reconstruct the images.

In **Figure 4.25**, we present the image of the two mediums we created in numerical simulation in different cases in order to observe the impact of our sound speed correction.

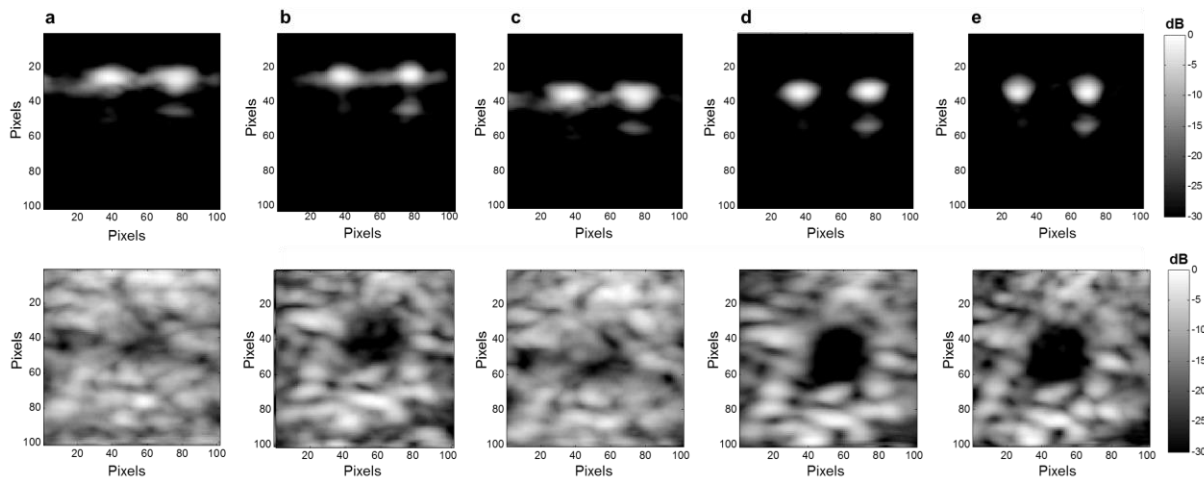


Figure 4.25 - Numerical simulation to observe phase aberration correction, amplitude amplification and sound speed correction impact on transcranial B-mode images in two media. In each configuration, medium 1 (top) and medium 2 (bottom) are image. The 6×6 mm surface of interest are presented. Five configurations are detailed: (a) without any correction, (b) with phase and amplitude aberration correction using the speckle noise technique, (c) only with sound speed correction, (d) with phase aberration correction and amplitude amplification using the speckle noise technique, and with sound speed correction, (e) with phase aberration correction, amplitude amplification and sound speed correction, in the case of a punctual source in the medium during the learning step.

We observed that with phase and amplitude aberration correction (**Figure 4.25, b**) we significantly improve resolution and contrast. However we remained far from the image quality of our gold standard with a punctual source in the medium (**Figure 4.25, e**).

With the sound speed correction only (**Figure 4.25, c**), we corrected the error in depth in the image (compared to the reference image without skull). This error went from 18 pixels (without sound speed correction) down to 5 pixels (0.3 mm). However neither resolution nor contrast are really good.

With phase and amplitude aberration correction using the speckle noise technique and sound speed correction (**Figure 4.25, d**), we obtained images with similar quality both in resolution and contrast, compared to our gold standard with a punctual source in the medium (**Figure 4.25, e**).

4.3.2.5 Conclusion and perspectives

By combining the three types of corrections, we reached our goal to produce a transcranial image using the speckle noise technique, with similar resolution and contrast as the ones obtained with a punctual source in the medium.

As a perspective we will use plane wave illumination instead of focused ultrasound beam. Using the properties of synthetic imaging and plane wave imaging, we can reconstruct virtually any kind of delay laws from one single set of recorded data (Bruno-Félix Osmanski 2014). We designed a head phantom with acoustic properties (density, sound speed, attenuation) of the human brain and skull (**Figure 4.26**).



Figure 4.26 – Head phantom developed for transcranial Doppler imaging. Produced by True Phantom Solutions.

We chose to integrate mimicking blood vessel in front of both temporal window, with or without stenosis (from 10 to 50% stenosis). We imaged this head phantom with gadolinium injection in order to use MRI neuronavigation as gold standard. Further work will consist in testing our phase, amplitude and sound speed technique on this head phantom.

4.4 Chapter conclusion

In the first part of this chapter, we used a three step technique to precisely estimate sound speed (SSE) in a medium. The first step provided an estimate of the sound speed optimizing the spatial coherence of backscattered speckle noise. As this estimation can be degraded by aberrations occurring in the first propagation layers, a virtual point like reflector was created in order to identify and correct these aberrations. Finally a third correction step was introduced for an optimal estimation of liver sound speed in order to correct the bias introduced by the subcutaneous layer thickness. This technique was tested in ultrasound phantoms and *in vivo* in patients in the liver. In both case our method was able to find the speed of sound corresponding to the medium. We demonstrated that the SSE was related to the fat fraction. This analysis lead to the conclusion that SSE was able to diagnose healthy liver and steatosis (>10% biopsy) as well as biopsy and MRI. In addition to differentiate healthy liver and hepatic steatosis, we demonstrated that SSE, combined with the use of the Wood's formula, was able to give access to an ultrasound fat fraction (%). The latter was found to be highly correlated with gold standard fat fraction ($R^2 = 0.73$) and therefore enabled to grade hepatic steatosis with non-invasive ultrasound.

In the second part, by combining phase, amplitude and sound speed correction in numerical simulation, we reached our goal to produce transcranial images, with similar resolution, contrast and localization as the ones obtained with a punctual source in the medium.

Further investigation on our head phantom will be decisive. Aberration correction can solve the skull issue and therefore lead to transcranial ultrafast ultrasound imaging possibility along with its diversified applications. If we take the example of ultrafast Doppler, transcranial ultrasensitive Doppler, could be of a great medical interest. Indeed, since the first report of a correlation between brain activation and cerebral blood flow (CBF) (Fulton 1928), several studies have demonstrated changes of regional CBF during mental activities (Risberg 1986; Stroobant and Vingerhoets 2000). There is growing evidence to support the hypothesis of a relationship between mental activity and blood flow velocity (BFV) measured using TCD (big vessel scale), and that BFV is more rapid when subjects engage in cognitive activities as compared to non-thinking rest periods (Aaslid 1987; Droste, Harders, and Rastogi 1989). Transcranial ultrasensitive Doppler could make possible transcranial functional imaging at the neurovascular coupling scale. We demonstrated that functional imaging was feasible in human during brain surgery, and if we combine it with phase, amplitude and sound speed correction, it could become feasible transcranially, thus opening the possibility of new exciting clinical applications of functional ultrasound.

4.5 Chapter bibliography

- Aaslid, Rune. 1987. "Visually Evoked Dynamic Blood Flow Response of the Human Cerebral Circulation." *Stroke* 18 (4): 771–775.
- Aaslid, Rune, Thomas-Marc Markwalder, and Helge Nornes. 1982. "Noninvasive Transcranial Doppler Ultrasound Recording of Flow Velocity in Basal Cerebral Arteries." *Journal of Neurosurgery* 57 (6): 769–74. doi:10.3171/jns.1982.57.6.0769.
- Aubry, J.-F., M. Tanter, M. Pernot, J.-L. Thomas, and M. Fink. 2003. "Experimental Demonstration of Noninvasive Transskull Adaptive Focusing Based on Prior Computed Tomography Scans." *The Journal of the Acoustical Society of America* 113 (1): 84–93. doi:10.1121/1.1529663.
- Azhari, Haim. 2010. "Appendix A: Typical Acoustic Properties of Tissues." In *Basics of Biomedical Ultrasound for Engineers*, 313–14. John Wiley & Sons, Inc. <http://onlinelibrary.wiley.com/doi/10.1002/9780470561478.app1/summary>.
- Bamber, J. C., and C. R. Hill. 1981. "Acoustic Properties of Normal and Cancerous Human Liver-I. Dependence on Pathological Condition." *Ultrasound in Medicine & Biology* 7 (2): 121–33.
- Boed, Viktor. 1998. *Controls and Automation for Facilities Managers: Applications Engineering*. CRC Press.
- Bohs, L. 1992. "Phase Aberration Correction Using Echo Signals from Moving Targets II: Experimental System and Results." *Ultrasonic Imaging* 14 (2): 111–20. doi:10.1016/0161-7346(92)90002-D.
- Browne, Jacinta E., Amanda J. Watson, Peter R. Hoskins, and Alex T. Elliott. 2005. "Investigation of the Effect of Subcutaneous Fat on Image Quality Performance of 2D Conventional Imaging and Tissue Harmonic Imaging." *Ultrasound in Medicine & Biology* 31 (7): 957–964.
- Brunt, Elizabeth M. 2010. "Histopathology of Nonalcoholic Fatty Liver Disease." *World Journal of Gastroenterology* 16 (42): 5286. doi:10.3748/wjg.v16.i42.5286.

- Chassat, F. 1989. "Theoretical Evaluation of the Isoplanatic Patch of an Adaptive Optics System Working through the Atmospheric Turbulence." *Journal of Optics* 20 (1): 13.
- Chen, C. F., D. E. Robinson, L. S. Wilson, K. A. Griffiths, A. Manoharan, and B. D. Doust. 1987. "Clinical Sound Speed Measurement in Liver and Spleen in Vivo." *Ultrasonic Imaging* 9 (4): 221–35.
- Chiao, R. Y., L. J. Thomas, and S. D. Silverstein. 1997. "Sparse Array Imaging with Spatially-Encoded Transmits." In *1997 IEEE Ultrasonics Symposium Proceedings. An International Symposium (Cat. No.97CH36118)*, 2:1679–82 vol.2. doi:10.1109/ULTSYM.1997.663318.
- Christou, Ioannis, Robert A. Felberg, Andrew M. Demchuk, James C. Grotta, W. Scott Burgin, Marc Malkoff, and Andrei V. Alexandrov. 2001. "A Broad Diagnostic Battery for Bedside Transcranial Doppler to Detect Flow Changes With Internal Carotid Artery Stenosis or Occlusion." *Journal of Neuroimaging* 11: 236–42.
- Cooley, C. R., and B. S. Robinson. 1994. "Synthetic Focus Imaging Using Partial Datasets." In *1994 Proceedings of IEEE Ultrasonics Symposium*, 3:1539–42 vol.3. doi:10.1109/ULTSYM.1994.401884.
- D'Andrea, Antonello, Marianna Conte, Massimo Cavallaro, Raffaella Scarafile, Lucia Riegler, Rosangela Cocchia, Enrica Pezzullo, et al. 2016. "Transcranial Doppler Ultrasonography: From Methodology to Major Clinical Applications." *World Journal of Cardiology* 8 (7): 383. doi:10.4330/wjc.v8.i7.383.
- D'Andrea, Antonello, Marianna Conte, Raffaella Scarafile, Lucia Riegler, Rosangela Cocchia, Enrica Pezzullo, Massimo Cavallaro, et al. 2016. "Transcranial Doppler Ultrasound: Physical Principles and Principal Applications in Neurocritical Care Unit." *Journal of Cardiovascular Echography* 26 (2): 28. doi:10.4103/2211-4122.183746.
- Dasarathy, Srinivasan, Jaividhya Dasarathy, Amer Khiyami, Rajesh Joseph, Rocio Lopez, and Arthur J. McCullough. 2009. "Validity of Real Time Ultrasound in the Diagnosis of Hepatic Steatosis: A Prospective Study." *Journal of Hepatology* 51 (6): 1061–67. doi:10.1016/j.jhep.2009.09.001.
- Deffieux, Thomas, Jean-Luc Gennisson, Laurence Bousquet, Marion Corouge, Simona Coscinea, Dalila Amroun, Simona Tripon, et al. 2015. "Investigating Liver Stiffness and Viscosity for Fibrosis, Steatosis and Activity Staging Using Shear Wave Elastography." *Journal of Hepatology* 62 (2): 317–24. doi:10.1016/j.jhep.2014.09.020.
- Derode, Arnaud, and Mathias Fink. 1993. "Spatial Coherence of Ultrasonic Speckle in Composites." *Ultrasonics, Ferroelectrics, and Frequency Control, IEEE Transactions on* 40 (6): 666–675.
- Droste, D. W., A. G. Harders, and E. Rastogi. 1989. "Two Transcranial Doppler Studies on Blood Flow Velocity in Both Middle Cerebral Arteries during Rest and the Performance of Cognitive Tasks." *Neuropsychologia* 27 (10): 1221–30. doi:10.1016/0028-3932(89)90034-1.
- Duck, Francis A. 1990. "Acoustic Properties of Tissue at Ultrasonic Frequencies." In *Physical Properties of Tissues*, 73–135. Elsevier. <http://linkinghub.elsevier.com/retrieve/pii/B9780122228001500085>.
- Fink, Mathias. 1992. "Time Reversal of Ultrasonic Fields. I. Basic Principles." *Ultrasonics, Ferroelectrics and Frequency Control, IEEE Transactions on* 39 (5): 555–566.

- Flax, S. W., and M. O'Donnell. 1988. "Phase-Aberration Correction Using Signals from Point Reflectors and Diffuse Scatterers: Basic Principles." *IEEE Transactions on Ultrasonics, Ferroelectrics, and Frequency Control* 35 (6): 758–67. doi:10.1109/58.9333.
- Foucher, J., E. Chanteloup, J. Vergniol, L. Castéra, B. Le Bail, X. Adhoute, J. Bertet, P. Couzigou, and V. de Lédinghen. 2006. "Diagnosis of Cirrhosis by Transient Elastography (FibroScan): A Prospective Study." *Gut* 55 (3): 403–8. doi:10.1136/gut.2005.069153.
- Foucher, Juliette, Laurent Castéra, Pierre-Henri Bernard, Xavier Adhoute, David Laharie, Julien Bertet, Patrice Couzigou, and Victor de Lédinghen. 2006. "Prevalence and Factors Associated with Failure of Liver Stiffness Measurement Using FibroScan in a Prospective Study of 2114 Examinations." *European Journal of Gastroenterology & Hepatology* 18 (4): 411–12.
- Fulton, John Farquhar. 1928. "Observations upon the Vascularity of the Human Occipital Lobe during Visual Activity." *Brain* 51 (3): 310–320.
- Goumard, Claire, Fabiano Perdigo, Julien Cazejust, Stéphane Zalinski, Olivier Soubrane, and Olivier Scatton. 2014. "Is Computed Tomography Volumetric Assessment of the Liver Reliable in Patients with Cirrhosis?" *HPB: The Official Journal of the International Hepato Pancreato Biliary Association* 16 (2): 188–94. doi:10.1111/hpb.12110.
- Idilman, Ilkay S., Hatice Aniktar, Ramazan Idilman, Gokhan Kabacam, Berna Savas, Atilla Elhan, Azim Celik, Kadir Bahar, and Musturay Karcaaltincaba. 2013. "Hepatic Steatosis: Quantification by Proton Density Fat Fraction with MR Imaging versus Liver Biopsy." *Radiology* 267 (3): 767–75. doi:10.1148/radiol.13121360.
- Ivancevich, Nikolas M., Jeremy J. Dahl, and Stephen W. Smith. 2009. "Comparison of 3-D Multi-Lag Cross-Correlation and Speckle Brightness Aberration Correction Algorithms on Static and Moving Targets." *IEEE Transactions on Ultrasonics, Ferroelectrics, and Frequency Control* 56 (10): 2157. doi:10.1109/TUFFC.2009.1298.
- Jaeger, Michael, and Martin Frenz. 2015. "Towards Clinical Computed Ultrasound Tomography in Echo-Mode: Dynamic Range Artefact Reduction." *Ultrasonics* 62 (September): 299–304. doi:10.1016/j.ultras.2015.06.003.
- Jaeger, Michael, Gerrit Held, Sara Peeters, Stefan Preisser, Michael Grünig, and Martin Frenz. 2014. "Computed Ultrasound Tomography in Echo Mode for Imaging Speed of Sound Using Pulse-Echo Sonography: Proof of Principle." *Ultrasound in Medicine & Biology*, September. doi:10.1016/j.ultrasmedbio.2014.05.019.
- James, *Oliver, and Christopher Day. 1999. "Non-Alcoholic Steatohepatitis: Another Disease of Affluence." *The Lancet* 353 (9165): 1634–36. doi:10.1016/S0140-6736(99)00163-4.
- Janiec, Dorota J., Erica R. Jacobson, Amy Freeth, Laurie Spaulding, and Hagen Blaszyk. 2005. "Histologic Variation of Grade and Stage of Non-Alcoholic Fatty Liver Disease in Liver Biopsies." *Obesity Surgery* 15 (4): 497–501. doi:10.1381/0960892053723268.
- Karaman, M., Pai-Chi Li, and M. O'Donnell. 1995. "Synthetic Aperture Imaging for Small Scale Systems." *IEEE Transactions on Ultrasonics, Ferroelectrics, and Frequency Control* 42 (3): 429–42. doi:10.1109/58.384453.
- Krishnan, S., K. W. Rigby, and M. O'Donnell. 1997. "Improved Estimation of Phase Aberration Profiles." *IEEE Transactions on Ultrasonics, Ferroelectrics, and Frequency Control* 44 (3): 701–13. doi:10.1109/58.658333.
- Lacefield, James C., Wayne C. Pilkington, and Robert C. Waag. 2002. "Distributed Aberrators for Emulation of Ultrasonic Pulse Distortion by Abdominal Wall." *Acoustics Research Letters Online* 3: 47.

- Lediju, Muyinatu A., Michael J. Pihl, Stephen J. Hsu, Jeremy J. Dahl, Caterina M. Gallippi, and Gregg E. Trahey. 2009. "A Motion-Based Approach to Abdominal Clutter Reduction." *IEEE Transactions on Ultrasonics, Ferroelectrics, and Frequency Control* 56 (11): 2437–49. doi:10.1109/TUFFc.2009.1331.
- Lediju, Muyinatu A., Gregg E. Trahey, Brett C. Byram, and Jeremy J. Dahl. 2011. "Short-Lag Spatial Coherence of Backscattered Echoes: Imaging Characteristics." *IEEE Transactions on Ultrasonics, Ferroelectrics, and Frequency Control* 58 (7): 1377–88. doi:10.1109/TUFFc.2011.1957.
- Leporq, Benjamin, Simon A. Lambert, Maxime Ronot, Valerie Vilgrain, and Bernard E. Van Beers. 2014. "Quantification of the Triglyceride Fatty Acid Composition with 3.0 T MRI: QUANTIFICATION OF TRIGLYCERIDE FATTY ACID COMPOSITION WITH MRI." *NMR in Biomedicine* 27 (10): 1211–21. doi:10.1002/nbm.3175.
- Li, Pai-Chi, and Meng-Lin Li. 2003. "Adaptive Imaging Using the Generalized Coherence Factor." *IEEE Transactions on Ultrasonics, Ferroelectrics, and Frequency Control* 50 (2): 128–41. doi:10.1109/TUFFc.2003.1182117.
- Li, Pai-Chi, and M. O'Donnell. 1995. "Phase Aberration Correction on Two-Dimensional Conformal Arrays." *IEEE Transactions on Ultrasonics, Ferroelectrics, and Frequency Control* 42 (1): 73–82. doi:10.1109/58.368310.
- Lin, Steven C., Elhamy Heba, Tanya Wolfson, Brandon Ang, Anthony Gamst, Aiguo Han, John W. Erdman, et al. 2015. "Noninvasive Diagnosis of Nonalcoholic Fatty Liver Disease and Quantification of Liver Fat Using a New Quantitative Ultrasound Technique." *Clinical Gastroenterology and Hepatology* 13 (7): 1337–1345.e6. doi:10.1016/j.cgh.2014.11.027.
- Lindsey, Brooks D., Heather A. Nicoletto, Ellen R. Bennett, Daniel T. Laskowitz, and Stephen W. Smith. 2014. "3-D Transcranial Ultrasound Imaging with Bilateral Phase Aberration Correction of Multiple Isoplanatic Patches: A Pilot Human Study with Microbubble Contrast Enhancement." *Ultrasound in Medicine & Biology* 40 (1): 90–101. doi:10.1016/j.ultrasmedbio.2013.09.006.
- Lockwood, G. R., J. R. Talman, and S. S. Brunke. 1998. "Real-Time 3-D Ultrasound Imaging Using Sparse Synthetic Aperture Beamforming." *IEEE Transactions on Ultrasonics, Ferroelectrics, and Frequency Control* 45 (4): 980–88. doi:10.1109/58.710573.
- Mallart, Raoul. 1991. "The van Cittert–Zernike Theorem in Pulse Echo Measurements." *The Journal of the Acoustical Society of America* 90 (5): 2718. doi:10.1121/1.401867.
- Mallart, Raoul, and Mathias Fink. 1994. "Adaptive Focusing in Scattering Media through Sound-speed Inhomogeneities: The van Cittert Zernike Approach and Focusing Criterion." *The Journal of the Acoustical Society of America* 96 (6): 3721–32. doi:10.1121/1.410562.
- Marinoni, Marinella, Andrea Ginanneschi, Paolo Forleo, and Luigi Amaducci. 1997. "Technical Limits in Transcranial Doppler Recording: Inadequate Acoustic Windows." *Ultrasound in Medicine & Biology* 23 (8): 1275–77. doi:10.1016/S0301-5629(97)00077-X.
- Marsac, Laurent. 2013. *Focalisation Ultrasonore Adaptative et Application À La Thérapie Du Cerveau*. Paris 7. <http://www.theses.fr/2013PA077106>.
- Måsøy, Svein-Erik, Tonni F. Johansen, and Bjørn Angelsen. 2003. "Correction of Ultrasonic Wave Aberration with a Time Delay and Amplitude Filter." *The Journal of the Acoustical Society of America* 113 (4 Pt 1): 2009–20.
- McCormack, Lucas, Henrik Petrowsky, Wolfram Jochum, Katarzyna Furrer, and Pierre-Alain Clavien. 2007. "Hepatic Steatosis Is a Risk Factor for Postoperative Complications After

- Major Hepatectomy: A Matched Case-Control Study.” *Annals of Surgery* 245 (6): 923–30. doi:10.1097/01.sla.0000251747.80025.b7.
- Mehta, Sanjeev R, E Louise Thomas, Jimmy D Bell, Desmond G Johnston, and Simon D Taylor-Robinson. 2008. “Non-Invasive Means of Measuring Hepatic Fat Content.” *World Journal of Gastroenterology: WJG* 14 (22): 3476–83. doi:10.3748/wjg.14.3476.
- Mézière, Fabien. 2014. “Propagation Des Ultrasons En Milieux Poreux Anisotropes: Application À L’os Trabéculaire.” Université Paris. Diderot (Paris 7). <https://hal.archives-ouvertes.fr/tel-01128763/>.
- Mishra, Poonam, and Zobair M. Younossi. 2007. “Abdominal Ultrasound for Diagnosis of Nonalcoholic Fatty Liver Disease (NAFLD).” *The American Journal of Gastroenterology* 102 (12): 2716–17. doi:10.1111/j.1572-0241.2007.01520.x.
- Montaldo, Gabriel, Mickael Tanter, and Mathias Fink. 2011. “Time Reversal of Speckle Noise.” *Physical Review Letters* 106 (5). doi:10.1103/PhysRevLett.106.054301.
- Moppett, I. K., and R. P. Mahajan. 2004. “Transcranial Doppler Ultrasonography in Anaesthesia and Intensive Care.” *British Journal of Anaesthesia* 93 (5): 710–24. doi:10.1093/bja/aeh205.
- Moreno, José A., Eduard Mesalles, Juan Gener, Antonio Tomasa, Adolfo Ley, Josep Roca, and Jaime Fernández-Llamazares. 2000. “Evaluating the Outcome of Severe Head Injury with Transcranial Doppler Ultrasonography.” *Neurosurgical Focus* 8 (1): 1–7. doi:10.3171/foc.2000.8.1.1702.
- Moura Almeida, Alessandro de, Helma Pinchemel Cotrim, Daniel Batista Valente Barbosa, Luciana Gordilho Matteoni de Athayde, Adimeia Souza Santos, Almir Galvão Vieira Bitencourt, Luiz Antonio Rodrigues de Freitas, Adriano Rios, and Erivaldo Alves. 2008. “Fatty Liver Disease in Severe Obese Patients: Diagnostic Value of Abdominal Ultrasound.” *World Journal of Gastroenterology: WJG* 14 (9): 1415–18. doi:10.3748/wjg.14.1415.
- Ng, G.C., P.D. Freiburger, W.F. Walker, and G.E. Trahey. 1997. “A Speckle Target Adaptive Imaging Technique in the Presence of Distributed Aberrations.” *IEEE Transactions on Ultrasonics, Ferroelectrics, and Frequency Control* 44 (1): 140–51. doi:10.1109/58.585209.
- Nock, Levin, Gregg E. Trahey, and Stephen W. Smith. 1989. “Phase Aberration Correction in Medical Ultrasound Using Speckle Brightness as a Quality Factor.” *The Journal of the Acoustical Society of America* 85 (5): 1819–33. doi:10.1121/1.397889.
- O’Donnell, M., and S. W. Flax. 1988. “Phase Aberration Measurements in Medical Ultrasound: Human Studies.” *Ultrasonic Imaging* 10 (1): 1–11.
- Osmanski, Bruno-Félix. 2014. *Utilisation de L’imagerie Échographique Ultrarapide Pour de Nouvelles Applications Dans Le Domaine Médical et Des Neurosciences*. Paris 7. <http://www.theses.fr/2014PA077081>.
- Osmanski, Bruno-Felix, Gabriel Montaldo, Mickaël Tanter, and Mathias Fink. 2012. “Aberration Correction by Time Reversal of Moving Speckle Noise.” *IEEE Transactions on Ultrasonics, Ferroelectrics and Frequency Control* 59 (7): 1575–83. doi:10.1109/TUFFC.2012.2357.
- Palmeri, Mark L., Amy C. Sharma, Richard R. Bouchard, Roger W. Nightingale, and Roger W. Nightingale. 2005. “A Finite-Element Method Model of Soft Tissue Response to Impulsive Acoustic Radiation Force.” *Ultrasonics, Ferroelectrics, and Frequency Control, IEEE Transactions on* 52 (10): 1699–1712.

- Pernot, Mathieu, Gabriel Montaldo, Mickael Tanter, and Mathias Fink. 2006. “‘Ultrasonic Stars’ for Time-Reversal Focusing Using Induced Cavitation Bubbles.” *Applied Physics Letters* 88 (3): 34102. doi:10.1063/1.2162700.
- Prada, C., F. Wu, and M. Fink. 1991. “The Iterative Time Reversal Mirror: A Solution to Self-focusing in the Pulse Echo Mode.” *The Journal of the Acoustical Society of America* 90 (2): 1119–29. doi:10.1121/1.402301.
- Prada, Claire, and Mathias Fink. 1994. “Eigenmodes of the Time Reversal Operator: A Solution to Selective Focusing in Multiple-Target Media.” *Wave Motion* 20 (2): 151–63. doi:10.1016/0165-2125(94)90039-6.
- Ratziu, Vlad, Frédéric Charlotte, Agnès Heurtier, Sophie Gombert, Philippe Giral, Eric Bruckert, André Grimaldi, Frédérique Capron, Thierry Poynard, and LIDO Study Group. 2005. “Sampling Variability of Liver Biopsy in Nonalcoholic Fatty Liver Disease.” *Gastroenterology* 128 (7): 1898–1906.
- Risberg, J. 1986. “Regional Cerebral Blood Flow in Neuropsychology.” *Neuropsychologia* 24 (1): 135–40. doi:10.1016/0028-3932(86)90047-3.
- Robert, Jean-Luc, and Mathias Fink. 2008. “Green’s Function Estimation in Speckle Using the Decomposition of the Time Reversal Operator: Application to Aberration Correction in Medical Imaging.” *The Journal of the Acoustical Society of America* 123 (2): 866. doi:10.1121/1.2816562.
- Sandrin, Laurent, Mickaël Tanter, J.-L. Gennisson, Stefan Catheline, and Mathias Fink. 2002. “Shear Elasticity Probe for Soft Tissues with 1-D Transient Elastography.” *Ultrasonics, Ferroelectrics and Frequency Control, IEEE Transactions on* 49 (4): 436–446.
- Sasso, Magali, Michel Beaugrand, Victor de Ledinghen, Catherine Douvin, Patrick Marcellin, Raoul Poupon, Laurent Sandrin, and Véronique Miette. 2010. “Controlled Attenuation Parameter (CAP): A Novel VCTETM Guided Ultrasonic Attenuation Measurement for the Evaluation of Hepatic Steatosis: Preliminary Study and Validation in a Cohort of Patients with Chronic Liver Disease from Various Causes.” *Ultrasound in Medicine & Biology* 36 (11): 1825–35. doi:10.1016/j.ultrasmedbio.2010.07.005.
- Sharma, Amit, April Ashworth, Martha Behnke, Adrian Cotterell, Marc Posner, and Robert A. Fisher. 2013. “Donor Selection for Adult- to- Adult Living Donor Liver Transplantation: Well Begun Is Half Done.” *Transplantation* 95 (3): 501–6. doi:10.1097/TP.0b013e318274aba1.
- Son, Jee-Young, Jae Young Lee, Nam-Joon Yi, Kwang-Woong Lee, Kyung-Suk Suh, Kwang Gi Kim, Jeong Min Lee, Joon Koo Han, and Byung Ihn Choi. 2015. “Hepatic Steatosis: Assessment with Acoustic Structure Quantification of US Imaging.” *Radiology* 278 (1): 257–264.
- Stroobant, Nathalie, and Guy Vingerhoets. 2000. “Transcranial Doppler Ultrasonography Monitoring of Cerebral Hemodynamics during Performance of Cognitive Tasks: A Review.” *Neuropsychology Review* 10 (4): 213–231.
- Sumida, Yoshio, Atsushi Nakajima, and Yoshito Itoh. 2014. “Limitations of Liver Biopsy and Non-Invasive Diagnostic Tests for the Diagnosis of Nonalcoholic Fatty Liver Disease/nonalcoholic Steatohepatitis.” *World Journal of Gastroenterology: WJG* 20 (2): 475–85. doi:10.3748/wjg.v20.i2.475.
- Suzuki, K., N. Hayashi, Y. Sasaki, M. Kono, A. Kasahara, H. Fusamoto, Y. Imai, and T. Kamada. 1992. “Dependence of Ultrasonic Attenuation of Liver on Pathologic Fat and Fibrosis:

- Examination with Experimental Fatty Liver and Liver Fibrosis Models.” *Ultrasound in Medicine & Biology* 18 (8): 657–66.
- Tanter, M, J L Thomas, and M Fink. 1998. “Focusing and Steering through Absorbing and Aberrating Layers: Application to Ultrasonic Propagation through the Skull.” *The Journal of the Acoustical Society of America* 103 (5 Pt 1): 2403–10.
- Tchelepi, Hisham, Philip W. Ralls, Randall Radin, and Edward Grant. 2002. “Sonography of Diffuse Liver Disease.” *Journal of Ultrasound in Medicine: Official Journal of the American Institute of Ultrasound in Medicine* 21 (9): 1023-1032-1034.
- Thomas, J. L., and M. A. Fink. 1996. “Ultrasonic Beam Focusing through Tissue Inhomogeneities with a Time Reversal Mirror: Application to Transskull Therapy.” *IEEE Transactions on Ultrasonics, Ferroelectrics, and Frequency Control* 43 (6): 1122–29. doi:10.1109/58.542055.
- Trotter, James F., Karen A. Wisniewski, Norah A. Terrault, James E. Everhart, Milan Kinkhabwala, Robert M. Weinrieb, Jeffrey H. Fair, et al. 2007. “Outcomes of Donor Evaluation in Adult-to-Adult Living Donor Liver Transplantation.” *Hepatology* 46 (5): 1476–84. doi:10.1002/hep.21845.
- Vignon, F., J.F. Aubry, M. Tanter, and M. Fink. 2004. “High Resolution Ultrasonic Brain Imaging: Noninvasive Adaptive Focusing Based on Twin Arrays.” In , 1:231–34. IEEE. doi:10.1109/ULTSYM.2004.1417709.
- White, D N, J M Clark, J N Chesebrou, M N White, and J K Campbell. 1968. “Effect of the Skull in Degrading the Display of Echoencephalographic B and C Scans.” *The Journal of the Acoustical Society of America* 44 (5): 1339–45. doi:10.1121/1.1911266.
- Wieckowska, Anna, and Ariel E. Feldstein. 2008. “Diagnosis of Nonalcoholic Fatty Liver Disease: Invasive versus Noninvasive.” *Seminars in Liver Disease* 28 (4): 386–95. doi:10.1055/s-0028-1091983.
- Wood, A. B. (Albert Beaumont). 1930. *A Textbook of Sound: Being an Account of the Physics of Vibrations with Special Reference to Recent Theoretical and Technical Developments*. New York: Macmillan. <http://archive.org/details/textbookofsoundb00wood>.
- Xia, Ming-Feng, Hong-Mei Yan, Wan-Yuan He, Xiao-Ming Li, Chao-Lun Li, Xiu-Zhong Yao, Ruo-Kun Li, Meng-Su Zeng, and Xin Gao. 2012. “Standardized Ultrasound Hepatic/renal Ratio and Hepatic Attenuation Rate to Quantify Liver Fat Content: An Improvement Method.” *Obesity (Silver Spring, Md.)* 20 (2): 444–52. doi:10.1038/oby.2011.302.
- Yu, Hee Chul, Heecheon You, Ho Lee, Zhe-Wu Jin, Jang Il Moon, and Baik Hwan Cho. 2004. “Estimation of Standard Liver Volume for Liver Transplantation in the Korean Population.” *Liver Transplantation* 10 (6): 779–83. doi:10.1002/lt.20188.
- Zamboni, Fausto, Alessandro Franchello, Ezio David, Giuseppe Rocca, Alessandro Ricchiuti, Bruna Lavezzo, Mario Rizzetto, and Mauro Salizzoni. 2001. “Effect of Macrovesicular Steatosis and Other Donor and Recipient Characteristics on the Outcome of Liver Transplantation.” *Clinical Transplantation* 15 (1): 53–57. doi:10.1034/j.1399-0012.2001.150109.x.
- Zhao, D., L. N. Bohs, and G. E. Trahey. 1992. “Phase Aberration Correction Using Echo Signals from Moving Targets I: Description and Theory.” *Ultrasonic Imaging* 14 (2): 97–110.
- Zwiebel, W. J. 1995. “Sonographic Diagnosis of Diffuse Liver Disease.” *Seminars in Ultrasound, CT, and MR* 16 (1): 8–15.

General Conclusion and Outlook

General Conclusion and Outlook

5. General Conclusion and Outlook

The objective of this thesis was to explore the potential of human brain ultrafast ultrasound imaging. Anatomy, blood flow and soft tissue stiffness have already been studied with ultrafast ultrasound imaging in humans and validated in several organs, such as, the breast and liver but not yet extended on the adult brain. The main limitation of transcranial ultrasound imaging is today the very strong skull-induced aberration artefact. Indeed, the bone, because of its composition, does not allow for ultrasound propagation as elsewhere in the human body. In the beginning of this thesis, we used ultrafast ultrasound imaging for the evaluation of soft tissue stiffness and neurofunctional imaging in the adult human brain during brain surgery in order to bypass initially the problem of skull aberration. In the final part we have developed a new aberration correction technique for speed sound estimation and for transcranial ultrasound imaging.

We first provided evidence of the benefit of using shear wave elastography (SWE) during brain surgery. This imaging technique helps surgeons to quantitatively distinguish benign and malignant brain tumors (especially in gliomas) and thus to provide the optimum extent of resection. In the neurosurgery field, we also demonstrated that SWE can detect changes due to increasing volume of brain parenchyma, such as in case of tumor growth or edemas. SWE could enable to draw a cut-off line between compensation and decompensation. A larger clinical study need to be conducted to precisely determinate the cut-off value to identify patients with intracranial hypertension during brain surgery. On the other hand, in order to overcome the limitations of 2D imaging and in particular to reduce the operator dependence, we also presented our new technique for 3D shear wave elastography using a matrix array. This technique could be of great interest for diagnostic in many organs such as heart and brain to map the tissue anisotropy, and it could also contribute to expand our current understanding of shear wave physics in medical applications.

In a second phase, we demonstrated the ability of ultrasound to identify, map and differentiate *in depth* cortical regions of activation in response to a stimulus, both in awake patients and in anaesthetized patients. We have demonstrated that ultrasound neurofunctional imaging has the potential to become a comprehensive and full-fledged modality of neuroimaging with major benefits for intraoperative use.

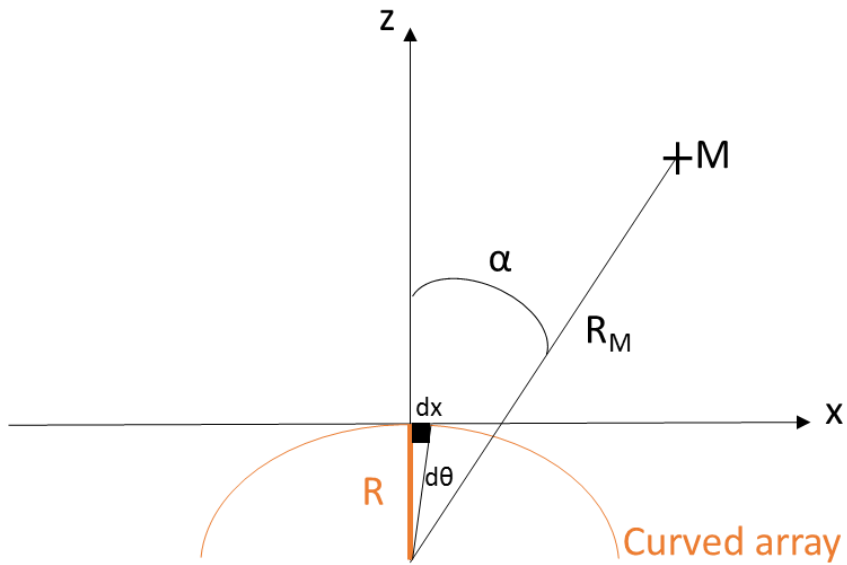
In a third part, we used a three-step technique to accurately calculate a sound speed estimation (SSE) corresponding to the illuminated medium. This technique has been tested in ultrasound phantoms and *in vivo* in patient's liver. In both cases, our method was able to find the sound speed corresponding to the medium. We demonstrated that SSE was related to the fat fraction. This analysis led to the conclusion that SSE was able to distinguish a healthy liver from a diseased liver with both biopsy and MRI as gold standard. Combined with the use of Wood's formula, we were even able to access a fat fraction measured by non-invasive ultrasound. Then we combined the phase, amplitude and sound speed aberration correction to perform transcranial ultrasound imaging in numerical simulation. We achieved our objective by obtaining images that faithfully represented the medium (lateral position and depth) and characterized by one resolution and one contrast similar to those obtained with a punctual source in the medium.

To validate this aberration correction technique *in vitro* we designed a head phantom with the acoustic characteristics of the skull and the brain. As an outlook, we will combine ultrafast plane wave imaging with our aberration correction technique (phase, amplitude, and sound speed) and we will use a phased array probe to make ultrafast transcranial imaging. As we have demonstrated the feasibility and usefulness of shear wave elastography and neurofunctional ultrasound imaging, and as we have developed a technique to improve the quality of ultrasound transcranial imaging, long term evolution is to be able to use ultrafast imaging and its various applications in a non-invasive transcranial way. Further investigation on our head phantom will be decisive. In the case of shear wave elastography (SWE), transcranial SWE could improve preoperative diagnostic by determining the tumor grade and therefore properly adapt the surgery. In the case of ultrafast Doppler, transcranial ultrasensitive Doppler, could be of a great medical interest. Indeed, since the first report of a correlation between brain activation and cerebral blood flow (CBF), several studies have demonstrated changes of regional CBF during mental activities. Transcranial ultrasensitive Doppler could make possible transcranial functional imaging at the neurovascular coupling scale.

Appendix

6. Appendix

6.1 Appendix 1: Delay law in the polar coordinate system



The delay law τ_M to virtually focus a point (M) in the polar coordinate system was calculated as followed, starting from the delay law expressed in case of linear array:

$$\tau_M = -\frac{1}{c} \sqrt{(x_o - x)^2 + (z_o - z)^2}$$

$$\left\{ \begin{array}{l} R d\theta = dx \\ i: \text{Piezoelectric element} \\ \theta_i = +i d\theta \end{array} \right.$$

Polar coordinates

$$\left\{ \begin{array}{l} R \sin(\theta_i) - R_M \sin(\alpha) \\ R \cos(\theta_i) - R_M \cos(\alpha) \end{array} \right.$$

$$\tau_M = -\frac{1}{c} \sqrt{(R \sin(\theta_i) - R_M \sin(\alpha))^2 + (R \cos(\theta_i) - R_M \cos(\alpha))^2}$$

$$\tau_M = -\frac{1}{c} \sqrt{\begin{aligned} &R^2 \sin^2(\theta_i) - 2RR_M \sin(\theta_i) \sin(\alpha) + R_M^2 \sin^2(\alpha) \\ &+ R^2 \cos^2(\theta_i) - 2RR_M \cos(\theta_i) \cos(\alpha) + R_M^2 \cos^2(\alpha) \end{aligned}}$$

$$\tau_M = -\frac{1}{c} \sqrt{\begin{aligned} &R^2(\sin^2(\theta_i) + \cos^2(\theta_i)) + R_M^2(\sin^2(\alpha) + \cos^2(\alpha)) \\ &- 2RR_M(\sin(\theta_i) \sin(\alpha) + \cos(\theta_i) \cos(\alpha)) \end{aligned}}$$

Where

$$\left\{ \begin{aligned} \sin^2(\theta_i) + \cos^2(\theta_i) &= 1 \\ \sin^2(\alpha) + \cos^2(\alpha) &= 1 \\ \sin(\theta_i) \sin(\alpha) + \cos(\theta_i) \cos(\alpha) &= \cos(\theta_i - \alpha) \end{aligned} \right.$$

$$\tau_M = -\frac{1}{c} \sqrt{R^2 + R_M^2 - 2RR_M \cos(\theta_i - \alpha)}$$

And the time from the array to the point M was: $T_0 = \frac{R_M - R}{2c}$

6.2 Appendix 2: the Wood's formula

By using the effective density (ρ_{eff}) and bulk modulus (κ_{eff}), the theoretical sound speed (c_{eff}^{th}) in the homogenized medium was obtained using the Wood's formula:

$$c_{eff}^{th} = \sqrt{\frac{\kappa_{eff}}{\rho_{eff}}} = \sqrt{\frac{1}{\left(\varphi_f \frac{1}{\kappa_f} + (1 - \varphi_f) \frac{1}{\kappa_l}\right) (\varphi_f \rho_f + (1 - \varphi_f) \rho_l)}}$$

where φ_f is the fat fraction in the liver, κ_f and κ_l are respectively the bulk modulus of the fat and of the liver, ρ_f and ρ_l are respectively the density of the fat and of the liver.

$$c_{eff}^{th} = \sqrt{\frac{1}{\varphi_f^2 \frac{\rho_f}{\kappa_f} + \varphi_f(1 - \varphi_f) \frac{\rho_l}{\kappa_f} + \varphi_f(1 - \varphi_f) \frac{\rho_f}{\kappa_l} + (1 - \varphi_f)^2 \frac{\rho_l}{\kappa_l}}}$$

$$c_{eff}^{th} = \sqrt{\frac{1}{\varphi_f^2 \left(\frac{\rho_f}{\kappa_f} - \frac{\rho_l}{\kappa_f} - \frac{\rho_f}{\kappa_l} + \frac{\rho_l}{\kappa_l} \right) + \varphi_f \left(\frac{\rho_l}{\kappa_f} + \frac{\rho_f}{\kappa_l} - 2 \frac{\rho_l}{\kappa_l} \right) + \frac{\rho_l}{\kappa_l}}}$$

$$c_{eff}^{th} = \sqrt{\frac{1}{b \times \varphi_f^2 + c \times \varphi_f + d}}$$

Where $b = \frac{\rho_f}{\kappa_f} - \frac{\rho_l}{\kappa_f} - \frac{\rho_f}{\kappa_l} + \frac{\rho_l}{\kappa_l}$, $c = \frac{\rho_l}{\kappa_f} + \frac{\rho_f}{\kappa_l} - 2 \frac{\rho_l}{\kappa_l}$, and $d = \frac{\rho_l}{\kappa_l}$

Résumé de thèse

7. Résumé de thèse

7.1 Imagerie médicale du cerveau

L'imagerie cérébrale est l'utilisation de diverses techniques pour directement ou indirectement imager la structure ou le fonctionnement du système nerveux. L'imagerie anatomique reflète la structure du système nerveux et permet le diagnostic des maladies intracrâniennes macroscopiques (i.e. les tumeurs) et des lésions. L'imagerie fonctionnelle est utilisée pour diagnostiquer les maladies métaboliques (i.e. la maladie d'Alzheimer) et les lésions à une échelle plus fine, pour trouver la relation entre l'activité dans une zone du cerveau et les fonctions mentales spécifiques associées, elle est également utilisée pour la recherche neurologique et la psychologie cognitive.

L'imagerie cérébrale est une discipline relativement nouvelle au sein de la médecine, des neurosciences et de la psychologie. Une série de progrès en mathématiques, en physique, en informatique et en imagerie clinique ont progressivement transformé le diagnostic et le traitement des troubles neurologiques et neurochirurgicaux entre la première radiographie et l'apparition de l'imagerie par résonance magnétique (IRM). Comme les nouvelles techniques d'imagerie apportent des informations de plus en plus subtiles et complexes dans le domaine du diagnostic, la gamme de problèmes auxquels les médecins et les neurochirurgiens devront faire face va certainement continuer à croître. L'objectif de cette thèse est de contribuer au développement de l'imagerie médicale du cerveau en étudiant les propriétés des ultrasons.

Dans ce chapitre d'introduction, nous présenterons les principales techniques d'imagerie cérébrale afin de positionner l'imagerie cérébrale par ultrasons au sein de ce contexte. Dans un second temps, nous détaillons les bases de l'imagerie ultrasonore conventionnelle afin d'introduire le nouveau concept d'imagerie ultrasonore ultra-rapide qui peut faire progresser les ultrasons dans le domaine de l'imagerie cérébral.

Les différentes modalités d'imagerie cérébrale actuellement utilisées en pratique clinique sont : le scanner, l'imagerie par résonance magnétique (IRM), l'imagerie nucléaire (la scintigraphie et la tomographie par émission de positrons, TEP), l'imagerie optique (proche infrarouge), l'électroencéphalographie, la magnétoencéphalographie, et les ultrasons.

Le scanner, est un type d'imagerie basé sur l'absorption des rayons-X par les tissus traversés sous des angles différents. Cela permet de produire des images en coupe du corps humain, c'est-à-dire des images tomographiques. Dans certains cas, des agents de contraste sont également injectés pour augmenter le rapport de contraste à bruit des images. Le scanner permet de faire de l'imagerie, de structure, de perfusion, en suivant par exemple les variations du volume sanguin (angiographie). Ces scans ne s'effectuent pas en temps réel et une analyse complète prend souvent plusieurs minutes. De plus cette technique d'imagerie expose le patient au rayonnement des rayons X et dans de nombreux cas à des agents de contrastes ionisant.

L'IRM utilise un champ magnétique (aimant) et des ondes radio. Son principe consiste à réaliser des images du corps humain grâce aux nombreux atomes d'hydrogène qu'il contient. Placés dans un puissant champ magnétique, tous les atomes d'hydrogène du patient s'orientent dans la même direction sous l'effet de résonance. Dès l'arrêt de cette stimulation magnétique, les atomes restituent l'énergie accumulée en produisant un signal qui est enregistré et traité par un système informatique pour former une image. L'IRM est une technique qui permet l'imagerie anatomique, vasculaire (angiographie), l'imagerie de rigidité des tissus mous (élastographie), et l'imagerie fonctionnelle (observation des changements de métabolisme). L'IRM est une modalité d'imagerie extrêmement sûre, par rapport à l'imagerie par rayons X, car aucun rayonnement ionisant n'est transmis. Toutefois, une attention particulière doit être portée à tous les matériaux ferromagnétiques qui peuvent être des sources d'artefact d'imagerie. Les pacemakers et les défibrillateurs sont donc contre-indiqués pour l'IRM. L'IRM est également une modalité d'imagerie très coûteuse et peu disponible en milieu hospitalier.

La scintigraphie et la tomographie par émission des positrons (TEP) sont des techniques nucléaires d'imagerie médicale fonctionnelle qui s'intéressent au métabolisme des organes. Leurs principes reposent sur l'administration et la détection d'un radiotraceur (radioélément couplé à une molécule de transport). La nature du radiotraceur varie selon l'objectif de l'examen. A titre d'exemple, un examen peut avoir pour but de visualiser les organes accumulant le traceur de façon excessive et traduisant une consommation trop importante de glucose. La consommation cellulaire en glucose étant par exemple augmentée au niveau des cellules tumorales, infectieuses ou inflammatoires du cerveau, l'imagerie nucléaire fonctionnelle peut être un bon outil de diagnostic de ce type de pathologie. Les inconvénients majeurs des techniques d'imagerie nucléaire sont l'exposition du patient au rayonnement et l'injection de radiotraceur.

La spectroscopie par proche infrarouge (SPIR) est apparue il y a une trentaine d'années et a très vite été appréciée pour réaliser des études fonctionnelles du cerveau chez l'enfant. La SPIR utilise un petit réseau de capteurs optiques fonctionnant dans le proche infrarouge. Les tissus biologiques sont relativement transparents à ces longueurs d'onde, permettant à la SPIR de détecter des changements d'absorption liés à la modification du ratio oxy/désoxyhémoglobine. La combinaison de plusieurs longueurs d'ondes permet de suivre précisément l'évolution de l'oxygénation des tissus à proximité des capteurs. Ces capteurs sont très compacts et peuvent s'intégrer dans un petit bonnet et sont donc très adaptés pour les

études fonctionnelles sur le nouveau-né et l'enfant. L'inconvénient principal de cette technique est sa limitation d'investigation à la surface du cortex.

L'électroencéphalographie (EEG) est une des seules modalités qui image l'activité électrique neuronale et non pas un effet indirect de cette activité neuronale (couplage neurovasculaire). Elle utilise des électrodes à la surface du crâne (parfois directement implantées dans le cerveau) pour mesurer une différence de potentiel entre 2 électrodes. En utilisant un grand nombre d'électrodes (de plusieurs dizaines à des centaines) on peut réaliser une cartographie relativement précise de l'activité électrique du cerveau.

La magnétoencéphalographie (MEG) est une technique de neuroimagerie fonctionnelle. La MEG utilise des magnétomètres très sensibles pour enregistrer les champs magnétiques produits par les courants électriques se produisant naturellement dans le cerveau. L'activité neuronale génère des courants électriques qui, à leur tour, génèrent des potentiels de champ électrique détectable par l'électroencéphalogramme (EEG). Ces courants neuronaux produisent également un champ magnétique qui est détectable par MEG. Cependant, alors que l'EEG mesure des courants extracellulaires, le MEG est une mesure des courants intracellulaires. L'un des avantages majeurs du MEG sur l'EEG est que le crâne et les tissus mous intermédiaires entre le cerveau et le cuir chevelu ne faussent pas les signaux MEG. La MEG est une technique reconnue pour l'évaluation préopératoire des patients atteints d'épilepsie et des patients atteints de tumeurs cérébrales et révèle également comment le cerveau traite l'information en temps normal, comme dans le langage et la mémoire. La technique MEG fournit des informations avec une résolution temporelle de l'ordre du millième de seconde et avec résolution spatiale élevée (< 5 mm). C'est une modalité d'imagerie non invasive et sûre mais dont le coût reste très élevé.

Les ultrasons (i.e. l'échographie) sont utilisés depuis plus de 40 ans dans le domaine médical. Cette technique d'imagerie est non-invasive, facile à utiliser, relativement portable, sûre, peu onéreuse et peut procurer des images en temps réel. Cependant, cette modalité est peu présente dans le domaine de l'imagerie cérébrale. Cela s'explique car le cerveau est protégé par le crâne qui est un très fort aberrateur pour les ultrasons, c'est-à-dire qu'il déforme le signal, rendant l'imagerie très difficile. Chez le nourrisson, comme le crâne est plus mince que chez l'adulte et que l'échographie peut bénéficier des fontanelles, l'imagerie échographique conventionnelle peut révéler des structures anatomiques et peut même constituer un outil de diagnostic de certaines pathologies. Chez l'adulte, l'imagerie anatomique est quasi-inexistante. A cause du crâne, seule l'imagerie des vaisseaux sanguins est possible. Cette technique non invasive est appelée Doppler transcrânien (TCD). L'imagerie TCD est une technique utilisée à l'heure actuelle en pratique clinique. Elle est réalisée en plaçant un transducteur basse fréquence (≤ 2 MHz) sur le cuir chevelu du patient, à la hauteur de fenêtres acoustiques spécifiques, afin de visualiser les vaisseaux intracrâniens et d'évaluer la vitesse du flux sanguin cérébral et ses variations. Cependant, son utilisation clinique est encore limitée aux mesures de vitesses locales uniquement dans les grosses artères, comme les artères cérébrales antérieures ou moyennes. Cette limitation à l'imagerie des grands vaisseaux est due à l'imagerie ultrasonore conventionnelle sur laquelle elle s'appuie.

L'imagerie ultrasonore est basée sur le principe pulse-écho. Une onde ultrasonore est transmise (impulsion) par un transducteur fait de cristaux piézo-électriques ou un transducteur micro-usiné capacitif (CMUT), qui oscille lorsqu'un signal électrique lui est appliqué. Ce signal électrique est alors converti en une onde cinétique ou mécanique : l'ultrason. Cette onde ultrasonore lorsqu'elle interagit avec les tissus biologiques, peut être réfléchiée et/ou diffusée en fonction des propriétés acoustiques du tissu, c'est ce processus qui va former un écho. Cet écho peut être reçu par le transducteur ultrasonore et une image pourra alors être formée en convertissant l'énergie mécanique en énergie électrique puis en analysant le signal reçu. Diverses méthodes de transmission, de réception et de traitement des ondes ultrasonores ont donné lieu à des techniques distinctes d'échographie qui permettent d'analyser de façons différentes l'interaction entre les échos et les tissus biologiques traversés. Les techniques d'ultrasons conventionnels et ultrarapides en sont deux exemples.

L'imagerie conventionnelle est basée sur le scan ligne par ligne en utilisant des faisceaux d'ultrasons focalisés. Ces faisceaux focalisés sont construits grâce à des lois de retards appliquées à l'onde émise par chaque élément du transducteur. Les hétérogénéités du milieu le long de la ligne balayée réfléchissent le faisceau focalisé, puis les échos rétrodiffusés sont reçus par le transducteur. En ajustant la loi de retard en réception, les ondes sont également focalisées en réception et chaque ligne de l'image peut être reconstruite (focalisation en synthétique). Pour reconstruire une image complète, il est nécessaire de répéter ce processus pour toutes les lignes et les temps, ce qui signifie que l'on doit effectuer plus d'une centaine de répétitions. Avec cette méthode, il est possible d'imager le corps humain en temps réel avec des fréquences d'imagerie allant jusqu'à 100 images/s. Différents types d'imageries ultrasonores conventionnelles, utilisant l'effet Doppler, sont utilisés en pratique clinique pour étudier les flux sanguins, comme le Doppler continu, pulsé et couleur.

Au contraire, l'imagerie ultrarapide est basée sur l'insonification du milieu par des ondes planes ou divergentes à la place des faisceaux focalisés décrits précédemment. Cette nouvelle approche permet d'augmenter la cadence d'imagerie jusqu'à 20 000 images/s. Les ondes planes et divergentes sont générées en appliquant une loi de retard plane ou circulaire sur les éléments du transducteur. Dans les deux cas, il est possible de reconstruire toute une image avec une seule émission ultrasonore ce qui n'est pas possible pour l'imagerie ultrasonore conventionnelle. En revanche, la résolution et le contraste de ces images sont réduits. Une façon de surmonter cette limitation est de sommer les échos rétrodiffusés de façon cohérente. La première application médicale de l'imagerie ultrarapide a été l'imagerie de la rigidité des tissus mous. Cette technique s'appelle l'élastographie par ondes de cisaillement ou la palpation à distance par force de radiation acoustique. L'élastographie est notamment très pertinente pour accéder à des changements de rigidité tissulaire (comme ceux observés dans les tumeurs). L'imagerie Doppler ultrarapide a été également développée pour l'imagerie du cerveau et sa sensibilité a été augmentée par le filtre spatiotemporel SVD (décomposition sur des valeurs singulières) développé au sein du laboratoire. Récemment, l'imagerie ultrarapide en quatre dimensions s'est également développée grâce à un prototype d'échographe ultrarapide avec 1024 voies électroniques, permettant notamment l'élastographie et l'imagerie Doppler en quatre dimensions.

Appliquée à l'imagerie cérébrale, l'imagerie ultrasonore ultrarapide a permis la reconstruction non invasive du réseau vasculaire cérébral sagittal et coronaire chez les nouveau-nés grâce à la résolution spatio-temporelle élevée de l'imagerie Doppler ultrasensible. Dans ce cas, la méthode était facilitée par la présence de fenêtres anatomiques souples préexistantes chez le nourrisson, les fontanelles. La même facilitation s'applique à toutes les études disponibles aujourd'hui sur les animaux, dans lesquelles ces derniers devaient passer par une craniotomie ou une chirurgie d'amincissement du crâne. Même en utilisant une imagerie ultrasonore ultrarapide, la nécessité d'utiliser des agents de contraste, l'élimination complète ou la réduction de l'épaisseur du crâne sont considérés comme étant les seules options jusqu'à présent pour empêcher le crâne d'entraver la pénétration des ondes ultrasonores dans le cerveau.

Comme il a été présenté dans ce chapitre, il existe un réel besoin médical de développer une modalité non invasive (i) pour l'imagerie anatomique, aussi précis que le scan CT mais qui soit non-ionisant; (ii) pour l'imagerie du flux sanguin et l'imagerie fonctionnelle, qui soit aussi sensibles que l'IRM mais portable et moins onéreux; et (iii) pour l'analyse de la rigidité des tissus mous, et qui soit aussi robuste que l'élastographie par résonance magnétique.

L'anatomie, le flux sanguin et la rigidité des tissus mous ont déjà été étudiés avec l'imagerie ultrasonore ultrarapide chez l'homme et validés sur plusieurs organes, tels que le sein et le foie, mais pas encore sur le cerveau adulte. La principale limitation de l'imagerie échographique transcrânienne est aujourd'hui le très fort artefact d'aberration induit par le crâne. En effet, l'os, de par sa composition ne permet pas la propagation des ultrasons comme ailleurs dans le corps humain. Le signal reçu est donc altéré et ne permet pas d'imagerie de qualité.

L'objectif de cette thèse est d'explorer le potentiel d'imagerie du cerveau humain par ultrasons. Une partie de cette thèse porte sur l'imagerie ultrasonore ultrarapide pour l'évaluation de la rigidité des tissus mous (chapitre II) et l'imagerie neuro-fonctionnelle (chapitre III) dans le cerveau humain adulte. Dans les chapitres II et III, ces techniques sont étudiées lors de chirurgie du cerveau chez l'homme afin de contourner le problème des aberrations induites par le crâne. Le chapitre IV est axé sur la correction d'aberration pour l'imagerie ultrasonore. Tout d'abord, une technique de correction d'aberration est étudiée dans le foie humain et permet de faire de l'échographie quantitative. Dans un second temps, cette technique est étudiée pour démontrer la faisabilité de l'imagerie échographique transcrânienne en simulation numérique.

7.2 Elastographie peropératoire du cerveau par onde de cisaillement et elastography 3D avec utilisation d'une sonde matricielle

La première application médicale principale de l'imagerie ultrasonore ultra-rapide était l'imagerie de la rigidité des tissus mous. Cette technique a été désignée comme élastographie par onde de cisaillement (SWE). Dans ce chapitre, nous nous proposons d'évaluer la contribution de l'élastographie par onde de cisaillement en neurochirurgie et de développer l'imagerie 3D à l'aide d'une sonde matricielle afin de pallier aux limitations du 2D.

L'élastographie est une famille de techniques qui illustrent les propriétés élastiques des tissus mous. Son développement a commencé il y a 20 ans et depuis, la pertinence de ses résultats a été cliniquement démontrée. La rigidité tissulaire peut être estimée à partir de l'analyse des déformations du tissu sous contrainte (méthodes quasi-statiques) ou par imagerie d'une onde de cisaillement mécanique induite (méthodes dynamiques). La technique qui nous intéressera dans ce chapitre est une méthode dynamique: l'élastographie par onde de cisaillement.

L'élastographie par onde de cisaillement consiste à générer une poussée en utilisant la force de radiation acoustique, puis, à imager la propagation des ondes de cisaillement résultantes à des cadences élevées grâce à l'imagerie ultrarapide, pour enfin cartographier la vitesse locale de l'onde de cisaillement, qui peut être utilisée pour déterminer la rigidité locale des tissus à l'aide de modèles rhéologiques.

Ces dix dernières années, l'élastographie par onde de cisaillement est devenu un outil majeur de diagnostic. Cette technique a été validée par des études cliniques sur différents organes et pour différentes applications telles que le diagnostic du cancer du sein, le diagnostic des nodules de la thyroïde et l'évaluation de la fibrose dans le foie. Dans ce chapitre nous allons nous intéresser au potentiel diagnostique de l'élastographie par onde de cisaillement dans le cerveau. Ce dernier étant protégé par le crâne qui empêche la propagation des ultrasons, nous allons nous intéresser au cas des chirurgies de tumeurs du cerveau afin d'avoir directement accès au cerveau.

Nous avons d'abord utilisé l'élastographie par onde de cisaillement peropératoire pour quantifier la rigidité des tumeurs et des tissus sains (parenchyme) du cerveau. Notre objectif était de déterminer si la rigidité tissulaire pouvait être un biomarqueur pour différencier les lésions bénignes des lésions malignes pendant des chirurgies du cerveau. Pour ce faire, nous avons réalisé une étude in vivo sur ce sujet sur 63 patients à l'hôpital de la Pitié Salpêtrière.

L'amélioration de la qualité de la résection des tumeurs cérébrales est un objectif primordial pour les neurochirurgiens. Malgré la dissection au microscope, dans certains cas, les chirurgiens ne peuvent pas toujours différencier les tissus normaux et les tumeurs cérébrales. C'est la raison pour laquelle la palpation des tissus par les chirurgiens est couramment utilisée, mais cela est très loin d'être des mesures qualitatives scientifiques. Dans notre étude, nous avons tenté de

définir un atlas de rigidité des tumeurs cérébrales, divisé en quatre principaux types de lésions. Cette étude est la première sur l'élastographie ultrasonore des tumeurs cérébrales, et elle a démontré que les rigidités des tumeurs les plus fréquentes sont significativement différentes. Nous avons mesuré des rigidités moyennes de 33.1 ± 5.9 kPa (3.3 ± 0.6 m/s) pour les méningiomes, 23.7 ± 4.9 kPa (2.8 ± 0.6 m/s) pour les gliomes de bas grade, 11.4 ± 3.6 kPa (1.9 ± 0.6 m/s) pour les gliomes de haut grade, et 16.7 ± 2.5 kPa (2.4 ± 0.4 m/s) pour les métastases. Nous avons également mesuré une rigidité moyenne de 7.3 ± 2.1 kPa (1.6 ± 0.5 m/s) dans le cerveau sain. Les méningiomes et les gliomes de bas grade sont des tumeurs bénignes pour lesquelles nous avons mesuré des valeurs élevées de rigidité, à l'inverse, les gliomes de haut grade et les métastases sont des tumeurs malignes pour lesquelles nous avons mesuré des valeurs faibles de rigidité. Une analyse de la courbe ROC nous a permis de conclure que les valeurs de rigidité mesurées par élastographie par onde de cisaillement permettent de différencier les tumeurs bénignes des tumeurs malignes (Aire sous la courbe ROC: 0.77 [0.64 – 0.87] (intervalle de confiance 95%) ($p < 10^{-4}$, sensibilité: 87.9%, spécificité: 60.7 %)

Dans le cas particulier des gliomes, la mesure de la rigidité pourrait être d'une valeur inestimable pour aider les chirurgiens à distinguer quantitativement les gliomes de haut grade (malins) et de bas grade (bénins). Les gliomes de bas grade ont une rigidité moyenne beaucoup plus élevée ($p=0.01$) que les gliomes de haut grade (Aire sous la courbe ROC : 0.76, $p = 0.002$, sensibilité: 77.8 %, spécificité: 64.3%). Cette différenciation est très importante car la qualité de la résection de la tumeur est étroitement liée au pronostic vital du patient et aux stratégies de traitement. De plus, il n'est pas toujours évident de différencier les gliomes bénins et malins en n'utilisant ni l'IRM ni les données peropératoires. L'utilisation de l'élastographie par onde de cisaillement peut donc diminuer le risque d'erreur dans le diagnostic peropératoire et aider à adapter la résection de la tumeur en fonction de son grade.

D'autre part, la mesure de rigidité peut améliorer la différenciation entre les gliomes de bas grade et le cerveau normal, les gliomes de bas grade ont une rigidité beaucoup plus élevée que le cerveau sain ($p = 0.007$). Les gliomes, sont des tumeurs cérébrales invasives qui s'étendent le long de la substance blanche. La chirurgie est alors un compromis élaboré entre la neurologie et l'oncologie où le grade (de bénin à malin) et les frontières de la tumeur sont des informations décisives pour les neurochirurgiens afin de maximiser la résection tumorale tout en minimisant le risque de morbidité neurologique permanente. Pour ce type de tumeurs, l'élastographie par onde de cisaillement peut aider les chirurgiens pendant la résection en améliorant la définition de la marge de résection, qui n'est pas évidente à l'œil nu, en réduisant cette marge au maximum ou en évitant de déborder sur les zones fonctionnelles.

Notre étude fournit des preuves pour justifier l'utilisation de l'élastographie par onde de cisaillement intra-opératoire dans la chirurgie de tumeur cérébrale: cette imagerie aide les chirurgiens à distinguer quantitativement les tumeurs cérébrales bénignes et malignes (surtout dans les gliomes) et donc à fournir l'étendue optimale de la résection. Comme un temps opératoire aussi court que possible est une préoccupation majeure en neurochirurgie, il est important de

noter que la mesure de rigidité ne prend pas beaucoup de temps. En outre, cette technologie semble être sûre, ni effets secondaires ni infections post-opératoires n'ont été observés.

Ce travail présente également des limites. Tout d'abord, la sonde a un champ d'imagerie maximal défini qui ne peut pas toujours inclure l'ensemble de la tumeur. Cependant, cela ne constitue pas un problème majeur car on peut facilement déplacer la sonde dans l'ouverture du crâne pour obtenir un dépistage complet de la tumeur. Concernant la profondeur du champ, aucun problème n'a été rencontré pour obtenir toute la lésion dans l'image, car le dispositif permet des acquisitions de 40 mm de profondeur. Cependant, les images ne pouvaient pas être réalisées en dessous de ce point, de sorte que les tissus environnants du cerveau normal profond et / ou l'hémisphère cérébral controlatéral n'étaient pas toujours visibles. Avec le dispositif utilisé dans cette étude, seulement 5% des cas ont été perdus en raison d'un manque de signal dans les tissus. Ce problème pourrait être résolu en utilisant une sonde de fréquence inférieure. A titre d'exemple à 3 MHz, des acquisitions de 150 mm de profondeur peuvent être obtenues mais avec une perte de résolution en contrepartie.

L'utilisation de l'élastographie par onde de cisaillement est actuellement limitée par les os du crâne et nécessite une craniotomie. Néanmoins, le Doppler transcrânien (TCD) a été développé pour faciliter les ondes ultrasonores passant par les fenêtres naturelles du crâne (fenêtre temporale ou occipitale). La technique TCD pourrait être améliorée afin de résoudre ce problème, par exemple l'utilisation de techniques de correction des aberrations (voir Chapitre 3) pourrait être mise en œuvre et appliquée à l'élastographie par onde de cisaillement. En perspective, après un certain développement, l'élastographie transcrânienne par onde de cisaillement pourrait être envisagée en préopératoire à travers les fenêtres du crâne.

Dans un second temps, nous avons cherché à mettre en évidence une relation entre la rigidité cérébrale des tissus sains mesurée par l'élastographie par onde cisaillement et la pression intracrânienne. Nous avons réalisé une étude *in vitro* sur des cerveaux de veaux et une étude clinique préliminaire sur ce sujet.

Il est bien connu que la pression dans le cerveau est hydrostatique. La pression hydrostatique est une force appliquée par un liquide à la surface d'un corps immergé. À l'intérieur du système sanguin cérébral, elle dépend du poids de la colonne de sang entre le cœur et un niveau donné. Chez les patients devant subir une intervention neurochirurgicale, la pression hydrostatique joue un rôle important dans la perfusion cérébrale. Le gradient de pression net qui provoque le mouvement du flux sanguin vers cerveau doit être maintenu dans une gamme de valeurs étroites. En effet, trop peu de pression pourrait causer une ischémie cérébrale (écoulement sanguin insuffisant dans le cerveau), et trop de pression pourrait faire augmenter dangereusement la pression intracrânienne (PIC), pouvant aller jusqu'à l'hypertension intracrânienne.

L'hypertension intracrânienne peut être causée par la non-compensation soit d'un volume croissant de parenchyme cérébral, soit d'une augmentation du flux sanguin cérébral ou soit d'une augmentation du liquide céphalo-rachidien (LCR). L'élastographie par onde de cisaillement ne

peut pas détecter de changements de la PIC dus à une augmentation du volume du flux sanguin cérébral, ni ceux dus à une augmentation du LCR. Cependant, l'élastographie par onde de cisaillement peut détecter des changements dus à l'augmentation du volume du parenchyme cérébral, comme par exemple dans des cas de croissance de tumeurs, d'œdèmes, ou d'hémorragie. Dans ces cas, la lésion applique une contrainte directive sur les tissus sains voisins, impliquant un changement de rigidité mesurable par élastographie par onde de cisaillement.

Dans le cas de la chirurgie du cerveau, le seul paramètre influençant la PIC et n'étant pas contrôlée par l'anesthésiste est la croissance du parenchyme cérébral. Notre hypothèse est que la rigidité locale du cerveau normal proche de la lésion peut fournir des informations sur la PIC globale, lorsque le LCR et le sang sont bien contrôlés.

Dans notre étude *in vitro*, nous avons cherché à étudier l'impact d'un stress sur la rigidité du cerveau sain à l'intérieur du cerveau de veau. Pour ce faire, nous avons introduit un ballonnet à l'intérieur d'un cerveau de veau maintenu sous pression dans une boîte en plexiglass. Un capteur de pression était placé dans le cerveau de veau à proximité du ballonnet. Nous avons augmenté le volume du ballonnet millimètre par millimètre et à chaque fois nous avons imagé le cerveau pour obtenir une valeur de rigidité moyenne et nous avons enregistré la pression (sonde de pression). Nous avons trouvé une relation linéaire entre le module de Young en kPa (SWE) et la pression intracorticale en mmHg (sonde de pression) pour chaque cerveau de veau, démontrant que l'élastographie par onde de cisaillement peut détecter une compression locale du parenchyme impliquée dans l'augmentation globale de la pression à l'intérieur du cortex. Cependant, les changements détectés *in vitro* se mesuraient en dizaines de kilo pascal, alors qu'un neurochirurgien est habituellement confronté à des variations beaucoup plus petites.

Pour notre étude *in vivo*, nous avons effectué des mesures de rigidité du cerveau sain avant et après la résection de la tumeur chez cinq patients du service de neurochirurgie de la Pitié Salpêtrière à Paris. Le tissu sain proche de la tumeur a été caractérisé par une valeur moyenne de 14.7 ± 9.9 kPa avant la résection et de 6.5 ± 1.6 kPa après la résection. Cette dernière valeur correspond à la rigidité des tissus sains trouvés dans la première partie de notre étude. Pour expliquer la dispersion des valeurs de rigidité avant résection, nous avons étudié l'influence du diamètre de la tumeur sur l'augmentation de la rigidité des tissus sains avoisinants. Nous avons remarqué que plus le diamètre de la tumeur augmentait, plus la rigidité des tissus sains avoisinant croissait.

Dans un des cinq cas de notre étude *in vivo*, nous avons pu mesurer en parallèle la PIC à l'aide d'un capteur de pression directement introduit dans le parenchyme cérébral. Nous avons enregistré la valeur de la PIC (mmHg) et la rigidité (kPa), avant et après ouverture de la dure-mère, puis après la résection complète de la tumeur. Nous avons constaté que la rigidité des tissus sains n'était pas impactée par l'ouverture de la dure-mère (de 19.3 à 15.5 kPa), alors que la PIC chutait (de 17 à 7mmHg). Mais nous avons pu observer la forte diminution de rigidité des tissus sains après la résection (de 15.5 à 3.7 kPa) en accord avec une nouvelle chute de PIC (de 7 à 1mmHg).

La rigidité cérébrale normale mesurée par élastographie par onde de cisaillement n'est donc pas directement corrélée avec la PIC, quand le volume sanguin ou les changements du LCR sont impliqués. Cependant, la rigidité cérébrale normale et la PIC semblent être corrélées lorsque les changements de PIC sont causés par, et uniquement par, les changements de volume du parenchyme cérébral.

Dans le cas de la chirurgie du cerveau, le seul paramètre influençant la PIC qui n'est pas contrôlé par l'anesthésiste est l'augmentation ou la diminution du volume du parenchyme cérébral. Dans ce cas, lorsque le LCR et le sang sont bien contrôlés, la raideur cérébrale normale mesurée par le SWE pourrait être un indicateur d'hypertension intracrânienne. Une plus grande étude clinique, comprenant des patients avec PIC normal, hypertension intracrânienne légère, modérée et sévère, doit être menée pour déterminer précisément la valeur seuil permettant d'identifier les patients atteints d'hypertension intracrânienne pendant la chirurgie du cerveau.

Enfin, après avoir étudié la contribution de l'élastographie par onde de cisaillement en 2D en neurochirurgie, nous avons construit un échographe capable de faire de l'élastographie par onde de cisaillement en 3D en utilisant une sonde matricielle.

En élastographie, la plupart des méthodes proposées ne donnent accès qu'à un plan d'imagerie 2D en raison des limitations logicielles et matérielles. L'une des conséquences majeures de l'imagerie restreinte au 2D concerne les hypothèses physiques sur la propagation des ondes de cisaillement et le problème inverse qui y est associé. De plus, le positionnement de la sonde reste dépendant de l'opérateur. Pour résoudre ces problèmes, plusieurs solutions ont été proposées dans la littérature pour étendre l'imagerie par ondes de cisaillement à la 3D. Une approche consistait à utiliser une matrice linéaire 1D en translation, qui permet la reconstruction plan par plan du volume élastique à l'aide d'un système d'imagerie 2D. Cependant, étant donné que l'emplacement du faisceau de poussée reste confiné à chaque plan d'imagerie 2D individuel, les problèmes inverses ne peuvent pas être étendus pour bénéficier de la propagation tridimensionnelle de l'onde de cisaillement, qui peut être utilisée pour estimer des propriétés mécaniques complexes telles qu'une anisotropie.

Nous avons étendu le travail de recherche initiale à une approche cliniquement applicable pour l'élastographie en temps réel en ondes de cisaillement 3D. Tout d'abord, afin d'éviter tout artefact lié à la respiration ou au mouvement pulsatile, nous avons choisi de pouvoir acquérir instantanément un volume entier de données pour l'organe imagé. Pour ce faire, le concept d'imagerie ultra-rapide a été étendu à l'imagerie volumétrique 3D ultrarapide. Nous avons développé l'imagerie ultrasonore 3D ultrarapide basée sur l'émission d'ondes divergentes ou planes émanant de sources virtuelles situées derrière une sonde ultrasonore 2D. En combinant de manière cohérente des émissions multiples et en échantillonnant les données des 1024 éléments piézoélectriques d'une sonde matricielle, nous avons démontré qu'il était possible d'effectuer une imagerie 3D par ultrasons à des milliers de volumes par seconde avec un contraste et une résolution élevés. Nous avons construit un scanner ultra-rapide adapté permettant l'acquisition

simultanée de centaines de canaux avec l'électronique appropriée pour la génération d'une onde de cisaillement à l'aide d'une force de radiation acoustique.

Pour notre étude *in vitro*, nous avons utilisé un fantôme de sein dédié à l'élastographie. Plusieurs poussées ont été combinées pour créer un seul volume élastique. Les poussées ont été placées aux cinq coins d'un pentagone inscrit dans un cercle de 10 mm. Pour pouvoir comparer nos résultats préliminaires avec une référence, des mesures de rigidité ont également été réalisées en 2D avec un dispositif Aixplorer (V9.1, supersonique Imagine, Aix-en-Provence, France) travaillant en mode élastographie à ondes de cisaillement avec une sonde linéaire (SC 6 -1, fréquence centrale 3 MHz, Supersonique Imagine, Aix-en-Provence, France).

Du fait que les vitesses d'onde de cisaillement ne peuvent pas être calculées à l'emplacement de la poussée, c'est-à-dire la source d'onde de cisaillement, 5 poussées successives ont été effectuées sur le côté du volume, conduisant à 5 séquences d'ondes de cisaillement indépendantes. Le volume de la vitesse d'onde de cisaillement a été extrait en mètres par seconde pour chaque emplacement de poussée en appliquant des filtres 3D directionnels et l'algorithme d'estimation de temps de vol 3D. La valeur moyenne de la vitesse d'onde de cisaillement dans une région d'intérêt de 10 x 10 x 10 mm située au milieu du volume s'est révélée être de $0,82 \pm 0,13$ m/s ($2,0 \pm 0,05$ kPa). En parallèle, une carte de vitesse d'onde de cisaillement bidimensionnelle a été acquise dans le même fantôme homogène avec une sonde linéaire. La valeur moyenne de la vitesse d'onde de cisaillement a été trouvée à $0,85 \pm 0,15$ m/s ($2,2 \pm 0,07$ kPa) dans une région d'intérêt de 30 mm de diamètre avec des valeurs minimales et maximales de 0,65 m/s (1,3 kPa) et de 1,08 m/s (3,5 kPa), respectivement. Les résultats obtenus par les 2 méthodes, 2D et 3D, étaient en accord.

La mesure *in vivo* a été effectuée sur un volontaire sain dans la zone supérieure droite du sein. Nous avons utilisé la même séquence ultrasonore que celle utilisée pour l'imagerie du fantôme ultrasonore. La valeur moyenne de la vitesse d'onde de cisaillement dans le volume entier (19,2 x 19,2 x 23,2 mm) s'est avérée être de $1,39 \pm 1,58$ m/s ($5,8 \pm 7,5$ kPa). L'acquisition et l'établissement de la cartographie était de 2 minutes, cette durée pourra être diminuée en suivant les progrès de l'informatique. Un autre commentaire important est que l'énergie déposée dans les tissus est relativement limitée, car une seule ou quelques poussées seulement sont nécessaires pour générer des cartes d'élasticité 3D entières.

Le passage au 3D élargit considérablement le champ des applications cliniques potentielles de l'échographie, de la cartographie des fibres du cœur jusqu'à la quantification de la contraction du muscle squelettique. En outre, nous avons également montré que la source d'onde de cisaillement peut être contrôlée dans l'espace 3D, ce qui ajoute un degré de liberté par rapport aux techniques standards. De telles ondes planes de cisaillement pourraient être utilisées pour récupérer des cartes d'atténuation de cisaillement et de dispersion, ce qui conduirait à une caractérisation rhéologique 3D complète et pourrait contribuer à élargir notre compréhension actuelle de la physique des ondes de cisaillement dans les applications médicales.

Une telle technologie n'a pas encore été testée sur le cerveau pendant la chirurgie (parce que le scanner n'est pas encore conforme au marquage CE), mais elle est envisagée pour surmonter

rapidement les limitations actuelles de l'élastographie 2D et élargir son champ d'application à de nouvelles approches diagnostiques basées sur des données d'onde de cisaillement volumiques avec une dépendance liée à l'opérateur réduite.

Dans ce chapitre, nous avons fourni plusieurs preuves de l'intérêt d'utiliser l'élastographie par onde de cisaillement pendant la chirurgie du cerveau. Nous avons également présenté notre nouvelle technique pour l'élastographie par onde de cisaillement en 3D à l'aide d'une sonde matricielle promettant une large gamme d'applications.

7.3 Imagerie neurofonctionnelle peropératoire par ultrasons

L'imagerie fonctionnelle (ou imagerie physiologique) est une technique d'imagerie médicale permettant de détecter ou de mesurer des changements de métabolisme, de flux sanguin, de composition chimique locale, ou d'absorption. Contrairement à l'imagerie de structure, l'imagerie fonctionnelle se concentre sur le suivi des activités physiologiques au sein d'un tissu ou d'un organe en employant des modalités d'images médicales qui utilisent très souvent des marqueurs. L'imagerie neuro-fonctionnelle est utilisée pour mesurer un aspect de la fonction cérébrale afin de comprendre la relation entre des fonctions mentales spécifiques et l'activité dans certaines zones du cerveau.

Un large spectre de méthodes est utilisé pour la neuroimagerie in vivo. L'activité cérébrale peut être détectée directement en mesurant l'activité électrique des neurones, comme par exemple avec la stimulation électrique corticale (ESM), l'imagerie calcique et l'imagerie fonctionnelle par colorant sensible au potentiel. Cependant, l'activité fonctionnelle du cerveau peut également être suivie par la mesure de l'apport sanguin, comme proposé pour la première fois par Lavoisier en 1920 et démontrée par Mosso en 1981. En effet, l'activité neuronale induit des changements spatio-temporels rapides du débit sanguin (CBF) et du volume sanguin (CBV) dans le réseau vasculaire cérébral, on parle de couplage neurovasculaire. Aujourd'hui, plusieurs modalités d'imagerie fonctionnelle exploitent les changements locaux du flux sanguin pour cartographier la réponse fonctionnelle aux stimuli cérébraux, telles que la microscopie multiphotonique, la tomographie par cohérence optique, la tomographie par émission de positrons et l'imagerie par résonance magnétique fonctionnelle (IRMf).

La localisation des régions hautement fonctionnelles est un véritable défi pendant les chirurgies du cerveau. Une cartographie précise des différentes zones fonctionnelles entourant la lésion peut indiquer au chirurgien où s'arrêter. La résection tumorale est donc réalisée dans le respect des limites fonctionnelles afin d'optimiser la précision de la résection tumorale tout en minimisant le risque de déficits fonctionnels postopératoires. Jusqu'à présent, il existe principalement deux techniques couramment utilisées pour l'imagerie fonctionnelle lors de chirurgies cérébrales: l'ESM,

où l'activité électrique des neurones est détectée directement et l'IRMf, basée sur le couplage neurovasculaire. Bien que la précision de l'ESM intraopératoire soit élevée, cette technique comporte plusieurs inconvénients comme la durée (il faut tester toutes les zones fonctionnelles une par une) et le risque de crise d'épilepsie (pouvant être provoquée par la stimulation électrique corticale). Ces dernières ont été rapidement contrôlées par le neurochirurgien par injection de sérum glacé directement sur le cortex. L'ESM peut être stressant pour le patient et dans certains cas ne peut pas être effectuée en raison de considérations cliniques. En outre, les neurochirurgiens ne stimulent normalement pas dans la profondeur d'un sillon non ouvert et ne stimulent donc pas l'ensemble du cortex en profondeur. En ce qui concerne les cartes d'activation IRMf, cette technique fournit une cartographie fonctionnelle non invasive utilisée par le chirurgien pour planifier la résection de la lésion. Cependant, le changement de pression, après l'ouverture de la dure-mère entraînant un déplacement du cerveau, reste un problème majeur lors de l'utilisation de la neuronavigation IRM et ne permet pas d'assurer une correspondance parfaite entre les images IRMf et la réalité chirurgicale.

Bien que la neuroimagerie fonctionnelle pendant la chirurgie intra-opératoire présente de nombreux avantages, aucune des techniques existantes ne fournit une modalité d'imagerie cérébrale en profondeur, simple, sûre, portable et caractérisé par une haute résolution pendant la chirurgie. L'échographie a le potentiel de répondre à ce besoin de cartographier les zones fonctionnelles pendant des chirurgies du cerveau. En effet, l'imagerie ultrasonore permet d'obtenir une bonne résolution spatio-temporelle en profondeur et est actuellement utilisée de manière courante pendant les chirurgies pour localiser le tissu tumoral (formes, limites) et caractériser la rigidité de la tumeur et celle des tissus sains, comme démontré dans le chapitre 2. Cependant, l'utilisation de l'échographie Doppler a été jusqu'à présent limitée à l'imagerie des gros vaisseaux, en raison de sa faible sensibilité. L'imagerie Doppler ultrasonore est basée sur l'effet Doppler, en évaluant le décalage de fréquence d'une onde pour un observateur (sonde ultrasonore) par rapport à une source se déplaçant dans le temps (globules rouges). La faible sensibilité du Doppler conventionnel est due à l'utilisation de faisceaux ultrasonores focalisés. Afin de surmonter cette limitation, l'imagerie ultrasonore ultrarapide a été développée dans notre laboratoire. Avec cette méthode d'imagerie, la programmation d'une seule onde plane dans le milieu suffit pour reconstruire une image entière. Les échos rétrodiffusés par les tissus suite au passage de l'onde plane sont stockés dans la mémoire d'un appareil d'échographie dans lequel la formation d'images est effectuée en parallèle. Cette approche permet la caractérisation du réseau vasculaire à l'échelle de l'image entière. Cette séquence Doppler ultrarapide permet d'obtenir un meilleur rapport de contraste de tissus (CTR) et donc une image Doppler de meilleure qualité. En effet, avec une cadence d'acquisition très élevée (jusqu'à 20 000 images par seconde), nous pouvons acquérir des images Doppler jusqu'à dix fois plus rapidement qu'en Doppler conventionnel. Cette technique permet donc d'améliorer la sensibilité sans sacrifier ni la résolution spatiale ni la résolution temporelle. Le Doppler ultrarapide est en effet le facteur clé pour pouvoir étudier les petits vaisseaux en profondeur dans les tissus tout en permettant une mesure quantitative pixel par pixel du flux sanguin.

De plus, il est possible d'extraire la puissance du signal Doppler des mesures Doppler ultrasensibles, en effectuant la moyenne temporelle de l'intensité du signal Doppler. La répétition de l'acquisition d'images Doppler ultrasensibles au fil du temps permet de suivre la dynamique de flux modulée par l'activité neuronale locale dans les petits vaisseaux. Dans notre laboratoire, il a été montré chez le rat que ce paramètre est associé à la réponse hémodynamique du volume de sang d'une région activée par le stimulus correspondant. Au cours de cette thèse, nous avons développé des séquences d'imagerie fonctionnelle par ultrasons (fUS) basées sur le Doppler ultrasensible en utilisant des échographes programmables (Aixplorer®, Supersonic Imagine), pour permettre l'imagerie de la dynamique de la microvascularisation du cerveau humain en réponse à l'activation cérébrale, en modifiant les paramètres d'émissions (fréquences d'imagerie), d'acquisitions (cadences), et de création d'images afin de préserver la haute résolution temporelle et spatiale (250 μm , 1 ms).

Afin de tester la capacité des ultrasons fonctionnels à détecter des zones fonctionnelles chez l'homme, nous avons mené une étude clinique sur 33 patients de l'hôpital la Pitié Salpêtrière. Nous avons écrit un protocole de recherche biomédical et enregistré nos patients dans la base de données Clinicat Trials (Protocol C14-66: Intraoperative Functional Ultrasound (FUSIMAGINE)). Les considérations éthiques ont été étudiées et approuvées par le Comité de Protection des Personnes – Ile-de-France VI – Pitié Salpêtrière" (CPPIDF6). Tous les patients inclus dans notre étude avaient des gliomes bas grade nécessitant une chirurgie assistée par ESM et ont signé un formulaire de consentement préalablement à l'étude. Pour 27 patients, le réveil pendant la phase de stimulation électrique corticale était programmé, les 6 autres patients étaient sous anesthésie générale pendant la totalité de leur intervention.

Pendant les chirurgies, après ouverture du crâne et de la dure-mère, les données ESM (cartographie corticale) ont été utilisées pour le positionnement de la sonde ultrasonore sur une zone fonctionnelle ciblée. Avec l'aide du neurochirurgien et d'une orthophoniste de bloc opératoire, nous avons très peu de temps pour choisir l'action liée à la zone fonctionnelle que nous allions étudier. La sonde ultrasonore était placée dans une capote de sonde stérile remplie de gel et placée directement sur le cortex après ouverture du crâne et de la dure-mère. Pour garantir son immobilité, la sonde ultrasonore était fixée sur un bras articulé autoclavable en acier inoxydable. Sous la supervision de l'orthophoniste, nous avons demandé aux patients d'effectuer l'action spécifique correspondant à l'étiquette de la cartographie ESM dans le cas d'une anesthésie locale (patient éveillé). Dans le cas d'une anesthésie générale, une tierce personne déplaçait ou caressait le segment du membre concerné. Pendant l'acquisition des images Doppler ultrasensibles, nous avons demandé aux patients ou à la tierce personne d'effectuer une action particulière, en alternant des périodes de référence et des périodes d'action. 220 secondes ont été nécessaires pour évaluer une zone fonctionnelle, représentant 55 acquisitions ultrasonores. Une acquisition ultrasonore durait 4 secondes, composée d'une seconde pour l'acquisition (un cycle cardiaque) et de 3 secondes pour le transfert et l'enregistrement des données. Une à trois actions différentes ont été testées pour chaque patient. Une séance complète pour un patient, pendant laquelle deux actions différentes en moyenne étaient testées, durait environ 8 minutes au total, lors d'une intervention chirurgicale durant en moyenne de 4 à 6 heures. Sur les 28 patients pour

lesquels il n'y a eu aucune complication chirurgicale, nous avons pu tester 51 actions (e.g, moteur main, sensitif main, moteur bouche, sensitif bouche, etc, ...). Dans 48 cas, la sonde a pu être correctement positionnée sur l'étiquette ESM correspondant à l'action choisie, et le fUS nous a permis d'imager la zone fonctionnelle.

En analysant les résultats des 48 cas, nous avons constaté qu'un stimulus entraînait une augmentation régulière du volume sanguin dans la région corticale associée, caractérisée par une augmentation de 20% du signal de Doppler de puissance pendant les stimuli. Des cartes d'activation ont été construites présentant le coefficient de corrélation entre le signal de Doppler de puissance et le motif temporel de stimulus. Les cartes d'activation démontrent une corrélation significative et localisée ($r > 0.41$) entre le signal de Doppler de puissance (PD) et le motif temporel de stimulus pendant l'action.

Nous avons démontré la capacité des ultrasons ultrarapides à identifier, cartographier et différencier en profondeur (3cm) les régions d'activation corticales en réponse à un stimulus, à la fois chez les patients éveillés et chez les patients anesthésiés. Nous avons démontré que l'imagerie fUS a le potentiel de devenir une modalité complète de neuroimagerie avec des avantages majeurs pour une utilisation peropératoire.

7.4 Focalisation dans du bruit de speckle pour l'échographie quantitative et la correction d'aberration

Dans le chapitre précédent, nous avons étudié les possibilités offertes par l'imagerie ultrarapide du cerveau chez l'homme. Cela a été possible pour les études *in vitro* (cerveaux de veaux) et *in vivo* chez des patients trépanés lors de chirurgies, quand nous avons eu un accès direct au cerveau. Dans cette partie de la thèse, nous nous sommes intéressés à corriger l'aberration (modification du faisceau ultrasonore) induite par le crâne afin de progresser vers l'imagerie ultra-rapide transcrânienne. Le crâne provoque de très fortes aberrations de phase et d'amplitude au faisceau ultrasonore, conduisant à un échec de la focalisation et ce fait a une qualité d'image très dégradée. Nous avons donc tout d'abord décidé de tester notre technique de correction d'aberration dans des conditions expérimentales plus faciles que le cas du crâne. Nous avons choisi d'étudier en premier le cas du foie. En effet, pour l'imagerie du foie, nous avons fait face à un milieu non homogène: le faisceau d'ultrasons doit traverser la graisse et le muscle sous-cutané avant d'atteindre le foie. Ces couches superficielles induisent une aberration de phase plus légère que dans le cerveau et ne provoquent pas d'aberration d'amplitude. Parmi les différentes maladies pouvant toucher le foie, il en existe une qui nécessite des mesures quantitatives, il s'agit de la stéatose ou maladie du foie gras. Nous avons décidé d'utiliser notre technique de correction d'aberration pour faire de l'échographie quantitative dans le foie pour le diagnostic de la stéatose.

Par la suite nous avons utilisé notre technique de correction d'aberration pour améliorer l'image échographique du cerveau en transcrânien en réalisant des simulations numériques.

Dans un premier temps, nous avons utilisé une technique d'adaptation de la focalisation dans le bruit de speckle pour l'échographie quantitative dans le foie. Il est connu que la vitesse du son dans les tissus mous varie avec la teneur en graisse, une relation entre la vitesse du son et le pourcentage de graisse dans le foie peut donc être trouvée. En calculant la vitesse du son de façon précise dans le foie, nous avons pour but d'accéder à son pourcentage de graisse, et donc au grade correspondant de stéatose hépatique.

La stéatose hépatique due à l'accumulation de graisse dans le foie est la cause la plus fréquente de maladie hépatique chronique et peut conduire à des conditions hépatiques sévères. La biopsie et l'IRM sont des techniques standard pour diagnostiquer la stéatose en pourcentage de graisse dans le foie. Ces techniques ne sont pas sans limites. Tout d'abord, la biopsie du foie souffre de problèmes d'échantillonnage: les biopsies hépatiques échantillonnent aussi peu que 1/50 000 de la masse totale du foie, ce qui entraîne souvent une information insuffisante pour un diagnostic définitif. Deuxièmement, c'est une méthode invasive impliquant certains risques, du stress et des dépenses supplémentaires. Enfin, l'évaluation histologique est subjective et dépend de l'expérience du médecin. En ce qui concerne l'IRM, il s'agit actuellement de la méthode d'imagerie non invasive la plus précise pour le diagnostic et la quantification de la stéatose hépatique. Cette technique permet d'estimer la fraction de graisse comme un ratio du nombre de protons de graisse sur le nombre de protons d'eau. Toutefois, l'IRM a également plusieurs limites : son coût, les contre-indications, et sa faible disponibilité. Bien que l'échographie conventionnelle soit largement utilisée par les radiologues pour l'évaluation de la stéatose hépatique, elle demeure qualitative. Par conséquent, il existe un besoin médical de développer des techniques non invasives qui peuvent quantifier de façon robuste le degré de stéatose hépatique.

Nous avons développé une méthode basée sur trois étapes pour déterminer de façon précise la vitesse du son dans un milieu multi couches. Pour obtenir une première estimation de la vitesse du son, nous nous basons sur l'étude de la fonction de cohérence spatiale des échos rétrodiffusés (théorème de Van Cittert-Zernike appliqué aux ultrasons) résultant d'un faisceau ultrasonore focalisé dans le milieu. En effet, la vitesse du son optimale est celle qui permet une cohérence spatiale maximale des échos provenant d'un foyer focalisé. Cependant la vitesse obtenue est une vitesse globale, caractérisant la totalité du parcours effectué par les ultrasons. Or, avant d'atteindre le foie, le faisceau ultrasonore traverse des couches de graisse et de muscle d'épaisseur différentes. Ces couches introduisent des distorsions du front d'onde ultrasonore et nuisent à la fiabilité de notre estimation de vitesse du son. Notre première estimation sert donc de point de départ d'un algorithme itératif permettant la correction des aberrations induites par les couches supérieures. Cet algorithme est basé sur la technique d'utilisation du bruit de speckle pour la création d'une source virtuelle et la correction d'aberration. La correction de ces aberrations améliore la précision de notre estimation de la vitesse du son. La dernière étape de notre technique a consisté à intégrer l'influence des couches superficielles dans le calcul, dans le cas d'un milieu

multicouche. Cette étape n'est pas entièrement automatique car elle nécessite la mesure des couches de graisse et de muscle par le médecin afin de les intégrer au calcul.

Pour nos expériences, aussi bien dans les fantômes ultrasons que *in vivo* chez des patients, nous avons utilisé une sonde courbe abdominale de 192 éléments piézoélectriques (sonde SC 6-1, Supersonic Imagine, Aix-en-Provence, France) pilotée par un scanner ultrasonore entièrement programmable Aixplorer (SuperSonic Imagine, Aix-en-Provence, France). Par rapport à la sonde linéaire utilisée dans les chapitres précédents, nous avons ici décidé d'utiliser une sonde courbe, tout d'abord pour agrandir notre champ de vision, et également pour permettre un examen plus en profondeur. En effet, le foie se tient derrière les couches de graisse et de muscle, et nous devons accéder à un échantillon de foie de taille non négligeable, cela nous entraînant dans des profondeurs optimales d'investigation de 6 cm de profondeur.

En émission, la matrice d'Hadamard a été utilisée pour encoder spatialement les formes d'onde. Ce type de codage spatiotemporel permet d'augmenter l'amplitude du signal émis, et permet également d'effectuer des focalisations virtuelles en post-traitement en combinant les signaux radiofréquences issus des différentes transmissions. La durée d'une acquisition ultrasonore était de deux secondes.

Avant de tester notre technique *in vivo* dans le foie humain, nous avons fait des expériences sur des fantômes ultrasonores. Nous avons réalisé des acquisitions sur deux fantômes calibrés: un fantôme ATS (modèle 551) caractérisé par une vitesse du son de $1,45 \text{ mm} \cdot \mu\text{s}^{-1}$ et un fantôme CIRS (modèle 054) caractérisé par une vitesse du son de $1,54 \text{ mm} \cdot \mu\text{s}^{-1}$. Pendant l'acquisition ultrasonore, la sonde était maintenue par un bras articulé. Tout d'abord, nous avons réalisé des mesures sur fantômes homogènes. Afin de trouver une estimation de la vitesse du son (SSE) moyenne dans un fantôme, 20 acquisitions avec repositionnement de la sonde ont été effectuées. La SSE moyenne pour le fantôme ATS s'est avérée être de $1,449 \pm 0,006 \text{ mm} \cdot \mu\text{s}^{-1}$ pour une vitesse sonore donnée par le constructeur de $1,450 \text{ mm} \cdot \mu\text{s}^{-1}$. La SSE moyenne pour le fantôme CIRS s'est avérée être de $1,544 \pm 0,003 \text{ mm} \cdot \mu\text{s}^{-1}$ pour une vitesse sonore donnée par le constructeur de $1,540 \text{ mm} \cdot \mu\text{s}^{-1}$. Ces résultats ont démontré que dans le cas fantôme homogène, le SSE obtenu était en bon accord avec la vitesse du son indiquée par le constructeur. Dans un second temps, nous avons recouvert le fantôme d'une couche d'eau. Nous avons fait varier la température de l'eau pour obtenir des couches superficielles caractérisées par des vitesses du son différentes ($1,46$, $1,48$ et $1,52 \text{ mm} \cdot \mu\text{s}^{-1}$), nous avons également joué sur l'épaisseur de la couche d'eau sur le fantôme (allant de 0 à 26 mm). Le but de l'étude fantôme était de trouver une SSE égale à la vitesse du son donnée par le fabricant du fantôme malgré la couche superficielle d'eau aberrante. Nous avons observé que, sans correction de l'influence des couches superficielles, la SSE variait en fonction de la vitesse du son dans la couche superficielle et de son épaisseur. Après correction de cette influence par intégration de la vitesse du son et de l'épaisseur de cette couche dans le calcul, la SSE correspond bien à nouveau à la vitesse du son donnée par le constructeur.

Suite à ces résultats encourageants, nous avons décidé d'essayer notre technique *in vivo*. Ce passage en clinique a été possible grâce au faible temps d'acquisition (2 secondes), pendant lequel un patient peut retenir son souffle.

Nous avons tout d'abord réalisé une étude clinique préliminaire de 17 patients du service de radiologie de l'hôpital Beaujon à Paris. Dans cette étude clinique pilote, nous avons démontré le potentiel de notre méthode pour la détection et la quantification non invasive de la stéatose hépatique. Notre approche permet une estimation précise de la vitesse ultrasonore dans le foie avec un écart type inférieur à 5%. Nous avons obtenu des SSE allant de 1,492 mm.µs⁻¹ à 1,604 mm.µs⁻¹ pour les patients caractérisés par des pourcentages de graisses de 2% à 17% par IRM et de 0% à 80 en biopsie. Nous avons utilisés l'IRM et la biopsie comme techniques de références, en accordant une attention particulière à l'IRM, car elle est à ce jour considérée comme l'approche la plus efficace pour l'estimation de la stéatose. Notre technique permet de trouver une corrélation linéaire très élevée ($R^2 = 0,69$) entre le pourcentage de graisse trouvé par IRM et la SSE, démontrant que nous pouvons quantifier la stéatose hépatique par ultrasons. De plus, la SSE est excellente pour différencier significativement les patients sains et malades ($p < 0,0001$, AUROC = 0,942). Notre technique permet d'établir une valeur de coupure entre les patients en bonne santé et les patients atteints de stéatose (critère SSE = 1.555 mm.µs⁻¹), ce diagnostic étant par exemple essentiel chez les patients qui subissent une transplantation hépatique due au risque de mauvaise survie du greffon.

Une des limitations de cette étude préliminaire est l'hétérogénéité de la population. Certains patients avaient des maladies hépatiques chroniques avec divers degrés de fibrose, ou même une cirrhose. Nous avons donc mené une autre étude avec une plus grande cohorte de patients, et nous avons conduit une analyse multi-variable pour évaluer l'influence de notre mesure de facteurs importants tels l'indice de masse corporelle (IMC) et la cirrhose.

Pour cette étude comportant un nombre beaucoup plus grand de patients (50 patients, ainsi qu'une cohorte de validation de 50 autres patients), nous avons réalisé une interface graphique pour permettre aux radiologues d'être indépendants pendant leurs examens. Cette étude clinique nous a permis de valider nos hypothèses en confirmant que la SSE calculée pouvait bien être reliée au pourcentage de graisse dans le foie. Sur les 50 patients de la cohorte de validation nous avons pu faire une analyse de la variabilité intra- et inter opérateur.

Pour des patients caractérisés par des pourcentages de graisse mesurés par IRM allant de 1% à 33%, nous avons trouvé des valeurs de SSE de 1.454 à 1.625 mm.µs⁻¹. Si l'on veut pouvoir quantifier avec précision la stéatose hépatique, l'intervalle de confiance entre 2 mesures ne doit pas dépasser $\pm 0,05$ mm.µs⁻¹. Une analyse de Bland-Altman a démontré un très bon accord entre les mesures intra-opérateur: standard déviation moyenne $\pm 0,016$ mm.µs⁻¹, de même que pour les mesures inter-opérateurs: MSD $\pm 0,024$ mm.µs⁻¹. Cependant, lors de notre étude clinique à plus grande échelle, nous avons remarqué un phénomène que nous n'avions pas pu observer avec notre cohorte de patients préliminaire : le pourcentage de graisse mesuré par IRM et notre SSE ne sont en fait pas corrélés de manière linéaire. Il nous est alors venu l'idée de tester la formule de Wood. Nous avons considéré le foie comme un milieu biphasique foie/graisse, caractérisé par un très faible pourcentage de graisse pour un foie sain, et à l'inverse par un pourcentage de graisse très élevé pour un foie stéatosique. La formule de Wood nous a permis de relier la vitesse du son, la densité, et le module d'élasticité, afin de déterminer la fraction de graisse dans le foie étudié.

Nous avons obtenu une corrélation de $R^2 = 0.61$ entre le modèle théorique de Wood et les données de la première cohorte de patients, et une corrélation de $R^2 = 0.65$ entre le modèle théorique de Wood et les données de la cohorte de validation. Nous avons également obtenu de très bonnes corrélations linéaires ($R^2 = 0.73$, et $R^2 = 0.76$) entre le pourcentage de graisse calculé par ultrasons et celui calculé par IRM.

Comme perspective importante, nous devrions poursuivre l'investigation et améliorer notre méthode afin de l'affranchir de l'étape de mesure des couches superficielles par le médecin.

Avec ce travail sur l'échographie quantitative dans le foie, nous avons appris beaucoup de choses sur la correction d'aberration de phase. La dernière partie se concentre sur la correction de l'aberration crânienne en simulation numérique vers la focalisation adaptative transcrânienne. Le cerveau est l'un des organes les mieux protégés du corps humain. Il baigne dans le liquide céphalo-rachidien qui peut atténuer les accélérations de la tête. La voûte crânienne qui l'entoure est composée de différents os liés par des sutures. L'os du crâne a un caractère particulièrement poreux en son centre et une épaisseur qui peut varier de 10 mm à 1 mm dans la zone temporale la plus mince. Néanmoins, l'os temporal reste un aberrateur extrêmement fort pour le faisceau ultrasonore, en raison de sa composition en couches de porosités différentes. Le crâne présente une structure à trois couches, avec une zone poreuse, appelée diploé, placée entre deux couches denses. La densité du crâne peut varier de 1000 à 2200 kg.m⁻³. La forte rupture d'impédance acoustique à l'interface peau/os et os/dure-mère est un facteur très limitant pour la transmission acoustique. Les variations spatiales de la vitesse du son induisent une distorsion de phase et d'amplitude du front d'onde se propageant dans le milieu. Ces aberrations dégradent la résolution spatiale. Un grand écart entre les vitesses acoustiques dans le tissu cérébral ($c \approx 1500$ m.s⁻¹) et dans le crâne (c varie de 2700 à 3000 m.s⁻¹), et une forte atténuation des ultrasons dans l'os du crâne, dégradent gravement la forme du faisceau ultrasonore.

Nous avons construit un modèle de simulation numérique pour tester notre algorithme de correction d'aberration de phase en présence d'un crâne (données issues d'un scan CT de crâne de singe). Nous avons créé deux milieux, un pour tester la résolution et un pour tester le contraste. Nous avons comparé la qualité de focalisation avec et sans correction d'aberration de phase, ainsi que la qualité des B-modes. La correction d'aberration de phase améliore beaucoup le contraste et la résolution, mais le B-mode est créé avec une erreur de profondeur. La correction d'amplitude peut apporter une amélioration supplémentaire soit en résolution (compensation de l'amplitude), soit en contraste (amplification d'amplitude), à choisir en fonction de l'application. Enfin, pour corriger l'erreur de profondeur, nous avons utilisé notre technique de mesure de la vitesse globale (étude de la cohérence spatiale en fonction de la vitesse du son testée). En calculant la vitesse du son de la barrette au point focal et en utilisant cette vitesse dans le « beamformer », nous avons obtenu des images B-mode caractérisées par un bon contraste, une bonne résolution, et respectant la profondeur.

Dans la première partie de ce chapitre, nous avons utilisé une technique en trois étapes pour calculer précisément la vitesse du son (SSE) dans un milieu. Cette technique a été testée dans des fantômes ultrasonores et *in vivo* dans les foies de patients. Dans les deux cas, notre méthode a été capable de trouver la vitesse du son correspondant au milieu. Nous avons démontré que la SSE était liée à la fraction de graisse. Cette analyse a permis de conclure que la SSE était en mesure de distinguer un foie sain et d'un foie malade (>10% de cellules de graisse en biopsie) aussi bien avec la biopsie qu'avec l'IRM comme méthode de référence. Combiné à l'utilisation de la formule de Wood, nous avons même pu avoir accès à une fraction de graisse mesurée par ultrasons (%). Cette dernière s'est avérée être fortement corrélée avec la fraction de graisse de référence ($R^2 = 0,73$) et a permis de grader la stéatose hépatique de manière non invasive. Dans la seconde partie nous avons combiné des corrections d'aberration de phase, d'amplitude et de vitesse du son pour faire de l'imagerie transcrânienne en simulation numérique. Nous avons atteint notre objectif en obtenant des images représentant fidèlement le milieu (position latérale et profondeur) caractérisées par une résolution et un contraste similaires à ceux obtenus avec une source ponctuelle dans le milieu. Afin de valider cette technique *in vitro* nous avons conçu un fantôme de tête possédant les caractéristiques acoustiques du crâne et du cerveau. Comme perspectives, nous combinerons l'imagerie ultrarapide par ondes planes avec une sonde « phased array » (de type cardiaque) pour améliorer la résolution de Doppler transcranien et pouvoir imager de plus petits vaisseaux qu'en TCD conventionnel, dans le but de pouvoir dans le futur faire de l'imagerie neurofonctionnelle transcrânienne.

7.5 Conclusion générale

L'objectif de cette thèse était d'explorer le potentiel de l'imagerie du cerveau humain par ultrasons. L'anatomie, le flux sanguin et la rigidité des tissus mous ont déjà été étudiés avec l'imagerie ultrasonore ultrarapide chez l'homme et validés sur plusieurs organes, tels que le sein et le foie, mais pas encore sur le cerveau adulte. La principale limitation de l'imagerie échographique transcrânienne est aujourd'hui le très fort artefact d'aberration induit par le crâne. En effet, l'os, de par sa composition ne permet pas la propagation des ultrasons comme ailleurs dans le corps humain. Le signal reçu est donc altéré et ne permet pas d'imagerie de qualité. Dans cette thèse, nous avons utilisé l'imagerie ultrasonore ultrarapide pour l'évaluation de la rigidité des tissus mous et l'imagerie neurofonctionnelle dans le cerveau humain adulte, lors de chirurgies du cerveau afin de contourner dans un premier temps le problème des aberrations induites par le crâne. La dernière partie de cette thèse était axée sur la correction d'aberration pour l'échographie quantitative et l'imagerie ultrasonore transcrânienne.

Nous avons tout d'abord fournis plusieurs preuves de l'intérêt d'utiliser l'élastographie par onde de cisaillement pendant la chirurgie du cerveau. Nous avons également présenté notre nouvelle technique pour l'élastographie par onde de cisaillement en 3D à l'aide d'une sonde matricielle dans le but de pouvoir dépasser les limitations du 2D et notamment être moins dépendant de l'opérateur.

Dans un second volet, nous avons démontré la capacité des ultrasons ultrarapides à identifier, cartographier et différencier en profondeur (3cm) les régions corticales d'activation en réponse à un stimulus, à la fois chez les patients éveillés et chez les patients anesthésiés. Nous avons démontré que l'imagerie neurofonctionnelle par ultrasons a le potentiel de devenir une modalité complète de neuroimagerie avec des avantages majeurs pour une utilisation peropératoire.

Dans un troisième volet, nous avons utilisé une technique en trois étapes pour calculer précisément la vitesse du son (SSE) dans un milieu. Cette technique a été testée dans des fantômes ultrasonores et *in vivo* dans les foies de patients. Dans les deux cas, notre méthode a été capable de trouver la vitesse du son correspondant au milieu. Nous avons démontré que la SSE était liée à la fraction de graisse. Cette analyse a permis de conclure que la SSE était en mesure de distinguer un foie sain et d'un foie malade (>10% de cellules de graisse en biopsie) aussi bien avec la biopsie qu'avec l'IRM comme méthode de référence. Combiné à l'utilisation de la formule de Wood, nous avons même pu avoir accès à une fraction de graisse mesurée par ultrasons (%) de manière non invasive. Puis nous avons combiné la correction d'aberration de phase, d'amplitude et de vitesse du son pour faire de l'imagerie transcrânienne en simulation numérique. Nous avons atteint notre objectif en obtenant des images représentant fidèlement le milieu (position latérale et profondeur) et caractérisées par une résolution et un contraste similaires à ceux obtenus avec une source ponctuelle dans le milieu.

Afin de valider cette technique *in vitro* nous avons conçu un fantôme de tête possédant les caractéristiques acoustiques du crâne et du cerveau. Comme perspectives, nous combinerons l'imagerie ultrarapide par ondes planes avec notre technique de correction d'aberration (phase, amplitude, vitesse du son) en utilisant une sonde « phased array » (de type cardiaque) pour faire de l'imagerie ultrarapide transcrânienne. Comme nous avons démontré la faisabilité et l'utilité de l'élastographie par onde de cisaillement et de l'imagerie neurofonctionnelle par ultrasons, et que nous avons développé une technique permettant d'améliorer la qualité d'imagerie transcrânienne par ultrasons, la perspective à long terme est de pouvoir utiliser l'imagerie ultrarapide et ses diverses applications de manière non-invasive en transcrânien.

Scientific Output

8. Scientific output

Peer-reviewed Journal Articles

Imbault*, M., Dioguardiburgio*, M., Faccinnetto, A., Ronot, M., Gennisson, J-L., Vilgrain, V., Tanter, M. Clinical value of robust sound speed estimation for quantitative evaluation and grading of Hepatic Steatosis. (in preparation)

Imbault*, M., Jensen, J., Osmanski, B-F, Bo Stuart, M., Tsatsaris, V., Jensen, J-A., Lecarpentier, E., Tanter, M. Mapping of fetal vascular resistivity in the human placenta using ultrafast plane wave ultrasound imaging. (in preparation)

Imbault*, M., Chauvet*, D., Gennisson, J-L., Capelle, L., Tanter, M., 2017. Functional Ultrasound Imaging of the Human Brain Activity. (under review)

Imbault*, M., Faccinnetto*, A., Osmanski, B-F., Tissier, A., Deffieux, T., Gennisson, J-L., Vilgrain, V., Tanter, M., 2017. Robust sound speed estimation for ultrasound-based hepatic steatosis assessment. *Phys. Med. Biol.* doi: 10.1088/1361-6560/aa6226

Imbault*, M., Chauvet*, D., Capelle, L., Demene, C., Mossad, M., Karachi, C., Boch, A.-L., Gennisson, J.-L., Tanter, M., 2015. In Vivo Measurement of Brain Tumor Elasticity Using Intraoperative Shear Wave Elastography. *Ultraschall in der Medizin - European Journal of Ultrasound*. doi:10.1055/s-0034-1399152

Gennisson, J., Provost, J., Deffieux, T., Papadacci, C., **Imbault**, M., Pernot, M., Tanter, M., others, 2015. 4-D ultrafast shear-wave imaging. *Ultrasonics, Ferroelectrics, and Frequency Control*, IEEE Transactions on 62, 1059–1065. doi:10.1109/TUFFC.2014.006936

The UFFC 2015 Outstanding Paper Award

Provost, J., Papadacci, C., Arango, J.E., **Imbault**, M., Fink, M., Gennisson, J.-L., Tanter, M., Pernot, M., 2014. 3D ultrafast ultrasound imaging in vivo. *Phys. Med. Biol.* 59, L1. doi:10.1088/0031-9155/59/19/L1

The Robert's Prize 2015 for the best paper in Physics in Medicine and Biology 2014

*These two author are co-first authors.

Peer-reviewed Abstracts

Imbault, M., Chauvet D., Capelle L., Serroune H., Gennisson J-L., Tanter, M., 2016. Functional Ultrasound Imaging of the Human Brain Activity: An Intraoperative Pilot Study for Cortical Functional Mapping. IEEE UIS, Tours.

Imbault, M., Demene, C., Mossad, M., Gennisson, J.L., Tanter, M., Chauvet, D., Capelle, L., Karachi, C., Boch, A.L., 2016. Improving brain tumor surgery using intra-operative shear wave elastography and ultrafast Doppler. WINE, Paris.

The 2015 WINE Best poster prize

Imbault, M., Faccinetto, A., Osmanski, B-F., Fink, M., Gennisson, J-L., Vilgrain, V., Tanter, M., 2015, Ultrasonic Assessment of hepatic steatosis using robust sound speed estimation, IEEE IUS, Taiwan.

The 2015 Student Paper Competition Award

Imbault, M., Chauvet, D., Capelle, L., Demene, C., Gennisson, J-L., Tanter, M., 2015, Improving brain tumor surgery using intra-operative shear wave elastography and micro Doppler, ITEC, Verona.

Imbault, M., Chauvet, D., Capelle, L., Demené, C., Gennisson, J-L., Tanter, M., 2014, Improving brain tumor surgery using intra-operative shear wave elastography and micro Doppler, Workshop neuroscience, Saclay.

Imbault, M., Demene, C., Mossad, M., Gennisson, J.L., Tanter, M., Chauvet, D., Capelle, L., Karachi, C., Boch, A.L., 2014. Intraoperative quantitative measurement of brain tumor stiffness and intracranial pressure assessment using ultrasound shear wave elastography, IEEE IUS, Chicago.

Papadacci, C., Villemain, O., Arango Ossa J-E., **Imbault**, M., Gennisson, J-L., M., Tanter, M., 2014. 3-D Ultrafast Imaging of the Heart In Vivo, IEEE IUS, Chicago.

Papadacci, C., Provot, J., Gennisson, J-L., Arango Ossa J-E., **Imbault**, M., Fink, M., Tanter, M., Pernot, M., 2014. 3D Ultrasound Backscatter Tensor Imaging (BTI): analysis of the full spatial coherence on a 2D matrix array probe, IEEE IUS, Chicago.

Gennisson, J-L., Deffieux T., Provost, J., Papadacci, C., Arango Ossa, J-E., **Imbault**, M., Pernot M., Tanter, M., 2014. Full 3D ultrafast shear wave imaging, IEEE IUS, Chicago.

Provost, J., Papadacci, C., Demene, C., Villemain, O., Arango Ossa, J-E., **Imbault**, M., Gennisson, J-L., Tanter, M., Pernot, M., 2014. 3-D Ultrafast Doppler Imaging In Vivo, IEEE IUS, Chicago.

Non Peer-reviewed Articles

Imbault, M., Serroune, H., Gennisson, J-l., Chauvet, D., Lehericy, S., Capelle, L., Tanter, M., 2016. Functional Ultrasound Imaging of the Human Brain Activity: An Intraoperative Pilot Study for Cortical Functional Mapping. In , 1–4. IEEE. doi:10.1109/ULTSYM.2016.7728505.

Imbault, M., Demene, C., Mossad, M., Gennisson, J.L., Tanter, M., Chauvet, D., Capelle, L., Karachi, C., Boch, A.L., 2014. Intraoperative quantitative measurement of brain tumor stiffness and intracranial pressure assessment using ultrasound shear wave elastography, in: Ultrasonics Symposium (IUS), 2014 IEEE International. IEEE, pp. 201–204.

Prizes

One of the 300 **2016 talents of the L’Oréal-UNESCO foundation for women and sciences**.

The UFFC 2015 Outstanding Paper Award for the paper entitled “4-D Ultrafast Shear-Wave Imaging” published in the IEEE Transactions on Ultrasonics, Ferroelectrics, and Frequency Control, Volume 62, No. 6, June 2015.

The Robert’s Prize 2015 for the best paper in Physics in Medicine and Biology 2014 for the paper entitled “3D ultrafast ultrasound imaging in vivo”.

The 2015 WINE Best poster prize for the poster entitled “Improving brain tumor surgery using intra-operative shear wave elastography and ultrafast Doppler”.

The 2015 Student Paper Competition Award for the paper entitled “Robust Sound Speed Estimation for Hepatic Steatosis Assessment” presented at the 2015 IEEE International Ultrasonics Symposium, October 21-24, 2015 – Taipei, Taiwan.